AUG 23 2000

RECEIVED
SEP 01 2000
OSTI

SANDIA REPORT

SAND2000-2017
Unlimited Release
Printed August 2000

Finite Element Numerical Solution of a Self-Adjoint Transport Equation for Coupled Electron-Photon Problems

Jennifer Liscum-Powell

Prepared by
Sandia National Laboratories
Albuquerque, New Mexico 87185 and Livermore, California 94550

Sandia is a multiprogram laboratory operated by Sandia Corporation,
a Lockheed Martin Company, for the United States Department of
Energy under Contract DE-AC04-94AL85000.

Sandia National Laboratories

Issued by Sandia National Laboratories, operated for the United States
Department of Energy by Sandia Corporation.

Available to DOE and DOE contractors from
U.S. Department of Energy
Office of Scientific and Technical Information
P.O. Box 62
Oak Ridge, TN 37831

Telephone: (865)576-8401
Facsimile: (865)576-5728
E-Mail: reports@adonis.osti.gov
Online ordering: http://www.doe.gov/bridge

Available to the public from
U.S. Department of Commerce
National Technical Information Service
5285 Port Royal Rd
Springfield, VA 22161

Telephone: (800)553-6847
Facsimile: (703)605-6900
E-Mail: orders@ntis.fedworld.gov
Online order: http://www.ntis.gov/ordering.htm

SAND2000-2017
Unlimited Release
Printed August 2000

Finite Element Numerical Solution of a Self-Adjoint Transport Equation for Coupled Electron-Photon Problems

Jennifer Liscum-Powell
Simulation Technology Research
Sandia National Laboratories
P.O. Box 5800
Albuquerque, NM 87185-1179

A novel approach is proposed for charged particle transport problems using a recently developed second-order, self-adjoint angular flux (SAAF) form of the Boltzmann transport equation with continuous slowing-down (CSD). A linear continuous (LC) in space and linear discontinuous (LD) in energy finite element discretization is implemented in the computer code DOET$_{1D}$: Discrete Ordinates Electron-Photon Transport in 1D. DOET$_{1D}$ is a one-dimensional, Cartesian coordinates, multigroup, discrete ordinates code for charged particle transport which employs CEPXS generated cross-sections to incorporate electron and photon transport physics.

The discrete ordinates SAAF transport equation is solved using scattering source iteration in conjunction with diffusion synthetic acceleration (DSA). The angular fluxes are computed simultaneously at all mesh points by solving a system of equations for each direction and each energy group. The application of LC finite elements in space yields a symmetric, positive definite coefficient matrix which is tridiagonal in structure and solved efficiently using a standard tridiagonal matrix solver. A second and unique within group iteration, referred to as upscatter, is introduced by the LD energy discretization. The upscatter iteration is separate from the source iteration and requires an independent acceleration scheme. A synthetic acceleration technique is derived to increase the rate of convergence of the upscatter iteration and implemented successfully in DOET$_{1D}$. The estimated spectral radius for the accelerated equations is sufficiently small that an efficient algorithm is achieved by performing at most two iterations for the DSA and upscatter steps.

Accurate charge and dose deposition profiles were obtained from the LD SAAF equation for several coupled electron-photon transport problems. Most importantly, it is demonstrated that the LD SAAF equation is able to accurately resolve charge and dose deposition at material interfaces between high-Z and low-Z materials.

Acknowledgements

This report was submitted to the University of New Mexico in partial fulfillment of the requirements for the degree of Doctor of Philosophy in Engineering.

I would like to thank my advisor and dissertation chair Dr. Anil Prinja for his guidance, enthusiasm and mentorship throughout the course of this research. I am thankful to my dissertation committee members Dr. Stanley Humphries, Dr. Leonard Lorence, Dr. Jim Morel, and Dr. Norman Roderick for both their valuable recommendations pertaining to my work and approval of this research.

Undertaking this research effort would not have been feasible without the unwavering support of my past and present supervisors at Sandia National Laboratories: Dr. Leann Adams Miller, Dr. William P. Ballard and Dr. Leonard Lorence. I am extremely grateful and fortunate to have had their backing.

Finally, I need to acknowledge Quint H. Powell for his tireless encouragement and faith in my ability in the darkest hours. I am forever grateful to you.

Contents

Figures

Tables

1 Introduction

Radiation transport codes are used to evaluate the effects of radiation from various sources on materials and systems. Predicting radiation transport or how radiation is propagated through matter and the energy and charge deposition that result is necessary to ascertain radiation effects. Radiation transport codes have been developed with the capability of analyzing a variety of radiation sources such as those produced by nuclear weapons (x-rays, gamma rays and neutrons), sources in space (electrons and ions) and accelerators (x-rays, gamma rays and electrons).[1] These codes can be used to study radiation effects on electronics, nuclear medicine and various industrial processes such as food irradiation.

Coupled electron-photon transport is used in the study of radiation effects on electronics such as transient radiation effects in electronics (TREE), system-generated electromagnetic pulse (SGEMP), internal electromagnetic pulse (IEMP), and X-ray dose enhancement. These radiation effects are observed following the impingement of x-rays (1 keV to 100 keV) and γ-rays (300 keV to 20 MeV) on electronics.

Transient radiation effects in electronics (TREE) are observed on a device level and are typically concerned with the generation of photocurrents in semiconductor devices, the creation of electric fields in oxides and the permanent degradation of device characteristics due to displacement producing radiation.[2] TREE is observed on a micron scale as depicted in Figure 1.1. In evaluating TREE, the output from radiation transport codes of primary interest is the differential dose in space in two and three dimensions.

IEMP is a pulse of transient electric and magnetic fields inside boxed subsystems such as circuit boards and multi-chip modules that is produced by currents of Compton electrons and photoelectrons and the return currents on conductors to replace ejected electrons.[2] When x-rays and γ-rays impinge on circuit boards or other enclosed electronics, photoelectron and Compton electron currents are emitted from all materials and in all directions. The densities of these emitted electrons depend on the material as well as the incident photon energy and intensity. IEMP effects are detailed on a printed circuit board in Figure 1.2 and result from the x-rays experiencing the photoelectric effect and γ-rays interacting through Compton scattering. The scale over which IEMP effects are observed is on the order of millimeters. Evaluating IEMP effects on enclosed electronics with radiation transport codes requires three-dimensional charge deposition profiles as well as three-dimensional forward and reverse electron emissions.

The photocurrent emission produced by x-ray photons impinging on a system's mechanical structure yields transient electric and magnetic fields on the outside of an object called SGEMP.[2] These electric and magnetic fields are generated by the

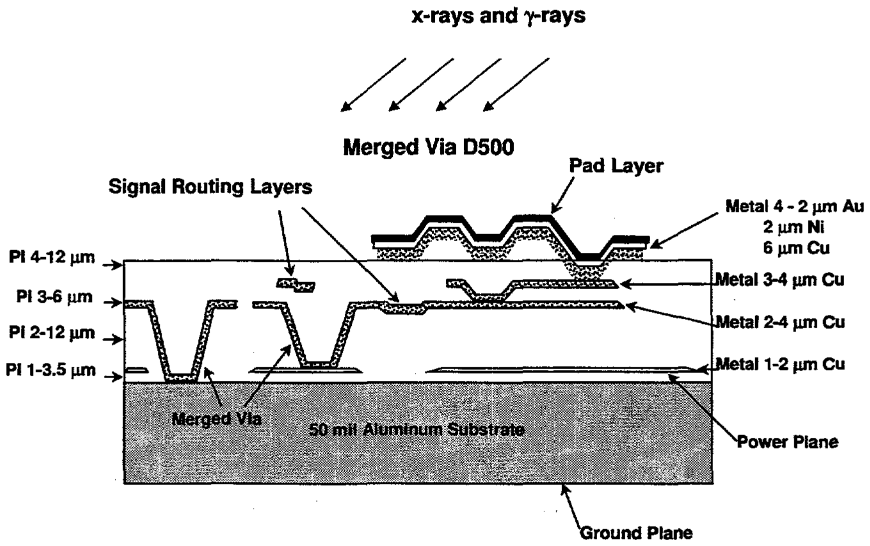

Figure 1.1: X-Rays and γ-Rays Impinging on a Device Resulting in TREE

emission of photoelectrons and Compton electrons as well as the currents which flow to replace the ejected electrons. SGEMP is often evaluated in relation to the x-ray irradiation of unshielded cables and cavities in nuclear weapons such as that depicted in Figure 1.3 and is observed on a system level. In evaluating the effects of cable SGEMP with radiation transport codes the two-dimensional charge-deposition profile is important while for cavity SGEMP the three-dimensional electron emission differential in space is desired.

Electron transport simulation is motivated by the importance of radiation hardness analysis and assessing the aforementioned phenomenon on the operation of electronic devices. Historically, the primary numerical technique for coupled electron-photon transport is the condensed history Monte Carlo method developed by Berger,[3] and used in production codes like the Integrated-TIGER-Series.[4] However, for charge deposition profiles that are used in studying the effects of SGEMP and IEMP in electronics it is difficult to obtain sufficient accuracy with Monte Carlo codes due to the statistical nature of this method; thus, a different method of solving coupled electron-photon transport problems is needed. Deterministic codes using the discrete ordinates method have been used extensively in neutral particle transport.[5,6] The discrete ordinates (S_n) method is a deterministic method for solving the transport equation in which the integro-differential form of the transport equation is solved in

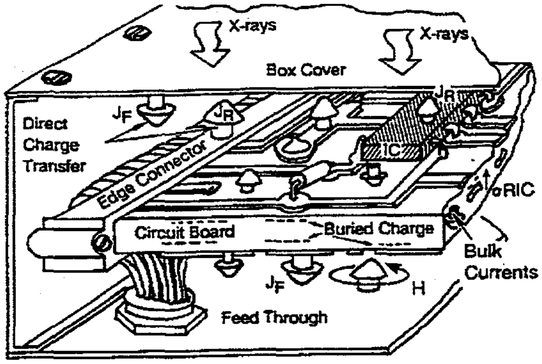

Courtesy of Burr Passenheim, "How to do Radiation Tests"

Figure 1.2: Printed Circuit Board Experiencing IEMP[2]

discrete angular directions.[5] In addition to the S_n approximation in angle, solving for the angular flux requires both a spatial and energy discretization scheme.

The discrete ordinates method was first applied to charged particle transport by Mehlhorn and Duderstadt[7] and Przybylski and Ligou.[8] Mehlhorn and Duderstadt formulated a discrete ordinates solution of the Fokker-Planck equation for charged particle transport in plasma and implemented it in the TIMEX code.[7] Przybylski and Ligou implemented the Boltzmann Fokker-Planck (BFP) equation in a one-dimensional, time-dependent code, BFP-1, using two numerical methods, a multigroup method and diamond differencing in both the space and energy variables.[8] The first discrete ordinates production code is the CEPXS/ONEDANT code package[9] which was later revised to the CEPXS/ONELD package when modifications were made to the ONEDANT solver to make it more suitable for electron transport problems, primarily through the addition of linear discontinuous spatial finite elements.[1]

Bartine, et. al., were the first to apply the discrete ordinates (S_n) method to coupled electron-photon transport in 1972 when they modified the solver in an existing one-dimensional discrete ordinates code (ANISN) to include a differenced form of the continuous slowing down (CSD) operator to simulate low-energy electrons.[10] The results that Bartine, et. al., obtained from their modified computer code were compared with experimental results showing that they simulated transport in low-Z materials (Al) well but experienced poor agreement with high-Z materials (Au).[10] These results brought to question whether or not the discrete ordinates method could be successfully used to solve electron transport problems. In 1979, Morel reported that the difficulties Bartine, et. al., observed in simulating electron transport in high-Z materials were not due to the use of the extended transport cross-section correction and suggested that future research be aimed at the treatment of inelastic electron processes.[11]

A successful application of discrete ordinates methods to coupled electron-

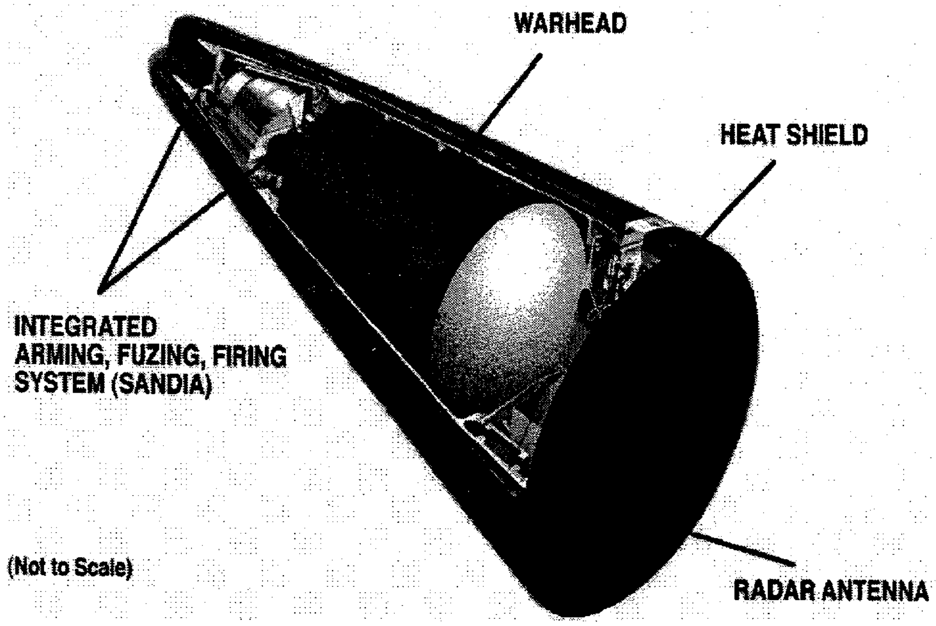

Figure 1.3: Unshielded Cables and Cavity Experience SGEMP

photon transport in space-shielding calculations was demonstrated by Lorence, et. al., which also proved that the discrete ordinates method is more efficient than the Monte Carlo technique.[12] Lorence, et. al.,[12] also concluded that the problems encountered by Bartine, et. al., in high-Z materials were most likely due to incomplete cross-sections for bremsstrahlung generation rather than an inherent deficiency of the S_n method for electron transport problems. Lorence also encountered success predicting electron photoemissions using the discrete ordinates production code CEPXS/ONETRAN.[13] This work helped build the foundation for the application of the discrete ordinates method to coupled electron-photon transport problems.

Some of the more familiar codes that are currently used to solve coupled electron-photon transport problems include CEPXS/ONELD, ONEBFP, MC-ITS and MCNP. CEPXS/ONELD is a coupled electron-photon discrete ordinates transport code that solves the BFP equation in one-dimensional geometries using "pseudo" cross-sections in an S_n code initially developed for neutral particle transport.[9] ONELD uses a linear discontinuous finite element approximation in space, a S_2 synthetic acceleration method and Galerkin quadrature sets. The "pseudo" cross-sections generated by CEPXS are used to incorporate the continuous slowing down (CSD) term that is present for charged particle transport problems in the neutral particle transport equation. ONEBFP is a one-dimensional, discrete ordinates code that solves the BFP transport equation.[14] ONEBFP uses a high order linear nodal scheme in space and energy (i.e. the explicit differencing of the CSD term). MC-ITS is a multigroup adjoint, electron-photon transport Monte Carlo code developed at Sandia National

Laboratories (SNL).[4] MCNP is a Monte Carlo neutron photon transport code developed at Los Alamos National Laboratory (LANL) that has been modified to include electron transport capability.[15] All of these codes solve a first-order form of the Boltzmann transport equation.

With the new massively parallel computers there is great interest in taking advantage of parallel processing in the solution of transport problems. The increased computational efficiency and memory offered by parallel process computers allows more detailed, multi-dimensional problems to be solved in a realistic time frame. In the past, evaluating multi-dimensional, arbitrary geometry problems was only feasible using Monte Carlo codes such as MC-ITS and MCNP but with the advent of high performance computing it is now feasible to solve these problems with discrete ordinate codes such as ATTILA.[16] ATTILA is a three-dimensional, unstructured mesh, S_n code developed at LANL which solves a first-order form of the transport equation.[16] Currently, a great deal of time and energy is being spent parallelizing existing transport codes to take advantage of the parallel processing environment.

The parallelization of S_n codes solving the first-order form of the transport equation is not efficient on massively parallel platforms. This inefficiency arises from the method in which the solution of a S_n form of the first-order transport equation can be parallelized which is limited to using domain decomposition to partition the solution between processors. The transition from a first-order form of the transport equation to a second-order form is motivated by the system of equations that results with the numerical analysis of this form that yields a system of equations ideally suited for specific parallel computing architectures. For instance, recent work in neutral particle transport has shown that solving a second-order, even-odd parity form of the Boltzmann transport equation for neutral particles results in a symmetric, positive-definite (SPD) matrix equation which is ideal for parallel computing.[17] Matrix equations with a symmetric, positive definite coefficient matrix are favored due to the existence of efficient, robust numerical techniques for their solution. In the area of charged particle transport, Josef and Morel recently developed a two-dimensional, simplified spherical harmonics coupled electron-photon code that solves an even-odd parity, second-order formulation of the transport equation using "pseudo" cross-sections which also resulted in an SPD matrix.[18]

The traditional second-order, even-odd parity formulation of the transport equation is characterized by other advantages over the first-order form besides SPD matrix equations. One advantage of the traditional second-order equation over the first-order equation is that the even- and odd-parity equations can be solved on multidimensional finite element spatial meshes using standard continuous finite element discretizations.[19] The presence of re-entrant cells can make this difficult to accomplish using the standard first-order equation.[19] Fully consistent diffusion based synthetic acceleration equations are easily derived from the second-order, even- and odd- parity transport equations.[20] Another advantage is that a spherical harmonics or P_n angular discretization is more easily solved using the second-order form rather than the first-order form due to the strong coupling of the flux moments.[19] There are disadvantages associated with solving the even- and odd-parity equations. For instance, the standard S_n sweeping algorithm is not applicable, instead the system of equations is solved for each direction across the entire spatial domain. Another disadvantage is that the reflective boundary conditions for the even- and odd-parity equation are complex and can be difficult to implement.[17] The calculation of the full angular flux from the even- and odd- parity components is difficult. Solving the traditional second-order equation in void regions and pure scattering media is problematic.[19]

The second-order self-adjoint, angular flux (SAAF) equation has all the advantages of the traditional even- and odd-parity equation as well as some other advantages. One advantage of the SAAF equation over the even- and odd- parity equations is that the full angular flux is directly solved by the SAAF equation. The boundary conditions for reflective and reflective-like boundaries are much easier to implement for the SAAF equation in comparison with the even- and odd-parity equation. Unlike the even- and odd-parity equation the SAAF equation can be solved in void regions in the appropriate form.[19] Like the traditional second-order equation, the S_n form of the SAAF equation cannot be solved using the standard sweeping algorithm applied to the first-order equation. The most notable disadvantage of the SAAF equation in comparison to the even- and odd-parity equation is that it has twice the angular domain. The solution of the SAAF equation in pure scattering media is also problematic.

S_n solutions of the first-order form of the transport equation have been explored extensively for both neutronics applications (i.e. ONEDANT) and charged particle transport (i.e. ONEBFP, ONELD). Similarly, the second-order, even-odd parity form of the transport equation has been explored with success in neutral particle transport[5,17,21] and to some extent in charged particle transport.[18] In this research we take a novel approach for charged particle transport by starting with a second-order, self-adjoint form of the BFP equation using a linear continuous in space and linear discontinuous in energy finite element discretization. In actuality, a modified form of the BFP equation is solved that does not include the full Fokker-Planck operator but only the continuous slowing-down (CSD) term. This form of the transport equation will be referred to as the Boltzmann-CSD equation throughout this document and is detailed in the next chapter. The premise of this work is to explore the potential of the second-order, self-adjoint Boltzmann-CSD equation for solving charged-particle transport problems such as cable SGEMP.

A one-dimensional (Cartesian coordinates), multigroup S_n code will be developed using CEPXS generated electron and photon cross-sections to incorporate charged-particle physics and enable the solution of coupled electron-photon problems. The S_n approximation of the angular variable will use a standard Gauss quadrature set. This work will not include utilizing parallel computing techniques. The computer code developed will calculate the energy dependent particle fluxes, energy deposition profiles and charge deposition profiles for coupled electron-photon transport problems. Code verification will be accomplished by comparing results with ONEBFP for select problems.

In the next chapter a description of coupled electron-photon transport physics is provided along with a detailed description of the interaction cross-sections provided by CEPXS. Furthermore, the derivation of the BFP equation will be discussed, the Boltzmann-CSD equation will be defined and the coupled electron-photon transport equations presented.

This page intentionally blank.

2 Coupled Electron-Photon Transport

The interactions that photons and electrons undergo are significantly different. Electron and photon transport is coupled due to the fact that sources of electrons or photons produce a cascade of radiation as they propagate through matter which consists of electrons (e^-), photons (γ) and positrons (e^+).

2.1 Photon Interactions with Matter

Photons consist of gamma rays, continuous and characteristic X-rays, and annihilation radiation. Photons are classified according to their mode of origin.[22] The electromagnetic radiation that accompanies nuclear transitions are called gamma rays. Continuous X-rays or bremsstrahlung are emitted from radiative inelastic collisions of charged particles while characteristic X-rays are emitted during atomic transitions of bound electrons between shells. When an electron and positron combine annihilation radiation is emitted. Photon interactions are dominated by absorption and inelastic scattering collisions that reduce the photon's energy. The principal interactions of photons in matter are the photoelectric effect, inelastic (Compton) scattering , elastic (Thomson) scattering, pair production and photonuclear reactions.[23]

Photoelectric Effect Below energies of 100 keV the dominant interaction of photons for high-Z materials is the photoelectric effect. When the photoelectric effect takes place a photon interacts with an electron bound in an atom and is completely absorbed. An electron is ejected from the atom with an energy that is equal to the photon energy less the binding energy of the electron. The ejected electron is called a photoelectron. The absorption process is characterized by the emission of characteristic X-rays and Auger electrons as the atom transitions to fill the vacancy left by the ejected electron. The probability of photoelectric absorption is largest for high-Z materials and low-energy photons (< 100 keV).

Inelastic (Compton) Scattering In this scattering interaction a photon is scattered off an electron, losing energy and changing direction. This scattering also results in a recoil electron, referred to as a Compton electron, which is knocked loose from the target atom. This ionization primarily occurs with the outermost atomic shells and results in a cascade of Auger electrons and fluorescence photons that are very low in energy. This cascade of radiation is also referred to as relaxation radiation. The probability of photons undergoing a Compton scattering event increases with the incident photon energy and material atomic number.

Elastic (Thomson) Scattering In an elastic scattering event a photon is scattered off an electron and changes direction without experiencing a loss in energy. The probability of photons undergoing a Thomson scattering event is largest for low energy photons (< 100 keV).

Pair Production In this threshold process a photon with a minimum energy of 1.022 MeV is converted into an electron-positron pair in the field of an atomic nucleus. The photon is completely absorbed and an electron-positron pair is produced with a total energy equal to the incident photon. The probability of a photon undergoing pair production increases with photon energy and atomic number.

Photonuclear Reactions In photonuclear reactions or photodisintegration, photons are absorbed by an atomic nucleus and a nucleon is ejected. Photonuclear reactions are threshold processes in which the incident photon must possess enough energy to overcome the nucleon binding energy, usually several MeV. The probability for photonuclear reactions is orders of magnitude smaller than the combined probabilities of the photon interactions discussed above.[23]

2.2 Electron Interactions with Matter

The interactions of electrons with matter differ from photons due to the lack of absorption events, rather electrons are dominated by scattering events. Electrons are dominated by elastic scattering events in which there is deflection but no energy loss and inelastic scattering events which yield small energy losses and no deflection. Charged particles are characterized by a stopping power which is the energy loss per path length traveled in MeV/cm. For electrons there are three major types of interactions: elastic scattering, collisional inelastic scattering and radiative inelastic scattering.[23]

Collisional Inelastic Scattering An electron that undergoes a collisional inelastic scattering event loses energy as it undergoes a change in direction. Collisional scattering is often divided into two categories "hard" or "catastrophic" for large energy losses and "soft" for small energy losses. "Hard" collisions ionize the innermost atomic shells and result in the generation of secondary or "knock-on" electrons as well as a cascade of relaxation radiation made up of Auger electrons and fluorescence photons. "Soft" collisions ionize the outermost shells and/or excite the atom. "Knock-on" electrons and relaxation radiation produced by "soft" collisions are very low in energy. The inelastic cross-section rapidly increases as energy loss becomes small; that is, "soft" collisions dominate.

Radiative Inelastic Scattering When an electron undergoes radiative inelastic scattering it results in the production of bremsstrahlung. Radiative inelastic scattering or bremsstrahlung production dominates for high energy electrons in high-Z materials. At high energies, radiative scattering can give rise to electron-photon cascade showers because high-energy electrons yield high-energy photons which can undergo Compton scattering and pair-production producing more electrons that can also undergo radiative inelastic scattering.[23]

Elastic Scattering A electron undergoing an elastic scattering event experiences a directional change without significant energy loss. Elastic scattering interactions for electrons are highly forward peaked or highly anisotropic. Unlike photons, elastic scattering interactions are significant for electrons and play a major role in electron transport.

2.3 CEPXS Cross-Section Generating Code

The probability of an electron or photon undergoing a certain type of interaction is quantified by cross-sections. Electron cross-sections are many orders of magnitude greater than photon cross-sections.[1] The difference in magnitude between the cross-sections of photons and electrons means that their respective mean free paths are very different; and therefore, the scale over which interactions occur is different. For instance, if we consider a 1.0 MeV photon and a 1.0 MeV electron traveling through lead the mean free path for the photon is 1.25 cm while the electron's mean free path is only $3.0\text{x}10^{-6}$ cm.[1] This radical difference in the scale over which interactions occur for electrons and photons adds to the challenge of accurately modeling coupled electron-photon transport problems. The extremely small scale for electron interactions requires a high-order spatial discretization scheme or a very fine mesh to be accurately modeled.

Including real physics in a coupled electron-photon transport code is achieved through coupling to the appropriate cross-section sets. CEPXS is a multigroup Legendre cross-section generating code for electrons and photons developed in a collaboration between SNL and LANL.[24] The cross-sections generated by CEPXS allow coupled electron-photon transport calculations to be performed with standard discrete ordinates codes. CEPXS extracts electron cross-sections from the DATAPAC data set, photon cross-section information from Biggs-Lighthill data and treats ionization and relaxation with the same model employed by MC-ITS.[24] Coupling to CEPXS allows electron and photon transport to be modeled using "real" physics. CEPXS provides the following cross-sections for electron interactions with matter: elastic scattering, inelastic collisional scattering, inelastic radiative collisional scattering, "knock-on" electron production, radiative emission and K-shell impact ionization and relaxation.[24] For photon transport, CEPXS models: Compton scattering and electron production, photoelectric absorption, photoelectron production, and pair production.[24] For more detailed information on the treatment of the physics of electron and photon interactions in CEPXS, the reader is referred to the CEPXS Physics guide.

Photon cross-sections for these interactions are readily cast into the multigroup Legendre form needed by deterministic codes while electron cross-sections require additional approximations to be derived in this form. The fundamental differences between electron and neutral particle cross-sections are that electron cross-sections are highly forward peaked and their inelastic cross-section increases rapidly in magnitude as the energy loss goes to zero.[9] A standard multigroup Legendre representation of the electron elastic scattering cross-sections would be prohibitive requiring a large number of energy groups and a large order for the Legendre expansion resulting in high computational costs. To deal with the difficulties of casting electron cross-sections into a multigroup Legendre form two approximations are introduced:[9] (1) the extended transport cross-section correction and (2) the continuous slowing down approximation (CSDA).

The extended transport cross-section correction permits the forward-peaked electron scattering cross-section to be accurately represented by a modest order Legendre expansion.[11] In the extended transport correction the elastic scattering cross-section is corrected by removing a delta-function component representing within-group scattering.[11,25] The multigroup approximation for electron cross-sections is practical with the CSDA which treats the "soft" inelastic scattering interactions that dominate electron transport as a continuous slowing down of the electrons as they propagate through matter.[24] CSDA can be envisioned as a drag force on the electrons as they move through matter in the same way a drag force operates on a particle moving through a fluid. CSDA is implemented by solving a modified BFP transport equation for charged-particle calculations using a restricted stopping power in the CSD term.[10,26] The restricted stopping power accounts only for "soft" scattering collisions characterized by small energy losses with no deflection.

Solving the electron transport problems with standard discrete ordinate transport codes written for neutral particles requires the CSD term to be included through means of an approximation. CEPXS includes the option to generate special electron cross-sections that can be used with conventional discrete ordinate codes to effectively solve the BFP equation using the neutral particle Boltzmann transport equation.[9] The approach incorporated in CEPXS is based on the development of "pseudo" cross-sections which represent a differenced form of the CSD operator derived by Morel.[26,27] This approximation allows the BFP equation to be solved effectively in the neutral particle transport equation by including the CSD operator in the differential scattering cross-section using these "pseudo" cross-sections.

2.4 Coupled Electron-Photon Transport Equation

The purpose of radiation transport is to determine how particles move through materials and what effects their propagation has on the material through the mechanisms of energy and charge deposition. The angular flux, denoted as $\Psi(\mathbf{r}, E, \mathbf{\Omega})$, represents the flux of particles at position $\mathbf{r}$, with energy E and traveling in direction $\mathbf{\Omega}$, and yields physically interesting quantities such as the photon energy spectrum and electron currents. Energy deposition (dose) and charge deposition can also be determined by combining cross-sections with particle fluxes.

The angular flux can be determined by solving the three-dimensional, time-independent Boltzmann transport equation[5] which is written as

$$\begin{aligned} &\mathbf{\Omega} \cdot \nabla\Psi(\mathbf{r}, E, \mathbf{\Omega}) + \sigma_t(\mathbf{r}, E)\Psi(\mathbf{r}, E, \mathbf{\Omega}) = \\ &\int dE' \int d\mathbf{\Omega}' \, \sigma_s(\mathbf{r}, E' \to E, \mathbf{\Omega}' \cdot \mathbf{\Omega}) \cdot \Psi(\mathbf{r}, E', \mathbf{\Omega}') + Q(\mathbf{r}, E, \mathbf{\Omega}) \end{aligned} \tag{2.1}$$

where

$\Psi(\mathbf{r}, E, \mathbf{\Omega})$ = at position $\mathbf{r}$, with energy E and traveling in direction $\mathbf{\Omega}$
$\sigma_t(\mathbf{r}, E)$ = total cross-section at position $\mathbf{r}$, energy E
$\sigma_s(\mathbf{r}, E' \to E, \mathbf{\Omega}' \cdot \mathbf{\Omega})$ = differential scattering cross-section
$Q(\mathbf{r}, E, \mathbf{\Omega})$ = external source at position $\mathbf{r}$, energy E, and traveling in direction $\mathbf{\Omega}$

The direction $\mathbf{\Omega}$ is a unit vector which is depicted in Figure 2.2 and is mathematically represented by

$$\mathbf{\Omega} = \sqrt{1-\mu^2}\sin\phi\hat{i} + \sqrt{1-\mu^2}\cos\phi\hat{j} + \mu\hat{k} \tag{2.2}$$

The right-hand side of equation 2.1 represents the scattering source and external source. The scattering source is the integral of the cross-section differential in energy and angle. For charged-particle transport the scattering cross-sections are extremely forward peaked and equation 2.1 is not the best suited equation for modeling their transport through matter; rather the Boltzmann Fokker-Planck (BFP) equation is used.

2.4.1 Boltzmann Fokker-Planck Equation

The extremely forward-peaked scattering cross-section that characterizes charged-particle transport looks like a delta function around a scattering angle of 0° which

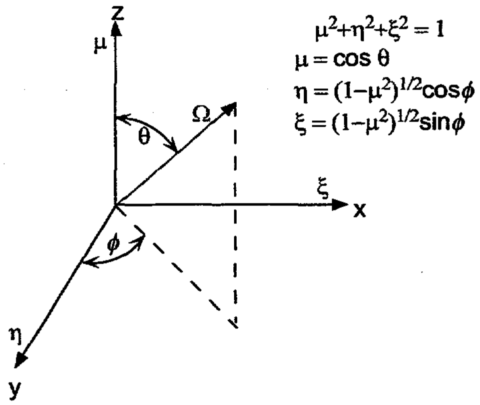

Figure 2.2: Angular Coordinate System

cannot be approximated with a typical polynomial expansion.[8] To overcome this problem, the Fokker-Planck approximation, is introduced into the Boltzmann transport equation. The BFP equation is derived from the linear Boltzmann transport equation for neutral particles by approximating the integral Boltzmann scattering operator with a differential operator using Taylor expansion techniques.[8,26] In elastic scattering the energy loss and scattering angle are coupled allowing the differential scattering cross-section to be expressed as follows:[26]

$$\sigma_s(\mathbf{r}, E' \rightarrow E, \mu_\circ) = \sigma_s(\mathbf{r}, E' \rightarrow E)\delta[\mu_\circ - f(E, E')] \tag{2.3}$$

The Fokker-Planck approximation replaces the integral scattering operator for extremely forward peaked scattering events with a three term differential operator. This operator, called the Fokker-Planck operator, effectively decouples energy loss and scattering angle by separating the scattering integral into a term that represents the change in direction without energy loss and two terms that combine to represent the redistribution of energy without a directional change.[26] The BFP equation[26] is

$$\begin{gathered}\boldsymbol{\Omega}\cdot\nabla\Psi(\mathbf{r},E,\boldsymbol{\Omega}) + \sigma_t(\mathbf{r},E)\Psi(\mathbf{r},E,\boldsymbol{\Omega}) = \qquad (2.4)\\ \int dE' \int d\boldsymbol{\Omega}'\, \sigma_s(\mathbf{r},E'\rightarrow E,\boldsymbol{\Omega}'\cdot\boldsymbol{\Omega})\cdot\Psi(\mathbf{r},E',\boldsymbol{\Omega}') + Q(\mathbf{r},E,\boldsymbol{\Omega}) + \pounds_{FP}\Psi(\mathbf{r},E,\boldsymbol{\Omega})\end{gathered}$$

where the Fokker-Plank operator, $\pounds_{FP}$, is

$$\frac{\partial}{\partial E}S(\mathbf{r},E) + \frac{\partial^2}{\partial E^2}S^*(\mathbf{r},E) + \frac{T(\mathbf{r},E)}{2}\left[\frac{\partial}{\partial\mu}(1-\mu^2)\frac{\partial}{\partial\mu} + \frac{1}{(1-\mu^2)}\frac{\partial^2}{\partial\phi^2}\right] \tag{2.5}$$

The first term in the operator describes continuous energy loss, with the energy loss per unit pathlength given by the stopping power. The second term in the Fokker-Planck operator contains the mean-square stopping power and estimates energy-loss straggling as particles "diffuse" in the energy space.[26] The final term causes particles to scatter continuously with a mean deflection per unit pathlength dictated by the momentum transfer. The stopping power, mean-square stopping power and momentum transfer are defined as follows:

$$S(\mathbf{r},E) = \int_0^\infty \sigma_s(\mathbf{r},E\rightarrow E')(E\rightarrow E')dE' \tag{2.6}$$

$$S^*(\mathbf{r},E) = \int_0^\infty \sigma_s(\mathbf{r},E\rightarrow E')(E\rightarrow E')^2dE' \tag{2.7}$$

$$T(\mathbf{r},E) = 2\pi\int_{-1}^{1} \sigma_s(\mathbf{r},E,\mu_\circ)(1-\mu_\circ)d\mu_\circ \tag{2.8}$$

Continuous Slowing Down Approximation The extremely large inelastic collisional cross-section is approximated through the introduction of the CSDA which treats "soft" inelastic collisions as a continuous energy loss without deflection. The CSDA corresponds to setting $S^*(\mathbf{r},E)=0$, ignoring energy-loss straggling,[26] and reducing equation 2.4 to:

$$\begin{aligned}\boldsymbol{\Omega}\cdot\nabla\Psi(\mathbf{r},E,\boldsymbol{\Omega})-\frac{\partial}{\partial E}S(\mathbf{r},E)\Psi(\mathbf{r},E,\boldsymbol{\Omega})+\sigma_t(\mathbf{r},E)\Psi(\mathbf{r},E,\boldsymbol{\Omega})=\\ \int dE'\int d\boldsymbol{\Omega}'\,\sigma_s(\mathbf{r},E'\to E,\boldsymbol{\Omega}'\cdot\boldsymbol{\Omega})\cdot\Psi(\mathbf{r},E',\boldsymbol{\Omega}')+Q(\mathbf{r},E,\boldsymbol{\Omega})\\ +\frac{T(\mathbf{r},E)}{2}\left[\frac{\partial}{\partial\mu}(1-\mu^2)\frac{\partial}{\partial\mu}+\frac{1}{(1-\mu^2)}\frac{\partial^2}{\partial\phi^2}\right]\Psi(\mathbf{r},E,\boldsymbol{\Omega})\end{aligned}\tag{2.9}$$

Implementing the CSDA approximation dictates the use of the restricted stopping power which is defined only for "soft" collisions. Consequently, the cross-sections, $\sigma_t(\mathbf{r},E)$ and $\sigma_s(\mathbf{r},E'\to E,\boldsymbol{\Omega}'\cdot\boldsymbol{\Omega})$, in equation 2.9 include only "hard" collisions. The term with restricted stopping power in equation 2.9 is referred to as the CSD operator.

Boltzmann-CSD Equation

A further modification can be made to the BFP equation for typical electron transport problems. The momentum transfer term in the Fokker-Planck operator is only important for heavy-charged particle transport and electron beam problems. Therefore, in typical electron transport problems it is often ignored and equation 2.4 is modified to become the Boltzmann-CSD equation:

$$\begin{aligned}\boldsymbol{\Omega}\cdot\nabla\Psi(\mathbf{r},E,\boldsymbol{\Omega})-\frac{\partial}{\partial E}S(\mathbf{r},E)\Psi(\mathbf{r},E,\boldsymbol{\Omega})+\sigma_t(\mathbf{r},E)\Psi(\mathbf{r},E,\boldsymbol{\Omega})=\\ \int dE'\int d\boldsymbol{\Omega}'\,\sigma_s(\mathbf{r},E'\to E,\boldsymbol{\Omega}'\cdot\boldsymbol{\Omega})\cdot\Psi(\mathbf{r},E',\boldsymbol{\Omega}')+Q(\mathbf{r},E,\boldsymbol{\Omega})\end{aligned}\tag{2.10}$$

which is the form of the transport equation used for e^- in this research.

2.4.2 Coupled Electron-Photon Transport Equations

Coupling occurs between the photon and electron transport equations (2.1, 2.9) as a result of the fact that electron interactions generate photons and photon interactions generate electrons. The coupled electron-photon equations are given as:

$$\begin{aligned}\boldsymbol{\Omega}\cdot\nabla\Psi_e(\mathbf{r},E,\boldsymbol{\Omega})-\frac{\partial}{\partial E}S(\mathbf{r},E)\Psi_e(\mathbf{r},E,\boldsymbol{\Omega})+\sigma_{t,e}(\mathbf{r},E)\Psi_e(\mathbf{r},E,\boldsymbol{\Omega})=\\ \int_0^\infty dE'\int_{4\pi}d\boldsymbol{\Omega}'\sigma_{s,e\to e}(\mathbf{r},E'\to E,\boldsymbol{\Omega}'\cdot\boldsymbol{\Omega})\Psi_e(\mathbf{r},E',\boldsymbol{\Omega}')\quad(2.11)\\ +\int_0^\infty dE'\int_{4\pi}d\boldsymbol{\Omega}'\sigma_{s,\gamma\to e}(\mathbf{r},E'\to E,\boldsymbol{\Omega}'\cdot\boldsymbol{\Omega})\Psi_\gamma(\mathbf{r},E',\boldsymbol{\Omega}')+Q_e(\mathbf{r},E,\boldsymbol{\Omega})\end{aligned}$$

$$\begin{aligned}\boldsymbol{\Omega}\cdot\nabla\Psi_\gamma(\mathbf{r},E,\boldsymbol{\Omega})+\sigma_{t,\gamma}(\mathbf{r},E)\Psi_\gamma(\mathbf{r},E,\boldsymbol{\Omega}) &= \\ \int_0^\infty dE'\int_{4\pi}d\boldsymbol{\Omega}'\sigma_{s,\gamma\to\gamma}(\mathbf{r},E'\to E,\boldsymbol{\Omega}'\cdot\boldsymbol{\Omega})\Psi_\gamma(\mathbf{r},E',\boldsymbol{\Omega}') & \qquad (2.12)\\ +\int_0^\infty dE'\int_{4\pi}d\boldsymbol{\Omega}'\sigma_{s,e\to\gamma}(\mathbf{r},E'\to E,\boldsymbol{\Omega}'\cdot\boldsymbol{\Omega})\Psi_e(\mathbf{r},E',\boldsymbol{\Omega}')+Q_\gamma(\mathbf{r},E,\boldsymbol{\Omega}) &\end{aligned}$$

where

$\Psi_e(\mathbf{r},E,\boldsymbol{\Omega}),\Psi_\gamma(\mathbf{r},E,\boldsymbol{\Omega})$ = Electron, photon angular flux
$\boldsymbol{\Omega}$ = Particle direction
$\sigma_{t,e}(\mathbf{r},E),\sigma_{t,\gamma}(\mathbf{r},E)$ = Electron, photon total cross-section
$\sigma_{s,e\to e}(\mathbf{r},E'\to E,\boldsymbol{\Omega}'\cdot\boldsymbol{\Omega})$ = e^- to e^- differential scattering and production cross-section

$\sigma_{s,\gamma\to e}(\mathbf{r},E'\to E,\boldsymbol{\Omega}'\cdot\boldsymbol{\Omega})$ = γ to e^- differential scattering cross-section
$\sigma_{s,\gamma\to\gamma}(\mathbf{r},E'\to E,\boldsymbol{\Omega}'\cdot\boldsymbol{\Omega})$ = γ to γ differential scattering cross-section
$\sigma_{s,e\to\gamma}(\mathbf{r},E'\to E,\boldsymbol{\Omega}'\cdot\boldsymbol{\Omega})$ = e^- to γ differential scattering cross-section
$S(\mathbf{r},E)$ = Electron restricted stopping power
$Q_e(\mathbf{r},E,\boldsymbol{\Omega}),Q_\gamma(\mathbf{r},E,\boldsymbol{\Omega})$ = External source

The units associated with the angular fluxes, Ψ_e and Ψ_γ, and the external sources, Q_e and Q_γ, are $\left(\frac{\#}{cm^2\ \text{str MeV}}\right)$. The particle direction, Ω, has units of steradians (str). The total cross-sections are in cm^{-1} while the differential cross-sections have units of $\left(\frac{1}{\text{cm MeV str}}\right)$. The electron stopping power defines the energy loss per unit pathlength traveled and has units of $\left(\frac{MeV}{cm}\right)$. In equation 2.11, the "hard" collisions are treated with the integral operator while the "soft" collisions are treated by the CSD operator.

In the next chapter numerical solutions of the transport equation will be discussed. The scattering source iteration approach will also be introduced.

3 Numerical Solution of the Transport Equation

Numerical techniques used to solve particle transport problems utilize either stochastic or deterministic methods. The Monte Carlo technique is a stochastic method that simulates individual particle trajectories by "random walk". Codes that use the Monte Carlo (MC) method do not explicitly solve the transport equation, rather they construct particle histories by systematically sampling changes in position, energy and direction using cross-section derived probability distributions.[1] MC-ITS and MCNP are examples of MC codes that solve coupled electron-photon problems.[4,15] In deterministic methods, a discretized version of the transport equation is solved.[5] The discrete ordinates or S_n method (discrete angles) is the dominant deterministic method used in particle transport which was refined for neutral particle transport in the early 1950s at LANL.[1] In the S_n method, the scattering integral is evaluated using quadrature sets, such as the Gauss quadrature set, combined with a Legendre expansion of the scattering cross-section.

There are advantages and disadvantages associated with both the MC and deterministic methods, and consequently, there are proponents of each method for the solution of transport problems. Each method is associated with errors, for the MC method these errors are statistical in nature while deterministic methods are characterized by discretization errors. In evaluating charge deposition and electron currents necessary in the study of radiation effects in electronics deterministic codes have a definite advantage over MC codes. Determining the charge deposition is difficult for MC because of the inherently poor statistics due to the fact that charge deposition occurs at a point in space rather than over a path. Also the extremely fine spatial resolution required to get the charge deposition at a point is difficult to achieve with MC codes. The statistical nature of MC also makes it hard to determine photoelectric and Compton electron emission and currents. As discussed earlier in Chapter 1, charge deposition is important in evaluating IEMP and cable SGEMP while currents are necessary in evaluating cavity SGEMP. Accurately evaluating charge deposition and electron currents is one of the fundamental reasons for using S_n codes in charged-particle transport problems.

Traditionally, coupled electron-photon transport problems have been modeled using condensed-history Monte Carlo codes or deterministic codes using the S_n method for neutral particle transport coupled with CEPXS generated cross-sections.[4,9] In this discrete ordinates approach the BFP equation is effectively solved by incorporating a CEPXS generated "pseudo" cross-section that lumps the CSD operator together with the electron differential scattering cross-section.[9,27] These "pseudo" cross-sections were derived by Morel by discretizing the explicit CSD operator using the diamond difference (DD) method.[27] Lazo and Morel applied a LD approximation to the CSD operator which also resulted in "pseudo" cross-sections.[28] These "pseudo" cross-sections allowed the BFP equation to be solved using well-established, neutral particle discrete ordinate codes such as ONEDANT[6] effectively solving coupled electron-photon transport problems without the need to develop new discrete ordinates codes specifically for charged-particle transport problems.

Over the years several methods have been developed to solve electron energy and charge deposition by reproducing the continuous slowing down operator using various difference schemes on the BFP equation. For instance, Przybylski and Ligou[8] applied the DD scheme to a coupled treatment of the energy and space variables. Honrubia and Aragonés[29] applied a linear discontinuous (LD) finite element scheme to the BFP equation to both space and energy to provide a coupled treatment of these variables. Despite the research efforts that have been directed towards the solution of charged particle transport problems, few production codes are available such as CEPXS/ONELD and ONEBFP.[9,14]

Due to the CSD term and the rapid loss of energy experienced by charged particles, solving electron transport problems requires higher order discretization schemes. Higher order schemes can refer to higher order discontinuous spatial representations in finite element methods or higher order continuous nodal methods. Moving to a higher order continuous scheme like the linear nodal method does not guarantee that oscillations will be damped as they still lack the flexibility to handle the sharp gradients experienced due to rapid energy loss or at material interfaces between high-Z and low-Z materials. However, discontinuous discretization schemes tend to be more robust.

The research presented in this document employs a deterministic method to solve the Boltzmann-CSD transport equation for coupled electron-photon transport problems. The transport equation is discretized in angle using discrete ordinates and in space and energy using finite elements. The scattering kernel is expanded using Legendre polynomials and multigroup cross-sections from CEPXS are used. Here a brief overview of the multigroup approximation, Legendre expansion of the scattering kernel and the angle, space and energy discretization schemes employed in this work is provided. For reference, the continuous one-dimensional Boltzmann-CSD equation is given below as

$$\mu\frac{\partial}{\partial x}\Psi(x,E,\mu) - \frac{\partial}{\partial E}\left\{S(x,E)\Psi(x,E,\mu)\right\} + \sigma_t(x,E)\Psi(x,E,\mu) = \int_0^\infty dE' \int_{-1}^{1} d\mu' \sigma_s(x,E' \to E,\mu_o)\Psi(x,E',\mu') + Q(x,E,\mu) \tag{3.1}$$

where $\mu_o = \mathbf{\Omega}' \cdot \mathbf{\Omega}$.

3.1 Multigroup Approximation

Treating the energy domain with the multigroup approximation requires that the energy range be divided into G intervals as depicted in Figure 3.2. The particles in group g are those with energies between $E_{g+1/2}$ and $E_{g-1/2}$ and the traditional notation is that the group with the highest energy is $g = 1$ and the group with lowest energy is $g = G$. The group angular flux is defined as

$$\Psi_g(\mathbf{r}, \mathbf{\Omega}) = \frac{1}{\Delta E_g} \int_{E_{g+1/2}}^{E_{g-1/2}} dE\, \Psi(\mathbf{r}, E, \mathbf{\Omega}) \tag{3.2}$$

The integral over all energies is then defined as follows

$$\int_0^\infty dE = \sum_{g=1}^{G} \int_g dE = \sum_{g=1}^{G} \Delta E_g$$

Multigroup cross-sections are treated as constants within each energy group and are defined in CEPXS as

$$\sigma_g(\mathbf{r}) = \frac{1}{\Delta E_g} \int_{E_{g+1/2}}^{E_{g-1/2}} dE\, \sigma(\mathbf{r}, E) \tag{3.3}$$

Introducing the multigroup approximation into the one-dimensional scattering source in equation 3.1 transforms it as follows

$$\begin{gathered} \int_0^\infty dE' \int_{-1}^{1} d\mu'\, \sigma_s(x, E' \to E, \mu_o)\Psi(x, E', \mu') = \\ \sum_{g'=1}^{G} \int_g dE \int_{g'} dE' \int_{-1}^{1} d\mu'\, \sigma_s(x, E' \to E, \mu_o)\Psi(x, E', \mu') \end{gathered} \tag{3.4}$$

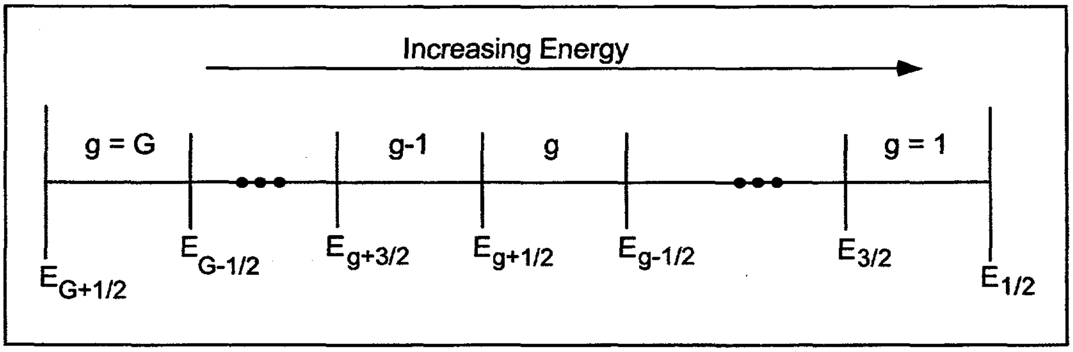

Figure 3.2: Division of Energy Range into G Groups

The multigroup differential scattering cross-section from group g' to g is defined as

$$\sigma_s^{g'\to g}(x,\mu_o) = \int_g dE \int_{g'} dE'\, \sigma_s(x, E' \to E, \mu_o) \tag{3.5}$$

and the multigroup scattering source in group g becomes

$$Q_g^S = \sum_{g'=1}^{G} \frac{\Delta E_{g'}}{\Delta E_g} \int_{-1}^{1} d\mu'\, \sigma_s^{g'\to g}(x,\mu_o)\Psi_{g'}(x,\mu') \tag{3.6}$$

3.2 Legendre Expansion of Scattering Cross-Section

The differential scattering cross-section appearing in the scattering source in equation 3.1 will be expressed as a Legendre expansion as depicted below

$$\sigma_s^{g'\to g}(\mathbf{r}, \boldsymbol{\Omega}'\cdot\boldsymbol{\Omega}) = \sum_{l=0}^{\infty} \frac{(2l+1)}{4\pi} \sigma_{s,l}^{g'\to g}(\mathbf{r}) P_l(\mu_\circ) \tag{3.7}$$

where $\sigma_{s,l}^{g'\to g}(\mathbf{r})$ are the Legendre moments of the scattering cross-section from $g' \to g$. Introducing the Legendre expansion of the scattering cross-section into a general multigroup scattering source gives

$$\begin{aligned} &\sum_{g'=1}^{G} \frac{\Delta E_{g'}}{\Delta E_g} \int_{4\pi} d\Omega'\, \sigma_s^{g'\to g}(\mathbf{r}, \boldsymbol{\Omega}'\cdot\boldsymbol{\Omega})\Psi_{g'}(\mathbf{r},\boldsymbol{\Omega}') \\ &= \sum_{g'=1}^{G} \frac{\Delta E_{g'}}{\Delta E_g} \sum_{l=0}^{\infty} \frac{(2l+1)}{4\pi} \sigma_{s,l}^{g'\to g}(\mathbf{r}) \phi_{g',l}(\mathbf{r}) \end{aligned} \tag{3.8}$$

where the Legendre moments of the flux are defined as

$$\phi_{g',l}(\mathbf{r}) = \int_{4\pi} d\Omega'\, P_l(\mu)\Psi_{g'}(\mathbf{r},\boldsymbol{\Omega}') \tag{3.9}$$

and

$$\begin{aligned} P_l(\mu_\circ) &= P_l(\boldsymbol{\Omega}'\cdot\boldsymbol{\Omega}) \\ &= P_l(\mu)P_l(\mu') + 2\sum_{m=1}^{l} \frac{(l-m)!}{(l+m)!} P_l^m(\mu)P_l^m(\mu')\cos[m(\phi-\phi')] \end{aligned} \tag{3.10}$$

which in 1-D reduces to

$$P_l(\mu_\circ) = P_l(\mu)P_l(\mu') \tag{3.11}$$

$P_l^m(\mu)$ and $P_l^m(\mu')$ are the associated Legendre functions given by

$$P_l^m(\mu) = (-1)^m(1-\mu^2)^{m/2}\frac{d^m}{d\mu^m}(\mu^2-1) \tag{3.12}$$

With the Legendre expansion of the scattering cross-section the one-dimensional scattering source in equation 3.1 becomes

$$\begin{aligned} &\int_0^\infty dE' \int_{-1}^{1} d\mu' \, \sigma_s(x, E' \to E, \mu')\Psi(x, E', \mu') \\ &= \sum_{g'=1}^{G} \frac{\Delta E_{g'}}{\Delta E_g} \sum_{l=0}^{L} \frac{(2l+1)}{4\pi} \, \sigma_{s,l}^{g' \to g}(x) \, P_l(\mu)\phi_{g',l}(x) \end{aligned} \tag{3.13}$$

The order of the Legendre expansion is truncated to a maximum value L which determines the degree of anisotropy incorporated into the scattering kernel. For isotropic scattering, $L = 0$, the total scattering cross-section ($\sigma_{s,0}$) and scalar flux (ϕ_0) make up the scattering source.

3.3 Discrete Ordinates Formulation

Using discrete ordinates angular discretization requires that equation 3.1 be evaluated for a finite number of distinct angles, μ_n, and a quadrature approximation is used to evaluate the integral term in angle. If a quadrature formula on the interval $-1 \leq \mu \leq 1$ with N ordinates μ_n and associated weights, w_n, is chosen a discrete ordinates approximation of order N is said to result.[5] In the discrete ordinates formulation the angular flux, $\Psi(x, E, \mu)$, becomes $\Psi(x, E, \mu_n)$ and is written as $\Psi_n(x, E)$.

The scalar flux and Legendre flux moments in discrete ordinates is approximated using a quadrature formula as follows:

$$\phi(x) = \frac{1}{2}\sum_{n=1}^{N} w_n \Psi_n(x, E) \tag{3.14}$$

and

$$\phi_l(x) = \frac{1}{2}\sum_{n=1}^{N} w_n P_l(\mu_n) \Psi_n(x, E) \tag{3.15}$$

where w_n are the weights associated with each discrete ordinate. The quadrature formula is normalized by $\sum_n w_n = 2$. The quadrature formulas are normally taken to be symmetric about $\mu = 0$ which is accomplished by requiring

$$\begin{aligned} \mu_n &> 0, \\ \mu_{N+1-n} &= -\mu_n, \quad n = 1, 2, \ldots, \frac{N}{2}. \\ w_{N+1-n} &= w_n \end{aligned}$$

Incorporating discrete ordinates into the scattering source given in equation 3.13 above yields,

$$\sum_{g'}^{G} \frac{\Delta E_{g'}}{\Delta E_g} \sum_{l=0}^{L} \frac{(2l+1)}{4\pi} \sigma_{s,l}^{g' \to g}(x)\, P_l(\mu_n) \phi_{g',l}(x) \tag{3.16}$$

In discrete ordinates codes the order of the Legendre expansion of the scattering cross-section is dictated by the order of discrete ordinates, N, where $L = N - 1$.[11]

Utilizing the multigroup approximation, the Legendre expansion of the scattering kernel and discrete ordinates the one-dimensional Boltzmann-CSD equation in 3.1 is written as

$$\begin{aligned}\mu_n \frac{\partial}{\partial x} \Psi_n(x, E) - \frac{\partial}{\partial E} \{S(x, E)\Psi_n(x, E)\} + \sigma_t(x, E)\Psi_n(x, E) = \\ \sum_{g'}^{G} \frac{\Delta E_{g'}}{\Delta E_g} \sum_{l=0}^{L} \frac{(2l+1)}{4\pi} \sigma_{s,l}^{g' \to g}(x)\, P_l(\mu_n) \phi_{g',l}(x) + Q_n(x, E)\end{aligned} \tag{3.17}$$

3.4 Space and Energy Discretization of the Transport Equation

To obtain a numerical solution of the equation 3.17 it must first be discretized in space and energy to derive a system of equations. The first step is to introduce a two-dimensional grid which subdivides the space and energy domain into discrete cells or groups as shown in Figure 3.3. Numerically, this discretization is represented by integrating equation 3.17 over the gth energy group and the kth spatial cell. The next step is to relate the cell-edge angular fluxes with cell-averaged angular fluxes and relate the group-edge angular fluxes with the group-averaged angular fluxes using closure relationships or the basis expansion of the flux depending on the discretization method.

Closure relationships are used with finite difference methods and are derived from auxiliary relationships depending on the method used such as Diamond Difference (DD) or step. When finite element methods are used the basis expansion of the flux depends on the trial functions used such as Linear Discontinuous (LD) trial functions. A brief introduction to the finite difference and finite element methods of discretization follows.

3.4.1 Finite Difference Methods

To introduce finite difference methods we will discuss the implementation of the well-known diamond difference (DD) approach. In applying DD to equation 3.17 we first discretize the energy domain by dividing it into G discrete energy groups of width ΔE_g as depicted in Figure 3.3. Each energy group is bounded by an upper energy, $E_{g-1/2}$, and a lower energy, $E_{g+1/2}$, where $\Delta E_g = E_{g-1/2} - E_{g+1/2}$. Using the multigroup

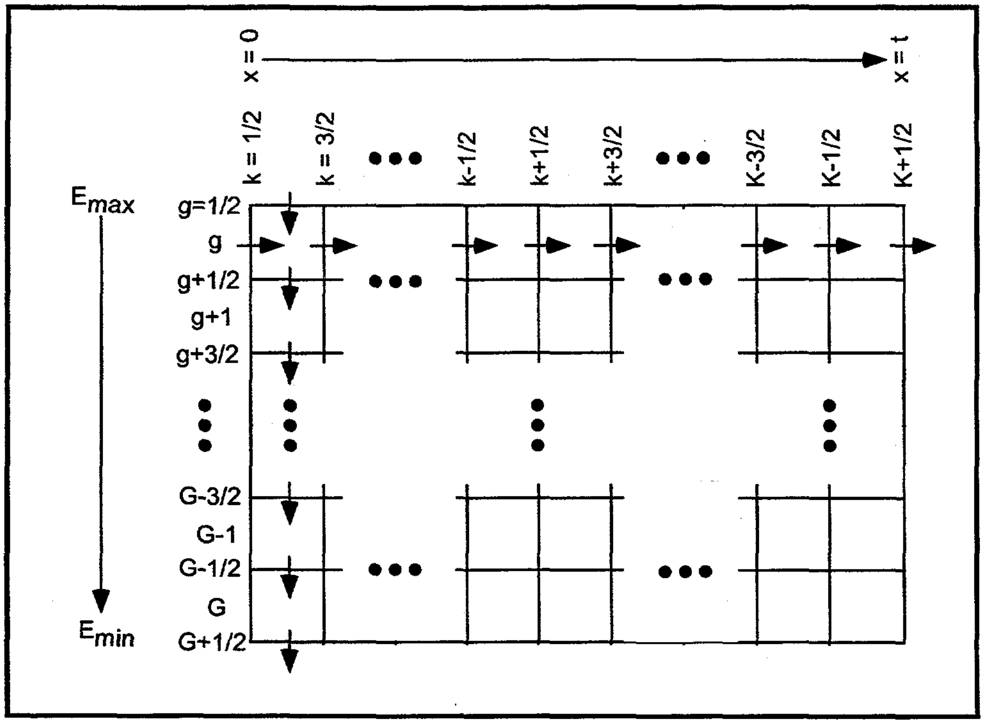

Figure 3.3: Energy and Spatial Discretization of Problem Domain

approach means that the cross-sections (σ_g) and stopping powers (S_g) are piecewise constant parameters in each respective group.

The closure relationship applied in the DD method is a simple linear average across the energy group or spatial cell and is described mathematically below

$$\Psi_{n,g}(x) = \frac{1}{2}\left[\Psi_{n,g-1/2}(x) + \Psi_{n,g+1/2}(x)\right] \tag{3.18}$$

$$\Psi_{n,k}(E) = \frac{1}{2}\left[\Psi_{n,k+1/2}(E) + \Psi_{n,k-1/2}(E)\right] \tag{3.19}$$

The group-averaged flux is defined as

$$\Psi_{n,g}(x) = \frac{1}{\Delta E_g}\int_{E_{g+1/2}}^{E_{g-1/2}} \Psi_n(x,E)dE \tag{3.20}$$

Similarly, the cell-averaged, group-averaged angular flux, $\Psi_{n,g,k}$, is defined as

$$\Psi_{n,g,k} = \frac{1}{\Delta x_k}\int_{x_{k-1/2}}^{x_{k+1/2}} \Psi_{n,g}(x)dx \tag{3.21}$$

Discretizing the energy domain in equation 3.17 is accomplished by integrating over an energy cell from $E_{g+1/2}$ to $E_{g-1/2}$. We evaluate this integration and introduce the multigroup stopping power and the energy closure relationship to get a DD in energy discretized form of equation 3.17. To get a spatially discretized version of the DD in energy equation, integrate it over the kth cell and introduce the DD in space closure relationship.

The DD method is a second-order accurate scheme that is not strictly positive and can yield negative angular fluxes resulting in oscillations. For electron transport problems higher order accurate schemes are often needed due to the CSD term and the rapid loss of energy experienced by electrons.

3.4.2 Finite Element Methods

As with all methods, implementing the finite element method in space and energy requires discretizing the spatial and energy domain into discrete cells or groups as depicted in Figure 3.3. Representing equation 3.17 in compact operator notation gives

$$\pounds\Psi_n(x,E) = q_n(x,E) \tag{3.22}$$

$$\pounds = \frac{\partial}{\partial x} - \frac{\partial}{\partial E}S(x,E) + \sigma_t(x,E) \tag{3.23}$$

The scattering and external source are represented by $q_n(x,E)$ in the above equation. A finite element representation of the angular flux, $\Psi_n(x,E)$, is introduced. A two-dimensional basis expansion of the angular flux in space and energy is given below

$$\Psi_n(x,E) \approx \tilde{\Psi}_n(x,E) = \sum_{g=1}^{G}\sum_{k=1}^{K} B_{g,k}(x,E)\psi_{n,g,k} \tag{3.24}$$

$B_{g,k}(x,E)$ are the basis or trial functions in space and energy and $\psi_{n,g,k}$ are the expansion coefficients, respectively. The residual of the transport equation is defined by introducing the approximation $\tilde{\Psi}_n(x,E)$ yielding

$$\pounds\tilde{\Psi}_n(x,E) - q_n(x,E) \neq 0 \tag{3.25}$$

A weighted residual construction is used to obtain a linear system of equations by taking the inner product of the weight functions with equation 3.17. Here the Galerkin method is implemented which means that the weight functions and the basis functions are identical. The inner product of two functions $f(x)$ and $g(x)$ is the integral of their product over the entire domain of x. The inner product of the weight functions with equation 3.17 written in compact operator notation is shown below,

$$\langle\omega_E|\pounds\tilde{\Psi}_n(x,E)\rangle = \int_{E_{g+1/2}}^{E_{g-1/2}} dE\,[\omega_E\pounds\tilde{\Psi}_n(x,E)] \tag{3.26}$$

$$\langle\omega_x|\pounds\tilde{\Psi}_n(x,E)\rangle = \int_{x_{k-1/2}}^{x_{k+1/2}} dx\,[\omega_x\pounds\tilde{\Psi}_n(x,E)] \tag{3.27}$$

In evaluating the inner products above, the basis expansion or finite element representation of the angular flux is introduced.

Using linear discontinuous trial functions, introduces an extra degree of freedom by allowing a discontinuity at the cell edges and are third-order accurate. In the next chapter we will detail the application of LD trial functions in energy along with linear continuous trial functions in space in discretizing the SAAF formulation of the Boltzmann-CSD equation.

3.5 Scattering Source Iteration Method

To obtain a numerical solution of equation 3.17 the discretized equations must then be implemented in a computer model. We solve for the angular fluxes across the slab for a given energy group before proceeding to the next energy group. For a given energy group, the scattering source on the right-hand side of the equation depends on contributions from higher energy groups as well as a contribution from the current energy group due to elastic scattering events. Obtaining a solution to the transport equation within a given energy group given this dependence on the angular flux of the current group implies the need to iterate on this scattering source.

Writing equation 3.17 in source iteration form and introducing an iteration index, ℓ, on the angular flux gives

$$\mu_n \frac{\partial}{\partial x} \Psi_n^{\ell+1}(x,E) - \frac{\partial}{\partial E}\left\{S(x,E)\Psi_n^{\ell+1}(x,E)\right\} + \sigma_t(x,E)\Psi_n^{\ell+1}(x,E) \\ = Q_n^{S,\ell}(x,E) + q_n(x,E) \qquad (3.28)$$

The scattering source iteration method means that for each energy group we converge on the scattering source on the right-hand side.

Experience tells us that acceleration techniques are necessary to accelerate the source iteration for problems that are optically thick and have scattering ratios near unity such as electron transport problems.[30,31] The most successful acceleration methods, called synthetic acceleration methods, for source iteration use a "low-order" approximation to the transport equation such as the diffusion equation.[30,32] Chapter 5 will detail the application of synthetic acceleration to the second-order, self adjoint angular flux (SAAF) formulation of the Boltzmann-CSD equation.

The next chapter presents the derivation of SAAF formulation of the Boltzmann transport equation. Energy and spatial discretization of the SAAF equation using finite elements is also presented.

This page intentionally blank.

4 Self-Adjoint Formulation of the Transport Equation

The self-adjoint formulation of the transport equation is a second-order form. A primary motive to transition from solving a first-order form of the transport equation to a second-order form is the numerical system of equations that results with this form of the transport equation. Recent work has shown that solving a second-order, even-odd parity form of the Boltzmann transport equation for neutral particles results in a symmetric, positive definite matrix equation.[17] The symmetric matrix equations can be solved efficiently due to the existence of efficient, robust numerical techniques and are compatible with specific parallel computer architectures. Josef and Morel recently developed a two-dimensional, simplified spherical harmonics coupled electron-photon code that solves an even-odd parity, second-order formulation of the transport equation using "pseudo" cross-sections from CEPXS to approximate the CSD operator.[18]

Solving a second-order form of the transport equation has other advantages besides the system of equations resulting from the discretization of this equation. For instance, in neutral particle transport finite element treatments of the space and angle in the even-odd parity formulation of the transport equation have been shown to be both accurate and less susceptible to ray effects than standard discrete ordinates solutions to the first-order transport equation.[33] Miller also showed that strictly positive spatial differencing schemes can be developed for one-dimensional even-odd parity S_n equations with isotropic scattering that have both the thick and intermediate diffusion limits and are efficiently solved using source iteration with diffusion-synthetic acceleration (DSA).[17] According to Morel and McGhee, solving a second-order, even-odd parity form of the transport equation generally makes it easier to apply DSA because the discretized diffusion equation is derived from a discretized transport equation in second-order form.[20] Perhaps the most apparent disadvantage of the second-order form of the transport equation is that the second order derivative terms prevent a discontinuous discretization in space. This may prove most important in coupled electron-photon transport problems which generally require higher order discontinuous discretization schemes to yield accurate results.

The traditional method of formulating a second-order form of the transport equation is the even-odd parity formulation which is detailed by Lewis and Miller in "Computational Methods of Neutron Transport".[5] The even-odd parity transport equation derivation is based on the division of the angular flux into even and odd angular-parity components. The even-odd parity formulation is appealing because it allows one to consider only half of the normal angular domain; however, the boundary conditions for the even-odd parity equations are complex and the derivation for anisotropic scattering sources is convoluted.[5] A new method of deriving a second-order formulation of the transport equation has been developed by Morel called the self-adjoint form which eliminates the complexities introduced by the even-odd parity formulation.[34]

4.1 SAAF Formulation of the Boltzmann Transport Equation

The self-adjoint formulation of the transport equation was developed by Morel[34] to avoid separating the angular flux into even and odd-parity components. Consider the general S_n Boltzmann transport equation for neutral particles,

$$\mathbf{\Omega}_n \cdot \nabla \Psi_n(\mathbf{r}, E) + \sigma_t(\mathbf{r}, E)\Psi_n(\mathbf{r}, E) = Q_n(\mathbf{r}, E) \tag{4.1}$$

where $Q_n(\mathbf{r}, E)$ represents the scattering and external source. Deriving the self-adjoint, angular flux (SAAF) form of the above equation begins with solving it for $\Psi_n(\mathbf{r}, E)$ as follows:

$$\Psi_n(\mathbf{r}, E) = \frac{1}{\sigma_t(\mathbf{r}, E)}\left\{Q_n(\mathbf{r}, E) - \mathbf{\Omega}_n \cdot \nabla \Psi_n(\mathbf{r}, E)\right\} \tag{4.2}$$

We then substitute equation 4.2 for $\Psi_n(\mathbf{r}, E)$ back into our original first order equation to get the second-order, self-adjoint form of the transport equation for neutral particles:

$$\begin{aligned} -\mathbf{\Omega}_n \cdot \nabla\left\{\frac{1}{\sigma_t(\mathbf{r}, E)}\mathbf{\Omega}_n \cdot \nabla \Psi_n(\mathbf{r}, E)\right\} + \sigma_t(\mathbf{r}, E)\Psi_n(\mathbf{r}, E) &= Q_n(\mathbf{r}, E) \\ &- \mathbf{\Omega}_n \cdot \nabla\left\{\frac{1}{\sigma_t} Q_n(\mathbf{r}, E)\right\} \end{aligned} \tag{4.3}$$

In one-dimension equation 4.3 becomes

$$-\mu_n^2 \frac{\partial}{\partial x}\left\{\frac{1}{\sigma_t}\frac{\partial}{\partial x}\Psi_n(x, E)\right\} + \sigma_t \Psi_n(x, E) = Q_n(x, E) - \mu_n \frac{\partial}{\partial x}\left\{\frac{1}{\sigma_t} Q_n(x, E)\right\} \tag{4.4}$$

Boundary Conditions

For incoming directions, the boundary conditions for the SAAF formulation of the Boltzmann transport equation are identical to those used with the first-order formulation of the transport equation. For example, the boundary condition for a known incoming source on surface Γ for equation 4.3 is

$$\Psi_n(\mathbf{r}, E) = F_n(\mathbf{r}, E), \quad \mathbf{\Omega}_n \cdot \hat{n} < 0, \quad \mathbf{r} \in \Gamma \tag{4.5}$$

For a vacuum boundary condition $F_n(\mathbf{r}, E)$ is set equal to 0. An albedo boundary condition is specified as follows

$$\Psi_n(\mathbf{r}, E) = \alpha(E)\, \Psi_{n'}(\mathbf{r}, E), \ \mathbf{\Omega}_n \cdot \hat{n} < 0, \ \mathbf{r} \in \Gamma \tag{4.6}$$

where $\mathbf{\Omega}_n$ is the reflection angle corresponding to an incidence angle of $\mathbf{\Omega}_{n'}$ and $\hat{n} \cdot \mathbf{\Omega}_n = -\hat{n} \cdot \mathbf{\Omega}_{n'}$ and $(\mathbf{\Omega}_n \times \mathbf{\Omega}_{n'}) \cdot \hat{n} = 0$. The reflective boundary condition in which all outgoing particles are "reflected" back is obtained by setting $\alpha(E) = 1.0$.

Unlike the first-order formulation of the transport equation, the second-order SAAF formulation requires boundary conditions for the outgoing directions at the surfaces. This requirement is satisfied by applying equation 4.2 at the surface in the outgoing directions as depicted below

$$\Psi_n(\mathbf{r}, E) = \frac{1}{\sigma_t(\mathbf{r}, E)} \left\{ Q_n(\mathbf{r}, E) - \mathbf{\Omega}_n \cdot \nabla \Psi_n(\mathbf{r}, E) \right\} \quad \mathbf{\Omega}_n \cdot \hat{n} > 0, \quad \mathbf{r} \,\epsilon\, \Gamma \tag{4.7}$$

The derivation of the SAAF transport equation is much simpler and more direct than the even-odd parity formulation. Also, the boundary conditions do not need to be separated into an even- and odd-parity component. In the next section, we detail the derivation of the self-adjoint form of the Boltzmann-CSD equation with the explicit CSD term using linear discontinuous trial functions in energy.

4.2 SAAF Formulation of the Boltzmann-CSD Equation

Consider the general S_n Boltzmann-CSD (B-CSD) equation:

$$\mathbf{\Omega}_n \cdot \nabla \Psi_n - \frac{\partial}{\partial E} [S \Psi_n] + \sigma_t \Psi_n = Q_n \tag{4.8}$$

where the variable dependencies of the angular flux, cross-sections, scattering source and stopping power shown in earlier equations are omitted for simplicity. As discussed earlier in Chapter 2, the above equation is a modified version of the BFP equation using the CSD approximation and ignoring momentum transfer. The source, Q_n, on the left hand side contains the scattering source, Q_n^s, and the external source, q_n. The scattering source can be expanded as follows

$$Q_n^S = \int_0^\infty dE' \int_{4\pi} d\mathbf{\Omega}\, \sigma_s(\mathbf{r}, E' \to E, \mathbf{\Omega}' \cdot \mathbf{\Omega}) \Psi_n \tag{4.9}$$

where σ_s above is the differential scattering cross-section. Solving equation 4.8 for Ψ_n gives,

$$\Psi_n = \frac{1}{\sigma_t} \left\{ Q_n - \mathbf{\Omega}_n \cdot \nabla \Psi_n + \frac{\partial}{\partial E} [S \Psi_n] \right\} \tag{4.10}$$

Substituting equation 4.10 for Ψ_n into equation 4.8 yields the SAAF formulation of the B-CSD equation:

$$\begin{aligned} -\mathbf{\Omega}_n \cdot \nabla \left(\frac{1}{\sigma_t} \mathbf{\Omega}_n \cdot \nabla \Psi_n \right) + \mathbf{\Omega}_n \cdot \nabla \left(\frac{1}{\sigma_t} \frac{\partial}{\partial E} [S \Psi_n] \right) &- \frac{\partial}{\partial E} [S \Psi_n] \\ + \sigma_t \Psi_n &= Q_n - \mathbf{\Omega}_n \cdot \nabla \left(\frac{1}{\sigma_t} Q_n \right) \end{aligned} \tag{4.11}$$

The coupled space-energy derivative term in the above SAAF is not a self-adjoint operator. The presence of a non-self-adjoint operator on the left-hand side will destroy the symmetric positive definite matrix that is expected from the second-order form of the transport equation when a continuous spatial discretization scheme is applied. To eliminate this coupled space-energy derivative term, we derive an energy discretized SAAF equation by first applying an energy discretization scheme to equation 4.8 before deriving the SAAF formulation as detailed next.

4.2.1 LD in Energy SAAF Boltzmann-CSD Equation

Consider the one-dimensional, S_n B-CSD equation

$$\begin{aligned}\mu_n \frac{\partial}{\partial x}\Psi_n(x,E) - \frac{\partial}{\partial E}\{S(x,E)\Psi_n(x,E)\} &+ \sigma_t(x,E)\Psi_n(x,E) \\ &= Q_n^s(x,E) + q_n(x,E) \qquad (4.12)\end{aligned}$$

Equation 4.12 can be written in compact operator notation as follows

$$\pounds\Psi_n(x,E) = Q_n(x,E) \qquad (4.13)$$

$$\pounds = \frac{\partial}{\partial x} - \frac{\partial}{\partial E}S(x,E) + \sigma_t(x,E) \qquad (4.14)$$

where the scattering and external source on the right hand side of equation 4.12 are lumped into the variable $Q_n(x,E)$. To discretize equation 4.13 in energy a finite element representation of the angular flux, $\Psi_n(x,E)$, is introduced that utilizes the basis expansion of the angular flux in energy given below

$$\Psi_n(x,E) \approx \tilde{\Psi}_n(x,E) = \sum_{g=1}^{G} B_g(E)\psi_{n,g}(x) \qquad (4.15)$$

where $B_g(E)$ is the basis or trial function in energy and $\psi_{n,g}$ are expansion coefficients or group-edge fluxes. The residual of the transport equation (4.13) is defined by introducing the approximation $\tilde{\Psi}_n(x,E)$ into the equation giving

$$\pounds\tilde{\Psi}_n(x,E) - Q_n(x,E) \neq 0 \qquad (4.16)$$

A weighted residual minimization is used to obtain a linear system of equations by taking the inner product of the weight functions with equation 4.13. Here the Galerkin method is implemented in which the weight functions and basis functions are identical. The inner product of the weight function with equation 4.13 is shown below,

$$\langle\omega_E|\pounds\Psi_n(x,E)\rangle = \int_{E_{g+1/2}}^{E_{g-1/2}} dE\,[\omega_E\pounds\Psi_n(x,E)] \qquad (4.17)$$

In evaluating the inner product above, the basis expansion or finite element representation of the angular flux is introduced.

Linear Discontinuous Finite Elements The linear discontinuous (LD) trial functions allow a discontinuity in the angular flux at the energy inflow boundary, $E_{g-1/2}$, of an energy group. The LD finite element basis expansion used here is a Legendre basis:

$$\Psi_n(x,E) \;=\; p_0^g(E)\Psi_{n,g}^A(x) + p_1^g(E)\Psi_{n,g}^E(x) \tag{4.18}$$

where

$$\begin{aligned} p_0^g(E) &= 1 \\ p_1^g(E) &= \frac{2}{\Delta E_g}(E - E_g) \end{aligned}$$

Ψ_g^A is the group average angular flux and Ψ_g^E is the group slope angular flux. We refer to equation 4.18 as the slope-average representation of $\Psi_n(x,E)$. Figure 4.2 depicts the relationship between $\Psi_{n,g}^A$ and $\Psi_{n,g}^E$ and the group-edge angular fluxes, $\Psi_{n,g+1/2}$ and $\Psi_{n,g-1/2}$. The angular flux at the upper energy or inflow boundary for group g is defined as $\Psi_{n,g-1/2} = \Psi_{n,g}^A + \Psi_{n,g}^E$ while the angular flux at the lower energy or outflow boundary is $\Psi_{n,g+1/2} = \Psi_{n,g}^A - \Psi_{n,g}^E$. In applying the LD in energy finite element discretization it is important to note the polynomials are defined as

$$p_n^g(E) = P_n\left[\frac{2}{\Delta E_g}(E - E_g)\right]; \quad E_{g+1/2} \le E \le E_{g-1/2}$$

It follows that these polynomials $p_n^g(E)$ are orthogonal on the interval $E_{g+1/2} \le E \le E_{g-1/2}$ as depicted below:

$$\int_{E_{g+1/2}}^{E_{g-1/2}} dE\, p_n^g p_{n'}^g = \frac{\Delta E_g}{2n+1}\delta_{nn'} \quad \text{where} \quad \delta_{nn'} = \begin{cases} 1 & for\; n = n' \\ 0 & for\; n \ne n' \end{cases}$$

Furthermore, at the energy group edges these polynomials can be shown to reduce to

$$p_n^g(E_{g-1/2}) = 1 \quad \text{and} \quad p_n^g(E_{g+1/2}) = (-1)^n$$

To derive an LD in energy discretized SAAF equation we begin by taking the weighted residual of the basis functions with equation 4.12 which reduces it to the weak form. In taking the weighted residual the slope-average LD basis expansion for $\Psi_n(x,E)$ is used. Essentially, the inner product of $p_0^g(E)$ and $p_1^g(E)$ is taken with equation 4.12 separately. We start by taking the inner product of p_0^g with equation

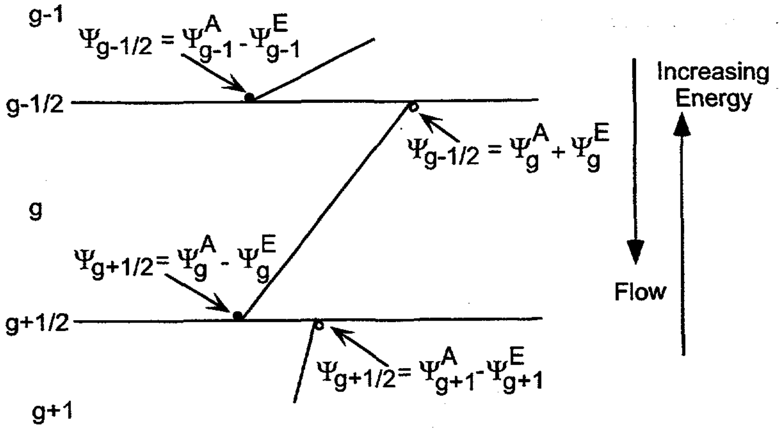

Figure 4.2: Linear Discontinuous Finite Elements in Energy: Slope-Average Form

4.12 and introducing the slope-average representation of $\Psi_n(x, E)$ as follows:

$$\begin{aligned}\Bigg\langle p_0^g \Bigg| \quad & \Bigg\{ \mu\frac{\partial}{\partial x}(p_0^g\Psi_g^A + p_1^g\Psi_g^E) - \frac{\partial}{\partial E}\Big[S(x,E)(p_0^g\Psi_g^A + p_1^g\Psi_g^E)\Big] \\ & + \sigma_t(x,E)(p_0^g\Psi_g^A + p_1^g\Psi_g^E) - Q^S(x,E) - q(x,E)\Bigg\}\Bigg\rangle = 0 \qquad (4.19)\end{aligned}$$

where the discrete ordinates index has been omitted for simplicity.

Each term in the above equation is reduced starting with the streaming term,

$$\begin{aligned}\mu\frac{\partial}{\partial x}\Big\langle p_0^g \Big| (p_0^g\Psi_g^A + p_1^g\Psi_g^E)\Big\rangle &= \mu\frac{\partial}{\partial x}\left\{\int_{E_{g+1/2}}^{E_{g-1/2}} dE\, p_0^g p_0^g\, \Psi_g^A + \int_{E_{g+1/2}}^{E_{g-1/2}} dE\, p_0^g p_1^g\, \Psi_g^E)\right\} \\ &= \Delta E_g \mu \frac{\partial \Psi_g^A}{\partial x} \qquad (4.20)\end{aligned}$$

Next, the CSD operator term is evaluated and the discontinuity at $E_{g-1/2}$ introduced as depicted below:

$$\begin{aligned}
\left\langle p_0^g \;\middle|\; \frac{\partial}{\partial E}\left[S(x,E)(p_0^g\Psi_g^A + p_1^g\Psi_g^E)\right]\right\rangle &= \int_{E_{g+1/2}}^{E_{g-1/2}} dE p_0^g \frac{\partial}{\partial E}\left[S(x,E)(p_0^g\Psi_g^A + p_1^g\Psi_g^E)\right] \\
&= p_0^g S(E)(p_0^g\Psi_g^A + p_1^g\Psi_g^E)\Big|_{E_{g+1/2}}^{E_{g-1/2}} - \int_{E_{g+1/2}}^{E_{g-1/2}} dE\frac{dp_0^g}{dE} S(E)(p_0^g\Psi_g^A + p_1^g\Psi_g^E) \\
&= p_0^g(E_{g-1/2})S(E_{g-1/2})\overbrace{\left[p_0^g(E_{g-1/2})\Psi_{g-1/2}^A + p_1^g(E_{g-1/2})\Psi_{g-1/2}^E\right]}^{\textbf{introduce discontinuity here}} \\
&- p_0^g(E_{g+1/2})S(E_{g+1/2})\left[p_0^g(E_{g+1/2})\Psi_{g+1/2}^A + p_1^g(E_{g+1/2})\Psi_{g+1/2}^E\right] \\
&= S_{g-1}[\Psi_{g-1}^A - \Psi_{g-1}^E] - S_g[\Psi_g^A - \Psi_g^E] \qquad (4.21)
\end{aligned}$$

The inner product of p_0^g with the removal term gives

$$\begin{aligned}
\left\langle p_0^g \middle| \sigma_t(p_0^g\Psi_g^A + p_1^g\Psi_g^E)\right\rangle &= \left\{\int_{E_{g+1/2}}^{E_{g-1/2}} dE\, p_0^g p_0^g\, \sigma_t\Psi_g^A + \int_{E_{g+1/2}}^{E_{g-1/2}} dE\, p_0^g p_1^g\, \sigma_t\Psi_g^E)\right\} \\
&= \Delta E_g \sigma_{t,g}\Psi_g^A \qquad (4.22)
\end{aligned}$$

Before evaluating the inner product of p_0^g with the scattering source, we note that with the LD finite element representation of Ψ in energy $Q^S(x,E)$ can be shown to be equivalent to the following

$$Q^S(x,E) \Rightarrow Q_g^S(x) = \sum_{l=0}^{L}(2l+1)P_l(\mu)\sum_{g'=1}^{G}\frac{\Delta E_{g'}}{\Delta E_g}\sigma_{s,l}^{g'\to g}(x)\phi_{l,g'}(x) \qquad (4.23)$$

and it follows that

$$\langle p_0^g|Q^S(x,E)\rangle \Rightarrow \langle p_0^g|Q_g^S(x)\rangle = \Delta E_g Q_g^S(x) \qquad (4.24)$$

The multigroup external source, $q(x,E)$, is a known value and the inner product of p_0^g with it yields,

$$\langle p_0^g|q(x,E)\rangle = \langle p_0^g|q_g(x)\rangle = \Delta E_g q_g(x)$$

Evaluating each term of the inner product in equation 4.19 and dividing through by ΔE_g yields the following equation

$$\mu\frac{\partial\Psi_g^A}{\partial x} + \left(\sigma_{t,g} + \frac{S_g}{\Delta E_g}\right)\Psi_g^A - \frac{S_g}{\Delta E_g}\Psi_g^E = Q_g^S + q_g + \frac{S_{g-1}}{\Delta E_g}\left(\Psi_{g-1}^A - \Psi_{g-1}^E\right) \qquad (4.25)$$

To complete the LD finite element discretization in energy the inner product of p_1^g with equation 4.12 is taken as shown below

$$\begin{aligned}\Bigg\langle p_1^g \Bigg| \quad & \Bigg\{ \mu\frac{\partial}{\partial x}(p_0^g\Psi_g^A + p_1^g\Psi_g^E) - \frac{\partial}{\partial E}\Big[S(x,E)(p_0^g\Psi_g^A + p_1^g\Psi_g^E)\Big] \\ & + \sigma_t(x,E)(p_0^g\Psi_g^A + p_1^g\Psi_g^E) - Q^S(x,E) - q(x,E)\Bigg\}\Bigg\rangle = 0 \qquad (4.26)\end{aligned}$$

where the slope-average representation of Ψ has been introduced. The streaming term can be shown to reduce to

$$\mu\frac{\partial}{\partial x}\left\langle p_1^g \middle| (p_0^g\Psi_g^A + p_1^g\Psi_g^E)\right\rangle = \frac{\Delta E_g}{3}\mu\frac{\partial \Psi_g^E}{\partial x} \qquad (4.27)$$

Evaluating the CSD term and introducing the discontinuity at $E_{g-1/2}$ yields

$$\begin{aligned}\left\langle p_1^g \middle| \frac{\partial}{\partial E}\Big[S(x,E)(p_0^g\Psi_g^A + p_1^g\Psi_g^E)\Big]\right\rangle &= \int_{E_{g+1/2}}^{E_{g-1/2}} dE\, p_1^g\, \frac{\partial}{\partial E}\Big[S(x,E)(p_0^g\Psi_g^A + p_1^g\Psi_g^E)\Big] \\ &= p_1^g S(E)(p_0^g\Psi_g^A + p_1^g\Psi_g^E)\Big|_{E_{g+1/2}}^{E_{g-1/2}} - \int_{E_{g+1/2}}^{E_{g-1/2}} dE\, \frac{dp_1^g}{dE}\, S(E)(p_0^g\Psi_g^A + p_1^g\Psi_g^E) \\ &= p_1^g(E_{g-1/2})S(E_{g-1/2})\overbrace{\Big[p_0^g(E_{g-1/2})\Psi_{g-1/2}^A + p_1^g(E_{g-1/2})\Psi_{g-1/2}^E\Big]}^{\textbf{introduce discontinuity here}} \\ &- p_1^g(E_{g+1/2})S(E_{g+1/2})\Big[p_0^g(E_{g+1/2})\Psi_{g+1/2}^A + p_1^g(E_{g+1/2})\Psi_{g+1/2}^E\Big] - 2S_g\Psi_g^A \\ &= S_{g-1}[\Psi_{g-1}^A - \Psi_{g-1}^E] + S_g\Psi_g^A - S_g\Psi_g^E - 2S_g\Psi_g^A \\ &= S_{g-1}[\Psi_{g-1}^A - \Psi_{g-1}^E] - S_g\Psi_g^A - S_g\Psi_g^E \qquad (4.28)\end{aligned}$$

The inner product of p_1^g with the removal term gives,

$$\left\langle p_1^g \middle| \sigma_t(p_0^g\Psi_g^A + p_1^g\Psi_g^E)\right\rangle = \frac{\Delta E_g}{3}\sigma_{t,g}\Psi_g^E \qquad (4.29)$$

Finally, it can be shown that the scattering source and external source terms in equation 4.26 give

$$\begin{aligned}\langle p_1^g | Q^S(x,E)\rangle = \langle p_1^g | Q_g^S(x)\rangle = 0 \\ \langle p_1^g | q(x,E)\rangle = \langle p_1^g | q_g(x)\rangle = 0\end{aligned}$$

The inner product in equation 4.26 yields,

$$\mu\frac{\partial\Psi_g^E}{\partial x}+\left(\sigma_{t,g}+3\frac{S_g}{\Delta E_g}\right)\Psi_g^E+3\frac{S_g}{\Delta E_g}\Psi_g^A=3\frac{S_{g-1}}{\Delta E_g}\left(\Psi_{g-1}^A-\Psi_{g-1}^E\right) \tag{4.30}$$

Equations 4.25 and 4.30 make up the LD in energy discretized, first-order transport equation in slope-average form. Introducing an average removal cross-section, a slope removal cross-section and including the S_n index these equations can be written as

$$\mu_n\frac{\partial\Psi_{n,g}^A}{\partial x}+\sigma_{R,g}^A\Psi_{n,g}^A-\frac{S_g}{\Delta E_g}\Psi_{n,g}^E=Q_{n,g}^S+q_{n,g}+\frac{S_{g-1}}{\Delta E_g}\left(\Psi_{n,g-1}^A-\Psi_{n,g-1}^E\right) \tag{4.31}$$

$$\mu_n\frac{\partial\Psi_{n,g}^E}{\partial x}+\sigma_{R,g}^E\Psi_{n,g}^E+3\frac{S_g}{\Delta E_g}\Psi_{n,g}^A=3\frac{S_{g-1}}{\Delta E_g}\left(\Psi_{n,g-1}^A-\Psi_{n,g-1}^E\right) \tag{4.32}$$

where $\sigma_{R,g}^A$ and $\sigma_{R,g}^E$ have been defined as

$$\sigma_{R,g}^A = \sigma_{t,g}+\frac{S_g}{\Delta E_g} \tag{4.33}$$

$$\sigma_{R,g}^E = \sigma_{t,g}+3\frac{S_g}{\Delta E_g} \tag{4.34}$$

Equation 4.31 and 4.32 are referred to as the average and slope flux equations, respectively. Note that the scattering source only appears in the average flux equation as a result of the orthogonality of the Legendre polynomials. It is also important to note that the average angular flux depends on the slope angular flux, and similarly, the slope angular flux depends on the average angular flux. This coupling between the average and slope flux equations introduces an iteration within each energy group between $\Psi_{n,g}^A$ and $\Psi_{n,g}^E$. We refer to this coupling between the average and slope flux as within group "upscatter" which is discussed in more detail in Chapter 6.

Equations 4.31 and 4.32 can also be solved simultaneously avoiding the iteration that arises from the coupling by writing them in a matrix form:

$$\mu_n\frac{\partial}{\partial x}\vec{\Psi}_{n,g}+\begin{pmatrix}\sigma_{R,g}^A & -\frac{S_g}{\Delta E_g}\\ 3\frac{S_g}{\Delta E_g} & \sigma_{R,g}^E\end{pmatrix}\vec{\Psi}_{n,g}=\vec{Q}_{n,g}^S+\vec{q}_{n,g}+\frac{S_{g-1}}{\Delta E_g}\begin{pmatrix}1 & -1\\ 3 & -3\end{pmatrix}\vec{\Psi}_{n,g-1} \tag{4.35}$$

where $\vec{\Psi}_{n,g}=\left\{\begin{array}{cc}\Psi_{n,g}^A & \Psi_{n,g}^E\end{array}\right\}^T$, $\vec{Q}_{n,g}^S=\left\{\begin{array}{cc}Q_{n,g}^S & 0\end{array}\right\}^T$ and $\vec{q}_{n,g}=\left\{\begin{array}{cc}q_{n,g} & 0\end{array}\right\}^T$.

The next step is to transform the LD in E discretized B-CSD equations in both the slope-average component form and the matrix form into a second-order SAAF formulation.

Slope-Average Component Form of LD SAAF Equation The first step in the derivation of the slope-average component form of the LD in Energy SAAF (LD

SAAF) equation is to solve equations 4.31 and 4.32 for $\Psi_{n,g}^A$ and $\Psi_{n,g}^E$:

$$\begin{aligned}
\Psi_g^A &= \frac{1}{\sigma_{R,g}^A}\left\{Q_g^S + q_g + \frac{S_{g-1}}{\Delta E_g}\left(\Psi_{g-1}^A - \Psi_{g-1}^E\right) + \frac{S_g}{\Delta E_g}\Psi_g^E - \mu\frac{\partial \Psi_g^A}{\partial x}\right\} && (4.36)\\
\Psi_g^E &= \frac{1}{\sigma_{R,g}^E}\left\{3\frac{S_{g-1}}{\Delta E_g}\left(\Psi_{g-1}^A - \Psi_{g-1}^E\right) - 3\frac{S_g}{\Delta E_g}\Psi_g^A - \mu\frac{\partial \Psi_g^E}{\partial x}\right\} && (4.37)
\end{aligned}$$

The S_n index has been omitted for simplicity.

To obtain the SAAF formulation of the average angular flux equation, equation 4.36 for Ψ_g^A is substituted into equation 4.31 which gives

$$\begin{aligned}
-\mu^2\frac{\partial}{\partial x}\left(\frac{1}{\sigma_{R,g}^A}\frac{\partial \Psi_g^A}{\partial x}\right) &+ \sigma_{R,g}^A\Psi_g^A = Q_g^S - \mu\frac{\partial}{\partial x}\left(\frac{1}{\sigma_{R,g}^A}Q_g^S\right) + q_g - \mu\frac{\partial}{\partial x}\left(\frac{1}{\sigma_{R,g}^A}q_g\right)\\
&+ \frac{S_{g-1}}{\Delta E_g}\left[\Psi_{g-1}^A - \Psi_{g-1}^E\right] - \mu\frac{\partial}{\partial x}\left(\frac{1}{\sigma_{R,g}^A}\frac{S_{g-1}}{\Delta E_g}\left[\Psi_{g-1}^A - \Psi_{g-1}^E\right]\right)\\
&+ \frac{S_g}{\Delta E_g}\Psi_g^E - \mu\frac{\partial}{\partial x}\left(\frac{1}{\sigma_{R,g}^A}\frac{S_g}{\Delta E_g}\Psi_g^E\right) && (4.38)
\end{aligned}$$

Similarly, the SAAF slope equation is obtained by substituting equation 4.37 for Ψ_g^E into equation 4.32 giving

$$\begin{aligned}
-\mu^2\frac{\partial}{\partial x}\left(\frac{1}{\sigma_{R,g}^E}\frac{\partial \Psi_g^E}{\partial x}\right) + \sigma_{R,g}^E\Psi_g^E &= 3\frac{S_{g-1}}{\Delta E_g}\left[\Psi_{g-1}^A - \Psi_{g-1}^E\right]\\
&- \mu\frac{\partial}{\partial x}\left(\frac{1}{\sigma_{R,g}^E}3\frac{S_{g-1}}{\Delta E_g}\left[\Psi_{g-1}^A - \Psi_{g-1}^E\right]\right)\\
&- 3\frac{S_g}{\Delta E_g}\Psi_g^A + \mu\frac{\partial}{\partial x}\left(\frac{1}{\sigma_{R,g}^E}3\frac{S_g}{\Delta E_g}\Psi_g^A\right) && (4.39)
\end{aligned}$$

Block Matrix Form of the LD in E SAAF Equation A matrix form of the SAAF equation can also be derived by solving equation 4.35 for $\vec{\Psi}_{n,g}$. To simplify the derivation we define the following

$$\mathfrak{R}_g = \begin{pmatrix} \sigma_{R,g}^A & -\frac{S_g}{\Delta E_g} \\ 3\frac{S_g}{\Delta E_g} & \sigma_{R,g}^E \end{pmatrix} \quad \text{and} \quad \mathcal{S}_{g-1} = \frac{S_{g-1}}{\Delta E_g}\begin{pmatrix} 1 & -1 \\ 3 & -3 \end{pmatrix}$$

and the first-order, Block LD equation becomes

$$\mu\frac{\partial}{\partial x}\vec{\Psi}_g + \mathfrak{R}_g\vec{\Psi}_g = \vec{Q}_g^S + \vec{q}_g + \mathcal{S}_{g-1}\vec{\Psi}_{g-1} \tag{4.40}$$

We then solve the above equation for $\vec{\Psi}_g$ to get

$$\vec{\Psi}_g = \Re_g^{-1}\left\{\vec{Q}_g^S + \vec{q}_g + \mathcal{S}_{g-1}\vec{\Psi}_{g-1} - \mu\frac{\partial}{\partial x}\vec{\Psi}_g\right\} \tag{4.41}$$

Substituting this expression back into the first-order form of the Block LD equation yields the LD in E SAAF formulation written in block matrix form:

$$\begin{aligned} -\mu^2\frac{\partial}{\partial x}\left(\Re_g^{-1}\frac{\partial}{\partial x}\vec{\Psi}_g\right) + \Re_g\vec{\Psi}_g &= \vec{Q}_g^S - \mu\frac{\partial}{\partial x}\left(\Re_g^{-1}\vec{Q}_g^S\right) \\ &+ \vec{q}_g - \mu\frac{\partial}{\partial x}\left(\Re_g^{-1}\vec{q}_g\right) \\ &+ \mathcal{S}_{g-1}\vec{\Psi}_{g-1} - \mu\frac{\partial}{\partial x}\left(\Re_g^{-1}\mathcal{S}_{g-1}\vec{\Psi}_{g-1}\right) \end{aligned} \tag{4.42}$$

which is referred to as the Block LD SAAF equation. It should be noted that expanding the Block LD SAAF equation out does not yield the same equations for $\Psi_{n,g}^A$ and $\Psi_{n,g}^E$ given in equations 4.38 and 4.39.

4.3 Spatially Discretized SAAF Boltzmann-CSD Equation

Now that an energy discretized version of the SAAF formulation of the B-CSD equation using LD finite elements in energy has been derived, we need to discretize it spatially. The second-order spatial derivative present in the SAAF formulation prevents the use of discontinuous discretization schemes in space in order to preserve the symmetry. This may be the most apparent disadvantage of the second-order form of the transport equation especially in solving coupled electron-photon transport problems which generally require higher order discontinuous discretization schemes to yield accurate results. Finite elements using linear continuous (LC) trial functions will be used to discretize the spatial variable. Using LC finite elements in space with LD in energy strays from convention, which dictates that the same discretization schemes be used in both variables.

Linear Continuous Trial Functions in Space Implementing a strict finite element approximation with LC basis functions, uses the finite element representation of the angular flux in space given below,

$$\Psi_g(x) = \sum_{k=1}^{K} B_k(x)\psi_{g,k} \tag{4.43}$$

where $\psi_{g,k}$ are the expansion coefficients or cell-edge angular fluxes and $B_k(x)$ are the basis or trial functions. The linear continuous basis functions are described mathematically as follows:

$$B_{k-1}(x) = \left\{ \begin{array}{cc} 0 & x \leq x_{k-3/2} \\ \frac{x-x_{k-3/2}}{\Delta x_{k-1}} & x_{k-3/2} \leq x \leq x_{k-1/2} \\ \frac{x_{k+1/2}-x}{\Delta x_k} & x_{k-1/2} \leq x \leq x_{k+1/2} \\ 0 & x \geq x_{k+1/2} \end{array} \right\} \tag{4.44}$$

$$B_{k}(x) = \left\{ \begin{array}{cc} 0 & x \leq x_{k-1/2} \\ \frac{x-x_{k-1/2}}{\Delta x_{k}} & x_{k-1/2} \leq x \leq x_{k+1/2} \\ \frac{x_{k+3/2}-x}{\Delta x_{k+1}} & x_{k+1/2} \leq x \leq x_{k+3/2} \\ 0 & x \geq x_{k+3/2} \end{array} \right\} \tag{4.45}$$

$$B_{k+1}(x) = \left\{ \begin{array}{cc} 0 & x \leq x_{k+1/2} \\ \frac{x-x_{k+1/2}}{\Delta x_{k+1}} & x_{k+1/2} \leq x \leq x_{k+3/2} \\ \frac{x_{k+5/2}-x}{\Delta x_{k+2}} & x_{k+3/2} \leq x \leq x_{k+5/2} \\ 0 & x \geq x_{k+5/2} \end{array} \right\} \tag{4.46}$$

The orthogonality of the basis functions gives

$$\big\langle B_k(x) \big| B_j(x) \big\rangle = 0 \text{ for } j \neq k-1, k, k+1$$

Figure 4.3 depicts the linear continuous basis functions used in the finite element discretization. It can be shown that in one-dimension the use of linear continuous finite elements is equivalent to using diamond difference.

4.3.1 LC in x, LD SAAF Equation

To apply the LC basis functions in space the inner product of $B_k(x)$ is taken with the LD SAAF equations 4.38 and 4.39. First, consider the LD SAAF equation for the average angular flux, $\Psi^A_{n,g}$, and take the inner product of $B_k(x)$ with equation 4.38 as depicted below

$$\begin{aligned} \Bigg\langle \quad B_k(x) \Bigg| \Bigg\{ & -\mu^2 \frac{\partial}{\partial x}\left(\frac{1}{\sigma^A_{R,g}} \frac{\partial \Psi^A_g}{\partial x}\right) + \sigma^A_{R,g}\Psi^A_g - Q^S_g + \mu \frac{\partial}{\partial x}\left(\frac{1}{\sigma^A_{R,g}} Q^S_g\right) \\ & -q_g + \mu \frac{\partial}{\partial x}\left(\frac{1}{\sigma^A_{R,g}} q_g\right) - \frac{S_{g-1}}{\Delta E_g}\left[\Psi^A_{g-1} - \Psi^E_{g-1}\right] + \mu \frac{\partial}{\partial x}\left(\frac{1}{\sigma^A_{R,g}} \frac{S_{g-1}}{\Delta E_g}\left[\Psi^A_{g-1} - \Psi^E_{g-1}\right]\right) \\ & -\frac{S_g}{\Delta E_g}\Psi^E_g + \mu \frac{\partial}{\partial x}\left(\frac{1}{\sigma^A_{R,g}} \frac{S_g}{\Delta E_g}\Psi^E_g\right) \Bigg\} \Bigg\rangle = 0 \end{aligned} \tag{4.47}$$

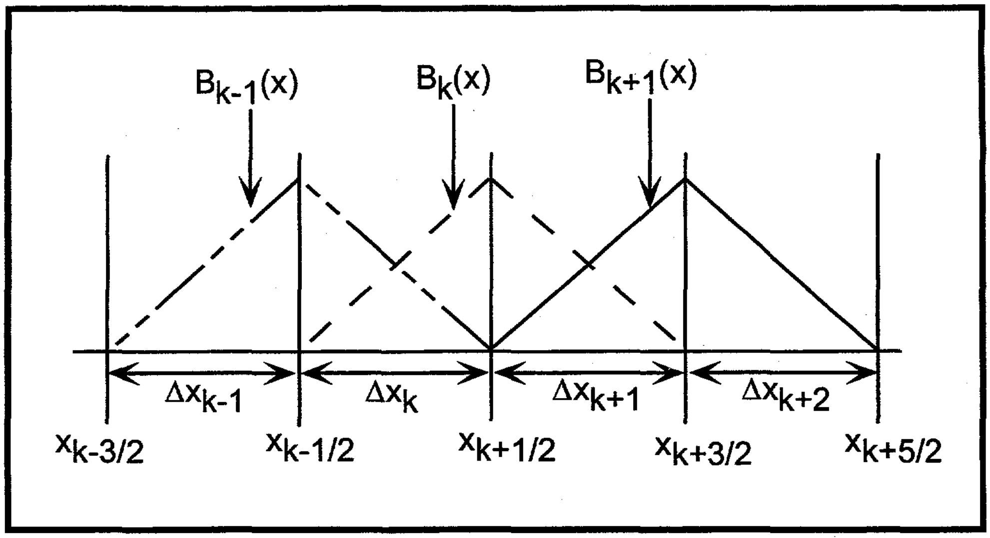

Figure 4.3: Linear Continuous Basis Functions in Space

where the S_n index is dropped for convenience. We evaluate each term in the above equation to get a spatially discretized LD SAAF equation for $\Psi^A_{n,g}$. Begin by considering the inner product of $B_k(x)$ with the first term in the equation above as follows

$$\begin{aligned}
\left\langle B_k(x) \right| & - \left. \mu^2 \frac{\partial}{\partial x}\left(\frac{1}{\sigma^A_{R,g}}\frac{\partial \Psi^A_g}{\partial x}\right)\right\rangle = -\mu^2 \int_{x_{k-1/2}}^{x_{k+3/2}} dx B_k \frac{d}{dx}\left(\frac{1}{\sigma^A_{R,g}}\frac{d\Psi^A_g}{dx}\right) \\
&= -\mu^2 B_k \frac{1}{\sigma^A_{R,g}}\frac{d\Psi^A_g}{dx}\Bigg|_{x_{k-1/2}}^{x_{k+3/2}} + \mu^2 \int_{x_{k-1/2}}^{x_{k+3/2}} dx \frac{dB_k}{dx}\frac{1}{\sigma^A_{R,g}}\frac{d\Psi^A_g}{dx} \\
&= -\frac{\mu^2}{\Delta x_k \sigma^A_{R,g,k}}\Psi^A_{g,k-1/2} + \left(\frac{\mu^2}{\Delta x_k \sigma^A_{R,g,k}} + \frac{\mu^2}{\Delta x_{k+1}\sigma^A_{R,g,k+1}}\right)\Psi^A_{g,k+1/2} \\
&- \frac{\mu^2}{\Delta x_{k+1}\sigma^A_{R,g,k+1}}\Psi^A_{g,k+3/2} \qquad (4.48)
\end{aligned}$$

The inner product with the removal term reduces to

$$\begin{aligned}
\left\langle B_k(x) \middle| \sigma^A_{R,g}\Psi^A_g \right\rangle &= \int_{x_{k-1/2}}^{x_{k+3/2}} dx B_k \sigma^A_{R,g}\Psi^A_g \\
&= \frac{1}{6}\Delta x_k \sigma^A_{R,g,k}\Psi^A_{g,k-1/2} \\
&+ \frac{1}{3}\left(\Delta x_k \sigma^A_{R,g,k} + \Delta x_{k+1}\sigma^A_{R,g,k+1}\right)\Psi^A_{g,k+1/2} \\
&+ \frac{1}{6}\Delta x_{k+1}\sigma^A_{R,g,k+1}\Psi^A_{g,k+3/2} \qquad (4.49)
\end{aligned}$$

To simplify the evaluation of the inner product of $B_k(x)$ with the scattering source the following cell-edge scattering sources are defined

$$Q^{S,L}_{g,k} = \sum_{\ell=0}^{L}(2\ell+1)P_\ell(\mu)\sum_{g'=1}^{G}\frac{\Delta E_{g'}}{\Delta E_g}\sigma^{g'\to g}_{s,\ell,k}\phi_{l,g,k-1/2} \tag{4.50}$$

$$Q^{S,R}_{g,k} = \sum_{\ell=0}^{L}(2\ell+1)P_\ell(\mu)\sum_{g'=1}^{G}\frac{\Delta E_{g'}}{\Delta E_g}\sigma^{g'\to g}_{s,\ell,k}\phi_{l,g,k+1/2} \tag{4.51}$$

$$Q^{S,L}_{g,k+1} = \sum_{\ell=0}^{L}(2\ell+1)P_\ell(\mu)\sum_{g'=1}^{G}\frac{\Delta E_{g'}}{\Delta E_g}\sigma^{g'\to g}_{s,\ell,k+1}\phi_{l,g,k+1/2} \tag{4.52}$$

$$Q^{S,R}_{g,k+1} = \sum_{\ell=0}^{L}(2\ell+1)P_\ell(\mu)\sum_{g'=1}^{G}\frac{\Delta E_{g'}}{\Delta E_g}\sigma^{g'\to g}_{s,\ell,k+1}\phi_{l,g,k+3/2} \tag{4.53}$$

Using these cell-edge scattering source, the inner products of the scattering source yield

$$\left\langle B_k(x)\middle| Q^S_g\right\rangle = \frac{1}{6}\Delta x_k Q^{S,L}_{g,k} + \frac{1}{3}\Delta x_k Q^{S,R}_{g,k} + \frac{1}{3}\Delta x_{k+1} Q^{S,L}_{g,k+1} + \frac{1}{6}\Delta x_{k+1} Q^{S,R}_{g,k+1} \tag{4.54}$$

and

$$\begin{aligned} -\mu\left\langle B_k(x)\middle|\frac{d}{dx}\left(\frac{1}{\sigma^A_{R,g}}Q^S_g\right)\right\rangle &= \frac{1}{2}\frac{\mu}{\sigma^A_{R,g,k}}Q^{S,L}_{g,k} + \frac{1}{2}\frac{\mu}{\sigma^A_{R,g,k}}Q^{S,R}_{g,k} - \frac{1}{2}\frac{\mu}{\sigma^A_{R,g,k+1}}Q^{S,L}_{g,k+1} \\ &- \frac{1}{2}\frac{\mu}{\sigma^A_{R,g,k+1}}Q^{S,R}_{g,k+1} \end{aligned} \tag{4.55}$$

Applying the LC finite elements to the external source yields,

$$\langle B_k(x) \mid q_g\rangle = \frac{1}{2}\left(\Delta x_k q_{g,k} + \Delta x_{k+1} q_{g,k+1}\right) \tag{4.56}$$

and

$$-\mu\left\langle B_k(x)\middle|\frac{d}{dx}\left(\frac{1}{\sigma^A_{R,g}}q_g\right)\right\rangle = \frac{\mu}{\sigma^A_{R,g,k}}q_{g,k} - \frac{\mu}{\sigma^A_{R,g,k+1}}q_{g,k+1} \tag{4.57}$$

Next, the spatially discretized slowing-down source into group g is given by evaluating the following,

$$\begin{aligned} \left\langle B_k(x)\middle|\frac{S_{g-1}}{\Delta E_g}\left(\Psi^A_{g-1} - \Psi^E_{g-1}\right)\right\rangle &= \frac{1}{6}\Delta x_k\frac{S_{g-1,k}}{\Delta E_g}(\Psi^A_{g-1} - \Psi^E_{g-1})_{k-1/2} \\ +\frac{1}{3}\left(\Delta x_k\frac{S_{g-1,k}}{\Delta E_g}\right. &+ \left.\Delta x_{k+1}\frac{S_{g-1,k+1}}{\Delta E_g}\right)(\Psi^A_{g-1} - \Psi^E_{g-1})_{k+1/2} \\ &+ \frac{1}{6}\Delta x_{k+1}\frac{S_{g-1,k+1}}{\Delta E_g}(\Psi^A_{g-1} - \Psi^E_{g-1})_{k+3/2} \end{aligned} \tag{4.58}$$

and the derivative of the slowing-down source becomes

$$
\begin{aligned}
-\mu\left\langle B_k(x)\left|\frac{d}{dx}\left[\frac{1}{\sigma^A_{R,g}}\frac{S_{g-1}}{\Delta E_g}(\Psi^A_{g-1} - \Psi^E_{g-1})\right]\right.\right\rangle &= \frac{1}{2}\frac{\mu}{\sigma^A_{R,g,k}}\frac{S_{g-1,k}}{\Delta E_g}(\Psi^A_{g-1}-\Psi^E_{g-1})_{k-1/2} \\
&+\frac{1}{2}\left(\frac{\mu}{\sigma^A_{R,g,k}}\frac{S_{g-1,k}}{\Delta E_g} - \frac{\mu}{\sigma^A_{R,g,k+1}}\frac{S_{g-1,k+1}}{\Delta E_g}\right)(\Psi^A_{g-1}-\Psi^E_{g-1})_{k+1/2} \\
&- \frac{1}{2}\frac{\mu}{\sigma^A_{R,g,k+1}}\frac{S_{g-1,k+1}}{\Delta E_g}(\Psi^A_{g-1}-\Psi^E_{g-1})_{k+3/2}
\end{aligned}
\qquad (4.59)
$$

where $(\Psi^A_{g-1}-\Psi^E_{g-1})_{k\pm1/2} = \Psi^A_{g-1,k\pm1/2}-\Psi^E_{g-1,k\pm1/2}$. Proceeding with the discretization of the slope flux contributions to the average angular flux gives:

$$
\begin{aligned}
\left\langle B_k(x)\left|\frac{S_g}{\Delta E_g}\Psi^E_g\right.\right\rangle &= \frac{1}{6}\Delta x_k\frac{S_{g,k}}{\Delta E_g}\Psi^E_{g,k-1/2} \\
&+ \frac{1}{3}\left(\Delta x_k\frac{S_{g,k}}{\Delta E_g} + \Delta x_{k+1}\frac{S_{g,k+1}}{\Delta E_g}\right)\Psi^E_{g,k+1/2} \\
&+ \frac{1}{6}\Delta x_{k+1}\frac{S_{g,k+1}}{\Delta E_g}\Psi^E_{g,k+3/2}
\end{aligned}
\qquad (4.60)
$$

and

$$
\begin{aligned}
-\mu\left\langle B_k(x)\left|\frac{d}{dx}\left(\frac{1}{\sigma^A_{R,g}}\frac{S_g}{\Delta E_g}\Psi^E_g\right)\right.\right\rangle &= \frac{1}{2}\frac{\mu}{\sigma^A_{R,g,k}}\frac{S_{g,k}}{\Delta E_g}\Psi^E_{g,k-1/2} \\
&+\frac{1}{2}\left(\frac{\mu}{\sigma^A_{R,g,k}}\frac{S_{g,k}}{\Delta E_g} - \frac{\mu}{\sigma^A_{R,g,k+1}}\frac{S_{g,k+1}}{\Delta E_g}\right)\Psi^E_{g,k+1/2} \\
&- \frac{1}{2}\frac{\mu}{\sigma^A_{R,g,k+1}}\frac{S_{g,k+1}}{\Delta E_g}\Psi^E_{g,k+3/2}
\end{aligned}
\qquad (4.61)
$$

We follow the same procedure to discretize the LD SAAF equation for the slope flux. Finally the spatially discretized LD SAAF equations given below are obtained,

$$
\begin{aligned}
&\left(\tfrac{1}{6}\Delta x_k \sigma^A_{R,g,k} - \tfrac{\mu_n^2}{\Delta x_k \sigma^A_{R,g,k}}\right)\Psi^A_{n,g,k-1/2} \\
&+\left(\tfrac{1}{3}[\Delta x_k \sigma^A_{R,g,k} + \Delta x_{k+1}\sigma^A_{R,g,k+1}] + \tfrac{\mu_n^2}{\Delta x_k \sigma^A_{R,g,k}} + \tfrac{\mu_n^2}{\Delta x_{k+1}\sigma^A_{R,g,k+1}}\right)\Psi^A_{n,g,k+1/2} \\
&+\left(\tfrac{1}{6}\Delta x_{k+1}\sigma^A_{R,g,k+1} - \tfrac{\mu_n^2}{\Delta x_{k+1}\sigma^A_{R,g,k+1}}\right)\Psi^A_{n,g,k+3/2} \\
&=\left(\tfrac{1}{6}\Delta x_k + \tfrac{1}{2}\tfrac{\mu_n}{\sigma^A_{R,g,k}}\right)Q^{S,L}_{n,g,k} + \left(\tfrac{1}{3}\Delta x_k + \tfrac{1}{2}\tfrac{\mu_n}{\sigma^A_{R,g,k}}\right)Q^{S,R}_{n,g,k} \\
&+\left(\tfrac{1}{3}\Delta x_{k+1} - \tfrac{1}{2}\tfrac{\mu_n}{\sigma^A_{R,g,k+1}}\right)Q^{S,L}_{n,g,k+1} + \left(\tfrac{1}{6}\Delta x_{k+1} - \tfrac{1}{2}\tfrac{\mu_n}{\sigma^A_{R,g,k+1}}\right)Q^{S,R}_{n,g,k+1} \\
&+\left(\tfrac{1}{2}\Delta x_k + \tfrac{\mu_n}{\sigma^A_{R,g,k}}\right)q_{n,g,k} + \left(\tfrac{1}{2}\Delta x_{k+1} - \tfrac{\mu_n}{\sigma^A_{R,g,k+1}}\right)q_{n,g,k+1} \\
&+\left(\tfrac{1}{6}\Delta x_k + \tfrac{1}{2}\tfrac{\mu_n}{\sigma^A_{R,g,k}}\right)\tfrac{S_{g-1,k}}{\Delta E_g}(\Psi^A_{n,g-1} - \Psi^E_{n,g-1})_{k-1/2} \\
&+\left[\left(\tfrac{1}{3}\Delta x_k + \tfrac{1}{2}\tfrac{\mu_n}{\sigma^A_{R,g,k}}\right)\tfrac{S_{g-1,k}}{\Delta E_g} + \left(\tfrac{1}{3}\Delta x_{k+1} - \tfrac{1}{2}\tfrac{\mu_n}{\sigma^A_{R,g,k+1}}\right)\tfrac{S_{g-1,k+1}}{\Delta E_g}\right](\Psi^A_{n,g-1} - \Psi^E_{n,g-1})_{k+1/2} \\
&+\left(\tfrac{1}{6}\Delta x_{k+1} - \tfrac{1}{2}\tfrac{\mu_n}{\sigma^A_{R,g,k+1}}\right)\tfrac{S_{g-1,k+1}}{\Delta E_g}(\Psi^A_{n,g-1} - \Psi^E_{n,g-1})_{k+3/2} \\
&+\left(\tfrac{1}{6}\Delta x_k + \tfrac{1}{2}\tfrac{\mu_n}{\sigma^A_{R,g,k}}\right)\tfrac{S_{g,k}}{\Delta E_g}\Psi^E_{n,g,k-1/2} \\
&+\left[\left(\tfrac{1}{3}\Delta x_k + \tfrac{1}{2}\tfrac{\mu_n}{\sigma^A_{R,g,k}}\right)\tfrac{S_{g,k}}{\Delta E_g} + \left(\tfrac{1}{3}\Delta x_{k+1} - \tfrac{1}{2}\tfrac{\mu_n}{\sigma^A_{R,g,k+1}}\right)\tfrac{S_{g,k+1}}{\Delta E_g}\right]\Psi^E_{n,g,k+1/2} \\
&+\left(\tfrac{1}{6}\Delta x_{k+1} - \tfrac{1}{2}\tfrac{\mu_n}{\sigma^A_{R,g,k+1}}\right)\tfrac{S_{g,k+1}}{\Delta E_g}\Psi^E_{n,g,k+3/2}
\end{aligned}
\tag{4.62}
$$

and

$$
\begin{aligned}
&\left(\tfrac{1}{6}\Delta x_k \sigma^E_{R,g,k} - \tfrac{\mu_n^2}{\Delta x_k \sigma^E_{R,g,k}}\right)\Psi^E_{n,g,k-1/2} \\
&+\left(\tfrac{1}{3}[\Delta x_k \sigma^E_{R,g,k} + \Delta x_{k+1}\sigma^E_{R,g,k+1}] + \tfrac{\mu_n^2}{\Delta x_k \sigma^E_{R,g,k}} + \tfrac{\mu_n^2}{\Delta x_{k+1}\sigma^E_{R,g,k+1}}\right)\Psi^E_{n,g,k+1/2} \\
&+\left(\tfrac{1}{6}\Delta x_{k+1}\sigma^E_{R,g,k+1} - \tfrac{\mu_n^2}{\Delta x_{k+1}\sigma^E_{R,g,k+1}}\right)\Psi^E_{n,g,k+3/2} \\
&=\left(\tfrac{1}{2}\Delta x_k + \tfrac{3}{2}\tfrac{\mu_n}{\sigma^E_{R,g,k}}\right)\tfrac{S_{g-1,k}}{\Delta E_g}(\Psi^A_{n,g-1} - \Psi^E_{n,g-1})_{k-1/2} \\
&+\left[\left(\Delta x_k + \tfrac{3}{2}\tfrac{\mu_n}{\sigma^E_{R,g,k}}\right)\tfrac{S_{g-1,k}}{\Delta E_g} + \left(\Delta x_{k+1} - \tfrac{3}{2}\tfrac{\mu_n}{\sigma^E_{R,g,k+1}}\right)\tfrac{S_{g-1,k+1}}{\Delta E_g}\right](\Psi^A_{n,g-1} - \Psi^E_{n,g-1})_{k+1/2} \\
&+\left(\tfrac{1}{2}\Delta x_{k+1} - \tfrac{3}{2}\tfrac{\mu_n}{\sigma^E_{R,g,k+1}}\right)\tfrac{S_{g-1,k+1}}{\Delta E_g}(\Psi^A_{n,g-1} - \Psi^E_{n,g-1})_{k+3/2} \\
&-\left(\tfrac{1}{2}\Delta x_k + \tfrac{3}{2}\tfrac{\mu_n}{\sigma^E_{R,g,k}}\right)\tfrac{S_{g,k}}{\Delta E_g}\Psi^A_{n,g,k-1/2} \\
&-\left[\left(\Delta x_k + \tfrac{3}{2}\tfrac{\mu_n}{\sigma^E_{R,g,k}}\right)\tfrac{S_{g,k}}{\Delta E_g} + \left(\Delta x_{k+1} - \tfrac{3}{2}\tfrac{\mu_n}{\sigma^E_{R,g,k+1}}\right)\tfrac{S_{g,k+1}}{\Delta E_g}\right]\Psi^A_{n,g,k+1/2} \\
&-\left(\tfrac{1}{2}\Delta x_{k+1} - \tfrac{3}{2}\tfrac{\mu_n}{\sigma^E_{R,g,k+1}}\right)\tfrac{S_{g,k+1}}{\Delta E_g}\Psi^A_{n,g,k+3/2}
\end{aligned}
\tag{4.63}
$$

Auxiliary Boundary Conditions Both equations 4.62 and 4.63 require an auxiliary boundary condition for the outgoing directions at the slab edges. A discretized form of these auxiliary boundary conditions are obtained by applying LC finite elements to equations 4.31 and 4.32 over the k^{th} cell. For the average flux SAAF equation, the inner product of B_k with equation 4.31 over the k^{th} cell yields

$$\begin{aligned}
& \left(\mu_n + \tfrac{2}{3}\Delta x_k \sigma^A_{R,g,k}\right) \Psi^A_{n,g,k+1/2} - \left(\mu_n - \tfrac{1}{3}\Delta x_k \sigma^A_{R,g,k}\right) \Psi^A_{n,g,k-1/2} \\
= \; & \tfrac{1}{3}\Delta x_k \left(Q^{S,L}_{n,g,k} + 2Q^{S,R}_{n,g,k}\right) + \Delta x_k q_{n,g,k} \\
+ \; & \tfrac{1}{3}\Delta x_k \tfrac{S_{g-1,k}}{\Delta E_g} \left\{ (\Psi^A_{n,g-1} - \Psi^E_{n,g-1})_{k-1/2} + 2(\Psi^A_{n,g-1} - \Psi^E_{n,g-1})_{k+1/2} \right\} \\
+ \; & \tfrac{1}{3}\Delta x_k \tfrac{S_{g,k}}{\Delta E_g} \left(\Psi^E_{n,g,k-1/2} + 2\Psi^E_{n,g,k+1/2}\right)
\end{aligned} \tag{4.64}$$

For the K^{th} cell, at the right edge of the slab, the boundary condition for outgoing directions ($\mu_n > 0$) is determined by solving equation 4.64 for $\Psi^A_{n,g,K+1/2}$ to get

$$\begin{aligned}
\Psi^A_{n,g,K+1/2} \; = \; & \left(\mu_n + \tfrac{2}{3}\Delta x_K \sigma^A_{R,g,K}\right)^{-1} \cdot \Big\{ \left(\mu_n - \tfrac{1}{3}\Delta x_K \sigma^A_{R,g,K}\right) \Psi^A_{n,g,K-1/2} \\
+ \; & \tfrac{1}{3}\Delta x_K \left(Q^{S,L}_{n,g,K} + 2Q^{S,R}_{n,g,K}\right) + \Delta x_K q_{n,g,K} \\
+ \; & \tfrac{1}{3}\Delta x_K \tfrac{S_{g-1,K}}{\Delta E_g} \left[(\Psi^A_{n,g-1} - \Psi^E_{n,g-1})_{K-1/2} + 2(\Psi^A_{n,g-1} - \Psi^E_{n,g-1})_{K+1/2} \right] \\
+ \; & \tfrac{1}{3}\Delta x_K \tfrac{S_{g,K}}{\Delta E_g} \left(\Psi^E_{n,g,K-1/2} + 2\Psi^E_{n,g,K+1/2}\right) \Big\}
\end{aligned} \tag{4.65}$$

For the cell at the left edge of the slab ($k = 1$), equation 4.64 is solved for $\Psi^A_{n,g,1/2}$ to get the boundary condition for the $\mu_n < 0$ directions:

$$\begin{aligned}
\Psi^A_{n,g,1/2} \; = \; & \left(\mu_n - \tfrac{1}{3}\Delta x_1 \sigma^A_{R,g,1}\right)^{-1} \cdot \Big\{ \left(\mu_n + \tfrac{2}{3}\Delta x_1 \sigma^A_{R,g,1}\right) \Psi^A_{n,g,3/2} \\
- \; & \tfrac{1}{3}\Delta x_1 \left(Q^{S,L}_{n,g,1} + 2Q^{S,R}_{n,g,1}\right) - \Delta x_1 q_{n,g,1} \\
- \; & \tfrac{1}{3}\Delta x_1 \tfrac{S_{g-1,1}}{\Delta E_g} \left[(\Psi^A_{n,g-1} - \Psi^E_{n,g-1})_{1/2} + 2(\Psi^A_{n,g-1} - \Psi^E_{n,g-1})_{3/2} \right] \\
- \; & \tfrac{1}{3}\Delta x_1 \tfrac{S_{g,1}}{\Delta E_g} \left(\Psi^E_{n,g,1/2} + 2\Psi^E_{n,g,3/2}\right) \Big\}
\end{aligned} \tag{4.66}$$

Similarly, for the slope flux equation LC finite elements are applied over the k^{th} cell to equation 4.32 yielding

$$\begin{aligned}
& \left(\mu_n + \tfrac{2}{3}\Delta x_k \sigma^E_{R,g,k}\right) \Psi^E_{n,g,k+1/2} - \left(\mu_n - \tfrac{1}{3}\Delta x_k \sigma^E_{R,g,k}\right) \Psi^E_{n,g,k-1/2} \\
= \; & \Delta x_k \tfrac{S_{g-1,k}}{\Delta E_g} \left\{ (\Psi^A_{n,g-1} - \Psi^E_{n,g-1})_{k-1/2} + 2(\Psi^A_{n,g-1} - \Psi^E_{n,g-1})_{k+1/2} \right\} \\
- \; & \Delta x_k \tfrac{S_{g,k}}{\Delta E_g} \left(\Psi^A_{n,g,k-1/2} + 2\Psi^A_{n,g,k+1/2}\right)
\end{aligned} \tag{4.67}$$

At the right-edge of the slab in the $\mu_n > 0$ directions we solve equation 4.67 for $\Psi^E_{n,g,K+1/2}$ to get

$$\begin{aligned}
\Psi^E_{n,g,K+1/2} &= \left(\mu_n + \tfrac{2}{3}\Delta x_K \sigma^E_{R,g,K}\right)^{-1} \cdot \Bigg\{ \left(\mu_n - \tfrac{1}{3}\Delta x_K \sigma^E_{R,g,K}\right) \Psi^E_{n,g,K-1/2} \\
&+ \Delta x_K \tfrac{S_{g-1,K}}{\Delta E_g} \left[(\Psi^A_{n,g-1} - \Psi^E_{n,g-1})_{K-1/2} + 2(\Psi^A_{n,g-1} - \Psi^E_{n,g-1})_{K+1/2} \right] \\
&- \Delta x_K \tfrac{S_{g,K}}{\Delta E_g} \left(\Psi^A_{n,g,K-1/2} + 2\Psi^A_{n,g,K+1/2} \right) \Bigg\}
\end{aligned} \tag{4.68}$$

and for $k = 1$ in the outgoing directions $\mu_n < 0$ we solve for $\Psi^E_{n,g,1/2}$ yielding,

$$\begin{aligned}
\Psi^E_{n,g,1/2} &= \left(\mu_n - \tfrac{1}{3}\Delta x_1 \sigma^E_{R,g,1}\right)^{-1} \cdot \Bigg\{ \left(\mu_n + \tfrac{2}{3}\Delta x_1 \sigma^E_{R,g,1}\right) \Psi^E_{n,g,3/2} \\
&- \Delta x_1 \tfrac{S_{g-1,1}}{\Delta E_g} \left[(\Psi^A_{n,g-1} - \Psi^E_{n,g-1})_{1/2} + 2(\Psi^A_{n,g-1} - \Psi^E_{n,g-1})_{3/2} \right] \\
&+ \Delta x_1 \tfrac{S_{g,1}}{\Delta E_g} \left(\Psi^A_{n,g,1/2} + 2\Psi^A_{n,g,3/2} \right) \Bigg\}
\end{aligned} \tag{4.69}$$

The SPD matrix equations represented in 4.62 and 4.63 are applicable for all the interior cells, $k = 2, \ldots, K-2$. That is they apply to all of the cell-edge average and slope fluxes except for those on the left ($k = 1/2$) and right ($k = K + 1/2$) boundaries. For the cells at the left boundary $k = 1$ and $k = K - 1$ the boundary conditions at $\Psi_{n,g,1/2}$ and $\Psi_{n,g,K+1/2}$ are applied. For the incoming directions, $\mu_n > 0$, the known boundary condition is moved to the right-hand side of equations 4.62 and 4.63. For the outgoing directions at the left boundary, equations 4.66 for $\Psi^A_{n,g,1/2}$ and 4.69 $\Psi^E_{n,g,1/2}$ are applied modifying equations 4.62 and 4.63 for the $k = 1$ cell. Similarly, at the right boundary equations 4.65 for $\Psi^A_{n,g,K+1/2}$ and 4.68 $\Psi^E_{n,g,K+1/2}$ are applied for the outgoing directions and equations 4.62 and 4.63 are modified for the $k = K - 1$ cell.

4.3.2 LC in x, Block LD SAAF

We derive a LC finite element discretized version of the Block LD SAAF equation by taking the inner product of B_k with equation 4.42. Following the same procedure as used in the discretization of the LD SAAF equation gives,

$$\begin{aligned}
&\left(\tfrac{1}{6}\Delta x_k \Re_{g,k} - \tfrac{\mu_n^2}{\Delta x_k}\Re_{g,k}^{-1}\right)\vec{\Psi}_{n,g,k-1/2} \\
&+ \left(\tfrac{1}{3}[\Delta x_k \Re_{g,k} + \Delta x_{k+1}\Re_{g,k+1}] + \tfrac{\mu_n^2}{\Delta x_k}\Re_{g,k}^{-1} + \tfrac{\mu^2}{\Delta x_{k+1}}\Re_{g,k+1}^{-1}\right)\vec{\Psi}_{n,g,k+1/2} \\
&+ \left(\tfrac{1}{6}\Delta x_{k+1}\Re_{g,k+1} - \tfrac{\mu_n^2}{\Delta x_{k+1}}\Re_{g,k+1}^{-1}\right)\vec{\Psi}^{A}_{n,g,k+3/2} \\
&= \left(\tfrac{1}{6}\Delta x_k \mathbf{I} + \tfrac{1}{2}\mu_n \Re_{g,k}^{-1}\right)\vec{Q}^{S,L}_{n,g,k} + \left(\tfrac{1}{3}\Delta x_k \mathbf{I} + \tfrac{1}{2}\mu_n \Re_{g,k}^{-1}\right)\vec{Q}^{S,R}_{n,g,k} \\
&+ \left(\tfrac{1}{3}\Delta x_{k+1}\mathbf{I} - \tfrac{1}{2}\mu_n \Re_{g,k+1}^{-1}\right)\vec{Q}^{S,L}_{n,g,k+1} + \left(\tfrac{1}{6}\Delta x_{k+1}\mathbf{I} - \tfrac{1}{2}\mu_n \Re_{g,k+1}^{-1}\right)\vec{Q}^{S,R}_{n,g,k+1} \\
&+ \left(\tfrac{1}{2}\Delta x_k \mathbf{I} + \mu_n \Re_{g,k}^{-1}\right)\vec{q}_{n,g,k} + \left(\tfrac{1}{2}\Delta x_{k+1}\mathbf{I} - \mu_n \Re_{g,k+1}^{-1}\right)\vec{q}_{n,g,k+1} \\
&+ \left(\tfrac{1}{6}\Delta x_k \mathcal{S}_{g-1,k} + \tfrac{1}{2}\mu_n \Re_{g,k}^{-1}\mathcal{S}_{g-1,k}\right)\vec{\Psi}_{n,g-1,k-1/2} \\
&+ \left[\begin{array}{c} \left(\tfrac{1}{3}\Delta x_k \mathcal{S}_{g-1,k} + \tfrac{1}{2}\mu_n \Re_{g,k}^{-1}\mathcal{S}_{g-1,k}\right) \\ + \left(\tfrac{1}{3}\Delta x_{k+1}\mathcal{S}_{g-1,k+1} - \tfrac{1}{2}\mu_n \Re_{g,k+1}^{-1}\mathcal{S}_{g-1,k+1}\right) \end{array}\right]\vec{\Psi}_{n,g-1,k+1/2} \\
&+ \left(\tfrac{1}{6}\Delta x_{k+1}\mathcal{S}_{g-1,k+1} - \tfrac{1}{2}\mu_n \Re_{g,k+1}^{-1}\mathcal{S}_{g-1,k+1}\right)\vec{\Psi}_{n,g-1,k+3/2}
\end{aligned} \tag{4.70}$$

Equation 4.70 is a block matrix equation. Solving this form of the LD in E equation avoids the upscatter iteration that arises when the slope-average flux SAAF equations are solved separately.

Auxiliary Boundary Conditions The block LD SAAF equation requires auxiliary boundary conditions. We derive this auxiliary boundary condition (BC) in the same manner as described earlier for the average and slope equations. Applying LC finite elements over the k^{th} cell on equation 4.42 gives,

$$\begin{aligned}
\left(\mu_n \mathbf{I} + \tfrac{2}{3}\Delta x_k \Re_{g,k}\right)\vec{\Psi}_{n,g,k+1/2} &- \left(\mu_n \mathbf{I} - \tfrac{1}{3}\Delta x_k \Re_{g,k}\right)\vec{\Psi}_{n,g,k-1/2} \\
&= \tfrac{1}{3}\Delta x_k(\vec{Q}^{S,L}_{n,g,k} + 2\vec{Q}^{S,R}_{n,g,k}) + \Delta x_k \vec{q}_{n,g,k} \\
&+ \tfrac{1}{3}\Delta x_k \mathcal{S}_{g-1,k}(\vec{\Psi}_{n,g-1,k-1/2} + 2\vec{\Psi}_{n,g-1,k+1/2})
\end{aligned} \tag{4.71}$$

For outgoing directions ($\mu_n > 0$) at the right edge of the slab, the following boundary condition is used:

$$\begin{aligned}
\vec{\Psi}_{n,g,K+1/2} &= \left(\mu_n \mathbf{I} + \tfrac{2}{3}\Delta x_K \Re_{g,K}\right)^{-1}\cdot\Big\{\left(\mu_n \mathbf{I} - \tfrac{1}{3}\Delta x_K \Re_{g,K}\right)\vec{\Psi}_{n,g,K-1/2} \\
&+ \tfrac{1}{3}\Delta x_K(\vec{Q}^{S,L}_{n,g,K} + 2\vec{Q}^{S,R}_{n,g,K}) + \Delta x_K \vec{q}_{n,g,K} \\
&+ \tfrac{1}{3}\Delta x_K \mathcal{S}_{g-1,K}(\vec{\Psi}_{n,g-1,K-1/2} + 2\vec{\Psi}_{n,g-1,K+1/2})\Big\}
\end{aligned} \tag{4.72}$$

and for the $k = 1$ cell at the left boundary in outgoing directions ($\mu_n < 0$) we get,

$$\begin{aligned}
\vec{\Psi}_{n,g,1/2} &= \left(\mu_n \mathbf{I} - \tfrac{1}{3}\Delta x_1 \Re_{g,1}\right)^{-1}\cdot\Big\{\left(\mu_n \mathbf{I} + \tfrac{2}{3}\Delta x_1 \Re_{g,1}\right)\vec{\Psi}_{n,g,3/2} \\
&- \tfrac{1}{3}\Delta x_1(\vec{Q}^{S,L}_{n,g,1} + 2\vec{Q}^{S,R}_{n,g,1}) - \Delta x_1 \vec{q}_{n,g,1} \\
&- \tfrac{1}{3}\Delta x_1 \mathcal{S}_{g-1,1}(\vec{\Psi}_{n,g-1,/2} + 2\vec{\Psi}_{n,g-1,3/2})\Big\}
\end{aligned} \tag{4.73}$$

4.4 Source Iteration Form of SAAF Equation

The scattering source terms that are present on the right-hand side of the discretized SAAF equations depend on the values of the average angular flux in the current energy group, g, due to the contribution from elastic scattering events. To accommodate this dependence these equations are solved using the scattering source iteration method. Implementing this scheme means the solution is converged on the elastic scattering source on the right-hand side of these equations in each energy group before it proceeds to the next group. Initially, guesses are made for the angular flux values and a quadrature set and Legendre expansion of the cross-sections are used to evaluate the scattering integral. The SAAF transport equation is solved and the procedure is repeated until the convergence criteria is satisfied before proceeding to the next group.

The generalized source-iteration form of the neutral particle SAAF equation is given below as:

$$\begin{aligned} -\mu_n^2 \frac{\partial}{\partial x}\left\{\frac{1}{\sigma_t}\frac{\partial \Psi_n^{(\ell+1)}}{\partial x}\right\} + \sigma_t \Psi_n^{(\ell+1)} &= Q_n^{S(\ell)} - \mu_n \frac{\partial}{\partial x}\left\{\frac{1}{\sigma_t} Q_n^{S(\ell)}\right\} \\ &+ q_n - \mu_n \frac{\partial}{\partial x}\left\{\frac{1}{\sigma_t} q_n\right\} \end{aligned} \tag{4.74}$$

where q_n is the known source into group g from downscatter, slowing-down, and the fixed external source and ℓ is the source iteration index.

Experience tells us that the source iteration must be accelerated for problems that are optically thick and have scattering ratios near unity such as electron transport problems.[30,31] The most successful acceleration methods, called synthetic acceleration methods, for source iteration use a "low-order" approximation to the transport equation such as the diffusion equation[30,32] to estimate the error at a given iteration step. In the next chapter we will detail the derivation of a source acceleration technique for the solution of the LD SAAF equations.

5 Source Acceleration of SAAF Equations

The general application of synthetic acceleration[30,35,36] is detailed by considering a general matrix problem:

$$(\mathbf{A}-\mathbf{B})\,f = q \tag{5.1}$$

which is solved iteratively using the iteration scheme given below:

$$f^{(\ell+1)} = \mathbf{A}^{-1}\mathbf{B}f^{(\ell)} + \mathbf{A}^{-1}q \tag{5.2}$$

The exact error in f at the $(\ell+1)$ iteration step satisfies

$$(\mathbf{A}-\mathbf{B})\,\epsilon^{(\ell+1)} = q - (\mathbf{A}-\mathbf{B})\,f^{(\ell+1)} \tag{5.3}$$

where the error is defined by

$$\epsilon^{(\ell+1)} = f - f^{(\ell+1)} \tag{5.4}$$

The main idea of synthetic acceleration is to estimate the error in $f^{(\ell+1)}$ by solving the error equation using a low-order operator to approximate $(\mathbf{A}-\mathbf{B})$. The accelerated iteration scheme proceeds as follows

$$\begin{aligned} f^{(\ell+1/2)} &= \mathbf{A}^{-1}\mathbf{B}f^{(\ell)} + \mathbf{A}q^{-1} && (5.5)\\ \mathbf{L}\left(f^{(\ell+1)} - f^{(\ell+1/2)}\right) &= \mathbf{B}\left(f^{(\ell+1)} - f^{(\ell+1/2)}\right) && (5.6) \end{aligned}$$

where $\mathbf{L}$ is a low-order approximation to $(\mathbf{A}-\mathbf{B})$. The effectiveness of synthetic acceleration depends upon whether or not the low-order operator is less expensive to invert in comparison to $(\mathbf{A}-\mathbf{B})$. The low-order operator must damp out the error modes or Fourier modes that yield a spectral radius close to unity for the original iteration scheme to result in accelerated convergence. Problems occur if the low-order operator amplifies error modes that are not a problem in the original iteration scheme.

For neutral particle transport, discrete ordinate codes the most common acceleration technique used to increase the rate of convergence of the source iteration is diffusion synthetic acceleration (DSA).[32] DSA accelerates the source iteration by solving the diffusion equation at an intermediate step. However, as scattering becomes increasingly forward peaked DSA loses it effectiveness.[36] Various acceleration techniques have been introduced to accelerate problems that are characterized by highly forward-peaked scattering such as the angular multigrid acceleration (AMR) technique,[36] the modified P_N (MPSA) and modified DSA (MDSA),[31] and S_2 synthetic acceleration.[35] Here DSA is applied to the self-adjoint angular flux equation.

5.1 DSA Equations for SAAF

We begin by considering the exact SAAF B-CSD transport equation with isotropic scattering only

$$\begin{aligned}-\mu^2\frac{\partial}{\partial x}\left(\frac{1}{\sigma^A_{R,g}}\frac{\partial\Psi^A_g}{\partial x}\right) \quad + \quad \sigma^A_{R,g}\Psi^A_g &= \frac{\sigma_{s0,g}}{2}\int_{-1}^{1} d\mu'\Psi^A_g(x,\mu') \\ &- \frac{\mu}{2}\frac{\partial}{\partial x}\left[\frac{\sigma_{s0,g}}{\sigma^A_{R,g}}\int_{-1}^{1} d\mu'\Psi^A_g(x,\mu')\right] + Q_g(x,\mu) \qquad (5.7)\end{aligned}$$

where $Q_g(x,\mu)$ contains the known source into group g due to slowing-down, the fixed source, downscatter into group g and the contribution from the slope flux, Ψ^E_g. The source iteration form of equation 5.7 is

$$\begin{aligned}-\mu^2\frac{\partial}{\partial x}\left(\frac{1}{\sigma^A_{R,g}}\frac{\partial\Psi^{A(\ell+1/2)}_g}{\partial x}\right) \quad + \quad \sigma^A_{R,g}\Psi^{A(\ell+1/2)}_g &= \frac{\sigma_{s0,g}}{2}\int_{-1}^{1} d\mu'\Psi^{A(\ell)}_g(x,\mu') \\ &- \frac{\mu}{2}\frac{\partial}{\partial x}\left[\frac{\sigma_{s0,g}}{\sigma^A_{R,g}}\int_{-1}^{1} d\mu'\Psi^{A(\ell)}_g(x,\mu')\right] + Q_g(x,\mu) \, (5.8)\end{aligned}$$

We define the "exact" error as

$$\begin{aligned}f^{(\ell+1/2)}(x,\mu) &= \Psi^A_g(x,\mu) - \Psi^{A(\ell+1/2)}_g \qquad (5.9)\\ \phi^{(\ell+1/2)}(x) &= \frac{1}{2}\int_{-1}^{1} d\mu'\Psi^{A(\ell+1/2)}_g(x,\mu') \qquad (5.10)\end{aligned}$$

Subtracting equation 5.8 from equation 5.7 yields

$$\begin{aligned}-\mu^2\frac{\partial}{\partial x}\left(\frac{1}{\sigma^A_{R,g}}\frac{\partial f^{(\ell+1/2)}}{\partial x}\right) \quad +\sigma^A_{R,g}f^{(\ell+1/2)} &= \frac{\sigma_{s0,g}}{2}\int_{-1}^{1} d\mu'\left(\Psi^A_g(x,\mu') - \Psi^{A(\ell)}_g(x,\mu')\right) \\ &-\frac{\mu}{2}\frac{\partial}{\partial x}\left[\frac{\sigma_{s0,g}}{\sigma^A_{R,g}}\int_{-1}^{1} d\mu'\left(\Psi^A_g(x,\mu') - \Psi^{A(\ell)}_g(x,\mu')\right)\right] \qquad (5.11)\end{aligned}$$

The difference $\left(\Psi^A_g(x,\mu') - \Psi^{A(\ell)}_g(x,\mu')\right)$ in the integrands on the right-hand side is transformed by adding and subtracting $\Psi^{A(\ell+1/2)}_g$ as follows

$$\left(\Psi^A_g - \Psi^{A(\ell)}_g + \Psi^{A(\ell+1/2)}_g - \Psi^{A(\ell+1/2)}_g\right) = f^{(\ell+1/2)} + \Psi^{A(\ell+1/2)}_g - \Psi^{A(\ell)}_g \qquad (5.12)$$

and equation 5.11 becomes

$$\begin{aligned}
-\mu^2\frac{\partial}{\partial x}\left(\frac{1}{\sigma^A_{R,g}}\frac{\partial f^{(\ell+1/2)}}{\partial x}\right) &+ \sigma^A_{R,g} f^{(\ell+1/2)} - \frac{\sigma_{s0,g}}{2}\int_{-1}^{1} d\mu' f^{(\ell+1/2)}(x,\mu') \\
+\frac{\mu}{2}\frac{\partial}{\partial x}\left[\frac{\sigma_{s0,g}}{\sigma^A_{R,g}}\int_{-1}^{1} d\mu' f^{(\ell+1/2)}(x,\mu')\right] &= \sigma_{s0,g}\left(\phi_g^{(\ell+1/2)} - \phi_g^{(\ell)}\right) \\
&- \mu\frac{\partial}{\partial x}\left[\frac{\sigma_{s0,g}}{\sigma^A_{R,g}}\left(\phi_g^{(\ell+1/2)} - \phi_g^{(\ell)}\right)\right]
\end{aligned} \tag{5.13}$$

Writing equation 5.13 in discrete ordinates form yields

$$\begin{aligned}
-\mu_n^2\frac{\partial}{\partial x}\left(\frac{1}{\sigma^A_{R,g}}\frac{df_n^{(\ell+1/2)}}{dx}\right) &+ \sigma^A_{R,g} f_n^{(\ell+1/2)} - \sigma_{s0,g}\frac{1}{2}\sum_{m=1}^{N} w_m f_m^{(\ell+1/2)} \\
+\frac{\mu_n}{2}\frac{d}{dx}\left[\frac{\sigma_{s0,g}}{\sigma^A_{R,g}}\sum_{m=1}^{N} w_m f_m^{(\ell+1/2)}\right] &= \sigma_{s0,g}\left(\phi_g^{(\ell+1/2)} - \phi_g^{(\ell)}\right) \\
&- \mu_n\frac{d}{dx}\left[\frac{\sigma_{s0,g}}{\sigma^A_{R,g}}\left(\phi_g^{(\ell+1/2)} - \phi_g^{(\ell)}\right)\right]
\end{aligned} \tag{5.14}$$

The ability of a synthetic acceleration scheme to accelerate convergence can be adversely affected if the equations are not consistent with the transport equations to be accelerated. To ensure a consistent acceleration scheme is derived the low-order operator is introduced into a consistently discretized form of the error equation 5.14. The spatial discretization of the error equation using LC finite elements yields,

$$\begin{aligned}
&\left(\frac{1}{6}\tau_{g,k} - \frac{\mu_n^2}{\tau_{g,k}}\right) f_{n,k-1/2}^{(\ell+1/2)} \\
&+ \left(\frac{1}{3}\left[\tau_{g,k} + \tau_{g,k+1}\right] + \frac{\mu_n^2}{\tau_{g,k}} + \frac{\mu_n^2}{\tau_{g,k+1}}\right) f_{n,k+1/2}^{(\ell+1/2)} \\
&+ \left(\frac{1}{6}\tau_{g,k+1} - \frac{\mu_n^2}{\tau_{g,k+1}}\right) f_{n,k+3/2}^{(\ell+1/2)} \\
&= \left(a_k + \mu_n b_k\right)\frac{1}{2}\sum_{m=1}^{N} w_m f_{m,k-1/2}^{(\ell+1/2)} + \left(A_k + \mu_n B_k\right)\frac{1}{2}\sum_{m=1}^{N} w_m f_{m,k+1/2}^{(\ell+1/2)} \\
&+ \left(a_{k+1} - \mu_n b_{k+1}\right)\frac{1}{2}\sum_{m=1}^{N} w_m f_{m,k+3/2}^{(\ell+1/2)} \\
&+ \left(a_k + \mu_n b_k\right)\mathcal{R}^0_{k-1/2} + \left(A_k + \mu_n B_k\right)\mathcal{R}^0_{k+1/2} + \left(a_{k+1} - \mu_n b_{k+1}\right)\mathcal{R}^0_{k+3/2}
\end{aligned} \tag{5.15}$$

where

$$\begin{aligned}
\tau_{g,k} &= \Delta x_k \sigma^A_{R,g,k} \\
a_k &= \frac{1}{6}\Delta x_k \sigma_{s0,g,k} \\
b_k &= \frac{1}{2}\frac{\sigma_{s0,g,k}}{\sigma_{R,g,k}} \\
A_k &= \frac{1}{3}\left(\Delta x_k \sigma_{s0,g,k} + \Delta x_{k+1}\sigma_{s0,k+1}\right) \\
B_k &= \frac{1}{2}\left(\frac{\sigma_{s0,g,k}}{\sigma_{R,g,k}} - \frac{\sigma_{s0,k+1}}{\sigma_{R,g,k+1}}\right) \\
\mathcal{R}^0_{k-1/2} &= \phi^{(\ell+1/2)}_{k-1/2} - \phi^{(\ell)}_{k-1/2} \\
\mathcal{R}^0_{k+1/2} &= \phi^{(\ell+1/2)}_{k+1/2} - \phi^{(\ell)}_{k+1/2} \\
\mathcal{R}^0_{k+3/2} &= \phi^{(\ell+1/2)}_{k+3/2} - \phi^{(\ell)}_{k+3/2}
\end{aligned}$$

$\mathcal{R}^0_{k\pm1/2}$ are the scalar flux residuals at the cell-edges.

The low-order approximation to the "exact" error $f_n^{(\ell+1/2)}$ is given below:

$$f_n^{(\ell+1/2)}(x) \approx F^{(\ell+1/2)}(x) + 3\mu_n H^{(\ell+1/2)}(x) \tag{5.16}$$

where

$$\phi^{(\ell+1/2)} = \frac{1}{2}\sum_{n=1}^{N} w_n \Psi_n^{(\ell+1/2)} \tag{5.17}$$

$$F^{(\ell+1/2)} = \frac{1}{2}\sum_{n=1}^{N} w_n f_n^{(\ell+1/2)} \tag{5.18}$$

$$H^{(\ell+1/2)} = \frac{1}{2}\sum_{n=1}^{N} w_n \mu_n f_n^{(\ell+1/2)} \tag{5.19}$$

The low-order approximation to the error given in equation 5.16 is actually the diffusion approximation. Recall that the diffusion approximation relates the angular flux to the scalar flux and current as follows

$$\Psi_n(x) \approx \phi(x) + 3\mu_n J(x) \tag{5.20}$$

where $\phi(x)$ is the scalar flux and $J(x)$ is the current defined as:

$$\phi(x) = \frac{1}{2}\sum_{n=1}^{N} w_n \Psi_n(x) \quad \text{and} \quad J(x) = \frac{1}{2}\sum_{n=1}^{N} w_n \mu_n \Psi_n(x)$$

Thus, $F^{(\ell+1/2)}$ is referred to as the scalar component of the error, and similarly, $H^{(\ell+1/2)}$ is called the current component of the error. The discretized version of equation 5.16 gives

$$f^{(\ell+1/2)}_{n,k\pm1/2} = F^{(\ell+1/2)}_{k\pm1/2} + 3\mu_n H^{(\ell+1/2)}_{k\pm1/2} \tag{5.21}$$

which is introduced into equation 5.15 to yield

$$\begin{aligned}
&\left(\tfrac{1}{6}\tau_{g,k} - \tfrac{\mu_n^2}{\tau_{g,k}}\right)\left[F^{(\ell+1/2)}_{k-1/2} + 3\mu_n H^{(\ell+1/2)}_{k-1/2}\right] \\
&+ \left(\tfrac{1}{3}\left[\tau_{g,k} + \tau_{g,k+1}\right] + \tfrac{\mu_n^2}{\tau_{g,k}} + \tfrac{\mu_n^2}{\tau_{g,k+1}}\right)\left[F^{(\ell+1/2)}_{k+1/2} + 3\mu_n H^{(\ell+1/2)}_{k+1/2}\right] \\
&+ \left(\tfrac{1}{6}\tau_{g,k+1} - \tfrac{\mu_n^2}{\tau_{g,k+1}}\right)\left[F^{(\ell+1/2)}_{k+3/2} + 3\mu_n H^{(\ell+1/2)}_{k+3/2}\right] \\
&= \left(a_k + \mu_n b_k\right)\tfrac{1}{2}\sum_{m=1}^{N} w_m \left[F^{(\ell+1/2)}_{k-1/2} + 3\mu_m H^{(\ell+1/2)}_{k-1/2}\right] \\
&+ \left(A_k + \mu_n B_k\right)\tfrac{1}{2}\sum_{m=1}^{N} w_m \left[F^{(\ell+1/2)}_{k+1/2} + 3\mu_m H^{(\ell+1/2)}_{k+1/2}\right] \\
&+ \left(a_{k+1} - \mu_n b_{k+1}\right)\tfrac{1}{2}\sum_{m=1}^{N} w_m \left[F^{(\ell+1/2)}_{k+3/2} + 3\mu_m H^{(\ell+1/2)}_{k+3/2}\right] \\
&+ \left(a_k + \mu_n b_k\right)\mathcal{R}^0_{k-1/2} + \left(A_k + \mu_n B_k\right)\mathcal{R}^0_{k+1/2} + \left(a_{k+1} - \mu_n b_{k+1}\right)\mathcal{R}^0_{k+3/2}
\end{aligned} \tag{5.22}$$

which readily reduces to

$$\begin{aligned}
&\left(\frac{1}{6}\tau_{g,k} - \frac{\mu_n^2}{\tau_{g,k}}\right)\left[F^{(\ell+1/2)}_{k-1/2} + 3\mu_n H^{(\ell+1/2)}_{k-1/2}\right] \\
+\ &\left(\frac{1}{3}\left[\tau_{g,k} + \tau_{g,k+1}\right] + \frac{\mu_n^2}{\tau_{g,k}} + \frac{\mu_n^2}{\tau_{g,k+1}}\right)\left[F^{(\ell+1/2)}_{k+1/2} + 3\mu_n H^{(\ell+1/2)}_{k+1/2}\right] \\
+\ &\left(\frac{1}{6}\tau_{g,k+1} - \frac{\mu_n^2}{\tau_{g,k+1}}\right)\left[F^{(\ell+1/2)}_{k+3/2} + 3\mu_n H^{(\ell+1/2)}_{k+3/2}\right] \\
=\ &\left(a_k + \mu_n b_k\right)F^{(\ell+1/2)}_{k-1/2} + \left(A_k + \mu_n B_k\right)F^{(\ell+1/2)}_{k+1/2} + \left(a_{k+1} - \mu_n b_{k+1}\right)F^{(\ell+1/2)}_{k+3/2} \\
+\ &\left(a_k + \mu_n b_k\right)\mathcal{R}^0_{k-1/2} + \left(A_k + \mu_n B_k\right)\mathcal{R}^0_{k+1/2} + \left(a_{k+1} - \mu_n b_{k+1}\right)\mathcal{R}^0_{k+3/2}
\end{aligned} \tag{5.23}$$

The derivation proceeds by taking the 0^{th} and 1^{st} angular moments of equation 5.23. To take the 0^{th} angular moment we multiply through equation 5.23 by w_n and perform the summation over all the angles. The 1^{st} angular moment is taken by multiplying through equation 5.23 by $w_n\mu_n$ and performing the summation over all the angles.

The 0^{th} angular moment of equation 5.23 gives

$$\begin{aligned}
& \left(\frac{1}{6}\tau_{g,k} - \frac{2}{3}\frac{1}{\tau_{g,k}} - a_k\right) F_{k-1/2}^{(\ell+1/2)} \\
+ & \left(\frac{1}{3}\left[\tau_{g,k} + \tau_{g,k+1}\right] + \frac{2}{3}\left[\frac{1}{\tau_{g,k}} + \frac{1}{\tau_{g,k+1}}\right] - A_k\right) F_{k+1/2}^{(\ell+1/2)} \\
+ & \left(\frac{1}{6}\tau_{g,k+1} - \frac{2}{3}\frac{1}{\tau_{g,k+1}} - a_{k+1}\right) F_{k+3/2}^{(\ell+1/2)} \\
= & \; a_k\mathcal{R}_{k-1/2}^0 + A_k\mathcal{R}_{k+1/2}^0 + a_{k+1}\mathcal{R}_{k+3/2}^0
\end{aligned} \tag{5.24}$$

The 1^{st} angular moment of equation 5.23 yields

$$\begin{aligned}
& \left(\frac{1}{3}\tau_{g,k} - \frac{6}{5}\frac{1}{\tau_{g,k}}\right) H_{k-1/2}^{(\ell+1/2)} - \frac{2}{3}b_k F_{k-1/2}^{(\ell+1/2)} \\
+ & \left(\frac{2}{3}\left[\tau_{g,k} + \tau_{g,k+1}\right] + \frac{6}{5}\left[\frac{1}{\tau_{g,k}} + \frac{1}{\tau_{g,k+1}}\right]\right) H_{k+1/2}^{(\ell+1/2)} - \frac{2}{3}B_k F_{k+1/2}^{(\ell+1/2)} \\
+ & \left(\frac{1}{3}\tau_{g,k+1} - \frac{6}{5}\frac{1}{\tau_{g,k+1}}\right) H_{k+3/2}^{(\ell+1/2)} + \frac{2}{3}b_{k+1} F_{k+3/2}^{(\ell+1/2)} \\
= & \; \frac{2}{3}b_k\mathcal{R}_{k-1/2}^0 + \frac{2}{3}B_k\mathcal{R}_{k+1/2}^0 - \frac{2}{3}b_{k+1}\mathcal{R}_{k+3/2}^0
\end{aligned} \tag{5.25}$$

Equations 5.24 and 5.25 make up a block system for the scalar and current part of the error which is given below as

$$\begin{aligned}
& \begin{pmatrix} \left(\frac{1}{6}\tau_{g,k} - \frac{2}{3\tau_{g,k}} - a_k\right) & 0 \\ -\frac{2}{3}b_k & \left(\frac{1}{3}\tau_{g,k} - \frac{6}{5}\tau_{g,k}\right) \end{pmatrix} \cdot \begin{Bmatrix} F_{k-1/2}^{(\ell+1/2)} \\ H_{k-1/2}^{(\ell+1/2)} \end{Bmatrix} \\
+ & \begin{pmatrix} \begin{pmatrix} \frac{1}{3}(\tau_{g,k} + \tau_{g,k+1}) \\ +\frac{2}{3}(\frac{1}{\tau_{g,k}} + \frac{1}{\tau_{g,k+1}}) - A_k \end{pmatrix} & 0 \\ -\frac{2}{3}B_k & \begin{pmatrix} \frac{2}{3}(\tau_{g,k} + \tau_{g,k+1}) \\ -\frac{6}{5}(\frac{1}{\tau_{g,k}} + \frac{1}{\tau_{g,k+1}}) \end{pmatrix} \end{pmatrix} \cdot \begin{Bmatrix} F_{k+1/2}^{(\ell+1/2)} \\ H_{k+1/2}^{(\ell+1/2)} \end{Bmatrix} \\
+ & \begin{pmatrix} \left(\frac{1}{6}\tau_{g,k+1} - \frac{2}{3\tau_{g,k+1}} - a_{k+1}\right) & 0 \\ +\frac{2}{3}b_{k+1} & \left(\frac{1}{3}\tau_{g,k+1} - \frac{6}{5}\tau_{g,k+1}\right) \end{pmatrix} \cdot \begin{Bmatrix} F_{k+3/2}^{(\ell+1/2)} \\ H_{k+3/2}^{(\ell+1/2)} \end{Bmatrix} \\
= & \begin{Bmatrix} a_k\mathcal{R}_{k-1/2}^0 + A_k\mathcal{R}_{k+1/2}^0 + a_{k+1}\mathcal{R}_{k+3/2}^0 \\ \frac{2}{3}b_k\mathcal{R}_{k-1/2}^0 + \frac{2}{3}B_k\mathcal{R}_{k+1/2}^0 - \frac{2}{3}b_{k+1}\mathcal{R}_{k+3/2}^0 \end{Bmatrix}
\end{aligned} \tag{5.26}$$

The scalar and current parts of the error are not coupled for the interior cells of the slab from $k = 2, 3, \ldots, K-2$. However, they become coupled at the $k = 1$ and $k = K-1$ cells as a result of the boundary condition for outgoing directions at the left edge (x_L) and right edge (x_R) of the slab. The derivation of these boundary conditions is detailed in the next section.

5.1.1 Boundary Conditions for DSA Equations

Because the incoming boundary conditions associated with the transport equation are preserved, the DSA equation boundary conditions at the slab edges for incoming directions are simply

$$F_{1/2}^{(\ell+1/2)} = 0 \;\; \mu_n > 0 \quad \text{and} \quad F_{K+1/2}^{(\ell+1/2)} = 0 \;\; \mu_n < 0$$
$$H_{1/2}^{(\ell+1/2)} = 0 \;\; \mu_n > 0 \quad \text{and} \quad H_{K+1/2}^{(\ell+1/2)} = 0 \;\; \mu_n < 0$$

For the outgoing directions at both edges of the slab an auxiliary boundary condition for both $F^{(\ell+1/2)}$ and $H^{(\ell+1/2)}$ is needed. The derivation of these boundary conditions begins with the first order form of the error equation:

$$\mu_n \frac{df_n^{(\ell+1/2)}}{dx} + \sigma_{R,g}^A f_n^{(\ell+1/2)} - \frac{\sigma_{s0,g}}{2} \sum_{m=1}^{N} w_m f_m^{(\ell+1/2)} = \sigma_{s0,g}\left(\phi^{(\ell+1/2)} - \phi^{(\ell)}\right) \tag{5.27}$$

Applying LC finite elements to equation 5.27 over the k^{th} cell gives,

$$\begin{aligned} \left(\mu_n + \frac{2}{3}\tau_{g,k}\right) f_{n,k+1/2}^{(\ell+1/2)} \quad &- \quad \left(\mu_n - \frac{1}{3}\tau_{g,k}\right) f_{n,k-1/2}^{(\ell+1/2)} = \\ \frac{1}{3}\Delta x_k \sigma_{s0,g,k} \frac{1}{2} \sum_{m=1}^{N} w_m f_{m,k-1/2}^{(\ell+1/2)} \quad &+ \quad \frac{2}{3}\Delta x_k \sigma_{s0,g,k} \frac{1}{2} \sum_{m=1}^{N} w_m f_{m,k+1/2}^{(\ell+1/2)} \\ +\frac{1}{3}\Delta x_k \sigma_{s0,g,k} \mathcal{R}_{k-1/2}^{0} \quad &+ \quad \frac{2}{3}\Delta x_k \sigma_{s0,g,k} \mathcal{R}_{k+1/2}^{0} \end{aligned} \tag{5.28}$$

Recalling that $a_k = \frac{1}{6}\Delta x_k \sigma_{s0,g,k}$ (see pg. 58), the above equation can be written as

$$\begin{aligned} &\left(\mu_n + \frac{2}{3}\tau_{g,k}\right) f_{n,k+1/2}^{(\ell+1/2)} - \left(\mu_n - \frac{1}{3}\tau_{g,k}\right) f_{n,k-1/2}^{(\ell+1/2)} \\ &= 2a_k \frac{1}{2} \sum_{m=1}^{N} w_m f_{m,k-1/2}^{(\ell+1/2)} + 4a_k \frac{1}{2} \sum_{m=1}^{N} w_m f_{m,k+1/2}^{(\ell+1/2)} \\ &+2a_k \mathcal{R}_{k-1/2}^{0} + 4a_k \mathcal{R}_{k+1/2}^{0} \end{aligned} \tag{5.29}$$

To get the boundary condition for the $k = 1$ cell and directions $\mu_n < 0$ we solve the above equation for $f_{n,1/2}^{(\ell+1/2)}$ to get

$$\begin{aligned} f_{n,1/2}^{(\ell+1/2)} \; = \; &\left(\mu_n - \frac{1}{3}\tau_{g,1}\right)^{-1} \cdot \left\{ \left(\mu_n + \frac{2}{3}\tau_{g,1}\right) f_{n,3/2}^{(\ell+1/2)} \right. \\ &-2a_1 \frac{1}{2} \sum_{m=1}^{N} w_m f_{m,1/2}^{(\ell+1/2)} - 4a_1 \frac{1}{2} \sum_{m=1}^{N} w_m f_{m,3/2}^{(\ell+1/2)} \\ &\left. -2a_1 \mathcal{R}_{1/2}^{0} - 4a_1 \mathcal{R}_{3/2}^{0} \right\} \end{aligned} \tag{5.30}$$

Equation 5.30 for $f_{n,k-1/2}^{(\ell+1/2)}$ is valid for the $\mu_n < 0$ directions. For the $\mu_n > 0$ directions where there is a vacuum or known source the boundary condition is preserved which means that $f_{n,k-1/2}^{(\ell+1/2)} = 0$. A reflective boundary condition at x_L for the $\mu > 0$ directions will also depend on equation 5.30. Next, we take the 0^{th} angular moment of equation 5.30 as detailed below

$$\begin{aligned}
\frac{1}{2}\sum_{n=1}^{N} w_n f_{n,1/2}^{(\ell+1/2)} &= \frac{1}{2}\sum_{n=1}^{N/2} w_n f_{n,1/2}^{(\ell+1/2)} \\
&+\frac{1}{2}\sum_{n=\frac{N}{2}+1}^{N} w_n \left\{ \begin{array}{l} \left(\mu_n - \frac{1}{3}\tau_{g,1}\right)^{-1} \cdot \left[\left(\mu_n + \frac{2}{3}\tau_{g,1}\right) f_{n,3/2}^{(\ell+1/2)} \right. \\ -2a_1 \frac{1}{2}\sum_{m=1}^{N} w_m f_{m,1/2}^{(\ell+1/2)} - 4a_1 \frac{1}{2}\sum_{m=1}^{N} w_m f_{m,3/2}^{(\ell+1/2)} \\ \left. -2a_1 \mathcal{R}_{1/2}^{0} - 4a_1 \mathcal{R}_{3/2}^{0} \right] \end{array} \right\} \qquad (5.31)
\end{aligned}$$

Introducing the low-order approximation to the error into the above equation yields

$$\begin{aligned}
F_{1/2} &= \frac{1}{2}\sum_{n=\frac{N}{2}+1}^{N} w_n \left\{ \left(\mu_n - \frac{1}{3}\tau_{g,1}\right)^{-1} \cdot \left[\left(\mu_n + \frac{2}{3}\tau_{g,1}\right) [F_{3/2}^{(\ell+1/2)} + 3\mu_n H_{3/2}^{(\ell+1/2)}] \right. \right. \qquad (5.32) \\
&\left. \left. -2a_1 F_{1/2}^{(\ell+1/2)} - 4a_1 F_{3/2}^{(\ell+1/2)} - 2a_1 \mathcal{R}_{1/2}^{0} - 4a_1 \mathcal{R}_{3/2}^{0} \right] \right\}
\end{aligned}$$

The following parameters are defined as

$$\begin{aligned}
\alpha^{x_L} &= \frac{1}{2}\sum_{n=\frac{N}{2}+1}^{N} w_n \left(\mu_n - \frac{1}{3}\tau_{g,1}\right)^{-1} \left(\mu_n + \frac{2}{3}\tau_{g,1}\right) \\
\beta^{x_L} &= \frac{1}{2}\sum_{n=\frac{N}{2}+1}^{N} w_n \mu_n \left(\mu_n - \frac{1}{3}\tau_{g,1}\right)^{-1} \left(\mu_n + \frac{2}{3}\tau_{g,1}\right) \\
\chi^{x_L} &= \frac{1}{2}\sum_{n=\frac{N}{2}+1}^{N} w_n \left(\mu_n - \frac{1}{3}\tau_{g,1}\right)^{-1}
\end{aligned}$$

and equation 5.37 becomes

$$\begin{aligned}
F_{1/2} &= \alpha^{x_L} F_{3/2}^{(\ell+1/2)} + 3\beta^{x_L} H_{3/2}^{(\ell+1/2)} - 2a_1 \chi^{x_L} F_{1/2}^{(\ell+1/2)} - 4a_1 \chi^{x_L} F_{3/2}^{(\ell+1/2)} \\
&- 2a_1 \chi^{x_L} \mathcal{R}_{1/2}^{0} - 4a_1 \chi^{x_L} \mathcal{R}_{3/2}^{0} \qquad (5.33)
\end{aligned}$$

Joining like terms and solving for $F_{1/2}$ gives

$$F_{1/2} = A_0^{x_L} F_{3/2}^{(\ell+1/2)} + B_0^{x_L} H_{3/2}^{(\ell+1/2)} - C_0^{x_L} (\mathcal{R}_{1/2}^{0} + 2\mathcal{R}_{3/2}^{0}) \qquad (5.34)$$

where

$$A_0^{xL} = \frac{(\alpha^{xL} - 4a_1\chi^{xL})}{(1+2a_1\chi^{xL})}; \quad B_0^{xL} = \frac{3\beta^{xL}}{(1+2a_1\chi^{xL})}; \quad C_0^{xL} = \frac{2a_1\chi^{xL}}{(1+2a_1\chi^{xL})}$$

The next step is to take the 1^{st} angular moment of equation 5.30:

$$\begin{aligned}
\frac{1}{2}\sum_{n=1}^{N} w_n\mu_n f_{n,1/2}^{(\ell+1/2)} &= \frac{1}{2}\sum_{n=1}^{N/2} w_n\mu_n f_{n,1/2}^{(\ell+1/2)} \\
&+\frac{1}{2}\sum_{n=\frac{N}{2}+1}^{N} w_n\mu_n \left\{ \begin{array}{l} \left(\mu_n - \frac{1}{3}\tau_{g,1}\right)^{-1} \cdot \Bigg[\left(\mu_n + \dfrac{2}{3}\tau_{g,1}\right) f_{n,3/2}^{(\ell+1/2)} \\ -2a_1\dfrac{1}{2}\displaystyle\sum_{m=1}^{N} w_m f_{m,1/2}^{(\ell+1/2)} - 4a_1\dfrac{1}{2}\displaystyle\sum_{m=1}^{N} w_m f_{m,3/2}^{(\ell+1/2)} \\ -2a_1\mathcal{R}_{1/2}^0 - 4a_1\mathcal{R}_{3/2}^0 \Bigg] \end{array} \right\}
\end{aligned} \tag{5.35}$$

Substituting the low-order approximation to the error into the above equation gives

$$\begin{aligned}
H_{1/2} &= \frac{1}{2}\sum_{n=\frac{N}{2}+1}^{N} w_n\mu_n \Bigg\{ \left(\mu_n - \frac{1}{3}\tau_{g,1}\right)^{-1} \cdot \Bigg[\left(\mu_n + \frac{2}{3}\tau_{g,1}\right) [F_{3/2}^{(\ell+1/2)} + 3\mu_n H_{3/2}^{(\ell+1/2)}] \\
&-2a_1 F_{1/2}^{(\ell+1/2)} - 4a_1 F_{3/2}^{(\ell+1/2)} - 2a_1\mathcal{R}_{1/2}^0 - 4a_1\mathcal{R}_{3/2}^0 \Bigg] \Bigg\}
\end{aligned} \tag{5.36}$$

To simplify the equation 5.36 the following parameters are defined as

$$\begin{aligned}
\varepsilon^{xL} &= \frac{1}{2}\sum_{n=\frac{N}{2}+1}^{N} w_n\mu_n \left(\mu_n - \frac{1}{3}\tau_{g,1}\right)^{-1}\left(\mu_n + \frac{2}{3}\tau_{g,1}\right) \\
\gamma^{xL} &= \frac{1}{2}\sum_{n=\frac{N}{2}+1}^{N} w_n\mu_n^2 \left(\mu_n - \frac{1}{3}\tau_{g,1}\right)^{-1}\left(\mu_n + \frac{2}{3}\tau_{g,1}\right) \\
\eta^{xL} &= \frac{1}{2}\sum_{n=\frac{N}{2}+1}^{N} w_n\mu_n \left(\mu_n - \frac{1}{3}\tau_{g,1}\right)^{-1}
\end{aligned}$$

and equation 5.36 becomes

$$\begin{aligned}
H_{1/2} &= \varepsilon^{xL} F_{3/2}^{(\ell+1/2)} + 3\gamma^{xL} H_{3/2}^{(\ell+1/2)} - 2a_1\eta^{xL} F_{1/2}^{(\ell+1/2)} - 4a_1\eta^{xL} F_{3/2}^{(\ell+1/2)} \\
&- 2a_1\eta^{xL}\mathcal{R}_{1/2}^0 - 4a_1\eta^{xL}\mathcal{R}_{3/2}^0
\end{aligned} \tag{5.37}$$

joining like terms gives,

$$\begin{aligned}
H_{1/2}^{(\ell+1/2)} &= (\varepsilon^{xL} - 4a_1\eta^{xL}) F_{3/2}^{(\ell+1/2)} + 3\gamma^{xL} H_{3/2}^{(\ell+1/2)} - 2a_1\eta^{xL} F_{1/2}^{(\ell+1/2)} \\
&- 2a_1\eta^{xL}(\mathcal{R}_{1/2}^0 + 2\mathcal{R}_{3/2}^0)
\end{aligned} \tag{5.38}$$

Substituting equation 5.34 for $F_{1/2}^{(\ell+1/2)}$ into the above equation yields,

$$H_{1/2}^{(\ell+1/2)} = A_1^{x_L} F_{3/2}^{(\ell+1/2)} + B_1^{x_L} H_{3/2}^{(\ell+1/2)} + C_1^{x_L}(\mathcal{R}_{1/2}^0 + 2\mathcal{R}_{3/2}^0) \tag{5.39}$$

where we defined:

$$\begin{aligned} A_1^{x_L} &= \varepsilon^{x_L} - 4a_1\eta^{x_L} - 2a_1\eta^{x_L} A_0^{x_L} \\ B_1^{x_L} &= 3\gamma^{x_L} - 2a_1\eta^{x_L} B_0^{x_L} \\ C_1^{x_L} &= 2a_1\eta^{x_L}[C_0^{x_L} - 1] \end{aligned}$$

Writing equations 5.34 and 5.39 in matrix form gives

$$\begin{aligned} \begin{Bmatrix} F_{1/2}^{(\ell+1/2)} \\ H_{1/2}^{(\ell+1/2)} \end{Bmatrix} &= \begin{pmatrix} A_0^{x_L} & B_0^{x_L} \\ A_1^{x_L} & B_1^{x_L} \end{pmatrix} \begin{Bmatrix} F_{3/2}^{(\ell+1/2)} \\ H_{3/2}^{(\ell+1/2)} \end{Bmatrix} + \begin{pmatrix} -C_0^{x_L} & 0 \\ C_1^{x_L} & 0 \end{pmatrix} \begin{Bmatrix} \mathcal{R}_{1/2}^0 \\ \mathcal{R}_{1/2}^1 \end{Bmatrix} \\ &+ \begin{pmatrix} -2C_0^{x_L} & 0 \\ 2C_1^{x_L} & 0 \end{pmatrix} \begin{Bmatrix} \mathcal{R}_{3/2}^0 \\ \mathcal{R}_{3/2}^1 \end{Bmatrix} \end{aligned} \tag{5.40}$$

where $\mathcal{R}_{1/2}^1 = J_{1/2}^{(\ell+1/2)} - J_{1/2}^{(\ell)}$ and $\mathcal{R}_{3/2}^1 = J_{3/2}^{(\ell+1/2)} - J_{3/2}^{(\ell)}$. For $k = 1$ equation 5.40 is substituted for $F_{1/2}$ and $H_{1/2}$ in equation 5.26 coupling the scalar and current part of the error at x_L.

Next, we derive the auxiliary boundary conditions for the outgoing direction at the right edge of the slab for the K^{th} cell. Solve equation 5.27 for $f_{n,K+1/2}^{(\ell+1/2)}$ to get

$$\begin{aligned} f_{n,K+1/2}^{(\ell+1/2)} &= \left(\mu_n + \frac{2}{3}\tau_{g,K}\right)^{-1} \cdot \Bigg\{ \left(\mu_n - \frac{2}{3}\tau_{g,K}\right) f_{n,K-1/2}^{(\ell+1/2)} \\ &+2a_K \frac{1}{2}\sum_{m=1}^{N} w_m f_{m,K-1/2}^{(\ell+1/2)} + 4a_K \frac{1}{2}\sum_{m=1}^{N} w_m f_{m,K+/2}^{(\ell+1/2)} \\ &+2a_K \mathcal{R}_{K-1/2}^0 + 4a_1 \mathcal{R}_{K+1/2}^0 \Bigg\} \end{aligned} \tag{5.41}$$

Equation 5.41 is only valid for the outgoing directions ($\mu_n > 0$) at the right-edge of the slab, for incoming directions the boundary condition is preserved and $F_{K+1/2} = 0$. Taking the 0^{th} angular moment of this equation yields

$$\begin{aligned} F_{K+1/2} &= \alpha^{x_R} F_{K-1/2}^{(\ell+1/2)} + 3\beta^{x_R} H_{K-1/2}^{(\ell+1/2)} + 2a_K\chi^{x_R} F_{K-1/2}^{(\ell+1/2)} + 4a_K\chi^{x_R} F_{K+/2}^{(\ell+1/2)} \\ &+ 2a_K\chi^{x_R}\mathcal{R}_{K-1/2}^0 + 4a_K\chi^{x_R}\mathcal{R}_{K+1/2}^0 \end{aligned} \tag{5.42}$$

where

$$\begin{aligned}
\alpha^{xR} &= \frac{1}{2}\sum_{n=1}^{N/2} w_n \left(\mu_n - \frac{1}{3}\tau_{g,K}\right)\left(\mu_n + \frac{2}{3}\tau_{g,K}\right)^{-1} \\
\beta^{xR} &= \frac{1}{2}\sum_{n=1}^{N/2} w_n \mu_n \left(\mu_n - \frac{1}{3}\tau_{g,K}\right)\left(\mu_n + \frac{2}{3}\tau_{g,K}\right)^{-1} \\
\chi^{xR} &= \frac{1}{2}\sum_{n=1}^{N/2} w_n \left(\mu_n + \frac{2}{3}\tau_{g,K}\right)^{-1}
\end{aligned}$$

Grouping terms in equation 5.42 and solving for $F_{K+1/2}$ gives

$$F_{K+1/2} = A_0^{xR} F_{K-1/2}^{(\ell+1/2)} + B_0^{xR} H_{K-1/2}^{(\ell+1/2)} + C_0^{xR}(\mathcal{R}_{K-1/2}^0 + 2\mathcal{R}_{K+1/2}^0) \qquad (5.43)$$

where

$$A_0^{xR} = \tfrac{(\alpha^{xR} + 2a_K\chi^{xR})}{(1-4a_K\chi^{xR})}; \quad B_0^{xR} = \tfrac{3\beta^{xR}}{(1-4a_K\chi^{xR})}; \quad C_0^{xR} = \tfrac{2a_K\chi^{xR}}{(1-4a_K\chi^{xR})}$$

The 1^{st} angular moment of equation 5.41 can be shown to yield

$$\begin{aligned}
H_{K+1/2} &= \varepsilon^{xR} F_{K-1/2}^{(\ell+1/2)} + 3\gamma^{xR} H_{K-1/2}^{(\ell+1/2)} + 2a_K\eta^{xR} F_{K-1/2}^{(\ell+1/2)} + 4a_K\eta^{xR} F_{K+/2}^{(\ell+1/2)} \\
&+ 2a_K\eta^{xR}(\mathcal{R}_{K-1/2}^0 + 2\mathcal{R}_{K+1/2}^0) \qquad (5.44)
\end{aligned}$$

where

$$\begin{aligned}
\varepsilon^{xR} &= \frac{1}{2}\sum_{n=1}^{N/2} w_n \mu_n \left(\mu_n - \frac{1}{3}\tau_{g,K}\right)\left(\mu_n + \frac{2}{3}\tau_{g,K}\right)^{-1} \\
\gamma^{xR} &= \frac{1}{2}\sum_{n=1}^{N/2} w_n \mu_n^2 \left(\mu_n - \frac{1}{3}\tau_{g,K}\right)\left(\mu_n + \frac{2}{3}\tau_{g,K}\right)^{-1} \\
\eta^{xR} &= \frac{1}{2}\sum_{n=1}^{N/2} w_n \mu_n \left(\mu_n + \frac{2}{3}\tau_{g,K}\right)^{-1}
\end{aligned}$$

Substituting equation 5.43 for $F_{K+1/2}$ into equation 5.44 gives the equation for $H_{K+1/2}$ for $\mu_n > 0$:

$$H_{K+1/2} = A_1^{xR} F_{K-1/2}^{(\ell+1/2)} + B_1^{xR} H_{K-1/2}^{(\ell+1/2)} + C_1^{xR}(\mathcal{R}_{K-1/2}^0 + 2\mathcal{R}_{K+1/2}^0) \qquad (5.45)$$

where

$$\begin{aligned}
A_1^{xR} &= \varepsilon^{xR} + 2a_K\eta^{xR} + 4a_K\eta^{xR}A_0^{xR} \\
B_1^{xR} &= 3\gamma^{xR} + 4a_K\eta^{xR}B_0^{xR} \\
C_1^{xR} &= 4a_K\eta^{xR}[1 + C_0^{xR}]
\end{aligned}$$

Writing the equations for $F_{K+1/2}$ and $H_{K+1/2}$ in matrix form below:

$$
\begin{aligned}
\left\{ \begin{array}{c} F_{K+1/2}^{(\ell+1/2)} \\ H_{K+1/2}^{(\ell+1/2)} \end{array} \right\} &= \begin{pmatrix} A_0^{x_R} & B_0^{x_R} \\ A_1^{x_R} & B_1^{x_R} \end{pmatrix} \left\{ \begin{array}{c} F_{K-1/2}^{(\ell+1/2)} \\ H_{K-1/2}^{(\ell+1/2)} \end{array} \right\} + \begin{pmatrix} C_0^{x_R} & 0 \\ C_1^{x_R} & 0 \end{pmatrix} \left\{ \begin{array}{c} \mathcal{R}_{K-1/2}^{0} \\ \mathcal{R}_{K-1/2}^{1} \end{array} \right\} \\
&+ \begin{pmatrix} 2C_0^{x_R} & 0 \\ 2C_1^{x_R} & 0 \end{pmatrix} \left\{ \begin{array}{c} \mathcal{R}_{K+1/2}^{0} \\ \mathcal{R}_{K+1/2}^{1} \end{array} \right\} \qquad (5.46)
\end{aligned}
$$

For the $K-1$ cell equation 5.46 is substituted into equation 5.26 resulting in coupling between the scalar and current parts of the error.

After equation 5.26 is solved for the errors across the slab (at $k+1/2$ for $k=1,2,\ldots,K-2$), we solve equation 5.40 to get the errors at x_L and equation 5.46 to get the errors at x_R. The scalar flux is then updated by adding the scalar part of the error, $F^{(\ell+1/2)}$, to $\phi_{g,0}^{(\ell+1/2)}$.

5.1.2 Implementation of DSA

Implementing the DSA equations in the computer code, we perform the following steps:

1. Solve the transport equation for Ψ_g^A at the $\ell+1/2$ iterate
2. Calculate flux moments at the $\ell+1/2$ iterate
3. Check to see if convergence criteria, ξ, is satisfied
    - If $\max\limits_{all\ k} \epsilon_k < \xi$ then, solution converged proceed to group $g+1$
    - If $\max\limits_{all\ k} \epsilon_k \geq \xi$ then, proceed to Step 4
4. Solve the DSA equation for the scalar component of the error, F, at the $\ell+1/2$ iterate
5. Update the scalar flux with the error to get $\phi_{g,0}^{(\ell+1)}$
6. Calculate new elastic scattering source at $\ell+1$ iterate
7. Repeat Steps 1 through 7 until convergence criteria is satisfied

The general source iteration form of the SAAF transport equation is given as

$$
\begin{aligned}
-\mu^2 \frac{\partial}{\partial x}\left\{ \frac{1}{\sigma_{R,g}^A} \frac{\partial \Psi^{A(\ell+1/2)}}{\partial x} \right\} + \sigma_{R,g}^A \Psi^{A(\ell+1/2)} &= Q^{S(\ell)} - \mu \frac{\partial}{\partial x}\left\{ \frac{1}{\sigma_{R,g}^A} Q^{S(\ell)} \right\} \\
&+ q - \mu \frac{\partial}{\partial x}\left\{ \frac{1}{\sigma_{R,g}^A} q \right\} \qquad (5.47)
\end{aligned}
$$

where $Q^{S(\ell)}$ is the elastic scattering group at the previous source iteration and q is the known source into this energy group from downscatter, slowing-down, etc. Solving equation 5.47 yields the values of Ψ_g^A at the $\ell+1/2$ iterate which are used to compute the flux moments at the $\ell+1/2$ iterate as follows

$$\phi_{g,l}^{(\ell+1/2)} = \frac{1}{2}\sum_{n=1}^{N} w_n P_l(\mu_n)\Psi_{n,g}^{A(\ell+1/2)} \tag{5.48}$$

These updated scalar fluxes are used in the DSA equations 5.26 on the right-hand side to calculate the scalar flux residuals: $\mathcal{R}^0 = \phi^{(\ell+1/2)} - \phi^{(\ell)}$. We then solve equation 5.26 to get the error at the $\ell+1/2$ iterate. The error is added to the scalar flux to get the updated value at $\ell+1$

$$\phi_{g,0}^{(\ell+1)} = \phi_{g,0}^{(\ell+1/2)} + F^{(\ell+1/2)} \tag{5.49}$$

The elastic scattering source is updated using $\phi_{g,0}^{(\ell+1)}$ as follows:

$$Q_g^{S(\ell+1)} = \sigma_{s0,g}\phi_{g,0}^{(\ell+1)} + \sum_{l=1}^{L}(2l+1)P_l(\mu_n)\sigma_{sl,g}\phi_{g,l}^{(\ell+1/2)} \tag{5.50}$$

In the next section the Fourier analysis on both the unaccelerated and accelerated source iteration schemes are presented to evaluate their respective rates of convergence.

5.2 Fourier Analysis

Fourier analysis is used to assess the rate of convergence we expect to see in the implementation of a given iteration scheme. It also allows one to ascertain what acceleration techniques will be applicable to increase this rate of convergence. In Fourier analysis a system of coupled differential equations is converted into an algebraic system of equations using Fourier transforms. For example, we are trying to solve the following system of equations

$$(\mathbf{A} - \mathbf{B})\,\vec{\Psi} = \vec{q} \tag{5.51}$$

which in source iteration form becomes,

$$\mathbf{A}\vec{\Psi}^{(\ell+1)} = \vec{q} + \mathbf{B}\vec{\Psi}^{(\ell)} \tag{5.52}$$

Defining the error associated with the ℓ^{th} iterate as $\epsilon^{(\ell+1)} = \vec{\Psi} - \vec{\Psi}^{(\ell+1)}$, and using the Fourier expansion of the spatial variable (x) gives ,

$$\epsilon(x,\mu) = \epsilon(\lambda,\mu)e^(i\lambda x) \tag{5.53}$$

We derive the following error equation

$$\begin{aligned} \mathbf{A}\vec{\epsilon}^{(\ell+1)} &= \mathbf{B}\vec{\epsilon}^{(\ell)} \\ &= \mathbf{A}^{-1}\mathbf{B}\vec{\epsilon}^{(\ell)} \end{aligned} \tag{5.54}$$

where $\mathbf{A}^{-1}\mathbf{B}$ is called the iteration matrix. The eigenvalues of the iteration matrix determine the rate of convergence. The maximum of the absolute values of these eigenvalues is the spectral radius, ρ. The closer ρ is to unity the slower the rate of convergence while the closer the ρ is to zero the more rapid the convergence. Next, the rate of convergence of the unaccelerated source iteration scheme is evaluated.

5.2.1 Unaccelerated Source Iteration

To perform a Fourier analysis on the unaccelerated source iteration scheme we start with the transport equation for the average angular flux:

$$\begin{aligned} -\mu^2 \frac{\partial}{\partial x}\left(\frac{1}{\sigma_{R,g}^A}\frac{\partial \Psi_g^A}{\partial x}\right) + \sigma_{R,g}^A \Psi_g^A &= \frac{\sigma_{s0,g}}{2}\int_{-1}^{1} d\mu' \Psi_g^A(x,\mu') \\ &- \frac{\mu}{2}\frac{\partial}{\partial x}\left(\frac{\sigma_{s0,g}}{\sigma_{R,g}^A}\int_{-1}^{1} d\mu' \Psi_g^A(x,\mu')\right) + q_g \end{aligned} \tag{5.55}$$

where the source, q_g, represents the known source due to downscatter from higher energy groups, slowing-down from the $g-1$ group, the presence of a fixed source and the contribution from the slope angular flux, Ψ_g^E, as follows:

$$\begin{aligned} q_g &= Q_g - \mu\frac{\partial}{\partial x}\left(\frac{1}{\sigma_{R,g}}Q_g\right) \\ &+ \frac{S_{g-1}}{\Delta E_g}\left[\Psi_{g-1}^A - \Psi_{g-1}^E\right] - \mu\frac{\partial}{\partial x}\left(\frac{1}{\sigma_{R,g}^A}\frac{S_{g-1}}{\Delta E_g}\left[\Psi_{g-1}^A - \Psi_{g-1}^E\right]\right) \\ &+ \frac{S_g}{\Delta E_g}\Psi_g^E - \mu\frac{\partial}{\partial x}\left(\frac{1}{\sigma_{R,g}^A}\frac{S_g}{\Delta E_g}\Psi_g^E\right) \end{aligned} \tag{5.56}$$

Assuming that all the physical data is constant let

$$z = x \cdot \sigma_{R,g}^A \quad \text{and} \quad c = \frac{\sigma_{s0,g}}{\sigma_{R,g}^A}$$

Dividing through equation 5.55 with $\sigma_{R,g}^A$ and using the definitions of z and c yields,

$$\begin{aligned} -\mu^2 \frac{\partial}{\partial z}\left(\frac{\partial \Psi_g}{\partial z}\right) + \Psi_g &= \frac{c}{2}\int_{-1}^{1} d\mu' \Psi_g(z,\mu') \\ &- \frac{\mu}{2}\frac{\partial}{\partial z}\left(c\int_{-1}^{1} d\mu' \Psi_g(z,\mu')\right) + \frac{q_g}{\sigma_{R,g}^A} \end{aligned} \tag{5.57}$$

The unaccelerated source iteration form of equation 5.57 becomes

$$\begin{aligned} -\mu^2 \frac{\partial}{\partial z}\left(\frac{\partial \Psi_g^{A(\ell+1)}}{\partial z}\right) + \Psi_g^{A(\ell+1)} &= \frac{c}{2}\int_{-1}^{1} d\mu' \Psi_g^{A(\ell)}(z,\mu') \\ &- \frac{\mu}{2}\frac{\partial}{\partial z}\left(c\int_{-1}^{1} d\mu' \Psi_g^{A(\ell)}(z,\mu')\right) + \frac{q_g}{\sigma_{R,g}^{A}} \end{aligned} \tag{5.58}$$

The error at the ℓ^{th} iterate and the g^{th} energy group is defined as

$$\epsilon_g^{(\ell)}(z) = \Psi_g^A(z) - \Psi_g^{A(\ell)}(z) \tag{5.59}$$

Subtracting equation 5.58 from equation 5.57 yields the error equation below

$$\begin{aligned} -\mu^2 \frac{\partial}{\partial z}\left(\frac{\partial \epsilon^{(\ell+1)}}{\partial z}\right) + \epsilon^{(\ell+1)} &= \frac{c}{2}\int_{-1}^{1} d\mu' \epsilon^{(\ell)}(z,\mu') \\ &- \frac{\mu}{2}\frac{\partial}{\partial z}\left(c\int_{-1}^{1} d\mu' \epsilon^{(\ell)}(z,\mu')\right) \end{aligned} \tag{5.60}$$

The goal of the Fourier analysis is to obtain a recurrence relationship relating $\epsilon^{(\ell+1)}$ to $\epsilon^{(\ell)}$. The error is thus redefined in terms of a Fourier mode number, λ, as follows:

$$\epsilon(z,\mu) = \tilde{\epsilon}(\lambda,\mu)e^{i\lambda z} \tag{5.61}$$

where $-\infty < z < +\infty$; $-\infty < \lambda < +\infty$; and $i = \sqrt{-1}$. Substituting this redefinition of the error into equation 5.60 yields,

$$\begin{aligned} -\mu^2 \frac{\partial}{\partial z}\left(\frac{\partial \tilde{\epsilon}^{(\ell+1)}(\lambda,\mu)e^{i\lambda z}}{\partial z}\right) + \tilde{\epsilon}^{(\ell+1)}(\lambda,\mu)e^{i\lambda z} &= \frac{c}{2}\int_{-1}^{1} d\mu' \tilde{\epsilon}^{(\ell)}(\lambda,\mu)e^{i\lambda z} \\ &- \frac{\mu}{2}\frac{\partial}{\partial z}\left(c\int_{-1}^{1} d\mu' \tilde{\epsilon}^{(\ell)}(\lambda,\mu)e^{i\lambda z}\right) \end{aligned} \tag{5.62}$$

The derivatives in equation 5.62 are evaluated to get

$$\frac{\partial}{\partial z}\left(\frac{\partial e^{i\lambda z}}{\partial z}\right) = (i\lambda)^2 e^{i\lambda z} = -\lambda^2 e^{i\lambda z} \tag{5.63}$$

$$\frac{\partial e^{i\lambda z}}{\partial z} = (i\lambda)e^{i\lambda z} \tag{5.64}$$

and equation 5.62 becomes

$$\begin{aligned} \mu^2\lambda^2 e^{i\lambda z}\tilde{\epsilon}^{(\ell+1)}(\lambda,\mu)e^{i\lambda z} + \tilde{\epsilon}^{(\ell+1)}(\lambda,\mu)e^{i\lambda z} &= \frac{c}{2}e^{i\lambda z}\int_{-1}^{1} d\mu' \tilde{\epsilon}^{(\ell)}(\lambda,\mu) \\ &- \frac{\mu}{2}ci\lambda e^{i\lambda z}\frac{\partial}{\partial z}\left(\int_{-1}^{1} d\mu' \tilde{\epsilon}^{(\ell)}(\lambda,\mu)\right) \end{aligned} \tag{5.65}$$

Divide through by $e^{i\lambda z}$ gives the following expression for $\tilde{\epsilon}^{(\ell+1)}$

$$\begin{aligned}
\left[1+\mu^2\lambda^2\right]\tilde{\epsilon}^{(\ell+1)}(\lambda,\mu) &= \frac{c}{2}\left[1-\mu i\lambda\right]\tilde{\epsilon}^{(\ell)} \\
\tilde{\epsilon}^{(\ell+1)} &= \frac{c}{2}\int_{-1}^{1}\frac{[1-\mu i\lambda]}{[1+\mu^2\lambda^2]}\tilde{\epsilon}^{(\ell)}d\mu \\
\tilde{\epsilon}^{(\ell+1)} &= \left(\frac{c}{\lambda}\arctan(\lambda)\right)\tilde{\epsilon}^{(\ell)} \\
\tilde{\epsilon}^{(\ell+1)} &= \gamma(\lambda)\tilde{\epsilon}^{(\ell)} \qquad (5.66)
\end{aligned}$$

where $c \leq 1$. The iteration will reach convergence if the following criteria is satisfied:

$$\max_{-\infty<\lambda<+\infty}|\gamma(\lambda)| < 1 \qquad (5.67)$$

The following limits of $\gamma(\lambda)$ are readily established,

$$\lim_{\lambda\to 0}|\gamma(\lambda)| = c \quad \text{and} \quad \lim_{\lambda\to\infty}|\gamma(\lambda)| = 0$$

The rate of convergence is dictated by the spectral radius, ρ, which is defined as

$$\rho = \max_{-\infty<\lambda<+\infty}|\gamma(\lambda)| \qquad (5.68)$$

As shown by the limits above, ρ for this iteration scheme is equal to the ratio of the scattering cross-section to the removal cross-section, c. This indicates that the rate of convergence for the unaccelerated source iteration will be the slowest for energy groups where c is close to one. A plot of the value of $\gamma(\lambda)$ as a function of λ is depicted in Figure 5.1 for the unaccelerated source iteration scheme. Figure 5.1 depicts that the spectral radius goes to unity for the low Fourier mode numbers which indicates that these are the modes that need to be accelerated. The low-order operator based on the diffusion approximation detailed earlier will be used to accelerate this iteration scheme. In the next section a Fourier analysis on the accelerated source iteration scheme using DSA is presented.

5.2.2 Accelerated Source Iteration

The accelerated source iteration scheme is:

$$\begin{aligned}
-\mu^2\frac{\partial^2\Psi^{A(\ell+1/2)}}{\partial z^2} + \Psi^{A(\ell+1/2)} &= c\,\phi^{(\ell)}(z) - \mu\, c\frac{\partial\phi^{(\ell)}(z)}{\partial z} \qquad (5.69) \\
\phi^{(\ell+1/2)}(z) &= \frac{1}{2}\int_{-1}^{1} d\mu\Psi^{A(\ell+1/2)} \qquad (5.70) \\
-\frac{1}{3}\frac{d^2F^{(\ell+1/2)}}{dz^2} + (1-c)F^{(\ell+1/2)} &= c[\phi^{(\ell+1/2)} - \phi^{(\ell)}] \qquad (5.71) \\
\phi^{(\ell+1)} &= \phi^{(\ell+1/2)} + F^{(\ell+1/2)} \qquad (5.72)
\end{aligned}$$

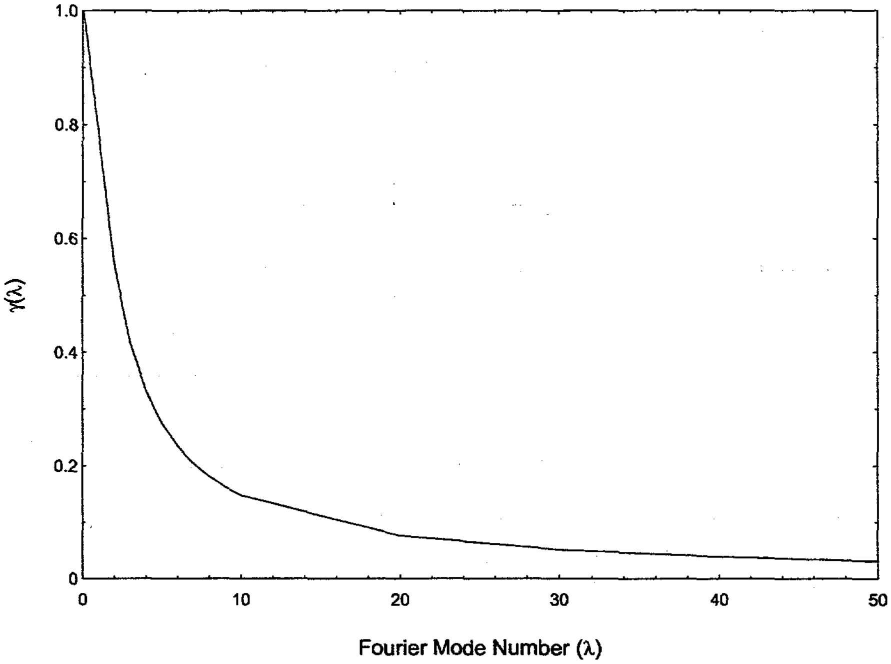

Figure 5.1: Unaccelerated Source Iteration Spectral Radius

where $z = x \cdot \sigma^A_{R,g}$ and $c = \frac{\sigma_{s0,g}}{\sigma^A_{R,g}}$.

In analyzing the above iteration scheme, the goal is to reduce the system to a recurrence relationship between $\phi^{(\ell+1)}(\lambda)$ and $\phi^{(\ell)}(\lambda)$ where λ is the Fourier mode number. We begin by introducing the following relationships

$$\begin{aligned} \Psi^{(\ell+1/2)}(z,\mu) &= \tilde{\Psi}^{(\ell+1/2)}(\lambda,\mu)e^{i\lambda z} \\ F^{(\ell+1/2)}(z) &= \tilde{F}^{(\ell+1/2)}(\lambda)e^{i\lambda z} \\ \phi^{(\ell+1/2)}(z) &= \tilde{\phi}^{(\ell+1/2)}(\lambda)e^{i\lambda z} \\ \phi^{(\ell)}(z) &= \tilde{\phi}^{(\ell)}(\lambda)e^{i\lambda z} \end{aligned}$$

in which the spatial variable z is expressed in terms of a Fourier mode number λ. Introducing the relationships for $\Psi(z,\mu)$ and $\phi(z)$ into equation 5.69 gives

$$-\mu^2\frac{\partial^2\tilde{\Psi}^{(\ell+1/2)}e^{i\lambda z}}{\partial z^2} + \tilde{\Psi}^{(\ell+1/2)}e^{i\lambda z} = c\,\tilde{\phi}^{(\ell)}e^{i\lambda z} - \mu\, c\frac{\partial\tilde{\phi}^{(\ell)}e^{i\lambda z}}{\partial z} \tag{5.73}$$

Evaluating the derivatives and dividing through by $e^{i\lambda z}$ yields,

$$\left(1+\mu^2\lambda^2\right)\tilde{\Psi}^{(\ell+1/2)} = c\,(1-\mu i\lambda)\,\tilde{\phi}^{(\ell)} \tag{5.74}$$

Solving for $\tilde{\Psi}^{(\ell+1/2)}$ gives

$$\tilde{\Psi}^{(\ell+1/2)} = \left[c\frac{(1-\mu i\lambda)}{(1+\mu^2\lambda^2)}\right]\tilde{\phi}^{(\ell)} \tag{5.75}$$

Replacing $\phi^{(\ell+1/2)}$ with $\tilde{\phi}^{(\ell+1/2)}e^{i\lambda\mu}$ in equation 5.70 and using the relationship above for $\tilde{\Psi}^{(\ell+1/2)}$ results in the following equation for $\tilde{\phi}^{(\ell+1/2)}$:

$$\begin{aligned}\tilde{\phi}^{(\ell+1/2)} &= \left\{\int_{-1}^{1}\left(\frac{1-\mu i\lambda}{1+\mu^2\lambda^2}\right)d\mu\right\}\tilde{\phi}^{(\ell)} \\ &= c\frac{\arctan(\lambda)}{\lambda}\tilde{\phi}^{(\ell)} \\ &= \gamma(\lambda)\tilde{\phi}^{(\ell)} \end{aligned}\tag{5.76}$$

where $\gamma(\lambda) = c\frac{\arctan(\lambda)}{\lambda}$ is the recurrence relationship for the unaccelerated source iteration scheme derived earlier. Next, equation 5.71 is transformed to get

$$-\frac{1}{3}\frac{d^2\tilde{F}^{(\ell+1/2)}e^{i\lambda z}}{dz^2} + (1-c)\tilde{F}^{(\ell+1/2)}e^{i\lambda z} = c[\tilde{\phi}^{(\ell+1/2)e^{i\lambda z}} - \tilde{\phi}^{(\ell)}e^{i\lambda z}] \tag{5.77}$$

yielding,

$$\left[\lambda^2 + 3(1-c)\right]\tilde{F}^{(\ell+1/2)} = 3c\left[\gamma(\lambda)-1\right]\tilde{\phi}^{(\ell)} \tag{5.78}$$

Solving for $\tilde{F}^{(\ell+1/2)}$ yields

$$\begin{aligned}\tilde{F}^{(\ell+1/2)} &= \frac{3c\left[\gamma(\lambda)-1\right]}{\left[\lambda^2+3(1-c)\right]}\tilde{\phi}^{(\ell)} \\ &= \alpha(\lambda)\tilde{\phi}^{(\ell)}\end{aligned}\tag{5.79}$$

where $\alpha(\lambda) = \frac{3c[\gamma(\lambda)-1]}{[\lambda^2+3(1-c)]}$. Finally, equation 5.72 is evaluated to get

$$\begin{aligned}\tilde{\phi}^{(\ell+1)} &= [\gamma(\lambda)+\alpha(\lambda)]\tilde{\phi}^{(\ell)} \\ &= \omega(\lambda)\tilde{\phi}^{(\ell)}\end{aligned}\tag{5.80}$$

where $\omega(\lambda) = \gamma(\lambda) + \alpha(\lambda)$. Thus, the accelerated iteration scheme will converge if the following condition is satisfied

$$\rho = \max_{(-\infty<\lambda<\infty)} |\omega(\lambda)| < 1 \tag{5.81}$$

where ρ is the spectral radius. Considering $\omega(\lambda)$ explicitly, it can be shown to reduce to the following expression

$$\omega(\lambda) = \frac{c}{[(1-c)+\frac{\lambda^2}{3}]}\left\{\frac{1+\frac{\lambda^2}{3}}{\lambda}\arctan(\lambda) - 1\right\} \tag{5.82}$$

Noting that $\omega(0) = 0$ and $\omega(\infty) = 0$, there is a maximum which, for $c = 1$, is 0.225. Figure 5.2 depicts a plot of $\omega(\lambda)$ as a function of λ. The plot depicted in Figure 5.2 is identical to that obtained when DSA is applied to a first-order formulation of the transport equation. The accelerated spectral radius is 4.5 times smaller than that for the unaccelerated scheme, and thus, results in faster convergence.

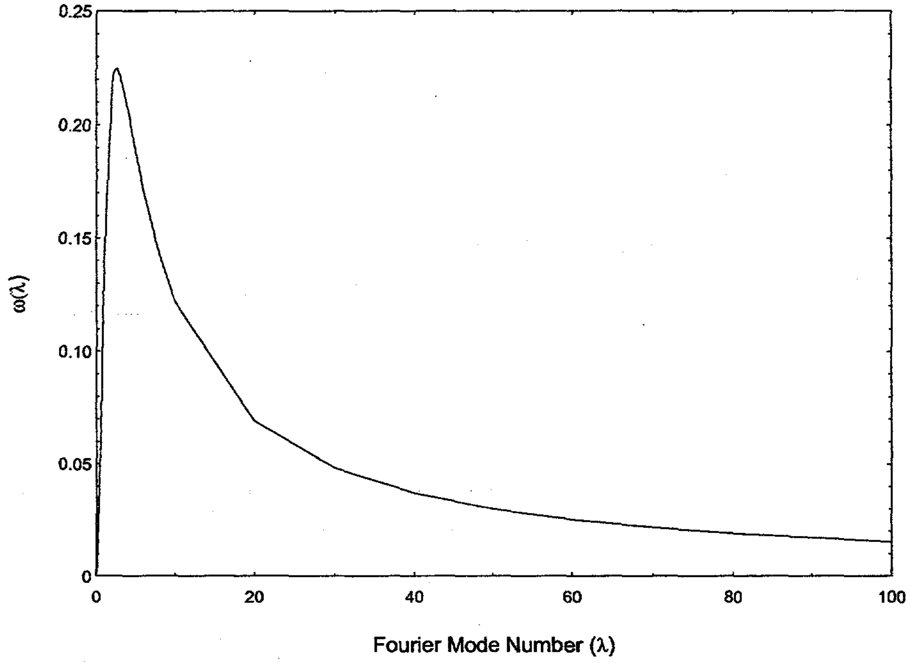

Figure 5.2: DSA Spectral Radius

5.3 Application of Source Acceleration

The effectiveness of DSA is demonstrated by looking at the acceleration achieved for two sample problems. First, we consider a one-group problem with the CSD operator turned off, isotropic scattering, S_8 and an arbitrarily chosen $c = 0.62$. For this problem, the spectral radius is calculated for each source iteration using the formula given below

$$\rho_g^{\ell+1} = \frac{\|\varepsilon_g^{\ell+1}\|}{\|\varepsilon_g^{\ell}\|} = \frac{\sqrt{\sum_{k=1}^{K}\left(\phi_{g,k}^{\ell+1} - \phi_{g,k}^{\ell}\right)^2}}{\sqrt{\sum_{k=1}^{K}\left(\phi_{g,k}^{\ell} - \phi_{g,k}^{\ell-1}\right)^2}} \tag{5.83}$$

The DSA spectral radius is determined for this one-group problem as the spatial mesh is refined. The results of this numerical experiment are depicted in Figure 5.3. As expected, the spectral radius approaches the analytical value of 0.225 as the spatial mesh is refined. For very coarse spatial meshes the spectral radius calculated for DSA is well below the theoretical value.

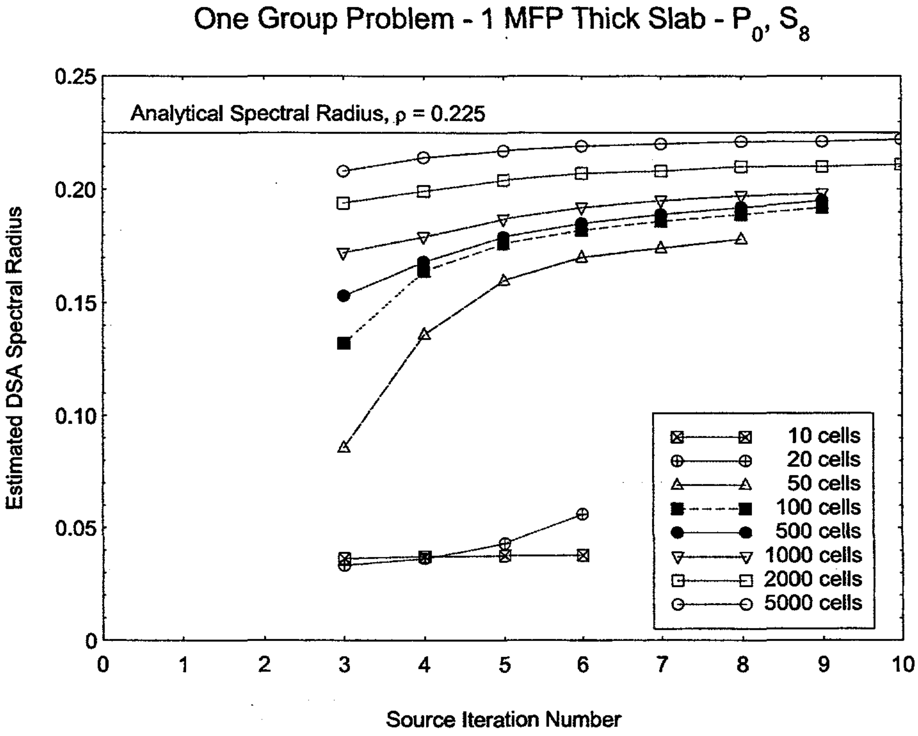

Figure 5.3: DSA Spectral Radius as Spatial Mesh is Refined

Next, we consider a 1.0 MeV electron beam normally incident on a slab of aluminum with P_0 scattering and a discrete ordinates order of 8 (S_8). The energy domain is divided into 40 energy groups and 100 spatial cells are used to discretize the slab. The energy discretization is reduced from the LD in energy presented in Chapter 4 to the lower-order diamond difference (DD) to eliminate the upscatter iteration. The DSA equations are exactly the same for the DD in energy approach except that the $\sigma^A_{R,g,k}$ in $\tau_{g,k}$ (see pg. 58) becomes $\sigma_{t,g,k} + 2\frac{S_g}{\Delta E_g}$.

The number of iterations it takes to reach convergence in each energy group is presented in Table 5.1 when DSA is turned off and on. In this table it is clear that turning on the DSA accelerates all of the energy groups having the most drastic effect on the rate of convergence in the lowest energy groups where c approaches unity. For the 40^{th} energy group, turning on DSA is 7.5 times faster than when DSA is turned off.

In the next chapter, the upscatter iteration that arises due to the LD in energy discretization is detailed. The rate of convergence for the unaccelerated upscatter iteration is evaluated. A synthetic acceleration scheme is derived to increase the rate of convergence of the upscatter iteration and its effectiveness evaluated using both analytical and discrete Fourier analysis.

Table 5.1: Iteration Summary: DSA OFF Vs. DSA ON

g	DSA OFF # of Iterations	DSA ON # of Iterations	Speed-Up
1	6	6	1.00
2	6	5	1.20
3	6	5	1.20
4	6	5	1.20
5	6	5	1.20
6	6	5	1.20
7	6	5	1.20
8	6	5	1.20
9	8	6	1.33
10	6	5	1.20
11	6	5	1.20
12	6	5	1.20
13	6	5	1.20
14	6	5	1.20
15	6	5	1.20
16	6	5	1.20
17	6	5	1.20
18	6	5	1.20
19	6	5	1.20
20	6	5	1.20
21	7	5	1.40
22	7	5	1.40
23	7	5	1.40
24	7	5	1.40
25	7	5	1.40
26	7	5	1.40
27	7	5	1.40
28	8	6	1.33
29	8	6	1.33
30	8	6	1.33
31	8	6	1.33
32	9	6	1.50
33	9	6	1.50
34	10	6	1.67
35	10	6	1.67
36	11	6	1.83
37	13	6	2.17
38	15	6	2.50
39	23	6	3.83
40	45	6	7.50
TOTAL	348	215	1.62

6 Upscatter Acceleration

In Chapter 4 the derivation of the LD in energy formulation of the SAAF equation was derived which can be written in a slope-average component form or a block matrix form. Recall that the slope-average component form of the SAAF equation yields two equations which are coupled as depicted below,

$$\begin{aligned}-\mu^2\frac{\partial}{\partial x}\left(\frac{1}{\sigma^A_{R,g}}\frac{\partial\Psi^A_g}{\partial x}\right) &+ \sigma^A_{R,g}\Psi^A_g = Q^S_g - \mu\frac{\partial}{\partial x}\left(\frac{1}{\sigma^A_{R,g}}Q^S_g\right) + q_g - \mu\frac{\partial}{\partial x}\left(\frac{1}{\sigma^A_{R,g}}q_g\right)\\ &+ \frac{S_{g-1}}{\Delta E_g}\left[\Psi^A_{g-1} - \Psi^E_{g-1}\right] - \mu\frac{\partial}{\partial x}\left(\frac{1}{\sigma^A_{R,g}}\frac{S_{g-1}}{\Delta E_g}\left[\Psi^A_{g-1} - \Psi^E_{g-1}\right]\right)\\ &+ \frac{S_g}{\Delta E_g}\Psi^E_g - \mu\frac{\partial}{\partial x}\left(\frac{1}{\sigma^A_{R,g}}\frac{S_g}{\Delta E_g}\Psi^E_g\right)\end{aligned}\tag{6.1}$$

and

$$\begin{aligned}-\mu^2\frac{\partial}{\partial x}\left(\frac{1}{\sigma^E_{R,g}}\frac{\partial\Psi^E_g}{\partial x}\right) + \sigma^E_{R,g}\Psi^E_g &= 3\frac{S_{g-1}}{\Delta E_g}\left[\Psi^A_{g-1} - \Psi^E_{g-1}\right]\\ &- \mu\frac{\partial}{\partial x}\left(\frac{1}{\sigma^E_{R,g}}3\frac{S_{g-1}}{\Delta E_g}\left[\Psi^A_{g-1} - \Psi^E_{g-1}\right]\right)\\ &- 3\frac{S_g}{\Delta E_g}\Psi^A_g + \mu\frac{\partial}{\partial x}\left(\frac{1}{\sigma^E_{R,g}}3\frac{S_g}{\Delta E_g}\Psi^A_g\right)\end{aligned}\tag{6.2}$$

where the discrete ordinates index is omitted for convenience.

The coupling between $\Psi^A_{n,g}$ and $\Psi^E_{n,g}$ introduces a second iteration within each energy group between equations 6.1 and 6.2 that is separate from the source iteration. We refer to this coupling between the average and slope angular fluxes in energy group g as within-group upscatter. This upscatter is not the result of physical processes in which particles are created in a higher energy group from a lower energy group. It is a within group upscatter due to the fact that the angular flux at the lower energy boundary, $\Psi_{g+1/2}$, contributes to the angular flux at the upper energy boundary, $\Psi_{g-1/2}$, as a result of the coupling between equations 6.1 and 6.2.

Introducing an upscatter iteration index, j, and writing the average angular flux SAAF equation (6.1) in terms of an iteration scheme gives

$$\begin{aligned}-\mu^2\frac{\partial}{\partial x}\left(\frac{1}{\sigma^A_{R,g}}\frac{\partial\Psi^{A(j+1)}_g}{\partial x}\right) + \sigma^A_{R,g}\Psi^{A(j+1)}_g &= \frac{S_g}{\Delta E_g}\Psi^{E(j)}_g - \mu\frac{\partial}{\partial x}\left(\frac{1}{\sigma^A_{R,g}}\frac{S_g}{\Delta E_g}\Psi^{E(j)}_g\right)\\ &+ q^A_g\end{aligned}\tag{6.3}$$

where q_g^A is defined as

$$\begin{aligned} q_g^A &= Q_g^S - \mu\frac{\partial}{\partial x}\left(\frac{1}{\sigma_{R,g}^A}Q_g^S\right) + q_g - \mu\frac{\partial}{\partial x}\left(\frac{1}{\sigma_{R,g}^A}q_g\right) \\ &+ \frac{S_{g-1}}{\Delta E_g}\left[\Psi_{g-1}^A - \Psi_{g-1}^E\right] - \mu\frac{\partial}{\partial x}\left(\frac{1}{\sigma_{R,g}^A}\frac{S_{g-1}}{\Delta E_g}\left[\Psi_{g-1}^A - \Psi_{g-1}^E\right]\right) \end{aligned} \tag{6.4}$$

which includes all known sources into equation 6.1 from scattering sources, slowing-down from the $g-1$ group and any fixed external source. Similarly, equation 6.2 for the slope flux becomes

$$\begin{aligned} -\mu^2\frac{\partial}{\partial x}\left(\frac{1}{\sigma_{R,g}^E}\frac{\partial\Psi_g^{E(j+1)}}{\partial x}\right) + \sigma_{R,g}^E\Psi_g^{E(j+1)} &= -3\frac{S_g}{\Delta E_g}\Psi_g^{A(j+1)} \\ &+ \mu\frac{\partial}{\partial x}\left(\frac{1}{\sigma_{R,g}^E}3\frac{S_g}{\Delta E_g}\Psi_g^{A(j+1)}\right) + q_g^E \end{aligned} \tag{6.5}$$

where q_g^E consist of the slowing-down source into the slope flux equation:

$$q_g^E = 3\frac{S_{g-1}}{\Delta E_g}\left[\Psi_{g-1}^A - \Psi_{g-1}^E\right] - \mu\frac{\partial}{\partial x}\left(\frac{1}{\sigma_{R,g}^E}3\frac{S_{g-1}}{\Delta E_g}\left[\Psi_{g-1}^A - \Psi_{g-1}^E\right]\right) \tag{6.6}$$

In the upscatter iteration the scattering source is treated as a known value and does not change for the j^{th} upscatter iterate. Also note that the most recent value of the average angular flux is used in the slope flux equation (6.5). In the next section a Fourier analysis is performed on these coupled equations to analyze the rate of convergence of this iteration process.

6.1 Fourier Analysis of Upscatter Iteration Scheme

Performing a Fourier analysis on the upscatter iteration scheme starts with the exact average and slope SAAF equations (6.1, 6.2) in conjunction with the upscatter iteration equations (6.3, 6.5). The average and slope errors are defined as follows

$$f^{A(j+1)} = \Psi_g^A - \Psi_g^{A(j+1)} \tag{6.7}$$

$$f^{E(j+1)} = \Psi_g^E - \Psi_g^{E(j+1)} \tag{6.8}$$

Subtracting equation 6.3 from equation 6.1 and using the definition of $f^{A(j+1)}$ yields,

$$\begin{aligned} -\mu^2\frac{\partial}{\partial x}\left(\frac{1}{\sigma_{R,g}^A}\frac{\partial f^{A(j+1)}}{\partial x}\right) + \sigma_{R,g}^A f^{A(j+1)} &= \frac{S_g}{\Delta E_g}f^{E(j)} \\ &- \mu\frac{\partial}{\partial x}\left(\frac{1}{\sigma_{R,g}^A}\frac{S_g}{\Delta E_g}f^{E(j)}\right) \end{aligned} \tag{6.9}$$

Similarly, equation (6.5) is subtracted from equation (6.2) which, with the definition of $f^{E(j+1)}$, gives

$$\begin{aligned}-\mu^2\frac{\partial}{\partial x}\left(\frac{1}{\sigma^E_{R,g}}\frac{\partial f^{E(j+1)}}{\partial x}\right)+\sigma^E_{R,g}f^{E(j+1)} &= -3\frac{S_g}{\Delta E_g}f^{A(j+1)} \\ &+ \mu\frac{\partial}{\partial x}\left(\frac{1}{\sigma^E_{R,g}}3\frac{S_g}{\Delta E_g}f^{A(j+1)}\right) \quad (6.10)\end{aligned}$$

The spatial dependence of the slope and average errors in equations (6.9) and (6.10) is expressed in terms of a Fourier mode number, λ, as follows

$$f^{A(j+1)} = \tilde{f}^{A(j+1)}e^{i\lambda x} \quad (6.11)$$

$$f^{E(j)} = \tilde{f}^{E(j)}e^{i\lambda x} \quad (6.12)$$

$$f^{E(j+1)} = \tilde{f}^{E(j+1)}e^{i\lambda x} \quad (6.13)$$

where $-\infty < x < +\infty$; $-\infty < \lambda < +\infty$; and $i = \sqrt{-1}$. The variables f^A and f^E are functions of x and μ while $\tilde{f}^A$ and $\tilde{f}^E$ depend on of λ and μ. Substituting the error expressions above into equation 6.9, we evaluate the spatial derivative terms and divide through by $e^{i\lambda x}$ to get,

$$\left(\frac{\mu^2\lambda^2}{\sigma^A_{R,g}}+\sigma^A_{R,g}\right)\tilde{f}^{A(j+1)} = \frac{S_g}{\Delta E_g}\left(1-\frac{\mu i\lambda}{\sigma^A_{R,g}}\right)\tilde{f}^{E(j)} \quad (6.14)$$

which can be reduced to

$$\tilde{f}^{A(j+1)} = \frac{S_g}{\Delta E_g}\left(\frac{1}{\sigma^A_{R,g}+\mu i\lambda}\right)\tilde{f}^{E(j)} \quad (6.15)$$

Next, the error expression in terms of the Fourier mode number is introduced into equation 6.10. Evaluating the spatial derivative terms and dividing through by $e^{i\lambda x}$ gives,

$$\left(\frac{\mu^2\lambda^2}{\sigma^E_{R,g}}+\sigma^E_{R,g}\right)\tilde{f}^{E(j+1)} = -3\frac{S_g}{\Delta E_g}\left(1-\frac{\mu i\lambda}{\sigma^E_{R,g}}\right)\tilde{f}^{A(j+1)} \quad (6.16)$$

after multiplying through by $\sigma^E_{R,g}$ and solving for $\tilde{f}^{E(j+1)}$ yields

$$\tilde{f}^{E(j+1)} = -3\frac{S_g}{\Delta E_g}\left(\frac{1}{\sigma^E_{R,g}+\mu i\lambda}\right)\tilde{f}^{A(j+1)} \quad (6.17)$$

Substituting the expression for $\tilde{f}^{A(j+1)}$ in equation (6.15) into the expression for $\tilde{f}^{E(j+1)}$ given in equation (6.17) yields

$$\begin{aligned}\tilde{f}^{E(j+1)} &= -3\frac{S_g^2}{\Delta E_g^2}\left(\frac{1}{(\sigma^E_{R,g}+\mu i\lambda)(\sigma^A_{R,g}+\mu i\lambda)}\right)\tilde{f}^{E(j)} \\ &= \omega(\lambda)\tilde{f}^{E(j)} \quad (6.18)\end{aligned}$$

Solving the recurrence relationship gives,

$$\tilde{f}^{E(j+1)} = \omega^{(j)}(\lambda)\tilde{f}^{E(j)} \tag{6.19}$$

where the dispersion function $\omega(\lambda)$ is defined by

$$\omega(\lambda) = -3\left(\frac{S_g}{\Delta E_g}\right)^2 \left(\frac{1}{(\sigma^E_{R,g} + \mu i\lambda)(\sigma^A_{R,g} + \mu i\lambda)}\right) \tag{6.20}$$

For the error associated with the iteration scheme to be sufficiently damped to allow the scheme to reach convergence, the dispersion function most satisfy the following condition:

$$\max_{-\infty<\lambda<\infty} |\omega(\lambda)| < 1 \tag{6.21}$$

The spectral radius, ρ, of the iteration scheme is defined by

$$\rho = \max_{-\infty<\lambda<\infty} |\omega(\lambda)| \tag{6.22}$$

where

$$\begin{aligned} |\omega(\lambda)| &= \sqrt{\omega(\lambda)\omega^*(\lambda)} \\ &= 3\left(\frac{S_g}{\Delta E_g}\right)^2 \sqrt{\frac{1}{\left(\sigma^{A2}_{R,g} + \mu^2\lambda^2\right)\left(\sigma^{E2}_{R,g} + \mu^2\lambda^2\right)}} \end{aligned}$$

for which it follows that

$$\lim_{\lambda\to 0} |\omega(\lambda)| = 3\left(\frac{S_g}{\Delta E_g}\right)^2 \frac{1}{\sigma^A_{R,g}\sigma^E_{R,g}} \quad \text{and} \quad \lim_{\lambda\to\infty} |\omega(\lambda)| = 0$$

Recalling the definitions of $\sigma^A_{R,g}$ and $\sigma^E_{R,g}$ (see page 43), it can be shown that for a pure CSD problem in which $\sigma_t = 0$, $|\omega(\lambda)| \to 1$ as $\lambda \to 0$. Figure 6.1 depicts a plot of $|\omega(\lambda)|$ as a function of Fourier mode number assuming the total cross-section is 0 and lumping the value $\frac{S_g}{\Delta E_g}$ into the Fourier mode number. This figure reveals that the upscatter iteration scheme is characterized by $\rho = 1$ and will not converge. In the upscatter iteration scheme, the higher Fourier modes are damped effectively as depicted in the plot of $|\omega(\lambda)|$ in Figure 6.1 which goes to zero as $\lambda \to \infty$. However, the flat Fourier modes are not damped effectively which is evident from the fact that $|\omega(0)| = 1.0$.

Lazo and Morel performed a Fourier analysis on the first-order, LD in energy discretized transport equation obtaining the same results.[28] Since the upscatter iteration scheme is characterized by $\rho = 1$, an acceleration scheme is necessary to damp the low-order Fourier modes to ensure convergence. The acceleration scheme that is applied must not introduce problems in the higher Fourier modes. The next section details the derivation of an acceleration scheme for the upscatter iteration.

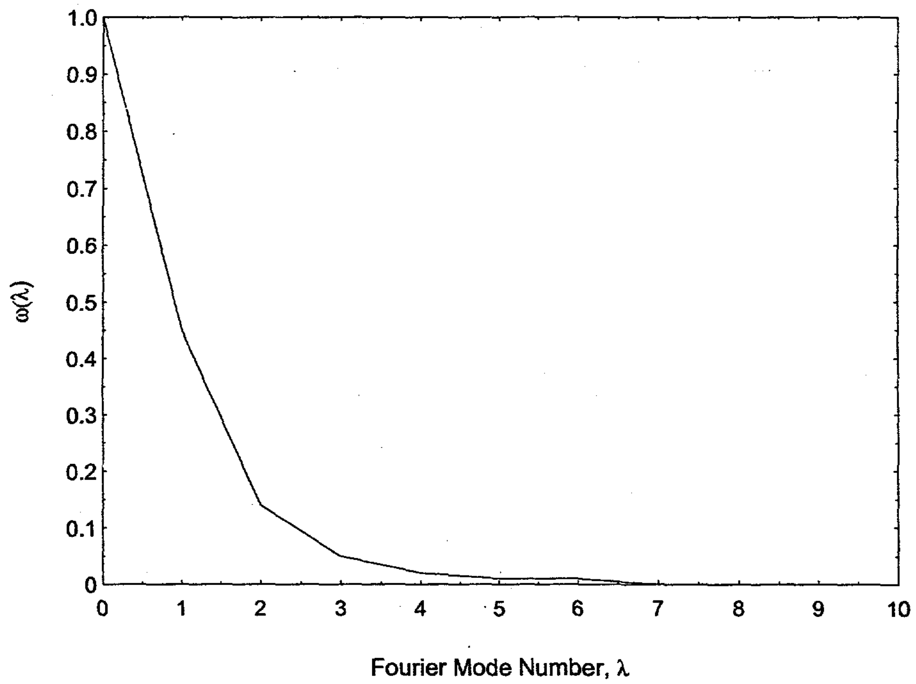

Figure 6.1: Upscatter Iteration Spectral Radius for Pure CSD Problem

6.2 Derivation of an Upscatter Acceleration Scheme

We begin by writing the average and slope SAAF equations at the $j + 1/2$ iterate

$$\begin{aligned} -\mu^2 \frac{\partial}{\partial x}\left(\frac{1}{\sigma^A_{R,g}}\frac{\partial \Psi_g^{A(j+1/2)}}{\partial x}\right) &+ \sigma^A_{R,g}\Psi_g^{A(j+1/2)} = \frac{S_g}{\Delta E_g}\Psi_g^{E(j)} \\ &- \mu\frac{\partial}{\partial x}\left(\frac{1}{\sigma^A_{R,g}}\frac{S_g}{\Delta E_g}\Psi_g^{E(j)}\right) + q_g^A \end{aligned} \tag{6.23}$$

and

$$\begin{aligned} -\mu^2 \frac{\partial}{\partial x}\left(\frac{1}{\sigma^E_{R,g}}\frac{\partial \Psi_g^{E(j+1/2)}}{\partial x}\right) &+ \sigma^E_{R,g}\Psi_g^{E(j+1/2)} = -3\frac{S_g}{\Delta E_g}\Psi_g^{A(j+1/2)} \\ &+ \mu\frac{\partial}{\partial x}\left(\frac{1}{\sigma^E_{R,g}}3\frac{S_g}{\Delta E_g}\Psi_g^{A(j+1/2)}\right) + q_g^E \end{aligned} \tag{6.24}$$

The average and slope error at the $j+1/2$ iterate are defined as

$$f^{A(j+1/2)} = \Psi_g^A - \Psi_g^{A(j+1/2)} \tag{6.25}$$

$$f^{E(j+1/2)} = \Psi_g^E - \Psi_g^{E(j+1/2)} \tag{6.26}$$

Subtracting equation 6.23 from equation 6.1 and adding and subtracting $\Psi_g^{E(j+1/2)}$ to the right-hand side yields

$$\begin{aligned} -\mu^2\frac{\partial}{\partial x}\left(\frac{1}{\sigma_{R,g}^A}\frac{\partial f_g^{A(j+1/2)}}{\partial x}\right) &+ \sigma_{R,g}^A f_g^{A(j+1/2)} - \frac{S_g}{\Delta E_g} f_g^{E(j+1/2)} \\ +\mu\frac{\partial}{\partial x}\left(\frac{1}{\sigma_{R,g}^A}\frac{S_g}{\Delta E_g} f_g^{E(j+1/2)}\right) &= \frac{S_g}{\Delta E_g}\left[\Psi_g^{E(j+1/2)} - \Psi_g^{E(j)}\right] \\ &- \mu\frac{\partial}{\partial x}\left(\frac{1}{\sigma_{R,g}^A}\frac{S_g}{\Delta E_g}\left[\Psi_g^{E(j+1/2)} - \Psi_g^{E(j)}\right]\right) \end{aligned} \tag{6.27}$$

Note that the right-hand side of the above equation contains a residual in terms of the slope angular flux, $\Psi_g^{E(j+1/2)} - \Psi_g^{E(j)}$. The next step is to subtract equation 6.24 from equation 6.2 to get

$$\begin{aligned} -\mu^2\frac{\partial}{\partial x}\left(\frac{1}{\sigma_{R,g}^E}\frac{\partial f_g^{E(j+1/2)}}{\partial x}\right) &+ \sigma_{R,g}^E f_g^{E(j+1/2)} + 3\frac{S_g}{\Delta E_g} f_g^{A(j+1/2)} \\ &- \mu\frac{\partial}{\partial x}\left(\frac{1}{\sigma_{R,g}^E}3\frac{S_g}{\Delta E_g} f_g^{A(j+1/2)}\right) = 0 \end{aligned} \tag{6.28}$$

There is no slope residual term in equation 6.28 because the updated value of Ψ_g^A is used in the slope angular flux equation. Equations 6.27 and 6.28 are second-order error equations for the average and slope errors, respectively. This coupled system of error equations is as complicated to solve as the unaccelerated equations and needs to be reduced to a lower order system using a low-order operator. The low-order operator is derived by neglecting the spatial derivative of f_g^E and f_g^A in equation 6.28 which is essentially a diamond difference approximation. Setting the spatial derivatives of the slope and flux errors to zero in equation 6.28 reduces it to

$$f_g^{E(j+1/2)} = -\frac{3\mathcal{S}_g}{\sigma_{R,g}^E} f_g^{A(j+1/2)} \tag{6.29}$$

where $\mathcal{S}_g = \frac{S_g}{\Delta E_g}$ is introduced to simplify the equation. This expression for $f_g^{E(j+1/2)}$ is then substituted into equation 6.27 and like terms are grouped together to get

$$\begin{aligned} -\mu^2\frac{\partial}{\partial x}\left(\frac{1}{\sigma_{R,g}^A}\frac{\partial f_g^{A(j+1/2)}}{\partial x}\right) &- \mu\frac{\partial}{\partial x}\left(\frac{3\mathcal{S}_g}{\sigma_{R,g}^A\sigma_{R,g}^E} f_g^{A(j+1/2)}\right) \\ &+ \left(\sigma_{R,g}^A + \frac{3\mathcal{S}_g^2}{\sigma_{R,g}^A\sigma_{R,g}^E}\right) f_g^{A(j+1/2)} = \mathcal{R}_g \end{aligned} \tag{6.30}$$

where the slope angular flux residual, $\mathcal{R}_g$, is defined as,

$$\mathcal{R}_g = \mathcal{S}_g\left[\Psi_g^{E(j+1/2)} - \Psi_g^{E(j)}\right] - \mu\frac{\partial}{\partial x}\left(\frac{\mathcal{S}_g}{\sigma^A_{R,g}}\left[\Psi_g^{E(j+1/2)} - \Psi_g^{E(j)}\right]\right) \tag{6.31}$$

The accelerated upscatter iteration scheme is presented in equations (6.32) through (6.38) with the S$_n$ angle index, n, included:

$$\begin{aligned}
-\mu_n^2\frac{d}{dx}\left(\frac{1}{\sigma^A_{R,g}}\frac{d\Psi_{n,g}^{A(j+1/2)}}{dx}\right) &+ \sigma^A_{R,g}\Psi_{n,g}^{A(j+1/2)} = \mathcal{S}_g\Psi_{n,g}^{E(j)} \\
&- \mu_n\frac{d}{dx}\left(\frac{\mathcal{S}_g}{\sigma^A_{R,g}}\Psi_{n,g}^{E(j)}\right) \qquad (6.32) \\
-\mu_n^2\frac{d}{dx}\left(\frac{1}{\sigma^E_{R,g}}\frac{d\Psi_{n,g}^{E(j+1/2)}}{dx}\right) &+ \sigma^E_{R,g}\Psi_{n,g}^{E(j+1/2)} = -3\mathcal{S}_g\Psi_{n,g}^{A(j+1/2)} \\
&+ \mu_n\frac{d}{dx}\left(\frac{3\mathcal{S}_g}{\sigma^E_{R,g}}\Psi_{n,g}^{A(j+1/2)}\right) \qquad (6.33) \\
\mathcal{R}_{n,g}^{(j+1/2)} &= \mathcal{S}_g\left[\Psi_{n,g}^{E(j+1/2)} - \Psi_{n,g}^{E(j)}\right] \\
&- \mu_n\frac{d}{dx}\left(\frac{\mathcal{S}_g}{\sigma^A_{R,g}}\left[\Psi_{n,g}^{E(j+1/2)} - \Psi_{n,g}^{E(j)}\right]\right) \qquad (6.34) \\
-\mu_n^2\frac{d}{dx}\left(\frac{1}{\sigma^A_{R,g}}\frac{df_{n,g}^{A(j+1/2)}}{dx}\right) &- \mu_n\frac{d}{dx}\left(3\frac{\mathcal{S}_g^2}{\sigma^A_{R,g}\sigma^E_{R,g}}f_{n,g}^{A(j+1/2)}\right) \\
&+ \left(\sigma^A_{R,g} + 3\frac{\mathcal{S}_g^2}{\sigma^E_{R,g}}\right)f_{n,g}^{A(j+1/2)} = \mathcal{R}_{n,g} \qquad (6.35) \\
f_{n,g}^{E(j+1/2)} = -3\frac{\mathcal{S}_g}{\sigma^E_{R,g}}&f_{n,g}^{A(j+1/2)} \qquad (6.36) \\
\Psi_{n,g}^{A(j+1)} &= \Psi_{n,g}^{A(j+1/2)} + f_{n,g}^{A(j+1/2)} \qquad (6.37) \\
\Psi_{n,g}^{E(j+1)} &= \Psi_{n,g}^{E(j+1/2)} + f_{n,g}^{E(j+1/2)} \qquad (6.38)
\end{aligned}$$

6.2.1 Fourier Analysis of Upscatter Acceleration Scheme

A Fourier analysis is performed on the upscatter acceleration scheme in equations (6.32) through (6.38) to evaluate whether or not it is effective. Initially the functions of x are expanded in terms of the Fourier mode numbers, λ, as follows:

$$\begin{aligned}
\Psi_{n,g}^{A(j+1/2)} &= \tilde{\Psi}_{n,g}^{A(j+1/2)}e^{i\lambda x} \\
\Psi_{n,g}^{E(j+1/2)} &= \tilde{\Psi}_{n,g}^{E(j+1/2)}e^{i\lambda x} \\
\mathcal{R}_{n,g}^{(j+1/2)} &= \tilde{\mathcal{R}}_{n,g}^{(j+1/2)}e^{i\lambda x} \\
f_{n,g}^{A(j+1/2)} &= \tilde{f}_{n,g}^{A(j+1/2)}e^{i\lambda x} \\
f_{n,g}^{E(j+1/2)} &= \tilde{f}_{n,g}^{E(j+1/2)}e^{i\lambda x}
\end{aligned}$$

The expressions above are used to reduce the acceleration scheme given in equations 6.32 through 6.38 to a recurrence relationship between $\Psi_{n,g}^{E(j+1)}$ and $\Psi_{n,g}^{E(j)}$.

First, the Fourier mode expansions of $\Psi_{n,g}^{A(j+1/2)}$ and $\Psi_{n,g}^{E(j)}$ are introduced into equation 6.32. Evaluating the spatial derivatives, dividing through by $e^{i\lambda x}$, and joining like terms gives

$$\left(1+\frac{\mu^2\lambda^2}{\sigma_{R,g}^{A^2}}\right)\tilde{\Psi}_{n,g}^{A(j+1/2)} = \frac{\mathcal{S}_g}{\sigma_{R,g}^{A}}\left(1-\frac{\mu i\lambda}{\sigma_{R,g}^{A}}\right)\tilde{\Psi}_{n,g}^{E(j)} \tag{6.39}$$

Solving for $\tilde{\Psi}_{n,g}^{A(j+1/2)}$ yields,

$$\begin{aligned}\tilde{\Psi}_{n,g}^{A(j+1/2)} &= \frac{\mathcal{S}_g}{\sigma_{R,g}^{A}}\left\{\frac{1}{\left(1+\frac{\mu i\lambda}{\sigma_{R,g}^{A}}\right)}\right\}\tilde{\Psi}_{n,g}^{E(j)}\\ &= \alpha(\lambda)\tilde{\Psi}_{n,g}^{E(j)}\end{aligned} \tag{6.40}$$

Next equation 6.33 is transformed to get

$$\left(1+\frac{\mu^2\lambda^2}{\sigma_{R,g}^{E^2}}\right)\tilde{\Psi}_{n,g}^{E(j+1/2)} = -3\frac{\mathcal{S}_g}{\sigma_{R,g}^{E}}\left(1-\frac{\mu i\lambda}{\sigma_{R,g}^{E}}\right)\tilde{\Psi}_{n,g}^{A(j+1/2)} \tag{6.41}$$

Solving for $\tilde{\Psi}_{n,g}^{E(j+1/2)}$ and substituting in the expression for $\tilde{\Psi}_{n,g}^{A(j+1/2)}$ derived in the previous step yields

$$\begin{aligned}\tilde{\Psi}_{n,g}^{E(j+1/2)} &= -3\frac{\mathcal{S}_g}{\sigma_{R,g}^{E}}\left\{\frac{1}{\left(1+\frac{\mu i\lambda}{\sigma_{R,g}^{E}}\right)}\right\}\alpha(\lambda)\tilde{\Psi}_{n,g}^{E(j)}\\ &= \omega(\lambda)\tilde{\Psi}_{n,g}^{E(j)}\end{aligned} \tag{6.42}$$

Then the slope residuals in equation (6.34) are evaluated using the above expression for $\tilde{\Psi}_{n,g}^{E(j+1/2)}$ giving

$$\begin{aligned}\tilde{\mathcal{R}}_{n,g}^{(j+1/2)} &= \mathcal{S}_g\left(1-\frac{\mu i\lambda}{\sigma_{R,g}^{A}}\right)\left[\omega(\lambda)-1\right]\tilde{\Psi}_{n,g}^{E(j)}\\ &= \chi(\lambda)\tilde{\Psi}_{n,g}^{E(j)}\end{aligned} \tag{6.43}$$

Introducing the Fourier mode expansion into the average flux error equation (6.35) gives

$$\left\{\sigma_{R,g}^{A}\left(1+\frac{\mu^2\lambda^2}{\sigma_{R,g}^{A^2}}\right)+3\frac{\mathcal{S}_g^2}{\sigma_{R,g}^{E}}\left(1-\frac{\mu i\lambda}{\sigma_{R,g}^{A}}\right)\right\}\tilde{f}_{n,g}^{A(j+1/2)} = \tilde{\mathcal{R}}_{n,g}^{(j+1/2)} \tag{6.44}$$

Solving for $\tilde{f}^{A(j+1/2)}_{n,g}$ and substituting equation 6.43 for $\tilde{\mathcal{R}}^{(j+1/2)}_{n,g}$ yields,

$$\begin{aligned} \tilde{f}^{A(j+1/2)}_{n,g} &= \left[\frac{1}{\left\{\sigma^A_{R,g}\left(1+\frac{\mu^2\lambda^2}{\sigma^{A^2}_{R,g}}\right)+3\frac{\mathcal{S}_g^2}{\sigma^E_{R,g}}\left(1-\frac{\mu i\lambda}{\sigma^A_{R,g}}\right)\right\}}\right]\chi(\lambda)\tilde{\Psi}^{E(j)}_{n,g} \\ &= \eta(\lambda)\tilde{\Psi}^{E(j)}_{n,g} \end{aligned} \tag{6.45}$$

Next, the slope error equation is evaluated using the expression above for $\tilde{f}^{A(j+1/2)}_{n,g}$ to get

$$\begin{aligned} \tilde{f}^{E(j+1/2)}_{n,g} &= -3\frac{\mathcal{S}_g}{\sigma^E_{R,g}}\eta(\lambda)\tilde{\Psi}^{E(j)}_{n,g} \\ &= \epsilon(\lambda)\tilde{\Psi}^{E(j)}_{n,g} \end{aligned} \tag{6.46}$$

Finally, the expression above is substituted into the Fourier transform of equation 6.38 yielding,

$$\begin{aligned} \tilde{\Psi}^{E(j+1)}_{n,g} &= \left(\omega(\lambda)+\epsilon(\lambda)\right)\tilde{\Psi}^{E(j)}_{n,g} \\ &= \beta(\lambda)\tilde{\Psi}^{E(j)}_{n,g} \end{aligned} \tag{6.47}$$

The parameter $\omega(\lambda)$ can be reduced to

$$\omega(\lambda) = \frac{-\Lambda}{\left(1+\frac{\mu i\lambda}{\sigma^A_{R,g}}\right)\left(1+\frac{\mu i\lambda}{\sigma^E_{R,g}}\right)} \tag{6.48}$$

where

$$\Lambda = 3\frac{\mathcal{S}_g^2}{\sigma^A_{R,g}\sigma^E_{R,g}} = 3\left(\frac{S_g}{\Delta E_g}\right)^2\frac{1}{\sigma^A_{R,g}\sigma^E_{R,g}} \tag{6.49}$$

Note that $\omega(\lambda)$ is identical to the dispersion relationship obtained for the unaccelerated iteration scheme in section 6.1. Expanding out the terms that make up $\epsilon(\lambda)$ yields

$$\epsilon(\lambda) = \frac{\Lambda}{\left(1+\frac{\mu i\lambda}{\sigma^A_{R,g}}\right)+\Lambda}\left\{\frac{\Lambda}{\left(1+\frac{\mu i\lambda}{\sigma^A_{R,g}}\right)\left(1+\frac{\mu i\lambda}{\sigma^E_{R,g}}\right)}+1\right\} \tag{6.50}$$

Thus, $\beta(\lambda)$ is equal to

$$\begin{aligned} \beta(\lambda) &= \frac{-\Lambda}{\left(1+\frac{\mu i\lambda}{\sigma^A_{R,g}}\right)\left(1+\frac{\mu i\lambda}{\sigma^E_{R,g}}\right)} \\ &+ \frac{\Lambda}{\left(1+\frac{\mu i\lambda}{\sigma^A_{R,g}}\right)+\Lambda}\left\{\frac{\Lambda}{\left(1+\frac{\mu i\lambda}{\sigma^A_{R,g}}\right)\left(1+\frac{\mu i\lambda}{\sigma^E_{R,g}}\right)}+1\right\} \end{aligned} \tag{6.51}$$

To evaluate the convergence rate for this acceleration scheme the parameter k is introduced where $k = \mu\lambda$ and the dispersion relationship β is redefined as a function of k as follows:

$$\begin{aligned} \beta(k) &= \frac{-\Lambda}{\left(1+\frac{ik}{\sigma^A_{R,g}}\right)\left(1+\frac{ik}{\sigma^E_{R,g}}\right)} \\ &+ \frac{\Lambda}{\left(1+\frac{ik}{\sigma^A_{R,g}}\right)+\Lambda}\left\{\frac{\Lambda}{\left(1+\frac{ik}{\sigma^A_{R,g}}\right)\left(1+\frac{ik}{\sigma^E_{R,g}}\right)}+1\right\} \end{aligned} \quad (6.52)$$

The spectral radius, ρ, for the upscatter acceleration scheme is defined as

$$\rho = \max_{-\infty<k<\infty} |\beta(k)| \quad (6.53)$$

where $|\beta(k)| = \sqrt{\beta(k)\beta^*(k)}$. The following limiting values can be readily established:

$$\lim_{k\to 0} |\beta(k)| = 0 \quad \text{and} \quad \lim_{k\to\infty} |\beta(k)| = 0$$

It can be shown that the maximum value of $\beta(k)$ is equal to 0.20 ($\rho = 0.20$). Figure 6.2 depicts the value of the dispersion relationship as a function of the Fourier mode number.

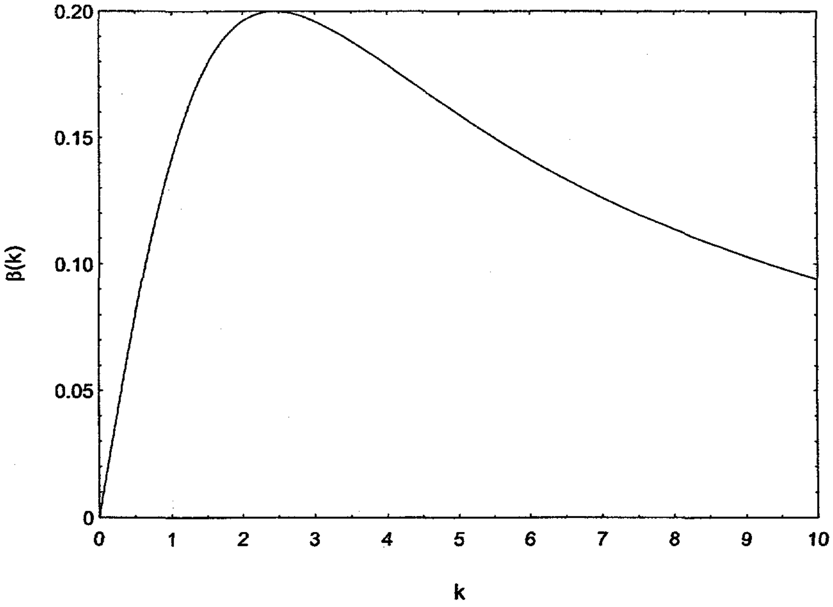

Figure 6.2: Upscatter Acceleration Scheme Spectral Radius for Pure CSD Problem

Before numerically implementing the upscatter acceleration scheme on an energy and spatial grid we perform a discrete Fourier analysis on the discretized equations.

6.2.2 Discrete Fourier Analysis of Upscatter Acceleration Scheme

A discrete Fourier analysis will reveal whether or not the acceleration scheme is affected by the spatial discretization and the cell mesh size. The discrete Fourier analysis starts with the spatially discretized versions of equations (6.32) through (6.38) which follow:

$$\begin{aligned} a^{A}_{n,g,k}\Psi^{A(j+1/2)}_{n,g,k-1/2} + b^{A}_{n,g,k}\Psi^{A(j+1/2)}_{n,g,k+1/2} + a^{A}_{n,g,k+1}\Psi^{A(j+1/2)}_{n,g,k+1/2} = \\ \mathcal{A}^{AE}_{n,g,k}\Psi^{E(j)}_{n,g,k-1/2} + \mathcal{B}^{AE}_{n,g,k}\Psi^{E(j)}_{n,g,k+1/2} + \mathcal{C}^{AE}_{n,g,k}\Psi^{E(j)}_{n,g,k+3/2} \end{aligned} \tag{6.54}$$

$$\begin{aligned} a^{E}_{n,g,k}\Psi^{E(j+1/2)}_{n,g,k-1/2} + b^{E}_{n,g,k}\Psi^{E(j+1/2)}_{n,g,k+1/2} + a^{E}_{n,g,k+1}\Psi^{E(j+1/2)}_{n,g,k+1/2} = \\ -\mathcal{A}^{EA}_{n,g,k}\Psi^{A(j+1/2)}_{n,g,k-1/2} - \mathcal{B}^{EA}_{n,g,k}\Psi^{A(j+1/2)}_{n,g,k+1/2} - \mathcal{C}^{EA}_{n,g,k}\Psi^{A(j+1/2)}_{n,g,k+3/2} \end{aligned} \tag{6.55}$$

$$\begin{aligned} & a^{f^A}_{n,g,k}f^{A(j+1/2)}_{n,g,k-1/2} + b^{f^A}_{n,g,k}f^{A(j+1/2)}_{n,g,k+1/2} + c^{f^A}_{n,g,k+1}f^{A(j+1/2)}_{n,g,k+1/2} = \\ & \mathcal{A}^{f^A}_{n,g,k}(\Psi^{E(j+1/2)}_{n,g,k-1/2} - \Psi^{E(j)}_{n,g,k-1/2}) + \mathcal{B}^{f^A}_{n,g,k}(\Psi^{E(j+1/2)}_{n,g,k+1/2} - \Psi^{E(j)}_{n,g,k+1/2}) \\ + \; & \mathcal{C}^{f^A}_{n,g,k}(\Psi^{E(j+1/2)}_{n,g,k+3/2} - \Psi^{E(j)}_{n,g,k+3/2}) \end{aligned} \tag{6.56}$$

$$f^{E(j+1/2)}_{n,g,k\pm1/2} = -3\frac{\mathcal{S}_{g,k}}{\sigma^{E}_{R,g,k}}f^{A(j+1/2)}_{n,g,k\pm1/2} \tag{6.57}$$

$$\Psi^{A(j+1)}_{n,g,k\pm1/2} = \Psi^{A(j+1/2)}_{n,g,k\pm1/2} + f^{A(j+1/2)}_{n,g,k\pm1/2} \tag{6.58}$$

$$\Psi^{E(j+1)}_{n,g,k\pm1/2} = \Psi^{E(j+1/2)}_{n,g,k\pm1/2} + f^{E(j+1/2)}_{n,g,k\pm1/2} \tag{6.59}$$

where the following coefficients are defined as

$$\begin{aligned}
a^{A}_{n,g,k} &= \left(\tfrac{1}{6}\Delta x_k\sigma^{A}_{R,g,k} - \tfrac{\mu_n^2}{\Delta x_k\sigma^{A}_{R,g,k}}\right) \\
b^{A}_{n,g,k} &= \left(\tfrac{1}{3}[\Delta x_k\sigma^{A}_{R,g,k} + \Delta x_{k+1}\sigma^{A}_{R,g,k+1}] + \tfrac{\mu_n^2}{\Delta x_k\sigma^{A}_{R,g,k}} + \tfrac{\mu_n^2}{\Delta x_{k+1}\sigma^{A}_{R,g,k+1}}\right) \\
\mathcal{A}^{AE}_{n,g,k} &= \left(\tfrac{1}{6}\Delta x_k + \tfrac{1}{2}\tfrac{\mu_n}{\sigma^{A}_{R,g,k}}\right)\mathcal{S}_{g,k} \\
\mathcal{B}^{AE}_{n,g,k} &= \left[\left(\tfrac{1}{3}\Delta x_k + \tfrac{1}{2}\tfrac{\mu_n}{\sigma^{A}_{R,g,k}}\right)\mathcal{S}_{g,k} + \left(\tfrac{1}{3}\Delta x_{k+1} - \tfrac{1}{2}\tfrac{\mu_n}{\sigma^{A}_{R,g,k+1}}\right)\mathcal{S}_{g,k+1}\right] \\
\mathcal{C}^{AE}_{n,g,k} &= \left(\tfrac{1}{6}\Delta x_{k+1} - \tfrac{1}{2}\tfrac{\mu_n}{\sigma^{A}_{R,g,k+1}}\right)\mathcal{S}_{g,k+1} \\
a^{E}_{n,g,k} &= \left(\tfrac{1}{6}\Delta x_k\sigma^{E}_{R,g,k} - \tfrac{\mu_n^2}{\Delta x_k\sigma^{E}_{R,g,k}}\right) \\
b^{E}_{n,g,k} &= \left(\tfrac{1}{3}[\Delta x_k\sigma^{E}_{R,g,k} + \Delta x_{k+1}\sigma^{E}_{R,g,k+1}] + \tfrac{\mu_n^2}{\Delta x_k\sigma^{E}_{R,g,k}} + \tfrac{\mu_n^2}{\Delta x_{k+1}\sigma^{E}_{R,g,k+1}}\right) \\
\mathcal{A}^{EA}_{n,g,k} &= \left(\tfrac{1}{2}\Delta x_k + \tfrac{3}{2}\tfrac{\mu_n}{\sigma^{E}_{R,g,k}}\right)\mathcal{S}_{g,k} \\
\mathcal{B}^{EA}_{n,g,k} &= \left[\left(\Delta x_k + \tfrac{3}{2}\tfrac{\mu_n}{\sigma^{E}_{R,g,k}}\right)\mathcal{S}_{g,k} - \left(\Delta x_{k+1} - \tfrac{3}{2}\tfrac{\mu_n}{\sigma^{E}_{R,g,k+1}}\right)\mathcal{S}_{g,k+1}\right] \\
\mathcal{C}^{EA}_{n,g,k} &= \left(\tfrac{1}{2}\Delta x_{k+1} - \tfrac{3}{2}\tfrac{\mu_n}{\sigma^{E}_{R,g,k+1}}\right)\mathcal{S}_{g,k+1}
\end{aligned}$$

For the error equations the coefficients are defined as

$$\begin{aligned}
\sigma^{f^A}_{g,k} &= \sigma^A_{R,g,k} + 3\frac{\mathcal{S}^2_{g,k}}{\sigma^E_{R,g,k}} \\
a^{f^A}_{n,g,k} &= \tfrac{1}{6}\Delta x_k \sigma^{f^A}_{g,k} + \tfrac{3}{2}\mu_n \frac{\mathcal{S}^2_{g,k}}{\sigma^A_{R,g,k}\sigma^E_{R,g,k}} - \frac{\mu^2_n}{\Delta x_k \sigma^A_{R,g,k}} \\
b^{f^A}_{n,g,k} &= \tfrac{1}{3}\Delta x_k \sigma^{f^A}_{g,k} + \tfrac{1}{3}\Delta x_{k+1} \sigma^{f^A}_{g,k+1} + \tfrac{3}{2}\mu_n \left(\frac{\mathcal{S}^2_{g,k}}{\sigma^A_{R,g,k}\sigma^E_{R,g,k}} - \frac{\mathcal{S}^2_{g,k+1}}{\sigma^A_{R,g,k+1}\sigma^E_{R,g,k+1}} \right) \\
&\quad + \frac{\mu^2_n}{\Delta x_k \sigma^A_{R,g,k}} + \frac{\mu^2_n}{\Delta x_{k+1} \sigma^A_{R,g,k+1}} \\
c^{f^A}_{n,g,k} &= \tfrac{1}{6}\Delta x_{k+1} \sigma^{f^A}_{g,k+1} - \tfrac{3}{2}\mu_n \frac{\mathcal{S}^2_{g,k+1}}{\sigma^A_{R,g,k+1}\sigma^E_{R,g,k+1}} - \frac{\mu^2_n}{\Delta x_{k+1} \sigma^A_{R,g,k+1}} \\
\mathcal{A}^{f^A}_{n,g,k} &= \mathcal{A}^{AE}_{n,g,k} \\
\mathcal{B}^{f^A}_{n,g,k} &= \mathcal{B}^{AE}_{n,g,k} \\
\mathcal{C}^{f^A}_{n,g,k} &= \mathcal{C}^{AE}_{n,g,k}
\end{aligned}$$

To perform the discrete Fourier analysis on the discretized accelerated upscatter scheme given in equations 6.54 through 6.59 the discrete ansatz given below for the angular fluxes and errors is needed:

$$\begin{aligned}
\Psi^{A(E)}_{n,g,k\pm1/2} &= \Psi^{A(E)}_{n,g} e^{i\lambda x_{k\pm1/2}} \\
f^{A(E)}_{n,g,k\pm1/2} &= f^{A(E)}_{n,g} e^{i\lambda x_{k\pm1/2}}
\end{aligned} \tag{6.60}$$

Using the expressions given above the goal of the discrete Fourier analysis is to determine an expression for $\Psi^{E(j+1)}$ in terms of $\Psi^{E(j)}$. The first step is to introduce the discrete ansatz for $\Psi^{A(j+1/2)}_{n,g,k\pm1/2}$ and $\Psi^{E(j)}_{n,g,k\pm1/2}$ into equation 6.54 which yields,

$$\begin{aligned}
&\left(a^A_{n,g,k} e^{i\lambda x_{k-1/2}} + b^A_{n,g,k} e^{i\lambda x_{k+1/2}} + a^A_{n,g,k+1} e^{i\lambda x_{k+3/2}} \right) \quad \Psi^{A(j+1/2)}_{n,g} = \\
&\left(\mathcal{A}^{AE}_{n,g,k} e^{i\lambda x_{k-1/2}} + \mathcal{B}^{AE}_{n,g,k} e^{i\lambda x_{k+1/2}} + \mathcal{C}^{AE}_{n,g,k} e^{i\lambda x_{k+3/2}} \right) \quad \Psi^{E(j)}_{n,g}
\end{aligned} \tag{6.61}$$

Choosing $x_{k+1/2}$ as the point the discrete ansatz is centered around, the next step is to multiply through the above equation by $e^{-i\lambda x_{k+1/2}}$ giving

$$\begin{aligned}
&\left(a^A_{n,g,k} e^{-i\lambda\Delta x} + b^A_{n,g,k} + a^A_{n,g,k+1} e^{i\lambda\Delta x} \right) \quad \Psi^{A(j+1/2)}_{n,g} = \\
&\left(\mathcal{A}^{AE}_{n,g,k} e^{-i\lambda\Delta x} + \mathcal{B}^{AE}_{n,g,k} + \mathcal{C}^{AE}_{n,g,k} e^{i\lambda\Delta x} \right) \quad \Psi^{E(j)}_{n,g}
\end{aligned} \tag{6.62}$$

Solving for $\Psi^{A(j+1/2)}_{n,g}$ yields

$$\begin{aligned}
\Psi^{A(j+1/2)}_{n,g} &= \left\{ \frac{\left(\mathcal{A}^{AE}_{n,g,k} e^{-i\lambda\Delta x} + \mathcal{B}^{AE}_{n,g,k} + \mathcal{C}^{AE}_{n,g,k} e^{i\lambda\Delta x} \right)}{\left(a^A_{n,g,k} e^{-i\lambda\Delta x} + b^A_{n,g,k} + a^A_{n,g,k+1} e^{i\lambda\Delta x} \right)} \right\} \Psi^{E(j)}_{n,g} \\
&= \alpha(\lambda\Delta x)\Psi^{E(j)}_{n,g}
\end{aligned} \tag{6.63}$$

The same procedure is applied to equation 6.55 using the expression for $\Psi^{A(j+1/2)}_{n,g}$ above to get

$$\begin{aligned}\Psi^{E(j+1/2)}_{n,g} &= \left\{\frac{-\left(\mathcal{A}^{EA}_{n,g,k}e^{-i\lambda\Delta x} + \mathcal{B}^{EA}_{n,g,k} + \mathcal{C}^{EA}_{n,g,k}e^{i\lambda\Delta x}\right)}{\left(a^{E}_{n,g,k}e^{-i\lambda\Delta x} + b^{E}_{n,g,k} + a^{E}_{n,g,k+1}e^{i\lambda\Delta x}\right)}\right\}\alpha(\lambda\Delta x)\Psi^{E(j)}_{n,g} \\ &= \omega(\lambda\Delta x)\Psi^{E(j)}_{n,g} \qquad (6.64)\end{aligned}$$

Similarly, evaluating equation 6.56 yields

$$\begin{aligned}f^{A(j+1/2)}_{n,g} &= \left\{\frac{\left(\mathcal{A}^{fA}_{n,g,k}e^{-i\lambda\Delta x} + \mathcal{B}^{fA}_{n,g,k} + \mathcal{C}^{fA}_{n,g,k}e^{i\lambda\Delta x}\right)}{\left(a^{fA}_{n,g,k}e^{-i\lambda\Delta x} + b^{fA}_{n,g,k} + c^{fA}_{n,g,k+1}e^{i\lambda\Delta x}\right)}\right\}\Big[\omega(\lambda\Delta x) - 1\Big]\Psi^{E(j)}_{n,g} \\ &= \chi(\lambda\Delta x)\Psi^{E(j)}_{n,g} \qquad (6.65)\end{aligned}$$

The slope flux error, $f^{E(j+1/2)}_{n,g}$, can be shown to reduce to

$$\begin{aligned}f^{E(j+1/2)}_{n,g} &= -f^{A(j+1/2)}_{n,g} \\ &= -\chi(\lambda\Delta x)\Psi^{E(j)}_{n,g} \qquad (6.66)\end{aligned}$$

Finally, we solve for $\Psi^{E(j+1)}_{n,g}$ to get

$$\begin{aligned}\Psi^{E(j+1)}_{n,g} &= \Psi^{E(j+1/2)}_{n,g} + f^{E(j+1/2)}_{n,g} \\ &= [\omega(\lambda\Delta x) - \chi(\lambda\Delta x)]\Psi^{E(j)}_{n,g} \\ &= \beta(\lambda\Delta x)\Psi^{E(j)}_{n,g} \qquad (6.67)\end{aligned}$$

Considering 1.0 MeV electrons on a 0.3 cm thick slab the stopping power and energy group structure are used together with the spatial cell size, Δx, to evaluate $\beta(\lambda\Delta x)$. In Figure 6.3 $\beta(\lambda\Delta x)$ is plotted as a function of $\lambda\Delta x$ as the spatial mesh is refined. The discrete Fourier analysis reveals that $\beta(\lambda\Delta x)$ approaches the continuous or analytic spectral radius of 0.20 as $\Delta x \to 0$. It should be noted that $\beta(\lambda\Delta x)$ is a periodic function with a period of $\lambda\Delta x = \pi$.

To further evaluate the effectiveness of the upscatter acceleration scheme it is numerically implemented and a pure CSD problem evaluated.

6.3 Application of Upscatter Acceleration

The continuous and discrete Fourier analysis indicate that the upscatter acceleration scheme is effective. Here the scheme is numerically implemented on an energy and spatial grid and a numerical experiment performed to estimate the spectral radius for

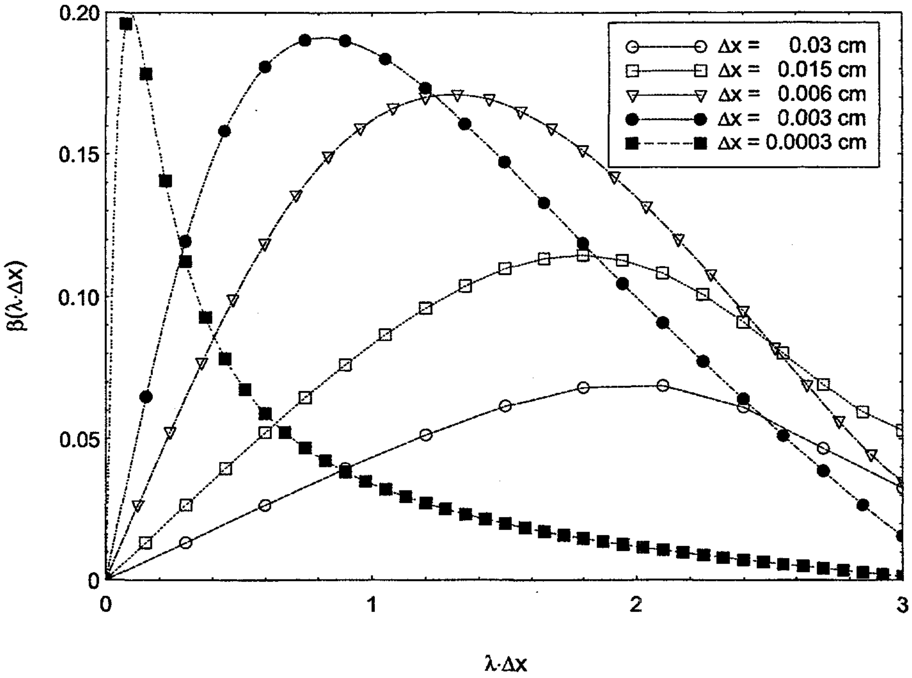

Figure 6.3: Discrete Fourier Spectral Radius of Upscatter Acceleration Scheme

a pure CSD problem. The upscatter iteration for a pure CSD problem is characterized by a theoretical spectral radius of 0.20. In the pure CSD problem the only removal from a given energy group is through the CSD term as the total cross-section and scattering source are set to zero. As part of the experiment, we will evaluate the spectral radius for several energy groups as the spatial cell width is refined.

The spectral radius at the $j+1$ iterate is defined as

$$\rho_{n,g}^{j+1} = \frac{||\varepsilon_{n,g}^{j+1}||}{||\varepsilon_{n,g}^{j}||} \tag{6.68}$$

where the error norms are given by[37]

$$||\varepsilon_{n,g}^{j+1}|| = \sqrt{\sum_{k=1}^{K}\left(\Psi_{n,g+1/2,k}^{j+1} - \Psi_{n,g+1/2,k}^{j}\right)^2} \tag{6.69}$$

$$||\varepsilon_{n,g}^{j}|| = \sqrt{\sum_{k=1}^{K}\left(\Psi_{n,g+1/2,k}^{j} - \Psi_{n,g+1/2,k}^{j-1}\right)^2} \tag{6.70}$$

Note that the definition of ρ^{j+1} requires a minimum of three upscatter iterations before an estimate can be made. The spectral radius, ρ_g, for the gth energy group is:

$$\rho_g = \max_{all\ n} \rho_{n,g}^{j+1} \tag{6.71}$$

The relative error at the $j+1$ upscatter iterate is calculated using the relative error norm formula[37] below:

$$\epsilon_{n,g}^{Rel} = \frac{\left\| \Psi_{n,g+1/2,k}^{j+1} - \Psi_{n,g+1/2,k}^{j} \right\|}{\left\| \Psi_{n,g+1/2,k}^{j} \right\|} \tag{6.72}$$

where

$$\begin{aligned} \left\| \Psi_{n,g+1/2,k}^{j+1} - \Psi_{n,g+1/2,k}^{j} \right\| &= \sqrt{\sum_{k=1}^{K} \left(\Psi_{n,g+1/2,k}^{j+1} - \Psi_{n,g+1/2,k}^{j} \right)^2} \\ \left\| \Psi_{n,g+1/2,k}^{j} \right\| &= \sqrt{\sum_{k=1}^{K} \left(\Psi_{n,g+1/2,k}^{j} \right)^2} \end{aligned}$$

Convergence in a given energy group is reached when the following relationship is satisfied

$$\max_{all\ n} \epsilon_{n,g}^{Rel} < \xi_0 \left(1 - \rho_g^{j+1}\right) \tag{6.73}$$

where ξ_0 is the tolerance.

6.3.1 Numerical Results

The earlier section revealed that the theoretical asymptotic rate of convergence for the pure CSD problem is equal to 0.20. In the pure CSD problem the only interaction of electrons is through the continuous slowing-down operator which tightly couples the problem in space and energy. Specifically, we consider 1.0 MeV electrons normally incident on a 0.3 cm thick slab of aluminum. The energy group structure is 40 linear energy groups with a cutoff energy of 1 keV. CEPXS generated stopping powers are used and all other cross-sections are zeroed out.

To assess the rate of convergence the spatial mesh was refined from 0.06 cm to 0.00015 cm corresponding to 5 cells to 2000 spatial cells, respectively. We look at the two highest energy groups (g=1,g=2) and the two lowest energy groups (g=39,g=40). The stopping power ranges from 3.16 MeV/cm in the highest energy group to 35.5 MeV/cm for the lowest energy group. Figure 6.3 depicts the estimated spectral radius for the highest energy group (g=1) as a function of the spatial mesh for each iteration. It is evident from this figure that as $\Delta x \to 0$ the calculated ρ approaches the analytical value of 0.20 as expected. This trend is also observed for the estimated ρ for g=2, g=39 and g = 40 (see Figures 6.4, 6.5, and 6.6).

The results depicted in Figures 6.4 through 6.7 are summarized in Table 6.1 which lists the final spectral radius estimate for each group as a function of the number of spatial cells. As expected the spectral radius approaches the analytic value of 0.20 as the spatial mesh is refined ($\Delta x \to 0$). For the lowest energy groups (g=39, g=40) the estimated spectral radius is much smaller than the analytic value and the solution converges rapidly. For instance, in the last energy group, g=40, the spectral radius changes from $\rho = 0.003$ for the coarsest spatial mesh (5 Δx) up to $\rho = 0.022$ when the spatial mesh is refined to (2000 Δx) corresponding to a $\Delta x = 0.0003$ cm.

Table 6.1: Summary of Spectral Radius Estimates for Upscatter Iteration

	ENERGY GROUP			
Spatial Mesh	g = 1	g = 2	g = 39	g = 40
5 Δx	0.050	0.037	0.008	0.003
10 Δx	0.063	0.064	0.013	0.005
20 Δx	0.109	0.109	0.025	0.008
50 Δx	0.165	0.166	0.044	0.014
100 Δx	0.185	0.186	0.058	0.018
500 Δx	0.194	0.195	0.064	0.022
1000 Δx	0.194	0.195	0.064	0.022
2000 Δx	0.194	0.195	0.064	0.022

The upscatter acceleration is expected to be the most effective for the lower energy groups that are characterized by large stopping powers. The results shown in Table 6.1 indicates that the upscatter acceleration scheme derived earlier is very effective for the pure CSD problem particularly in the lower energy groups where it takes five or less iterations to converge. Tables 6.2 through 6.4 present iteration summaries for 10 Δx, 100 Δx, and 1000 Δx with the upscatter acceleration turned on and off, respectively. These tables indicate how effective the upscatter acceleration is in reducing the number of iterations to convergence for the Pure CSD problem. Table 6.2 also shows that the extremely small spectral radius for g=40 of 0.022 is in line with the reduction in the number of iterations from 3834 with the acceleration off to 3 with the acceleration on for 10 Δx.

For real charged particle transport problems there are other interactions besides the slowing-down through the CSD term. Primarily, there is a scattering source due to both elastic and inelastic scattering events along with the removal of electrons through the slowing-down term. Experience tells us that the scattering source convergence must be accelerated. The DSA iteration scheme derived in Section 5.1 will be used to accelerate the scattering source iteration and the upscatter acceleration scheme derived in Section 6.2 will be used to accelerate the convergence between the average and slope flux SAAF equations. In the next chapter, the overall effectiveness of acceleration will be evaluated.

This page intentionally blank.

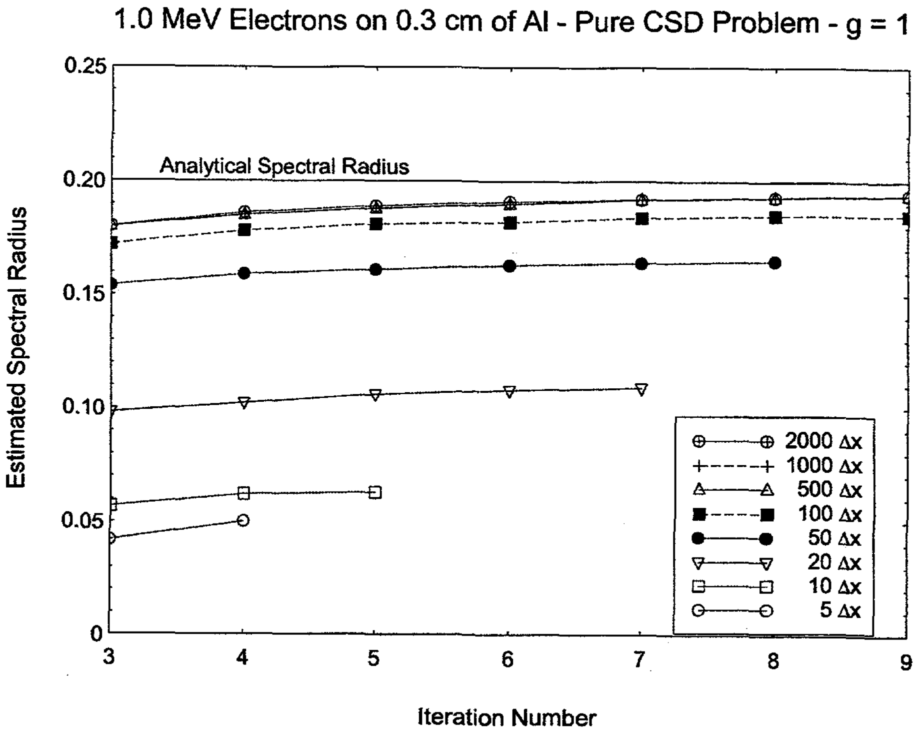

Figure 6.4: Estimated Upscatter Spectral Radius for g = 1

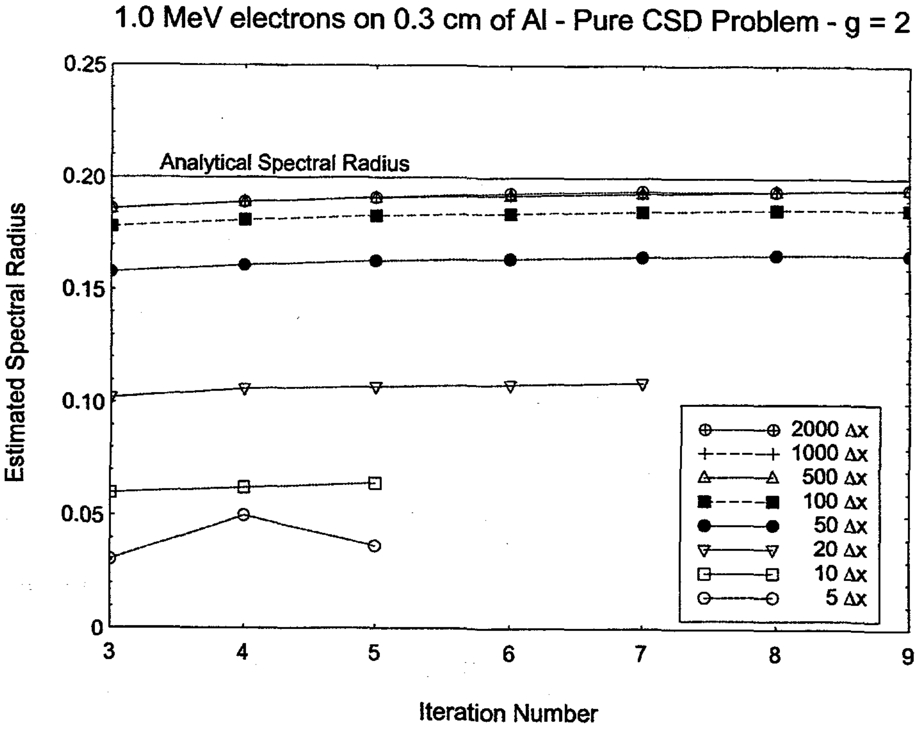

Figure 6.5: Estimated Upscatter Spectral Radius for g = 2

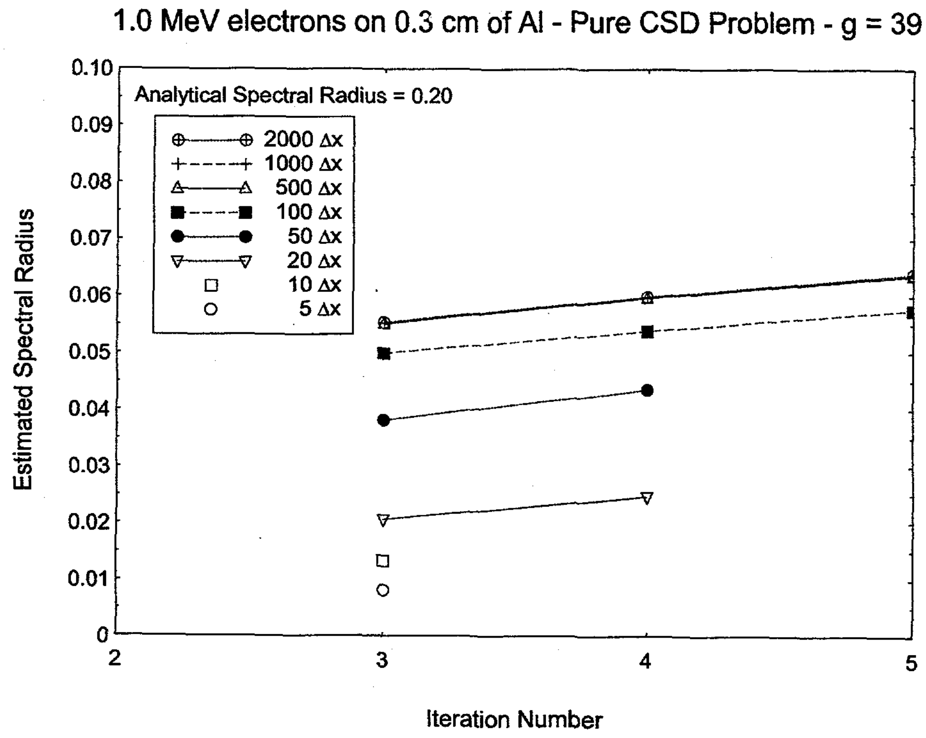

Figure 6.6: Estimated Upscatter Spectral Radius for g = 39

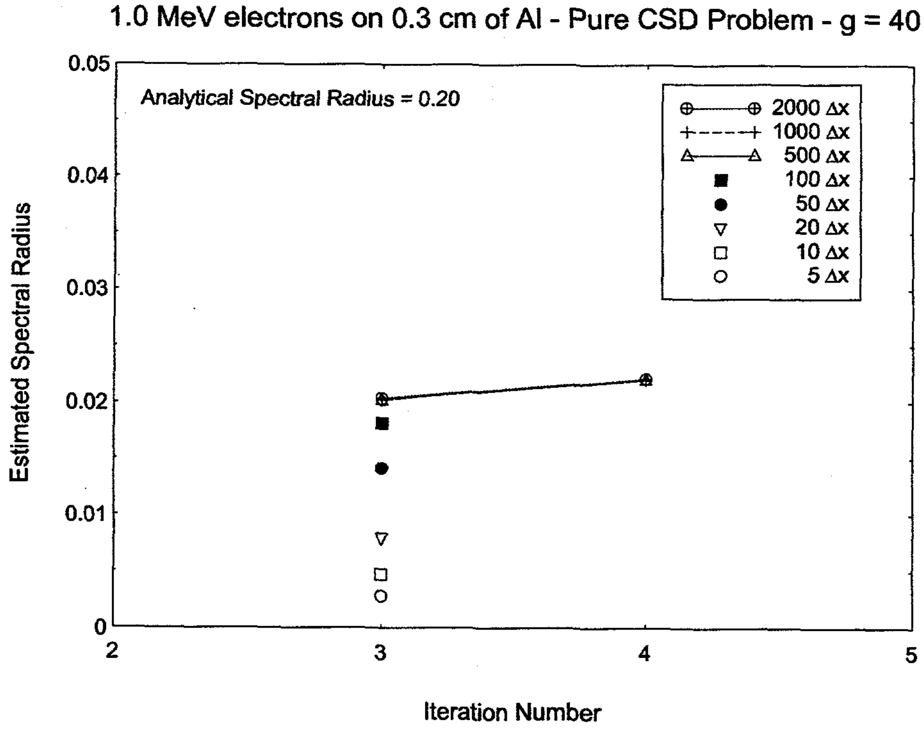

Figure 6.7: Estimated Upscatter Spectral Radius for g = 40

Table 6.2: Upscatter Iteration Summary for 10 Δx

Energy Group	UNACCELERATED Number of Iterations	ACCELERATED Number of Iterations
1	85	5
2	84	5
3	74	5
4	73	5
5	72	5
6	72	5
7	71	5
8	71	5
9	84	5
10	84	5
11	83	5
12	83	5
13	83	5
14	83	5
15	83	5
16	83	5
17	83	5
18	84	5
19	84	5
20	84	5
21	84	5
22	85	5
23	86	5
24	87	5
25	88	5
26	89	5
27	91	5
28	93	4
29	95	4
30	99	4
31	111	4
32	116	4
33	124	4
34	142	4
35	166	4
36	211	4
37	266	4
38	427	3
39	546	3
40	3834	3

Table 6.3: Upscatter Iteration Summary for 100 Δx

Energy Group	UNACCELERATED Number of Iterations	ACCELERATED Number of Iterations
1	51	9
2	51	9
3	50	9
4	49	9
5	48	9
6	47	9
7	47	9
8	46	9
9	45	9
10	44	9
11	43	8
12	42	8
13	41	8
14	40	8
15	39	8
16	40	8
17	40	8
18	39	8
19	38	8
20	38	8
21	37	8
22	37	8
23	36	8
24	36	8
25	35	8
26	35	8
27	34	7
28	34	7
29	34	7
30	34	7
31	34	7
32	34	7
33	34	7
34	35	6
35	37	6
36	39	6
37	43	6
38	43	5
39	50	5
40	160	3

Table 6.4: Upscatter Iteration Summary for 1000 Δx

Energy Group	UNACCELERATED Number of Iterations	ACCELERATED Number of Iterations
1	51	9
2	51	9
3	50	9
4	50	9
5	49	9
6	48	9
7	47	9
8	46	9
9	45	9
10	44	9
11	43	9
12	43	9
13	42	9
14	41	9
15	40	8
16	39	8
17	38	8
18	37	8
19	36	8
20	36	8
21	35	8
22	34	8
23	33	8
24	32	8
25	31	8
26	32	8
27	32	8
28	31	8
29	31	8
30	31	7
31	31	7
32	31	7
33	31	7
34	33	7
35	35	6
36	37	6
37	44	6
38	51	5
39	57	5
40	158	4

7 Solution Algorithm

The traditional first-order form of the transport equation is solved using a sweeping algorithm, in which we first march cell by cell in the forward angular directions and then march backward in the negative directions. In solving the second-order formulation, on the other hand, the angular fluxes are computed simultaneously at all mesh points by solving a system of equations for each direction and each energy group. This system of equations is represented by the matrix equation given below

$$\mathbf{A}_{n,g}\vec{\Psi}_{n,g} = \vec{Q}_{n,g} \tag{7.1}$$

where $\mathbf{A}_{n,g}$ is the coefficient matrix, $\vec{\Psi}_{n,g}$ are the angular fluxes at each cell-edge or mesh point, and $\vec{Q}_{n,g}$ is the known source into each group and each cell. $\mathbf{A}$ is a NxN square matrix where $N = K - 1$ and K is the total number of spatial cells. The application of linear continuous finite elements to the second-order energy discretized equation yields a symmetric, positive definite coefficient matrix which is tridiagonal in structure:

$$\mathbf{A} = \begin{pmatrix} b_1 & c_1 & 0 & \cdots & & & \\ a_2 & b_2 & c_2 & \cdots & & & \\ & & & \cdots & & & \\ & & & \cdots & a_{N-1} & b_{N-1} & c_{N-1} \\ & & & \cdots & 0 & a_N & b_N \end{pmatrix} \tag{7.2}$$

This system of equations is efficiently solved using a standard tridiagonal matrix solver.[38]

Incorporating the explicit continuous slowing-down operator means that the solution algorithm of the discretized SAAF equation also depends on the energy discretization scheme. Solving the LD SAAF equation means there are effectively two transport equations that must be solved for each direction. The slope and average angular flux transport equations are coupled as detailed in Chapter 6 which introduces an upscatter iteration in each energy group. Solving the block LD SAAF transport equation eliminates the upscatter iteration in each group and the coefficient matrix becomes a block tridiagonal matrix.

Regardless of the discretization scheme, the solution algorithm for the SAAF transport equation follows a general pattern. For each energy group, the transport equation is solved in each direction using a direct method. The known sources in each energy group include the source due to slowing-down from higher energy groups, downscatter sources, and fixed sources. A scattering source iteration method is utilized (see Section 3.5, pg. 33), where convergence on the within group scattering source in each energy group is realized before proceeding to the next energy group. The general algorithm is depicted in Figure 7.1. Next, the algorithm that is applied to the Block LD SAAF equation is detailed.

7.1 Block LD SAAF Equation Solution Algorithm

The spatially discretized block LD SAAF equation in source iteration form is

$$\begin{gathered}\underline{\alpha}_{n,g,k}\vec{\Psi}^{(\ell+1/2)}_{n,g,k-1/2}+\underline{\beta}_{n,g,k}\vec{\Psi}^{(\ell+1/2)}_{n,g,k+1/2}+\underline{\alpha}_{n,g,k+1}\vec{\Psi}^{(\ell+1/2)}_{n,g,k+3/2}=\vec{Q}_{n,g,k}\\ +\underline{\mathcal{A}}^{S}_{n,g,k}\vec{Q}^{ES,L(\ell)}_{n,g,k}+\underline{\mathcal{B}}^{S}_{n,g,k}\vec{Q}^{ES,R(\ell)}_{n,g,k}+\underline{\mathcal{C}}^{S}_{n,g,k+1}\vec{Q}^{ES,L(\ell)}_{n,g,k+1}+\underline{\mathcal{D}}^{S}_{n,g,k+1}\vec{Q}^{ES,R(\ell)}_{n,g,k+1}\end{gathered}\tag{7.3}$$

where ℓ is the source iteration index. On the right-hand side of the equation above, $\vec{Q}_{n,g,k}$, represents the sources into group g from downscatter interactions, slowing down from the $g-1$ group and fixed sources. The elastic scattering source, $\vec{Q}^{ES}_{n,g,k}$, depends on the angular flux in the current energy group and is the contribution we iterate on in the source iteration method. In equation 7.3 the block coefficients on the left hand side are defined as,

$$\begin{aligned}\underline{\alpha}_{n,g,k} &= \left(\tfrac{1}{6}\Delta x_k\Re_{g,k}-\tfrac{\mu_n^2}{\Delta x_k}\Re^{-1}_{g,k}\right)\\ \underline{\beta}_{n,g,k} &= \left(\tfrac{1}{3}[\Delta x_k\Re_{g,k}+\Delta x_{k+1}\Re_{g,k+1}]+\tfrac{\mu^2}{\Delta x_k}\Re^{-1}_{g,k}+\tfrac{\mu^2}{\Delta x_{k+1}}\Re^{-1}_{g,k+1}\right)\end{aligned}$$

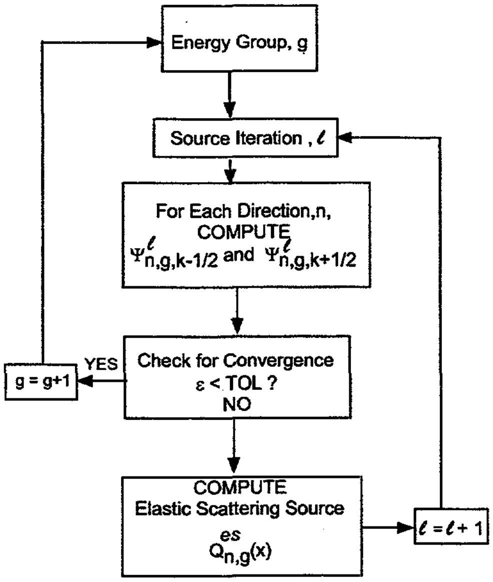

Figure 7.1: General Solution Algorithm Flow

$\vec{Q}_{g,k}$ is defined as

$$\begin{aligned}
\vec{Q}_{g,k} &= \underline{\mathcal{A}}^{S}_{n,g,k}\vec{Q}^{S,L}_{n,g,k} + \underline{\mathcal{B}}^{S}_{n,g,k}\vec{Q}^{S,R}_{n,g,k} + \underline{\mathcal{C}}^{S}_{n,g,k+1}\vec{Q}^{S,L}_{n,g,k+1} + \underline{\mathcal{D}}^{S}_{n,g,k+1}\vec{Q}^{S,R}_{n,g,k+1} \\
&+ \underline{\mathcal{A}}^{ex}_{n,g,k}\vec{q}_{n,g,k} + \underline{\mathcal{B}}^{ex}_{n,g,k+1}\vec{q}_{n,g,k+1} \\
&+ \underline{\mathcal{A}}^{CSD}_{n,g,k}\vec{\Psi}_{n,g-1,k-1/2} + \underline{\mathcal{B}}^{CSD}_{n,g,k}\vec{\Psi}_{n,g-1,k+1/2} + \underline{\mathcal{C}}^{CSD}_{n,g,k}\vec{\Psi}_{n,g-1,k+3/2}
\end{aligned}$$

where the coefficients on the scattering and fixed sources are defined below:

$$\begin{array}{lcl}
\underline{\mathcal{A}}^{S}_{n,g,k} = \left(\frac{1}{6}\Delta x_k \mathbf{I} + \frac{1}{2}\mu_n \Re^{-1}_{g,k}\right) & \text{and} & \underline{\mathcal{B}}^{S}_{n,g,k} = \left(\frac{1}{3}\Delta x_k \mathbf{I} + \frac{1}{2}\mu_n \Re^{-1}_{g,k}\right) \\
\underline{\mathcal{C}}^{S}_{n,g,k} = \left(\frac{1}{3}\Delta x_k \mathbf{I} - \frac{1}{2}\mu_n \Re^{-1}_{g,k}\right) & \text{and} & \underline{\mathcal{D}}^{S}_{n,g,k} = \left(\frac{1}{6}\Delta x_k \mathbf{I} - \frac{1}{2}\mu_n \Re^{-1}_{g,k}\right) \\
\underline{\mathcal{A}}^{ex}_{n,g,k} = \left(\frac{1}{2}\Delta x_k \mathbf{I} + \mu_n \Re^{-1}_{g,k}\right) & \text{and} & \underline{\mathcal{B}}^{ex}_{n,g,k} = \left(\frac{1}{2}\Delta x_{k+1} \mathbf{I} - \mu_n \Re^{-1}_{g,k+1}\right)
\end{array}$$

and the coefficients on the slowing-down source are defined as

$$\begin{aligned}
\underline{\mathcal{A}}^{CSD}_{n,g,k} &= \left(\tfrac{1}{6}\Delta x_k \mathcal{S}_{g-1,k} + \tfrac{1}{2}\mu_n \Re^{-1}_{g,k}\mathcal{S}_{g-1,k}\right) \\
\underline{\mathcal{B}}^{CSD}_{n,g,k} &= \left(\tfrac{1}{3}\Delta x_k \mathcal{S}_{g-1,k} + \tfrac{1}{2}\mu_n \Re^{-1}_{g,k}\mathcal{S}_{g-1,k}\right) + \left(\tfrac{1}{3}\Delta x_{k+1} \mathcal{S}_{g-1,k+1} - \tfrac{1}{2}\mu_n \Re^{-1}_{g,k+1}\mathcal{S}_{g-1,k+1}\right) \\
\underline{\mathcal{C}}^{CSD}_{n,g,k} &= \left(\tfrac{1}{6}\Delta x_{k+1} \mathcal{S}_{g-1,k+1} - \tfrac{1}{2}\mu_n \Re^{-1}_{g,k+1}\mathcal{S}_{g-1,k+1}\right)
\end{aligned}$$

Recall that earlier (Ch. 4) the following parameters were defined to simplify writing the block matrix equations:

$$\Re_g = \begin{pmatrix} \sigma^A_{R,g} & -\frac{S_g}{\Delta E_g} \\ 3\frac{S_g}{\Delta E_g} & \sigma^E_{R,g} \end{pmatrix} \text{ and } \mathcal{S}_{g-1} = \frac{S_{g-1}}{\Delta E_g}\begin{pmatrix} 1 & -1 \\ 3 & -3 \end{pmatrix}$$

where $\sigma^A_{R,g} = \sigma_{t,g} + \frac{S_g}{\Delta E_g}$ and $\sigma^E_{R,g} = \sigma_{t,g} + 3\frac{S_g}{\Delta E_g}$. From these definitions it can be deduced that the coefficients in the block matrix equation are all two-by-two matrices and the overall system is a block tridiagonal system.

The solution algorithm of the block LD equation proceeds like the general algorithm depicted in Figure 7.1. The details are presented in Table 7.1. Before the source iteration for a given energy group is started the known sources on the right-hand side of equation 7.3 due to downscatter from higher energy groups, slowing-down, and any fixed source are accumulated. In coupled electron-photon problems, the contribution to a particle species from a different species (e.g. $\gamma \rightarrow e^-$) is incorporated in the downscatter source into group, g.

The algorithm for the solution of the block LD SAAF equation is quite straight forward. The solution of the LD SAAF equation is more complicated due to the within-group upscatter.

Table 7.1: Block LD in E Solution Algorithm

Step 1	Accumulate downscatter source into group g
Step 2	Compute slowing-down source into group g from $g-1$
Step 3	Increment source iteration index, $\ell = \ell + 1$
Step 4	Solve equation 7.3 for $\Psi^{A(\ell+1/2)}_{n,g,k\pm 1/2}$ and $\Psi^{E(\ell+1/2)}_{n,g,k\pm 1/2}$
Step 5	Update scalar flux moments, $\phi^{(\ell+1/2)}_{g,k\pm 1/2}$
Step 6	If source acceleration is turned on, then
	(a) Solve source acceleration equations for scalar, $F^{(\ell+1/2)}_{k\pm 1/2}$, and current, $H^{(\ell+1/2)}_{k\pm 1/2}$, parts of error across slab (see Ch. 5)
	(b) Update scalar flux with scalar part of the error to get $\phi^{(\ell+1)}_{g,k\pm 1/2}$.
Step 7	Calculate L_2 error norm for $\Psi_{n,g+1/2,k}$, ε_{L2}
Step 8	Check whether or not convergence criteria, ξ, is satisfied
	(a) If $\varepsilon_{L2} < \xi$, proceed to next energy group, $g+1$, starting with **Step 1**
	(b) If $\varepsilon_{L2} \geq \xi$, proceed to **Step 9**
Step 9	Update elastic scattering source using $\phi^{(\ell+1)}_{g,k\pm 1/2}$ and return to **Step 3**

7.2 Slope-Average Component Form Solution Algorithm

Recall that the spatially continuous average and slope angular flux SAAF equations derived in Ch. 4 are

$$\begin{aligned}
-\mu^2\frac{\partial}{\partial x}\left(\frac{1}{\sigma^A_{R,g}}\frac{\partial \Psi^A_g}{\partial x}\right) &+ \sigma^A_{R,g}\Psi^A_g = Q^S_g - \mu\frac{\partial}{\partial x}\left(\frac{1}{\sigma^A_{R,g}}Q^S_g\right) + q_g - \mu\frac{\partial}{\partial x}\left(\frac{1}{\sigma^A_{R,g}}q_g\right) \\
&+ \frac{S_{g-1}}{\Delta E_g}\left[\Psi^A_{g-1} - \Psi^E_{g-1}\right] - \mu\frac{\partial}{\partial x}\left(\frac{1}{\sigma^A_{R,g}}\frac{S_{g-1}}{\Delta E_g}\left[\Psi^A_{g-1} - \Psi^E_{g-1}\right]\right) \\
&+ \frac{S_g}{\Delta E_g}\Psi^E_g - \mu\frac{\partial}{\partial x}\left(\frac{1}{\sigma^A_{R,g}}\frac{S_g}{\Delta E_g}\Psi^E_g\right) \qquad (7.4)
\end{aligned}$$

and

$$\begin{aligned}
-\mu^2\frac{\partial}{\partial x}\left(\frac{1}{\sigma^E_{R,g}}\frac{\partial \Psi^E_g}{\partial x}\right) + \sigma^E_{R,g}\Psi^E_g &= 3\frac{S_{g-1}}{\Delta E_g}\left[\Psi^A_{g-1} - \Psi^E_{g-1}\right] \\
&- \mu\frac{\partial}{\partial x}\left(\frac{1}{\sigma^E_{R,g}}3\frac{S_{g-1}}{\Delta E_g}\left[\Psi^A_{g-1} - \Psi^E_{g-1}\right]\right) \\
&- 3\frac{S_g}{\Delta E_g}\Psi^A_g + \mu\frac{\partial}{\partial x}\left(\frac{1}{\sigma^E_{R,g}}3\frac{S_g}{\Delta E_g}\Psi^A_g\right) \qquad (7.5)
\end{aligned}$$

It is important to note that the right-hand side of equation 7.4 for the average flux includes the scattering source, the fixed source, a slowing-down source and contributions from the slope angular flux. However, the right-hand side of equation 7.5 for the slope flux only includes a slowing-down source and a contribution from the average angular flux.

The LD SAAF equation is unique because it requires that two tridiagonal systems of equations are solved for each direction to get the slope and average angular fluxes, respectively. There are two different iteration schemes taking place in each energy group. The first iteration is the well-known scattering source iteration, in which we converge on the elastic scattering source. The second iteration arises from the coupling between the slope and average angular fluxes, and is called the upscatter iteration. Traditionally, in transport problems the inner iteration is the source or DSA iteration; however, the presence of the CSD term with an LD energy discretization introduces two nested iteration schemes in the inner iteration. Thus, each inner iteration in the LD SAAF solution contains both a source iteration and an upscatter iteration. Since the scattering source iteration and the upscatter iteration are essentially independent of each other different solution algorithms can be evaluated.

7.2.1 Algorithm A: Converge on Scattering Source

In Algorithm A the scattering source is converged completely for a given slope angular flux in each inner iteration. Table 7.2 (see pg. 105) presents this algorithm in detail. The table introduces two iteration indices: the scattering source iteration index, ℓ, and j the inner iteration index. For each iteration, j, as many source iterations as necessary are completed to reach convergence on the scattering source followed by one upscatter. The solution proceeds to the next energy group when the scattering source, the slope angular flux and the energy outflow angular flux ($\Psi_{n,g+1/2,k}$) are converged within a specified tolerance (e.g. 1×10^{-6}).

To evaluate the stability of this algorithm a numerical experiment is performed and the spectral radius for DSA estimated. Specifically, we consider 1.0 MeV electrons incident on an Al slab with isotropic scattering, P_0, and S_8 quadrature. The spectral radius for the DSA iteration or inner iteration is estimated for each energy group using the formula below:

$$\rho_g^{\ell+1} = \frac{\|\varepsilon_g^{\ell+1}\|}{\|\varepsilon_g^{\ell}\|} = \frac{\sqrt{\sum_{k=1}^{K}\left(\phi_{g,k}^{\ell+1} - \phi_{g,k}^{\ell}\right)^2}}{\sqrt{\sum_{k=1}^{K}\left(\phi_{g,k}^{\ell} - \phi_{g,k}^{\ell-1}\right)^2}} \tag{7.6}$$

The results are depicted in Figure 7.2 for energy groups g=1, 2, 39 and 40, respectively. The figure clearly shows that this algorithm is stable and the DSA spectral radius

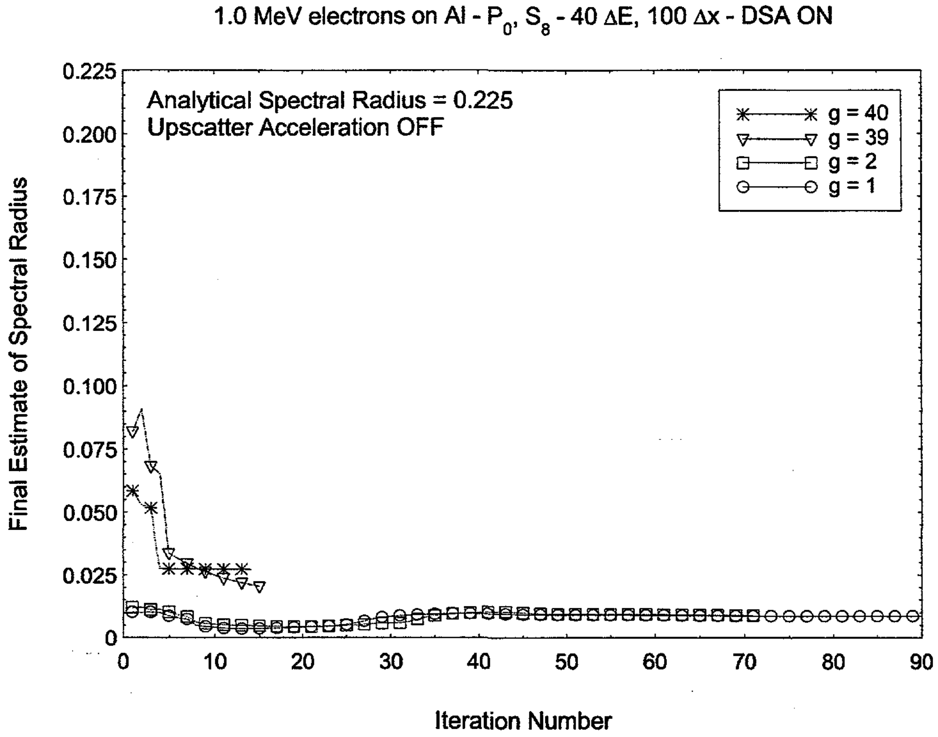

Figure 7.2: Estimated DSA Spectral Radius - Algorithm A

estimates are well below the analytical value of 0.225. DSA clearly remains effective in the presence of the upscatter iterations.

In the next section, the effect on the iteration stability of converging on the slope angular flux holding the scattering source constant is evaluated.

7.2.2 Algorithm B: Converge on Slope Angular Flux

In this algorithm the solution is modified to converge on the slope angular flux for a given scattering source in each inner iteration. Table 7.3 on pg. 106 presents this variation which is referred to as Algorithm B. There are two iteration indices associated with Algorithm B: the upscatter iteration index, ℓ, and the inner iteration index, j. For each iteration, j, as many upscatter iterations as necessary to reach convergence on the slope angular flux are performed followed by one source iteration. Like Algorithm A, the solution proceeds to the next energy group when the scattering source, the slope angular flux and the energy outflow angular flux ($\Psi_{n,g+1/2,k}$) have satisfied the convergence criteria.

To evaluate the stability of this algorithm the same problem is considered with 1.0 MeV electrons incident on Al as described earlier. The spectral radius is estimated for the upscatter iteration for each energy group with DSA off using the

Table 7.2: LD SAAF Algorithm A: Converge on Scattering Source

```
Step A-0   Increment inner iteration index, $j = j + 1$
Step A-1   Increment scattering source iteration index, $\ell = \ell + 1$
Step A-2   Solve for $\Psi^{A}_{n,g,k\pm1/2}$ at the $(j, \ell + 1/2)$ iterate
           $-\mu_n^2 \frac{d}{dx}\left(\frac{1}{\sigma^A_{R,g}} \frac{d\Psi^{A(j,\ell+1/2)}_{n,g}}{dx}\right) + \sigma^A_{R,g} \Psi^{A(j,\ell+1/2)}_{n,g} = Q^{S(j,\ell)}_{n,g} - \mu_n \frac{d}{dx}\left(\frac{1}{\sigma^A_{R,g}} Q^{S(j,\ell)}_{n,g}\right)$
           $+ \frac{S_g}{\Delta E_g} \Psi^{E(j)}_{n,g} - \mu \frac{d}{dx}\left(\frac{1}{\sigma^A_{R,g}} \frac{S_g}{\Delta E_g} \Psi^{E(j)}_{n,g}\right) + q^A_{n,g}$
Step A-3   Update flux moments
           $\phi^{(j,\ell+1/2)}_{g,l} = \frac{1}{2} \sum_{n=1}^{N} P_l(\mu_n) w_n \Psi^{A(j,\ell+1/2)}_{n,g}$
Step A-4   If source acceleration turned on, then
           (a) Solve for scalar and current part of error
               $-\frac{1}{3} \frac{d}{dx}\left(\frac{1}{\sigma^A_{R,g}} \frac{dF^{(j,\ell+1/2)}}{dx}\right) + \left(\sigma^A_{R,g} - \sigma_{g,S,0}\right) F^{(j,\ell+1/2)} = \sigma_{g,S,0}\left[\phi^{(j,\ell+1/2)}_{g,0} - \phi^{(j,\ell)}_{g,0}\right]$
               $-\frac{3}{5} \frac{d}{dx}\left(\frac{1}{\sigma^A_{R,g}} \frac{dH^{(j,\ell+1/2)}}{dx}\right) + \sigma^A_{R,g} H^{(j,\ell+1/2)} + \frac{1}{3} \frac{d}{dx}\left(\frac{\sigma_{g,S,0}}{\sigma^A_{R,g}} F^{(j,\ell+1/2)}\right)$
               $= -\frac{1}{3} \frac{d}{dx}\left[\frac{\sigma_{g,S,0}}{\sigma^A_{R,g}}\left(\phi^{(j,\ell+1/2)}_{g,0} - \phi^{(j,\ell)}_{g,0}\right)\right]$
           (b) Update scalar flux with scalar component of error
               $\phi^{(j,\ell+1)}_{g,0}(x) = \phi^{(j,\ell+1/2)}_{g,0} + F^{(j,\ell+1/2)}(x)$
Step A-5   Update elastic scattering source
           $Q^{S(j,\ell+1)}_{g} = \sigma_{s,0,g} \phi^{(j,\ell+1)}_{g,0} + \sum_{l=1}^{L} (2l+1) P_l(\mu_n) \sigma_{s,l,g} \phi^{(j,\ell+1/2)}_{g,l}$
Step A-6   Check for convergence on scattering source
           a  If convergence criteria satisfied, proceed to Step A-7
           b  If convergence criteria is NOT satisfied, return to Step A-1
Step A-7   Solve for $\Psi^{E}_{n,g,k\pm1/2}$ at the $j + 1/2$ iterate
           $-\mu_n^2 \frac{d}{dx}\left(\frac{1}{\sigma^E_{R,g}} \frac{d\Psi^{E(j+1/2)}_{n,g}}{dx}\right) + \sigma^E_{R,g} \Psi^{E(j+1/2)}_{n,g} = -3 \frac{S_g}{\Delta E_g} \Psi^{A(j,\ell+1)}_{n,g}$
           $+\mu_n \frac{\partial}{\partial x}\left(\frac{1}{\sigma^E_{R,g}} 3 \frac{S_g}{\Delta E_g} \Psi^{A(j,\ell+1)}_{n,g}\right) + q^E_{n,g}$
Step A-8   If upscatter acceleration is turned on, then
           (a) Solve for slope flux residual
               $\mathcal{R}^{(j+1/2)}_{n,g} = \frac{S_g}{\Delta E_g}\left[\Psi^{E(j+1/2)}_{n,g} - \Psi^{E(j)}_{n,g}\right] - \mu_n \frac{d}{dx}\left(\frac{1}{\sigma^A_{R,g}} \frac{S_g}{\Delta E_g}\left[\Psi^{E(j+1/2)}_{n,g} - \Psi^{E(j)}_{n,g}\right]\right)$
           (b) Solve for average flux error estimate
               $-\mu_n^2 \frac{d}{dx}\left(\frac{1}{\sigma^A_{R,g}} \frac{df^{A(j+1/2)}_{n,g}}{dx}\right) - \mu_n \frac{d}{dx}\left(3 \frac{S_g^2}{\sigma^A_{R,g} \sigma^E_{R,g}} f^{A(j+1/2)}_{n,g}\right) + \left(\sigma^A_{R,g} + 3 \frac{S_g^2}{\sigma^E_{R,g}}\right) f^{A(j+1/2)}_{n,g}$
               $= \mathcal{R}^{(j+1/2)}_{n,g}$
           (c) Solve for slope flux error estimate
               $f^{E(j+1/2)}_{n,g} = \frac{1}{\sigma^E_{R,g}}\left\{-3 \frac{S_g}{\Delta E_g} f^{A(j+1/2)}_{n,g}\right\}$
           (d) Update the slope angular flux with the error estimates
               $\Psi^{E(j+1)}_{n,g} = \Psi^{E(j+1/2)}_{n,g} + f^{E(j+1/2)}_{n,g}$
Step A-9   Check for convergence using L2 error norm on $\Psi_{n,g+1/2,k}$
           a  If convergence criteria satisfied, proceed to next energy group
           b  If convergence criteria NOT satisfied, return to Step A-0
```

Table 7.3: LD SAAF Algorithm B: Converge on Slope Flux

```
Step B-0  Increment inner iteration index, $j = j + 1$
Step B-1  Increment upscatter iteration index, $\ell = \ell + 1$
Step B-2  Solve for $\Psi^{A}_{n,g,k\pm1/2}$ at the $(j, \ell + 1/2)$ iterate
          $-\mu_n^2 \frac{d}{dx}\left(\frac{1}{\sigma^A_{R,g}} \frac{d\Psi^{A(j,\ell+1/2)}_{n,g}}{dx}\right) + \sigma^A_{R,g}\Psi^{A(j,\ell+1/2)}_{n,g} = Q^{S(j)}_{n,g} - \mu_n \frac{d}{dx}\left(\frac{1}{\sigma^A_{R,g}} Q^{S(j)}_{n,g}\right)$
          $+\frac{S_g}{\Delta E_g}\Psi^{E(j,\ell)}_{n,g} - \mu \frac{d}{dx}\left(\frac{1}{\sigma^A_{R,g}} \frac{S_g}{\Delta E_g}\Psi^{E(j,\ell)}_{n,g}\right) + q^A_{n,g}$
Step B-3  Solve for $\Psi^{E}_{n,g,k\pm1/2}$ at the $j, \ell + 1/2$ iterate
          $-\mu_n^2 \frac{d}{dx}\left(\frac{1}{\sigma^E_{R,g}} \frac{d\Psi^{E(j,\ell+1/2)}_{n,g}}{dx}\right) + \sigma^E_{R,g}\Psi^{E(j,\ell+1/2)}_{n,g} = -3\frac{S_g}{\Delta E_g}\Psi^{A(j,\ell+1/2)}_{n,g}$
          $+\mu_n \frac{\partial}{\partial x}\left(\frac{1}{\sigma^E_{R,g}} 3\frac{S_g}{\Delta E_g}\Psi^{A(j,\ell+1/2)}_{n,g}\right) + q^E_{n,g}$
Step B-4  If upscatter acceleration is turned on, then
          (a) Solve for slope flux residual
              $\mathcal{R}^{(j,\ell+1/2)}_{n,g} = \frac{S_g}{\Delta E_g}\left[\Psi^{E(j,\ell+1/2)}_{n,g} - \Psi^{E(j,\ell)}_{n,g}\right] - \mu_n \frac{d}{dx}\left(\frac{1}{\sigma^A_{R,g}} \frac{S_g}{\Delta E_g}\left[\Psi^{E(j,\ell+1/2)}_{n,g} - \Psi^{E(j,\ell)}_{n,g}\right]\right)$
          (b) Solve for average flux error estimate
              $-\mu_n^2 \frac{d}{dx}\left(\frac{1}{\sigma^A_{R,g}} \frac{df^{A(j,\ell+1/2)}_{n,g}}{dx}\right) - \mu_n \frac{d}{dx}\left(3\frac{S_g^2}{\sigma^A_{R,g}\sigma^E_{R,g}} f^{A(j,\ell+1/2)}_{n,g}\right) + \left(\sigma^A_{R,g} + 3\frac{S_g^2}{\sigma^E_{R,g}}\right) f^{A(j,\ell+1/2)}_{n,g}$
              $= \mathcal{R}^{(j,\ell+1/2)}_{n,g}$
          (c) Solve for slope flux error estimate
              $f^{E(j,\ell+1/2)}_{n,g} = \frac{1}{\sigma^E_{R,g}}\left\{-3\frac{S_g}{\Delta E_g} f^{A(j,\ell+1/2)}_{n,g}\right\}$
          (d) Update the average and slope angular flux with the error estimates
              $\Psi^{A(j,\ell+1)}_{n,g} = \Psi^{A(j,\ell+1/2)}_{n,g} + f^{A(j,\ell+1/2)}_{n,g}$
              $\Psi^{E(j,\ell+1)}_{n,g} = \Psi^{E(j,\ell+1/2)}_{n,g} + f^{E(j,\ell+1/2)}_{n,g}$
Step B-5  Check for convergence using L$_2$ error norm on $\Psi^{E}_{n,g,k}$
          a  If convergence criteria satisfied, proceed to Step B-6
          b  If convergence criteria NOT satisfied, return to Step B-1
Step B-6  Update flux moments
          $\phi^{(j+1/2)}_{g,l} = \frac{1}{2}\sum_{n=1}^{N} P_l(\mu_n) w_n \Psi^{A(j,\ell+1)}_{n,g}$
Step B-7  If source acceleration turned on, then
          (a) Solve for scalar and current part of error
              $-\frac{1}{3}\frac{d}{dx}\left(\frac{1}{\sigma^A_{R,g}} \frac{dF^{(j+1/2)}}{dx}\right) + \left(\sigma^A_{R,g} - \sigma_{g,S,0}\right) F^{(j+1/2)} = \sigma_{g,S,0}\left[\phi^{(j+1/2)}_{g,0} - \phi^{(j)}_{g,0}\right]$
              $-\frac{3}{5}\frac{d}{dx}\left(\frac{1}{\sigma^A_{R,g}} \frac{dH^{(j+1/2)}}{dx}\right) + \sigma^A_{R,g} H^{(j+1/2)} + \frac{1}{3}\frac{d}{dx}\left(\frac{\sigma_{g,S,0}}{\sigma^A_{R,g}} F^{(j+1/2)}\right)$
              $= -\frac{1}{3}\frac{d}{dx}\left[\frac{\sigma_{g,S,0}}{\sigma^A_{R,g}}\left(\phi^{(j+1/2)}_{g,0} - \phi^{(j)}_{g,0}\right)\right]$
          (b) Update scalar flux with scalar component of error
              $\phi^{(j+1)}_{g,0}(x) = \phi^{(j+1/2)}_{g,0} + F^{(j+1/2)}(x)$
Step B-8  Update elastic scattering source
          $Q^{S(j+1)}_{g} = \sigma_{s,0,g}\phi^{(j+1)}_{g,0} + \sum_{l=1}^{L}(2l+1)P_l(\mu_n)\sigma_{s,l,g}\phi^{(j+1/2)}_{g,l}$
Step B-9  Check for convergence on scattering source
          a  If convergence criteria satisfied, proceed to next energy group
          b  If convergence criteria is NOT satisfied, return to Step B-0
```

formulas presented in Chapter 6 (see pg. 90). This calculation is made at the end of the upscatter loop following **Step B-4** in Table 7.3. Figure 7.3 presents the spectral radius as a function of iteration number for groups 1, 2, 39 and 40. The results depicted clearly indicate that the upscatter iterations are effectively accelerated and the spectral radius is bounded from above by the theoretical value of 0.20.

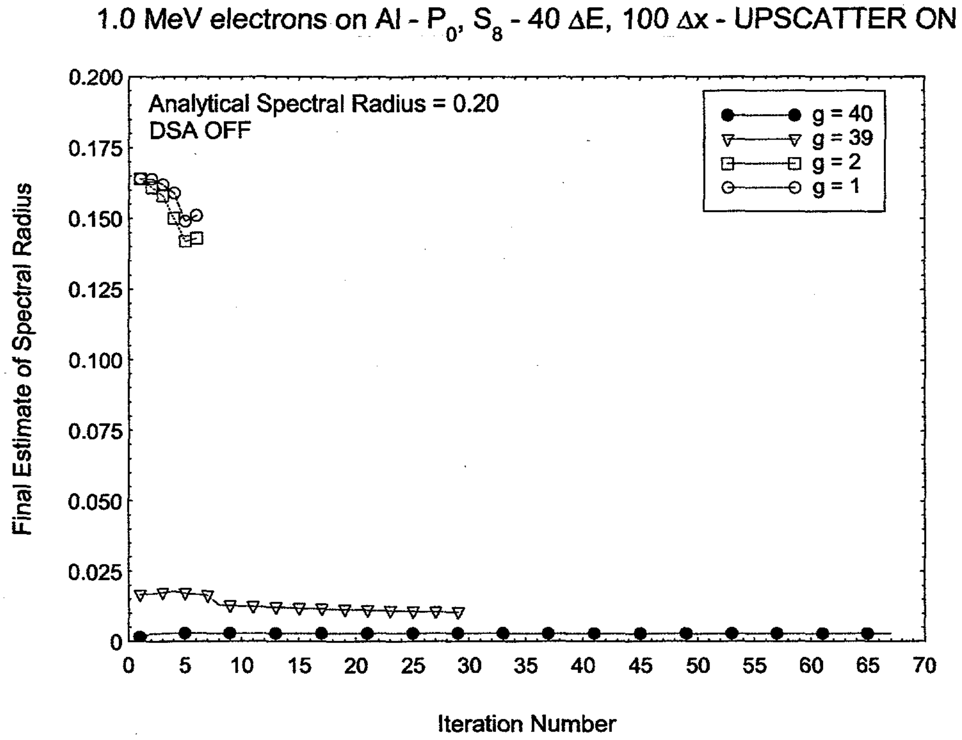

Figure 7.3: Estimated Upscatter Acceleration Spectral Radius - Algorithm B

7.3 Optimum Algorithm

The spectral radius estimate for DSA in Section 7.2.1 is made with the upscatter acceleration turned off. Likewise, the estimates for the upscatter spectral radius in Section 7.2.2 are calculated with the DSA turned off. To achieve the fastest rate of convergence both acceleration schemes should be utilized. In Table 7.4 the total CPU times to reach a solution on a 550 MHz PC are given for Algorithm A and B for four different combinations of acceleration: **(1)** Upscatter Acceleration OFF and DSA OFF, **(2)** Upscatter Acceleration ON and DSA OFF, **(3)** Upscatter Acceleration ON and DSA ON and **(4)** Upscatter Acceleration OFF and DSA ON. From this table Algorithm B seems to be more efficient for this problem, but the overall CPU times for both algorithms are comparable when both acceleration schemes are activated.

Table 7.4: Total CPU Time to Reach Converged Solution

Algorithm A: Converge on Scattering Source **CPU Time in seconds**			
Upscatter Acceleration \ Source Acceleration			
OFF\ OFF	ON\ OFF	ON\ ON	OFF\ ON
411.10	22.60	14.51	237.04

Algorithm B: Converge on Slope Flux **CPU Time in seconds**			
Upscatter Acceleration \ Source Acceleration			
OFF\ OFF	ON\ OFF	ON\ ON	OFF\ ON
236.30	16.88	12.18	141.11

To achieve an accurate solution, it is not necessary to fully converge on either the scattering source or the slope flux holding the other value constant. A solution can be obtained by performing a few source iterations followed by a few upscatter iterations for each inner iteration. A number of experiments were performed in which the number of source and upscatter iterations for each inner iteration were varied and CPU times compared. The final algorithm was chosen based on this optimization and performs two source iterations followed by two upscatter iterations per inner iteration (see Table 7.6). Table 7.5 presents the total CPU time to reach a solution on a 550 MHz PC implementing this optimum algorithm for the four different acceleration scenarios described above. The table indicates that this algorithm is much more efficient than the previous two algorithms and converges to a solution rapidly; given the small spectral radii, this is not surprising. With both DSA and upscatter on, it converges in 5.65 seconds while Algorithm A and B converged in 14.51 and 12.18 seconds, respectively.

Table 7.5: Optimum Algorithm - CPU Time to Reach Convergence Solution

Optimum Algorithm **CPU Time in seconds**			
Upscatter Acceleration \ Source Acceleration			
OFF\ OFF	ON\ OFF	ON\ ON	OFF\ ON
10.75	6.37	5.65	11.27

Figure 7.4 depicts the converged dose profiles for 1.0 MeV electrons incident on Al with isotropic scattering and S_8 for all three algorithms presented in this chapter. Since this is an electron beam problem and the B-CSD equation is not adequate for

modeling these types of problems a ONEBFP solution is not provided for comparison. The results depicted in Figure 7.4 are provided to demonstrate that all three algorithms yield the same results.

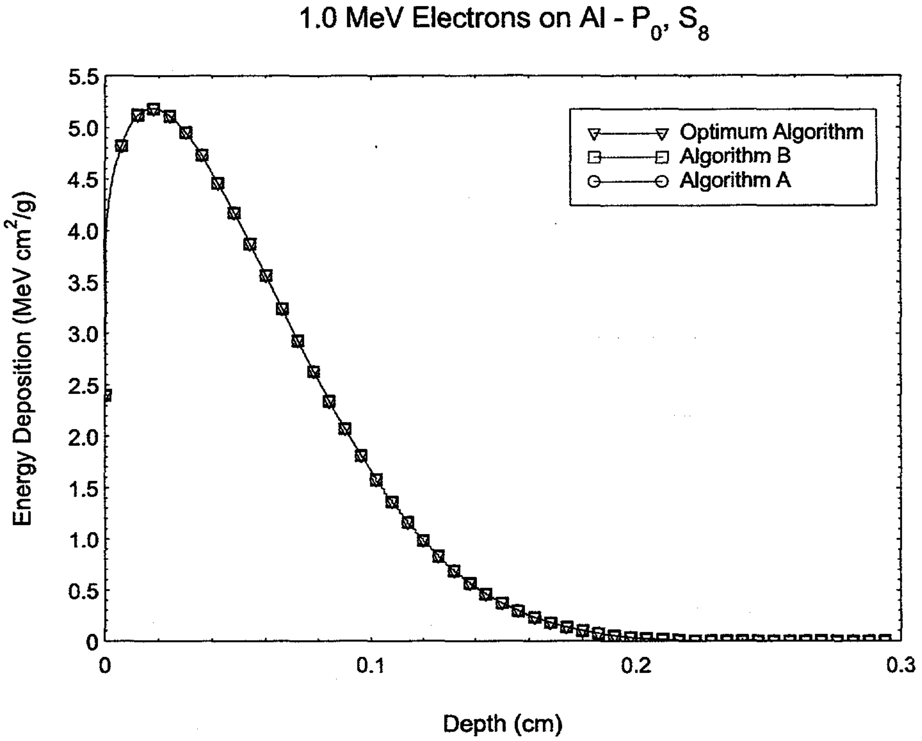

Figure 7.4: Converged Dose Profiles from Evaluated Algorithms

In the next chapter, the LD SAAF equation is applied to coupled charged-particle problems to demonstrate its applicability. The final optimized algorithm presented in Table 7.6 is used to obtain solutions for these problems. Solutions obtained from the LD SAAF equation will be compared with ONEBFP to verify accuracy.

Table 7.6: LD SAAF Optimum Algorithm

Step C.0 Increment "inner" iteration index, $j = j + 1$ reset $\ell = 0$ and $\kappa = 0$

Step C.1 Increment scattering source iteration index, $\ell = \ell + 1$

Step C.2 Solve for $\Psi^{A}_{n,g,k\pm1/2}$ at the $(\ell + 1/2)$ iterate

$$-\mu_n^2 \frac{d}{dx}\left(\frac{1}{\sigma^A_{R,g}}\frac{d\Psi^{A(\ell+1/2)}_{n,g}}{dx}\right) + \sigma^A_{R,g}\Psi^{A(\ell+1/2)}_{n,g} = Q^{S(\ell)}_{n,g} - \mu_n \frac{d}{dx}\left(\frac{1}{\sigma^A_{R,g}} Q^{S(\ell)}_{n,g}\right)$$
$$+\frac{S_g}{\Delta E_g}\Psi^{E(j)}_{n,g} - \mu \frac{d}{dx}\left(\frac{1}{\sigma^A_{R,g}}\frac{S_g}{\Delta E_g}\Psi^{E(j)}_{n,g}\right) + q^A_{n,g}$$

Step C.3 Update flux moments

$$\phi^{(\ell+1/2)}_{g,l} = \frac{1}{2}\sum_{n=1}^{N} P_l(\mu_n) w_n \Psi^{A(\ell+1/2)}_{n,g}$$

Step C.4 If source acceleration turned on, then

(a) Solve for scalar and current part of error

$$-\frac{1}{3}\frac{d}{dx}\left(\frac{1}{\sigma^A_{R,g}}\frac{dF^{(\ell+1/2)}}{dx}\right) + \left(\sigma^A_{R,g} - \sigma_{g,S,0}\right) F^{(\ell+1/2)} = \sigma_{g,S,0}\left[\phi^{(\ell+1/2)}_{g,0} - \phi^{(\ell)}_{g,0}\right]$$
$$-\frac{3}{5}\frac{d}{dx}\left(\frac{1}{\sigma^A_{R,g}}\frac{dH^{(\ell+1/2)}}{dx}\right) + \sigma^A_{R,g} H^{(\ell+1/2)} + \frac{1}{3}\frac{d}{dx}\left(\frac{\sigma_{g,S,0}}{\sigma^A_{R,g}} F^{(\ell+1/2)}\right)$$
$$= -\frac{1}{3}\frac{d}{dx}\left[\frac{\sigma_{g,S,0}}{\sigma^A_{R,g}}\left(\phi^{(\ell+1/2)}_{g,0} - \phi^{(\ell)}_{g,0}\right)\right]$$

(b) Update scalar flux with scalar component of error

$$\phi^{(\ell+1)}_{g,0}(x) = \phi^{(\ell+1/2)}_{g,0} + F^{(\ell+1/2)}(x)$$

Step C.5 Update elastic scattering source

$$Q^{S(\ell+1)}_{g} = \sigma_{s,0,g}\phi^{(\ell+1)}_{g,0} + \sum_{l=1}^{L}(2l+1)P_l(\mu_n)\sigma_{s,l,g}\phi^{(\ell+1/2)}_{g,l}$$

Step C.6 Check to see if reached limit on number of scattering source iterations

a If ℓ is equal to the limit of scattering source iterations proceed to **Step C.7**

b If ℓ is NOT equal to the limit of scattering source iterations proceed to **Step C.1**

Step C.7 Increment upscatter iteration index, $\kappa = \kappa + 1$

Step C.8 If $\kappa > 1$ solve for $\Psi^{E}_{n,g,k\pm1/2}$ at the $\kappa + 1/2$ iterate using most recent estimate of $\Psi^{A}_{n,g,k\pm1/2}$

Step C.9 Solve for $\Psi^{E}_{n,g,k\pm1/2}$ at the $\kappa + 1/2$ iterate

$$-\mu_n^2 \frac{d}{dx}\left(\frac{1}{\sigma^E_{R,g}}\frac{d\Psi^{E(\kappa+1/2)}_{n,g}}{dx}\right) + \sigma^E_{R,g}\Psi^{E(\kappa+1/2)}_{n,g} = -3\frac{S_g}{\Delta E_g}\Psi^{A(\ell+1/2)}_{n,g}$$
$$+\mu_n \frac{\partial}{\partial x}\left(\frac{1}{\sigma^E_{R,g}} 3\frac{S_g}{\Delta E_g}\Psi^{A(\ell+1/2)}_{n,g}\right) + q^E_{n,g}$$

Step C.10 If upscatter acceleration is turned on, then

(a) Solve for slope flux residual

$$\mathcal{R}^{(\kappa+1/2)}_{n,g} = \frac{S_g}{\Delta E_g}\left[\Psi^{E(\kappa+1/2)}_{n,g} - \Psi^{E(\kappa)}_{n,g}\right] - \mu_n \frac{d}{dx}\left(\frac{1}{\sigma^A_{R,g}}\frac{S_g}{\Delta E_g}\left[\Psi^{E(\kappa+1/2)}_{n,g} - \Psi^{E(\kappa)}_{n,g}\right]\right)$$

(b) Solve for average flux error estimate

$$-\mu_n^2 \frac{d}{dx}\left(\frac{1}{\sigma^A_{R,g}}\frac{df^{A(\kappa+1/2)}_{n,g}}{dx}\right) - \mu_n \frac{d}{dx}\left(3\frac{S_g^2}{\sigma^A_{R,g}\sigma^E_{R,g}} f^{A(\kappa+1/2)}_{n,g}\right) + \left(\sigma^A_{R,g} + 3\frac{S_g^2}{\sigma^E_{R,g}}\right) f^{A(\kappa+1/2)}_{n,g}$$
$$= \mathcal{R}^{(\kappa+1/2)}_{n,g}$$

(c) Solve for slope flux error estimate

$$f^{E(\kappa+1/2)}_{n,g} = \frac{1}{\sigma^E_{R,g}}\left\{-3\frac{S_g}{\Delta E_g} f^{A(\kappa+1/2)}_{n,g}\right\}$$

(d) Update the slope angular flux with the error estimates

$$\Psi^{E(\kappa+1)}_{n,g} = \Psi^{E(\kappa+1/2)}_{n,g} + f^{E(\kappa+1/2)}_{n,g}$$

Step C.11 Check to see if reached limit on number of upscatter iterations

a If κ is equal to the limit of scattering source iterations proceed to **Step C.12**

b If κ is NOT equal to the limit of scattering source iterations return to **Step C.7**

Step C.12 Check for convergence using L_2 error norm on $\Psi_{n,g+1/2,k}$

a If convergence criteria satisfied, proceed to next energy group

b If convergence criteria NOT satisfied, return to **Step C.0**

---

8 Application to Coupled Electron-Photon Problems

The numerical solution of the LD SAAF transport equation was implemented in the computer code DOET$_{1D}$: Discrete Ordinates Electron-Photon Transport in 1D. In this chapter DOET$_{1D}$ is used to solve a few coupled electron-photon problems to demonstrate its applicability. The primary interest of this research is determining whether or not the LD SAAF equation can accurately solve coupled electron-photon problems. The problems considered herein consist of a photon source incident on a slab that is either multilayered or composed of a single material. To demonstrate the accuracy of DOET$_{1D}$, results are compared with ONEBFP solutions. ONEBFP is a one-dimensional, discrete ordinates, multi-group code that solves the first-order Boltzmann Fokker-Planck transport equation utilizing linear nodal discretization in space and energy.[14] Throughout this chapter DOET$_{1D}$ or LD SAAF will be used when referring to the code developed in the course of this research.

Comparisons between ONEBFP and DOET$_{1D}$ will be made looking at the energy deposition and charge deposition profiles as well as the spatially integrated energy and charge deposition. Emitted currents at the physical boundaries and material interfaces will also be evaluated. Before discussing the application of DOET$_{1D}$ to coupled charged particle problems the formulas used to calculate the quantities of interest are presented.

The energy deposition in a spatial cell, k, is calculated in DOET$_{1D}$ as follows:

$$D_k = \sum_{g=1}^{G} \Delta E_g \, \sigma_{g,k}^{Edep} \, \phi_{g,k} + E_{G+1/2} S_{G,k} \phi_{G+1/2,k} \tag{8.1}$$

where $\sigma_{g,k}^{Edep}$ is the energy deposition cross-section (MeV/cm); $\phi_{g,k}$ is the scalar flux; $S_{G,k}$ is the restricted stopping power at the cutoff energy and $\phi_{G+1/2,k}$ is the scalar flux at the cutoff energy. The energy deposition cross-section from CEPXS includes the energy deposited through interactions as well as due to scattering below the cutoff energy.[24] The total energy deposited across a slab in MeV is defined as:

$$E_{total} = \sum_{k=1}^{K} \Delta x_k \, D_k \tag{8.2}$$

Charge deposition in e^-/cm is calculated in a spatial cell k by folding the charge deposition cross-section with the scalar flux and including the leakage below the energy cutoff

$$C_k = \sum_{g=1}^{G} \Delta E_g \, \sigma_{g,k}^{qdep} \, \phi_{g,k} + S_{G,k} \phi_{G+1/2,k} \tag{8.3}$$

The charge deposition cross-section, $\sigma_{g,k}^{qdep}$, is the net number of electrons deposited in the medium due to interactions of the particles. A positive charge deposition cross section corresponds to electron deposition, while a negative charge deposition cross-section corresponds to electron removal.[24] The integrated particle deposition (total number of e^-) is calculated by

$$Q_{total} = \sum_{k=1}^{K} \Delta x_k C_k \tag{8.4}$$

The forward and reverse currents for a given particle type are determined from:

$$J_F(x) = \frac{1}{2}\int_0^\infty \int_0^1 d\mu\, \mu\, \Psi(x,E,\mu) \simeq \sum_{g=1}^{G} \Delta E_g \frac{1}{2} \sum_{n=1}^{N/2} w_n\, \mu_n\, \Psi_{n,g,k} \tag{8.5}$$

$$J_R(x) = \frac{1}{2}\int_0^\infty \int_{-1}^0 d\mu\, \mu\, \Psi(x,E,\mu) \simeq \sum_{g=1}^{G} \Delta E_g \frac{1}{2} \sum_{n=N/2+1}^{N} w_n\, |\mu_n|\, \Psi_{n,g,k} \tag{8.6}$$

$$J_N(x) = J_F(x) - J_R(x) \tag{8.7}$$

where G in the equations above is the number of groups for the particle type of interest (e.g. γ or e^-).

A logarithmic spatial mesh is available in DOET$_{1D}$ which enables very fine spatial meshes at the boundaries and material interfaces. The minimum spatial cell width is determined as a fraction of the minimum electron range, R_{min} for a given material:

$$\Delta x_{min} = \xi \cdot R_{min}$$

where the default value of ξ is 0.25. A preprocessor code was written to write ONEBFP input files using the same spatial discretization as DOET$_{1D}$ to ensure comparisons are made between the exact same spatial discretizations.

The four problems presented in this chapter are aimed at demonstrating the successful application of the LD SAAF transport equation to coupled electron-photon problems. Two of the problems are for a photon source incident on a single layer of material, one is a high-Z material while the other is a low-Z material. Multilayer slabs are then looked at to evaluate the performance of the LD SAAF solution at material interfaces between high-Z and low-Z materials. All problems incorporate partially-coupled physics, that is $\gamma \rightarrow e^-$ but $e^- \nrightarrow \gamma$. The convergence criteria is set to 1×10^{-6} for all problems. Cross-sections are generated using CEPXS[9] and both codes utilize the same binary cross-section library, *bxslib*, for a given problem.

8.1 High Energy Photons Incident on Tungsten

The first problem presented is for high energy photons incident on a slab of high-Z material. Specifically, this problem consists of 6.0 MeV photons incident on a 4.0 cm thick slab of tungsten (Z=74, ρ=19.3 g/cm^3). The minimum cutoff energy is set equal to 25 keV. The energy discretization consisted of 30 linear groups for the photons, and initially, 50 logarithmic energy groups for the electrons. The Legendre scattering order is P_7 with S_8 angular quadrature. Positrons are ignored despite the incident photon energy being above the pair production threshold energy. The energy and charge deposition profiles are evaluated for a linear spatial discretization scheme as well as a logarithmic spatial mesh.

Initially the W slab was discretized into equal sized spatial cells corresponding to Δx values of 0.08 cm, 0.04 cm, and 0.02 cm. The energy deposition profiles for these discretization schemes are shown in Figure 8.1 along with the profile obtained from ONEBFP. This figure reveals that the DOET$_{1D}$ solution depends on the spatial mesh and appears to be converged for Δx = 0.02 cm. The energy deposition profile for the finest spatial mesh matches up quite well with the ONEBFP solution at the left boundary but slightly overestimates the profile until a depth of $\approx$ 1 cm. This can be quantified by considering the integrated energy deposition across the slab. ONEBFP yields an integrated energy deposition of 5.66 MeV while the LD SAAF with Δx = 0.02 cm deposits a total of 5.85 MeV in the W ($\approx$ 3% high). The most likely explanation for the excess energy deposition from DOET$_{1D}$ is that the energy mesh is not refined enough to accurately solve the CSD term. Since ONEBFP implements a fourth order linear nodal discretization in energy and space, it should not be as dependent on the energy mesh structure as the LD, LC in space discretization used in DOET$_{1D}$ is likely to be. The effects of refining the energy mesh on the energy deposition will be evaluated shortly.

Charge deposition profiles for these three spatial cell sizes are depicted in Figure 8.2. The charge deposition profile for this problem is flat across most of the slab; therefore, this figure focuses on the charge deposition in the first cm of the slab. The profiles depicted in Figure 8.2 reveal that adequately resolving the charge deposition profile requires a finer spatial mesh than the energy deposition profile. To enable a finer spatial mesh without using a prohibitively large number of cells a logarithmic mesh is used.

Although the energy deposition profiles do not demonstrate the same spatial dependence as the charge deposition profiles we present them for completeness. Figure 8.3 presents the energy deposition profiles from both ONEBFP and DOET$_{1D}$ for the logarithmic spatial mesh. As expected, using a logarithmic spatial mesh does not improve the energy deposition profile.

The charge deposition profiles obtained for the logarithmic spatial mesh are shown in Figure 8.4. This figure illustrates how powerful using a logarithmic spatial mesh is in accurately calculating charge deposition. The LD SAAF and ONEBFP solutions are almost indistinguishable except at the left boundary. The 6.0 MeV photons deposit a total of $-7.92 \times 10^{-3}\ e^-$ in the W slab according to ONEBFP, while the total from DOET$_{1D}$ is $-8.28 \times 10^{-3}\ e^-$. As expected the charge deposition does not depend on the energy mesh.

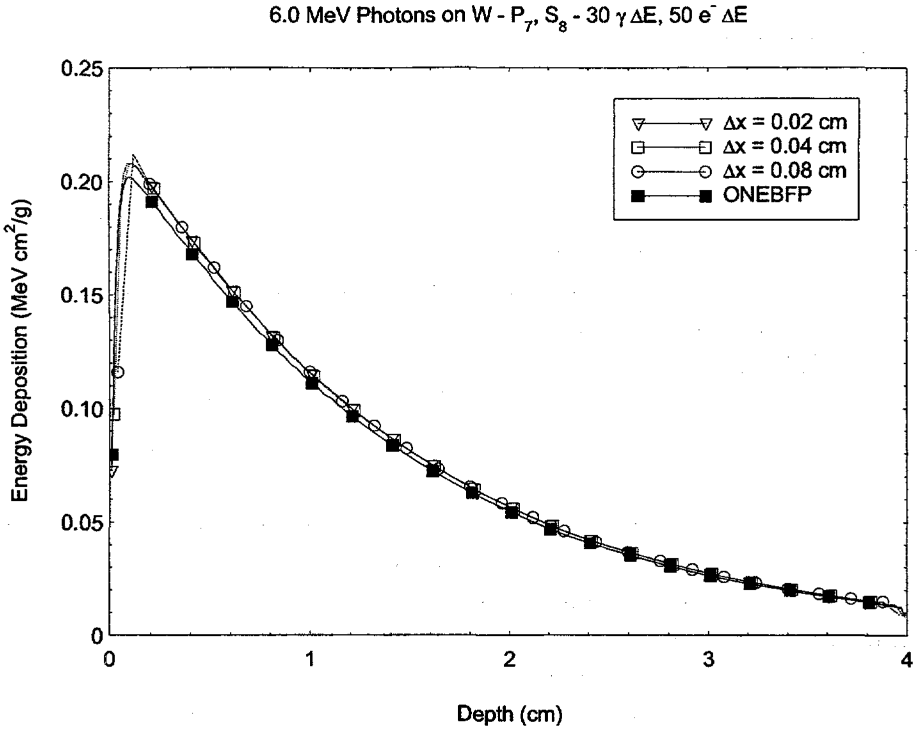

Figure 8.1: Energy Deposition: 6.0 MeV Photons on W - Constant Δx

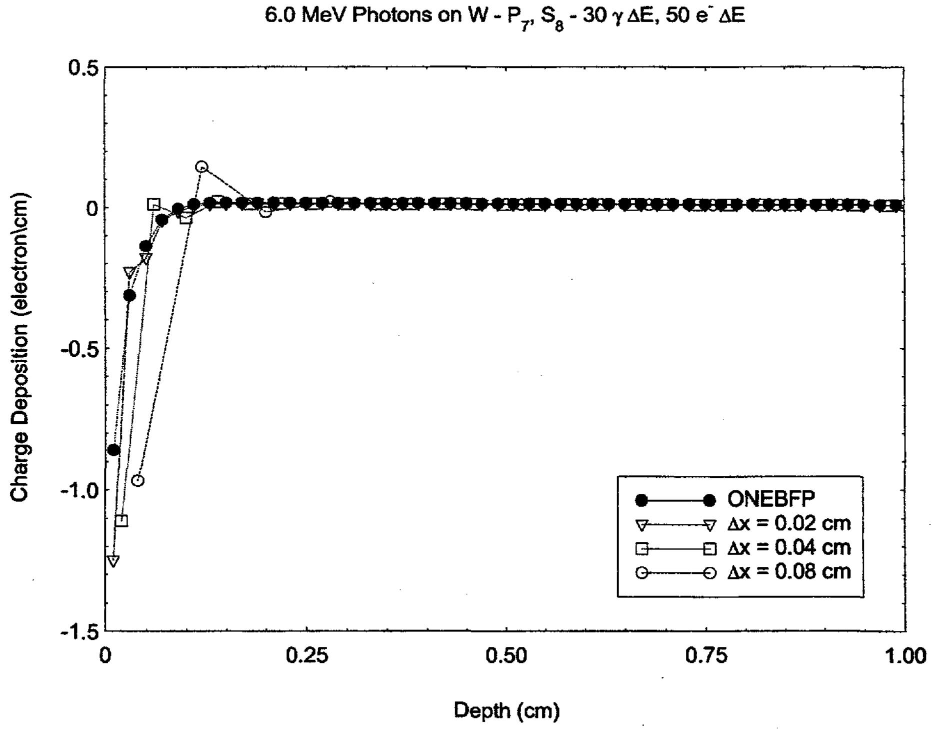

Figure 8.2: Charge Deposition: 6.0 MeV Photons on W - Constant Δx

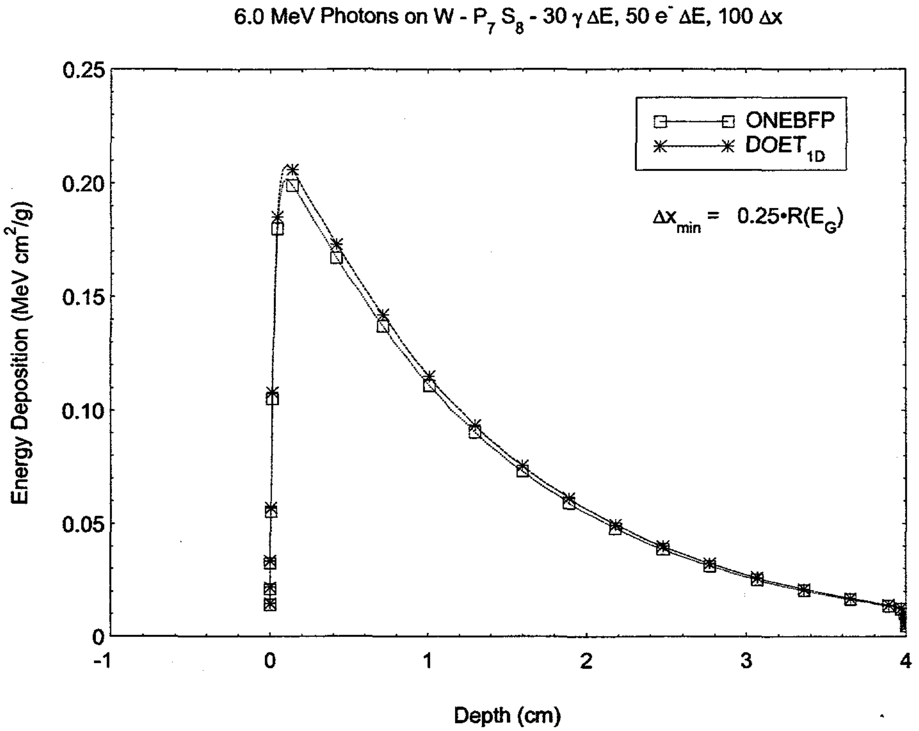

Figure 8.3: Energy Deposition: 6.0 MeV Photons on W - Log Δx

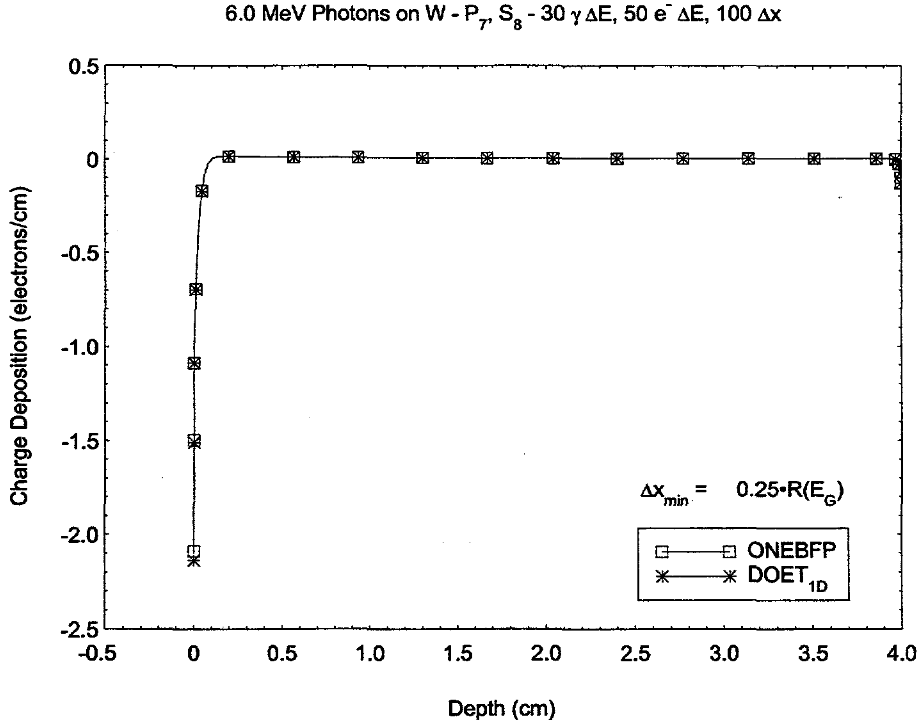

Figure 8.4: Charge Deposition for 6.0 MeV Photons on W: Log Δ x

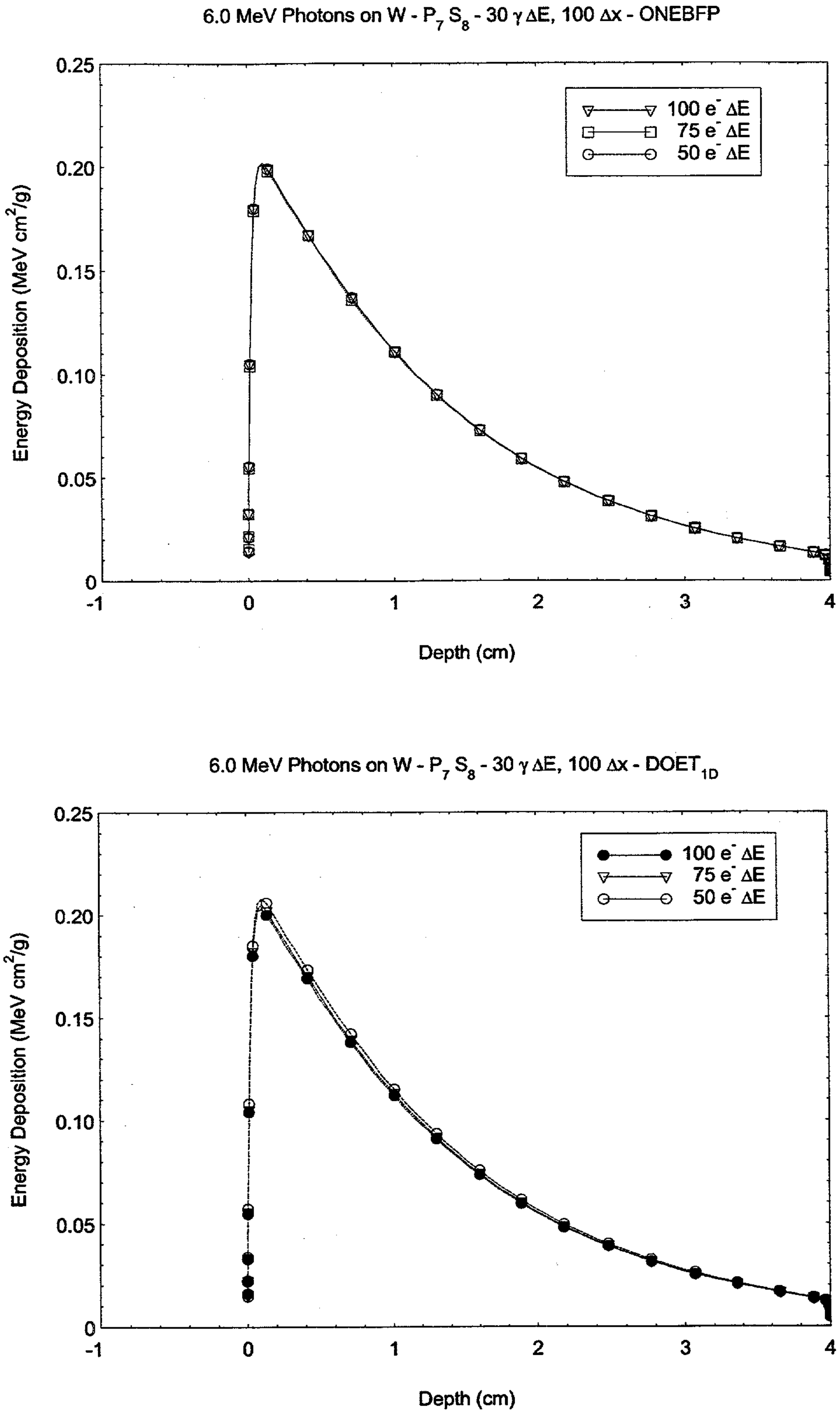

Figure 8.5: Energy Deposition as Function of Energy Mesh Size

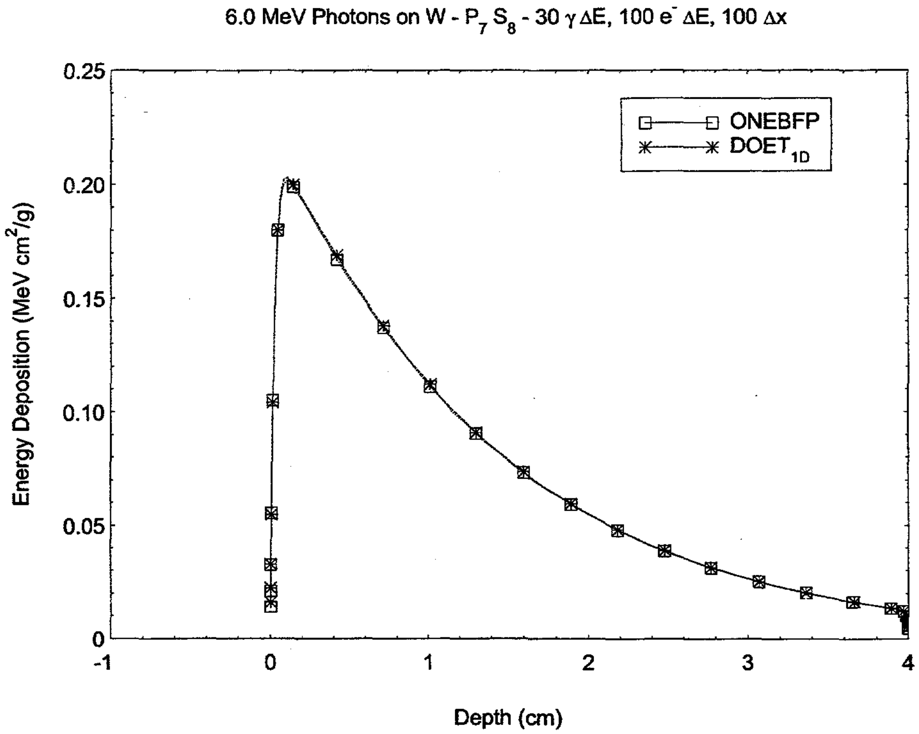

Figure 8.6: Converged Energy Deposition Profile for 6.0 MeV Photons on W

Since refining the spatial mesh had no effect on the energy deposition from the LD SAAF equation, the next step is to evaluate whether or not refining the energy mesh improves their accuracy. Figure 8.5 presents the energy deposition profiles from ONEBFP and DOET$_{1D}$ as the number of electron energy groups is refined from 50 to 100. Predictably, the ONEBFP profile does not change as the number of electron energy groups is increased. However, the DOET$_{1D}$ energy deposition profile does not appear to be converged until 100 electron energy groups are used. Figure 8.6 depicts the converged dose profiles and shows that the LD SAAF solution is almost indistinct from the ONEBFP solution. The total energy deposited from ONEBFP is 5.62 MeV while the LD SAAF equation deposits 5.70 MeV in the W ($\approx$ 1.5% high).

The aforementioned results indicate the LD SAAF equation can accurately solve coupled electron-photon problems involving high energy γ's on high-Z materials. However, to obtain accurate results the energy mesh and the spatial mesh must be refined adequately to yield accurate energy and charge deposition profiles. This is a disadvantage over ONEBFP which quickly converges in energy and space as expected since it uses higher order discretizations. Finer energy group structures are more costly in terms of computation time simply because the code must perform more work.

8.2 Low Energy Photons Incident on Silicon

Now consider 100 keV γ incident on a 0.01 cm thick slab of Si (Z=14, ρ=2.33 g/cm^3). The slab thickness is approximately one electron range thick. The energy discretization used is 40 γ energy groups while the number of e^- groups is increased from 40 to 80. A logarithmic spatial mesh is used. The order of Legendre scattering is P_7 with a quadrature order of S_8.

The energy deposition as a function of the number of e^- energy groups is presented in Figure 8.7. This figure clearly indicates that the ONEBFP solution quickly converges in energy while the DOET$_{1D}$ solution requires 80 e^- energy groups to reach a converged profile. The converged energy deposition profile is presented in Figure 8.8 and shows that the converged LD SAAF profile is practically indistinguishable from the ONEBFP solution. The total energy deposited by ONEBFP in the Si is 97.1 eV and 97.5 eV from DOET$_{1D}$, respectively.

Figure 8.9 depicts the charge deposition profiles for 100 keV γ incident on Si. The DOET$_{1D}$ solution matches the ONEBFP solution well with slight discrepancies at the left boundary of the slab. It is possible that refining the spatial mesh further could resolve the discrepancy at the boundary better but will most likely not make a difference in the integrated charge deposition. The total number of electrons removed from the Si in the ONEBFP solution is 2.01×10^{-4} e^- while DOET$_{1D}$ results in 2.08×10^{-4} e^- being removed form the Si. Charge balance is confirmed using the exiting electron currents at the slab boundaries presented in Table 8.1. The net number of electrons deposited is determined by $J_{x_L}^N - J_{x_R}^N$.

Table 8.1: Exiting Electron Currents from Silicon

	$J_{x_L}^N$	$J_{x_R}^N$	e^- Deposited
ONEBFP	-4.32×10^{-5}	1.57×10^{-4}	-2.00×10^{-4}
DOET$_{1D}$	-4.60×10^{-5}	1.62×10^{-4}	-2.08×10^{-4}

The results for this problem do not introduce any surprises into the accuracy of applying the LD SAAF equation to coupled electron-photon problems. Obviously, the converged DOET$_{1D}$ solution is accurate for single material slabs. However, true insight into the applicability of the LD SAAF solution to coupled electron-photon problems will not be gained until we evaluate how it performs for multilayer slabs at material interfaces between high-Z and low-Z materials. It is well-known that accurate solutions at material interfaces for coupled electron-photon problems typically require higher order discretization schemes.

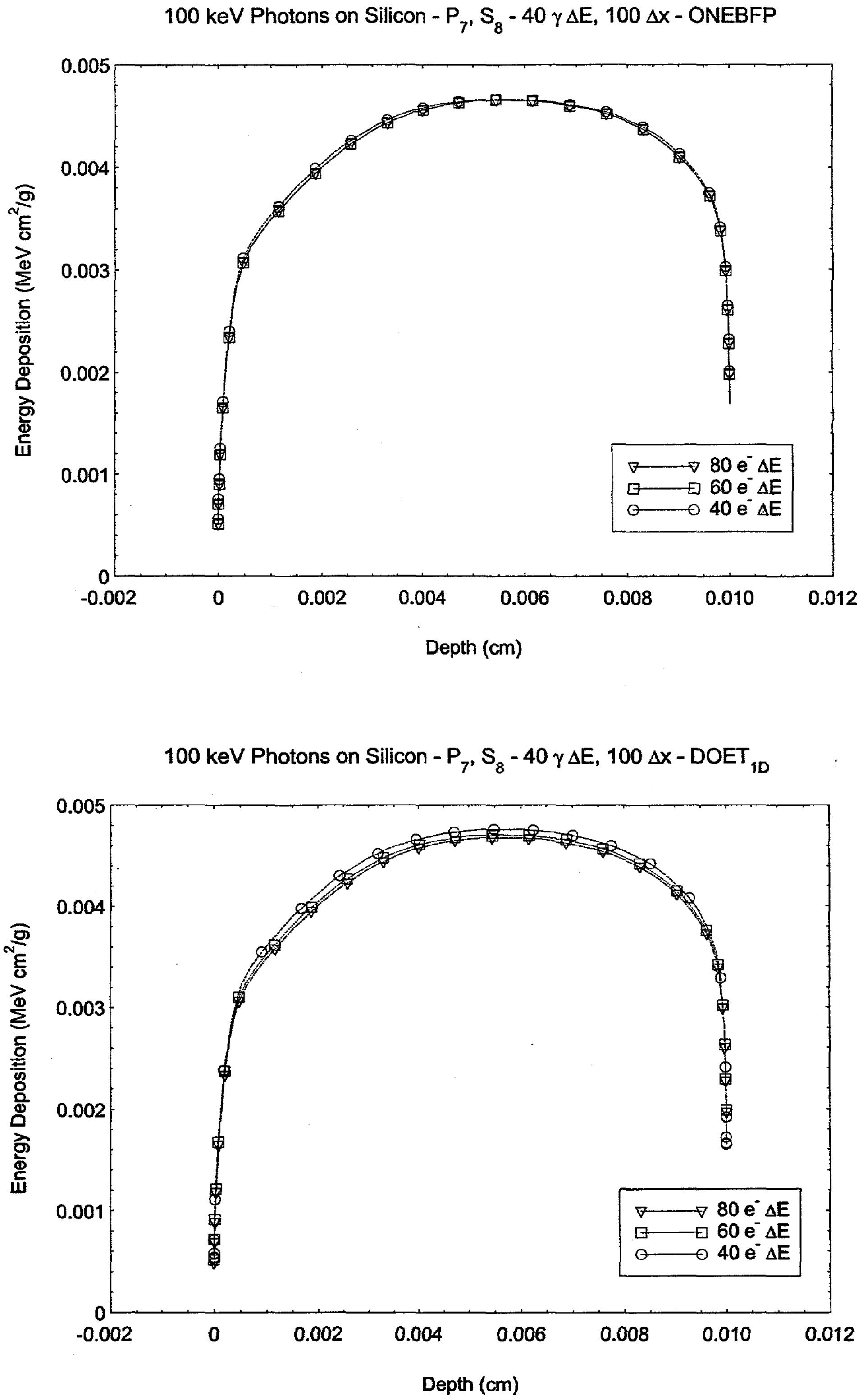

Figure 8.7: 100 keV γ on Si Energy Deposition as Function of Energy Mesh Size

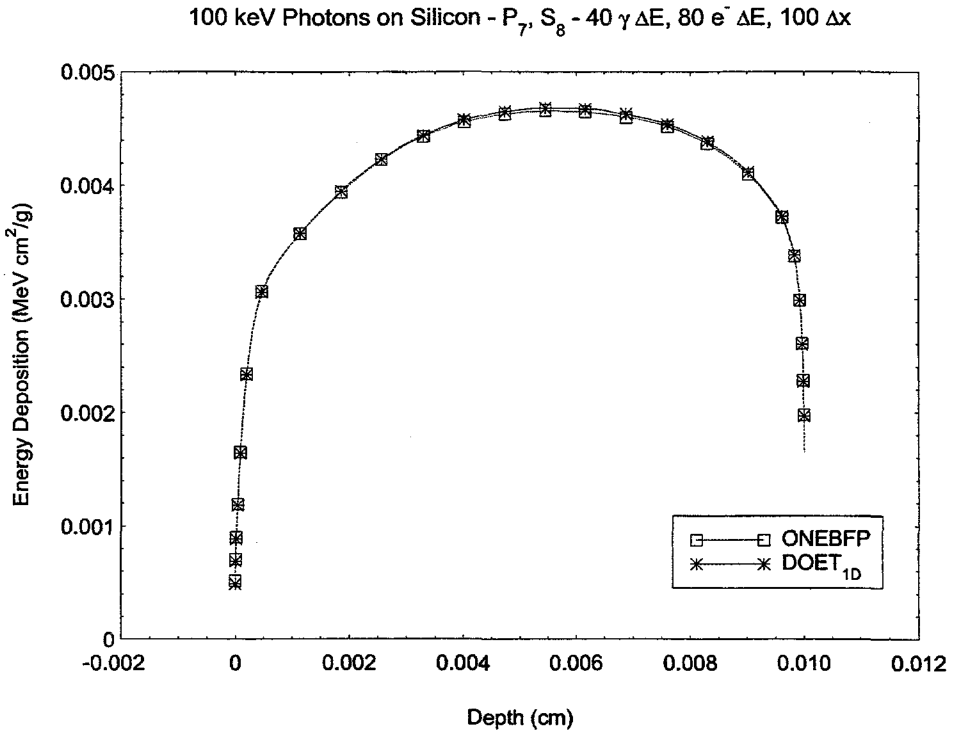

Figure 8.8: Converged Energy Deposition Profile for 100 keV γ on Si

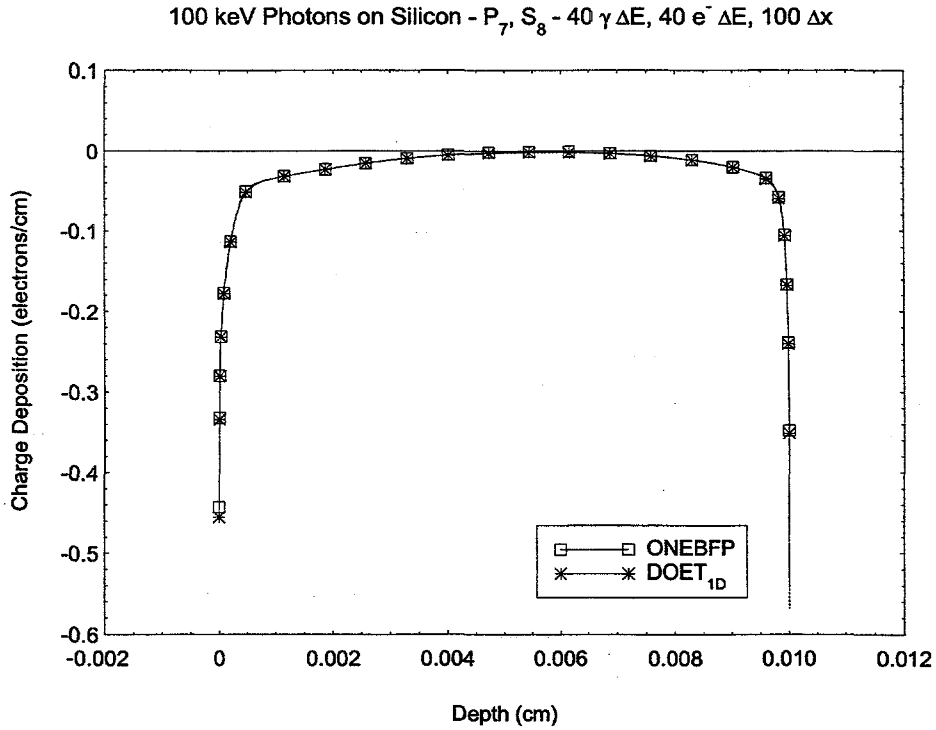

Figure 8.9: Charge Deposition Profile for 100 keV γ on Si

8.3 100 keV γ Incident on a Gold\Silicon Slab

In this problem 100 keV photons are incident on a slab made up of 0.001 cm of Gold (Z=79) and 0.001 cm of Silicon (Z=14). The cutoff energy is set to 1 keV and 40 energy groups are used for γ while the number of e^- energy groups is 80. We know from previous examples that this should be fine enough that DOET$_{1D}$ energy deposition will be converged. A Legendre scattering expansion of P$_7$ is used along with a quadrature order of S$_8$.

Initially, the focus is on the charge deposition profile in Au\Si slab because it is expected to be difficult to reach an adequate solution with the LC spatial discretization used in DOET$_{1D}$. Initially the logarithmic spatial mesh used has a minimum $\Delta x_{min} = 0.25 \cdot R_{min}$. The charge profile for this spatial mesh is presented in Figure 8.10. It is evident from this profile that this spatial mesh is not adequate for the LD SAAF to accurately determine the charge deposition at the material interface. In Figures 8.11 to 8.13 the minimum logarithmic spatial mesh cell at the material boundaries is refined from $\Delta x_{min} = 0.05 \cdot R_{min}$ to $\Delta x_{min} = 0.001 \cdot R_{min}$. The ONEBFP charge profile converges to a solution rather quickly, while the LD SAAF solution does not converge until the minimum logarithmic spatial cell at the material boundaries is set to $0.001 \cdot R_{min}$ (see Figure 8.13). While this spatial cell size may seem to be excessively small at the material boundaries it does not cost much in terms of iterations to converge ($\approx$ 2.5% more) or CPU time ($\approx$ 12 seconds more) considering the improvement in accuracy.

The total charge deposition in each material is summarized in Table 8.2 for the various logarithmic spatial meshes evaluated. This table indicates that ONEBFP is converged when $\Delta x_{min} = 0.25 \cdot R_{min}$ while DOET$_{1D}$ does not converge until $\Delta x_{min} = 0.001 \cdot R_{min}$. Table 8.3 presents the forward and reverse electron yields at the boundaries for this problem. These can be used to indicate whether or not charge is conserved in the respective codes. In Au, the charge conservation can be checked by calculating the value of $J^N(x = 0.0) - J^N(x = 0.001)$ which is -8.23×10^{-3} for DOET$_{1D}$ and -8.02×10^{-3} for ONEBFP. Since these values match up with the integrated charge depositions tabulated in Table 8.2 charge is conserved in the Au layer. Similarly, in the Si layer the charge balance is determined using $J^N(x = 0.001) - J^N(x = 0.002)$ yielding 1.99×10^{-3} and 1.97×10^{-3} for DOET$_{1D}$ and ONEBFP, respectively.

Figure 8.14 compares the converged energy deposition profiles from DOET$_{1D}$ and ONEBFP for the same spatial mesh as the converged charge deposition. This figure shows that DOET$_{1D}$ reaches an energy deposition profile that is slightly higher in the Au layer but fairly accurate in the Si layer. To quantify this difference the integrated energy deposition in each material layer are compared. ONEBFP deposits a total of 4.22 keV in the Au layer and 0.12 keV in the Si. On the other hand, DOET$_{1D}$ deposits a total of 4.27 keV in the Au layer and 0.122 keV in the Si layer which is 1.2% and 1.7% higher in the Au and Si layers than ONEBFP, respectively.

Table 8.2: Integrated Charge Deposition in Au and Si Layers

Total Charge Deposition in 10^{-3} electrons

	ONEBFP		DOET_{1D}	
Δx_{min}	Au	Si	Au	Si
$0.25 \cdot R_{min}$	-8.02	1.97	-8.44	1.59
$0.05 \cdot R_{min}$	-8.02	1.97	-8.29	1.87
$0.01 \cdot R_{min}$	-8.02	1.97	-8.24	1.96
$0.001 \cdot R_{min}$	-8.02	1.97	-8.23	1.98
$0.0001 \cdot R_{min}$	-8.02	1.97	-8.23	1.98

Table 8.3: Compton and Photo-Electron Yield at Material Interfaces

Yield in 10^{-3} electrons

Code	x = 0.0 cm Au→vacuum ($\mu < 0$)	x = 0.001 cm Au→Si ($\mu > 0$)	x = 0.001 cm Si→Au ($\mu < 0$)	x = 0.002 cm Si→vacuum ($\mu > 0$)
ONEBFP	3.84	6.06	1.78	2.29
DOET_{1D}	3.95	5.93	1.75	2.21

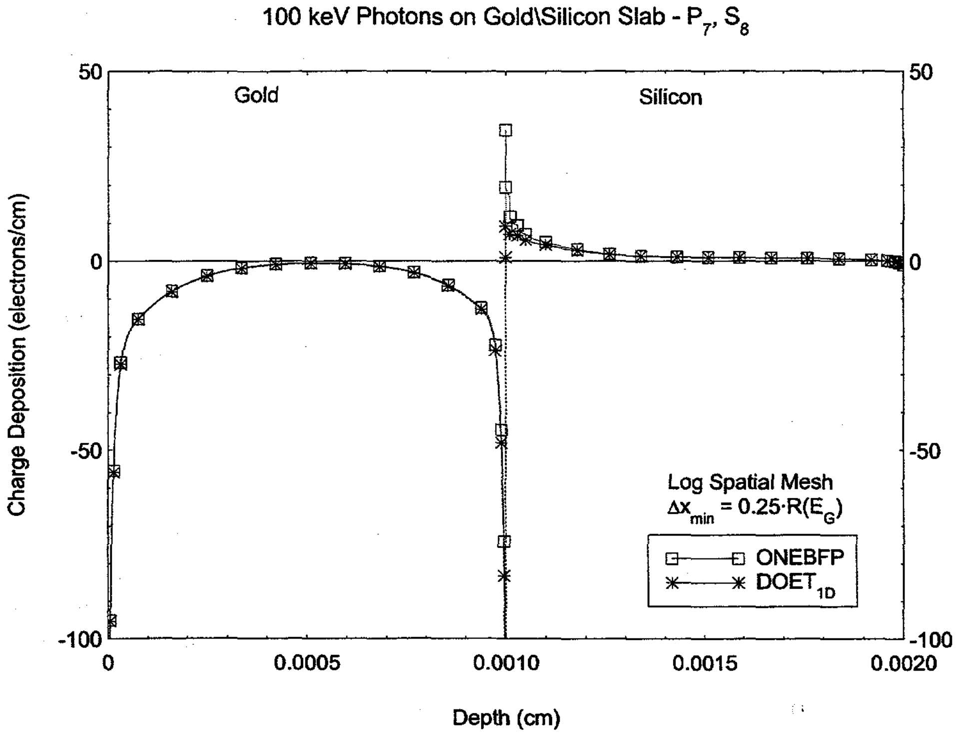

Figure 8.10: Charge Deposition in Au\Si for Log $\Delta x_{min} = 0.25 \cdot R_{min}$

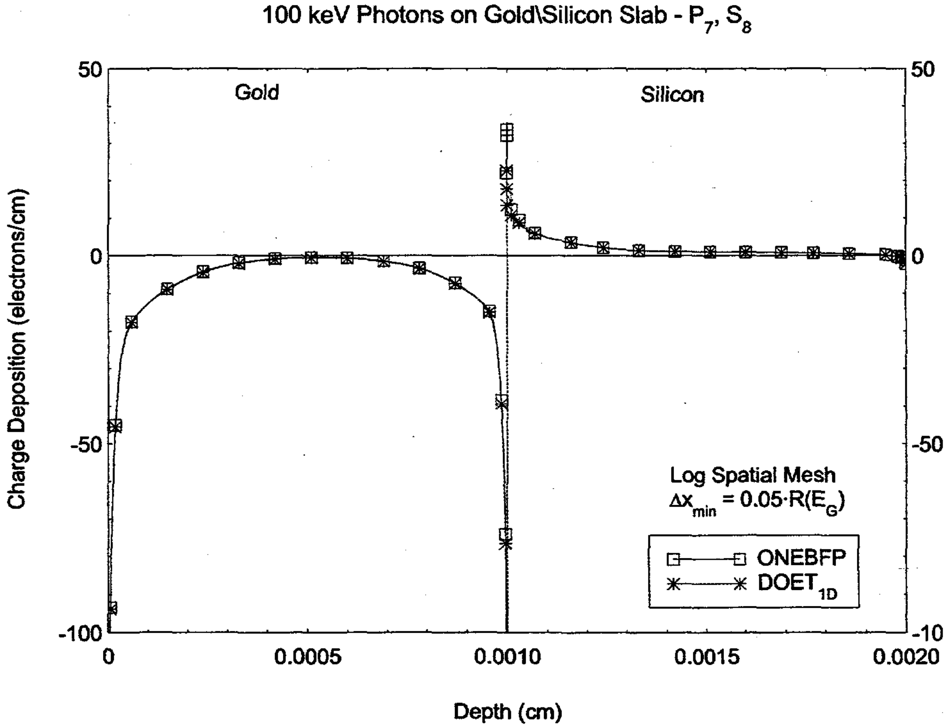

Figure 8.11: Charge Deposition in Au\Si for Log $\Delta x_{min} = 0.05 \cdot R_{min}$

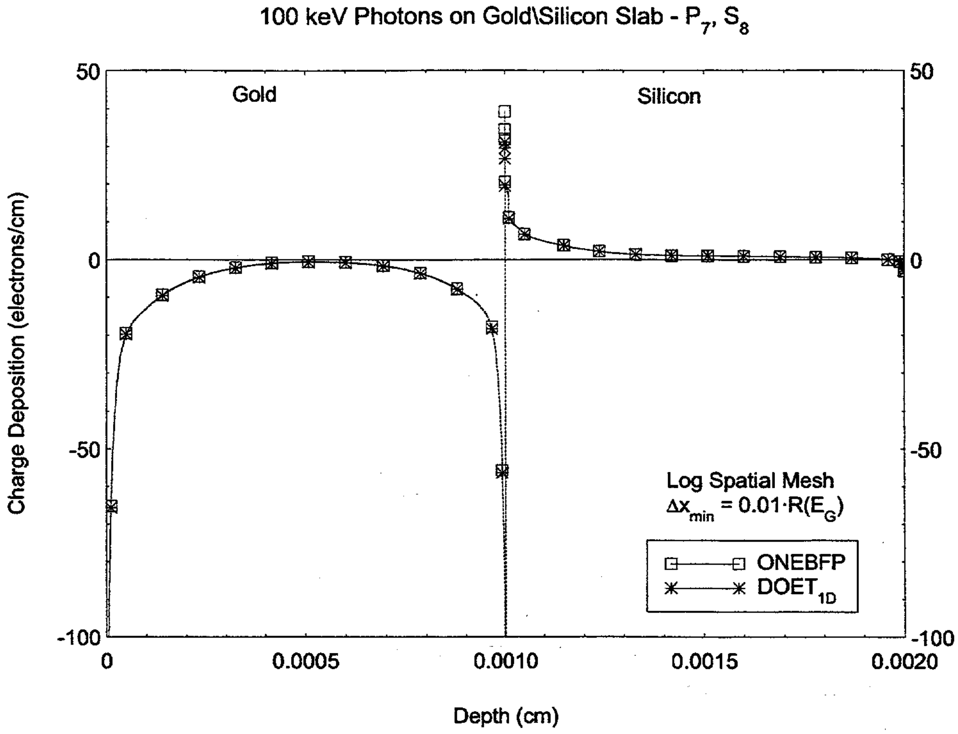

Figure 8.12: Charge Deposition in Au\Si for Log $\Delta x_{min} = 0.01 \cdot R_{min}$

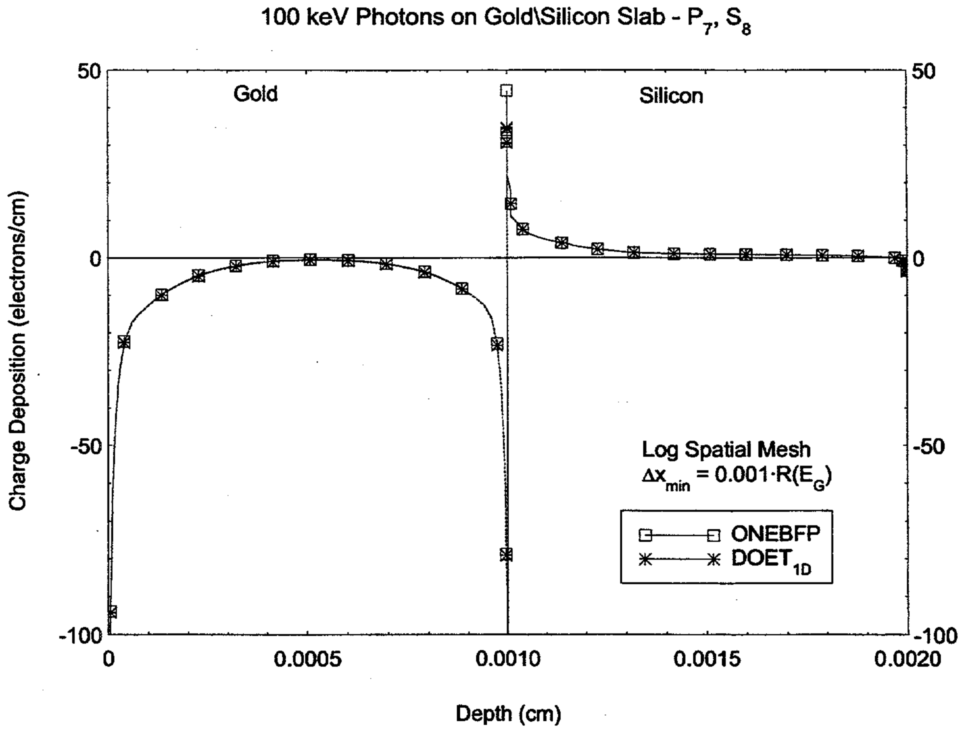

Figure 8.13: Charge Deposition in Au\Si for Log $\Delta x_{min} = 0.001 \cdot R_{min}$

Thus, it can be concluded that DOET_{1D} is fairly accurate in determining the energy and charge deposition for this problem.

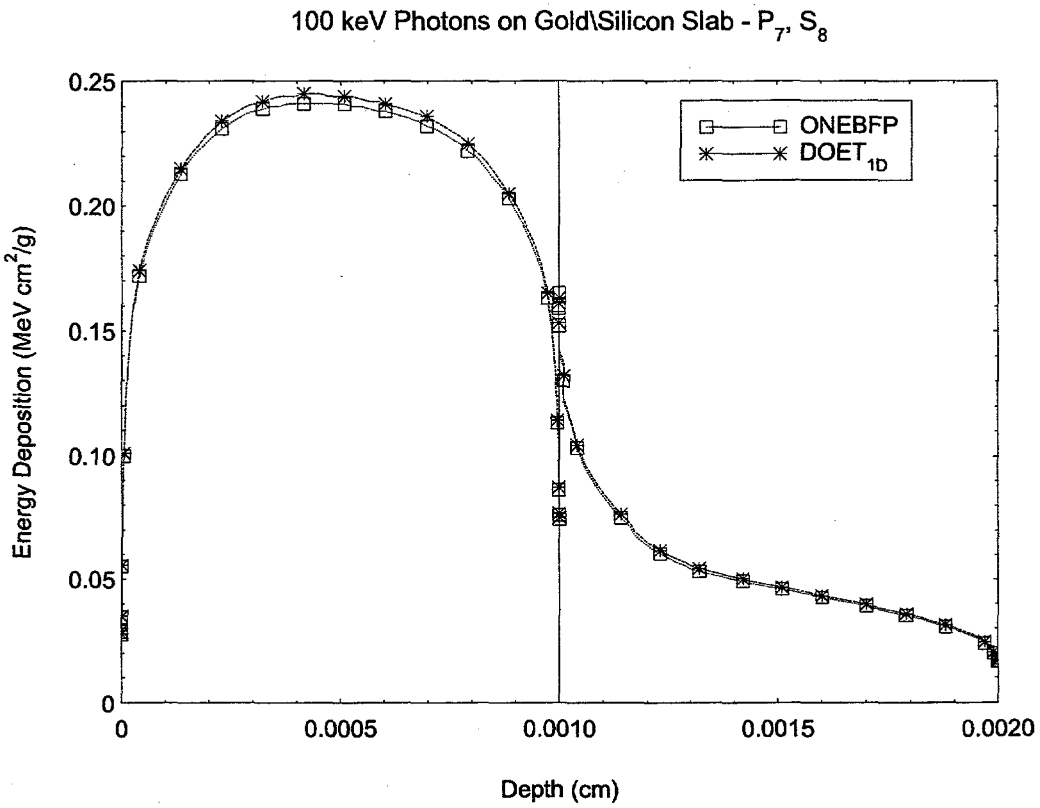

Figure 8.14: Energy Deposition in Au\Si

8.4 50 keV Photons Incident on a Cable

This problem represents the type of dimensions and materials that make up a cable for which SGEMP is important.[39] This is a slab of 5 material layers whose thicknesses and compositions are presented in Table 8.4. PTFE is composed of 0.2402 C(Z=6) and 0.7598 F(Z=9).

The Legendre order of scattering is P_{15} with a quadrature order of S_{16}. The energy structure is 40 linear photon groups and 80 logarithmic electron energy groups with a cutoff energy of 1 keV. A logarithmic spatial mesh is used with $\Delta x_{min} = 0.01 \cdot R_{min}$ for ONEBFP since refining the mesh more would not run. The DOET_{1D}

Table 8.4: Cable Material Layers

Layer	Material	Thickness (μ)	Z	Density (g/cm^3)
1	Cu	274	29	8.96
2	PTFE	905.3		2.2
3	Ag	12	47	10.5
4	Cu	116	29	8.96
5	Fe	478	26	7.86

profiles are for the converged solution which is at a logarithmic spatial mesh with $\Delta x_{min} = 0.001 \cdot R_{min}$.

The energy deposition profile across the slab is presented in Figure 8.15. The energy deposition profiles from ONEBFP and DOET$_{1D}$ overlap indicating that the electron energy group structure is adequate for the LD SAAF to have reached convergence. Table 8.5 summarizes the total energy deposited in each material layer. The results indicate that the total energy deposited across the material layers from the LD SAAF solution is ≈1.5% higher than that from ONEBFP.

Table 8.5: Integrated Energy Deposition in the Material Layers

	Total Energy Deposition in keV				
Code	Cu	PTFE	Ag	Cu	Fe
ONEBFP	23.1	0.453	2.02	5.71	8.91
DOET$_{1D}$	23.3	0.460	2.22	5.78	9.02

Figure 8.16 presents the charge deposition profiles from ONEBFP and DOET$_{1D}$ which are essentially indistinguishable from each other. The integrated charge deposition across the layers is presented in Table 8.6. DOET$_{1D}$ does an adequate job of determining the total charge in each of the material layers compared to ONEBFP except for the last layer. DOET$_{1D}$ yields a cumulative charge deposition across all the materials that is ≈ 0.60% higher than that deposited by ONEBFP. Table 8.7 presents the forward and reverse Compton and photo-electron yields at each of the material layers as well as the net number of electrons deposited in each layer. This table shows that DOET$_{1D}$ conserves charge in all the material layers but the last Fe layer while ONEBFP stops conserving charge in the Ag layer.

The results of this problem indicate that the LD SAAF solution can yield accurate results over the scale of a cable SGEMP problem. In fact it is able to

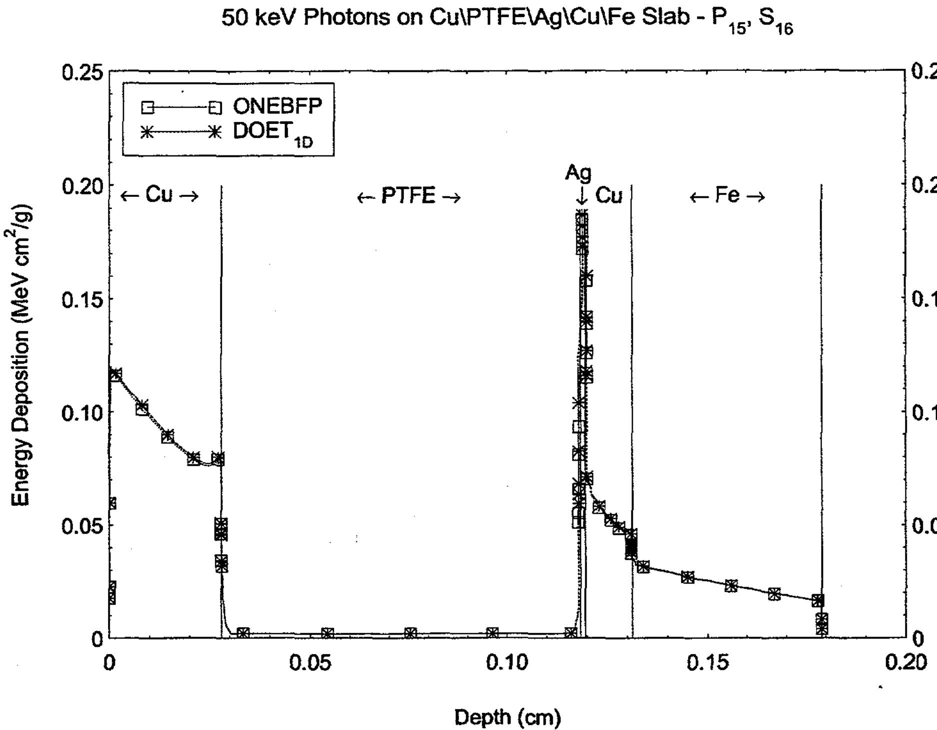

Figure 8.15: Energy Deposition in Cu\PTFE\ Ag\Cu\Fe Slab

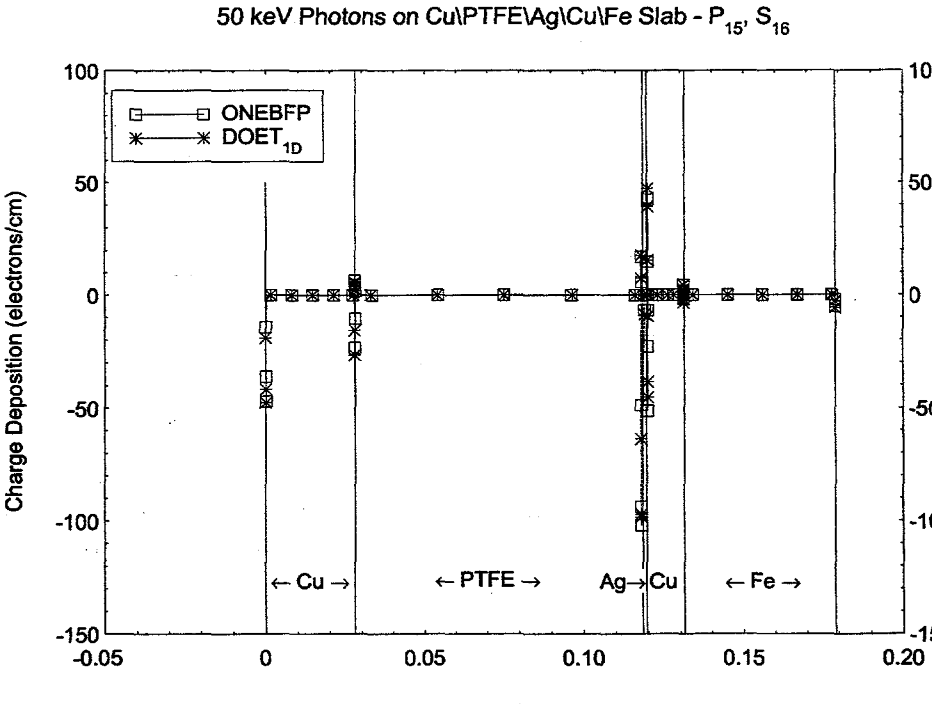

Figure 8.16: Charge Deposition in Cu\PTFE\ Ag\Cu\Fe Slab

conserve the charge better than ONEBFP which might need to use a finer spatial mesh than the code allowed. However, no firm conclusions should be made regarding DOET_{1D}'s ability to model cable SGEMP until it is expanded into two-dimensions.

Table 8.6: Integrated Charge Deposition in the Material Layers

	Total Charge Deposition in 10^{-3} electrons				
Code	Cu	PTFE	Ag	Cu	Fe
ONEBFP	-2.57	2.98	-3.02	0.0915	0.00152
DOET_{1D}	-2.62	3.02	-3.07	0.0924	0.00552

Table 8.7: Compton and Photo-Electron Yields in the Material Layers

	Forward Currents ($\mu > 0$)				
	Cu→PTFE x =0.02794 cm	PTFE→Ag x = 0.11847 cm	Ag→Cu x = 0.11967 cm	Cu→Fe x = 0.13127 cm	Fe→vacuum x = 0.17907
ONEBFP	1.55×10^{-3}	5.30×10^{-4}	3.73×10^{-3}	1.27×10^{-3}	3.23×10^{-4}
DOET_{1D}	1.58×10^{-3}	5.40×10^{-4}	3.80×10^{-3}	1.29×10^{-3}	3.28×10^{-4}
	Reverse Currents ($\mu < 0$)				
	Cu→vacuum x =0.0 cm	PTFE→Cu x = 0.02794 cm	Ag→PTFE x = 0.11847 cm	Cu→Ag x = 0.11967 cm	Fe→Cu x = 0.13127 cm
ONEBFP	1.37×10^{-3}	3.50×10^{-4}	2.30×10^{-3}	2.98×10^{-3}	9.30×10^{-4}
DOET_{1D}	1.39×10^{-3}	3.55×10^{-4}	2.34×10^{-3}	2.53×10^{-3}	9.51×10^{-4}
	Net Electron Deposition				
	Cu	PTFE	Ag	Cu	Fe
ONEBFP	-2.57×10^{-3}	2.97×10^{-3}	-2.52×10^{-3}	4.10×10^{-4}	1.70×10^{-5}
DOET_{1D}	-2.61×10^{-3}	3.03×10^{-3}	-3.07×10^{-3}	9.31×10^{-4}	1.11×10^{-5}

8.5 Quantifying the Computational Cost of LD SAAF Equation

An attempt is made to quantify the computational cost of DOET_{1D} compared to ONEBFP. *However, it should be noted that DOET_{1D} is a research code and was not designed to minimize computational costs but rather to fully understand the potential* *of utilizing a finite element solution of the SAAF equation.* DOET$_{1D}$ contains a number of information dumps throughout the calculation process that need to be removed to obtain a better estimate of the CPU time to a converged solution. We believe that removing these dumps will speed up the CPU time by at least a factor of two, but have not tested this theory to date. Table 8.8 presents the ratio of the DOET$_{1D}$ CPU time to that of ONEBFP for the four problems presented in this chapter. It is clear that the research code DOET$_{1D}$ is running slower than the production code ONEBFP, which we expected. However, due to the reasons mentioned earlier this data cannot be used to make a final conclusion regarding the computational costs of the LD SAAF approach.

Table 8.8: Ratio of CPU times for DOET$_{1D}$ to ONEBFP

	DOET$_{1D}$ CPU Time/ ONEBFP CPU Time
6.0 MeV γ's on W	2.05
100 keV γ's on Si	1.25
100 keV γ's on Au\Si	1.50
50 keV γ's on Cu\PTFE\Ag\Cu\Fe	2.85

This page intentionally blank.

9 Conclusions and Future Work

The finite element solution of the self-adjoint, angular flux equation in a one-dimensional, S_n, multigroup code has been implemented. A linear continuous approximation in space and a linear discontinuous approximation in energy were utilized. A successful demonstration of its ability to accurately solve coupled electron-photon problems was made.

The results of the four coupled charge particle problems presented in Chapter 8 indicate that the LD SAAF equation can yield accurate energy and charge deposition profiles in comparison with ONEBFP. The LD discretization in energy coupled with LC in space in DOET_{1D} requires finer energy group structures for the e^- to yield accurate energy deposition profiles. Similarly, accurate charge deposition profiles require very refined logarithmic spatial cells at the material interfaces. ONEBFP generally converges quicker in energy and space than DOET_{1D} but overall the LD SAAF solution compares well with the linear nodal discretization schemes used in ONEBFP.

Acceleration schemes were derived and implemented successfully in DOET_{1D} to decrease the rate of convergence for both the LD upscatter iteration and the scattering source iteration. A consistent synthetic source acceleration scheme (DSA) was derived and implemented in DOET_{1D} to improve the rate of convergence of the scattering source iteration (see Chapter 5). In Chapter 6 the derivation of an upscatter acceleration scheme to improve the rate of convergence of the upscatter iteration introduced by the LD energy discretization was successfully derived and implemented in DOET_{1D}.

A true comparison of the computational costs of ONEBFP and DOET_{1D} needs to be made to discern whether or not the LD SAAF equation offers any benefits over ONEBFP. At present there is difficulty in comparing the computational costs of ONEBFP and DOET_{1D} because the latter is a research code with a large number of information being written to output files that add to the run time while ONEBFP is a production code. The solution of the transport equations in DOET_{1D} is expected to be faster because it simultaneously solves the angular fluxes at each mesh point while ONEBFP uses a traditional sweeping algorithm. However, the LD energy discretization requires the upscatter acceleration which adds to the computational time. DOET_{1D} was developed as a research tool in order to evaluate the potential of applying the LD SAAF equation to charged particle problems. The true computational benefits of the LD SAAF equation may not be observed until it is implemented in multi-dimensions and on a parallel computing environment to take advantage of the symmetric, positive definite matrix. When this is achieved comparisons will need to be made with a similar multidimensional, parallelized first-order code to assess the benefits in computation time as well as evaluate the accuracy of solving the SAAF equation.

While the potential of applying the finite element solution of the SAAF equation to coupled electron-photon problems was demonstrated in one-dimension, to truly evaluate its applicability it needs to be expanded in multidimensions. Implementing the SAAF equation in multidimensions will require reevaluating the effectiveness of the acceleration schemes considered here. Implementing higher order finite element trial functions in both space and energy should also be evaluated. Finally, an effective method for solving void regions needs to be developed.

APPENDIX

Sample Block LD SAAF Solutions

A few results are presented here to demonstrate that the block LD solution presented in Chapter 4 (pg. 44) of the SAAF equations is valid.

High Energy Photons Incident on Tungsten

Figures A-1 and A-2 depict the energy and charge deposition for 6.0 MeV photons on a W slab in comparison to ONEBFP and the LD SAAF solution with upscatter iteration. The Block LD solution yields the same results as the iterative LD SAAF solution.

100 keV γ Incident on a Gold\Silicon Slab

Similarly, Figures A-3 and A-4 depict the charge and energy deposition profiles for 100 keV photons on a Au\Si slab in comparison to ONEBFP and the LD SAAF solution with upscatter iteration. The Block LD solution yields the same results as the iterative LD SAAF solution.

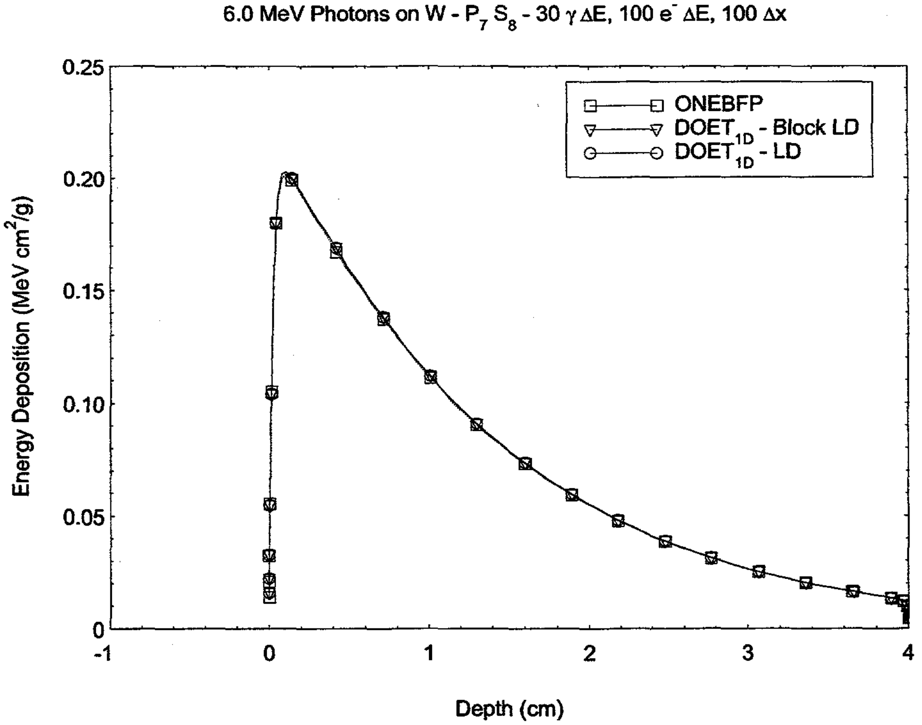

Figure A-1: Block LD Energy Deposition Profile for 6.0 MeV Photons on W

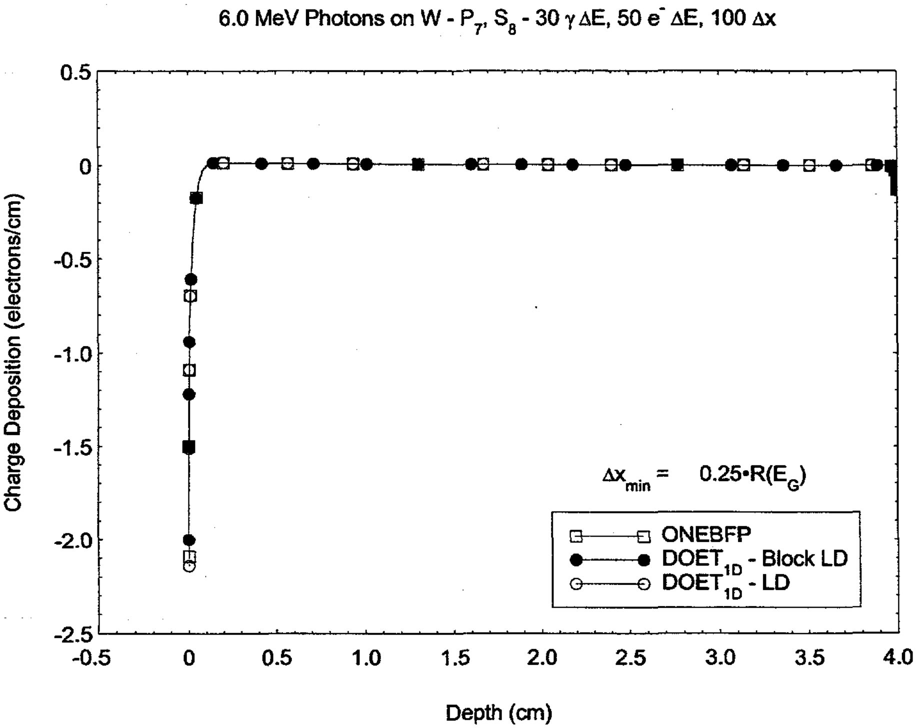

Figure A-2: Block LD Charge Deposition Profile for 6.0 MeV Photons on W

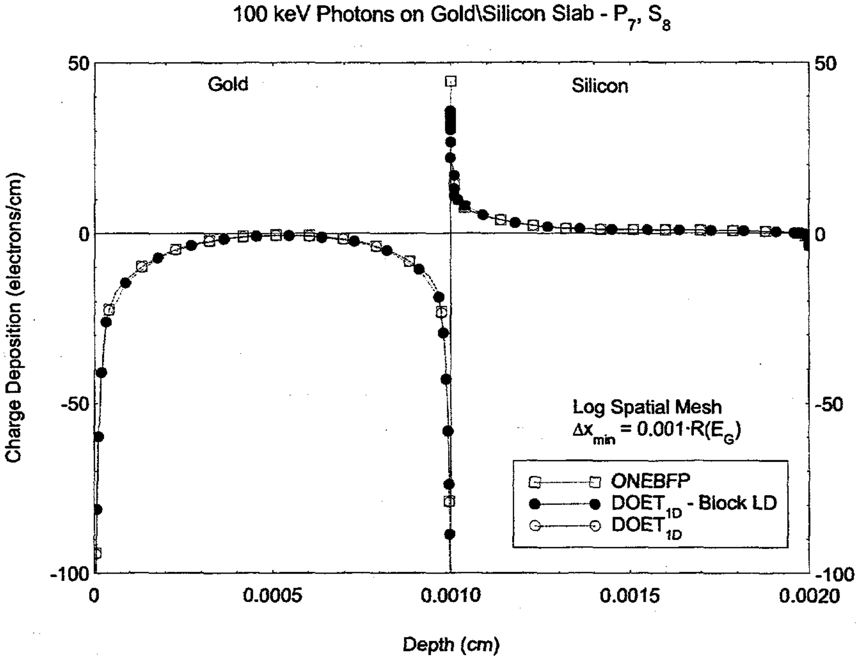

Figure A-3: 100 keV Photons on Au\Si Block LD Charge Deposition Profile

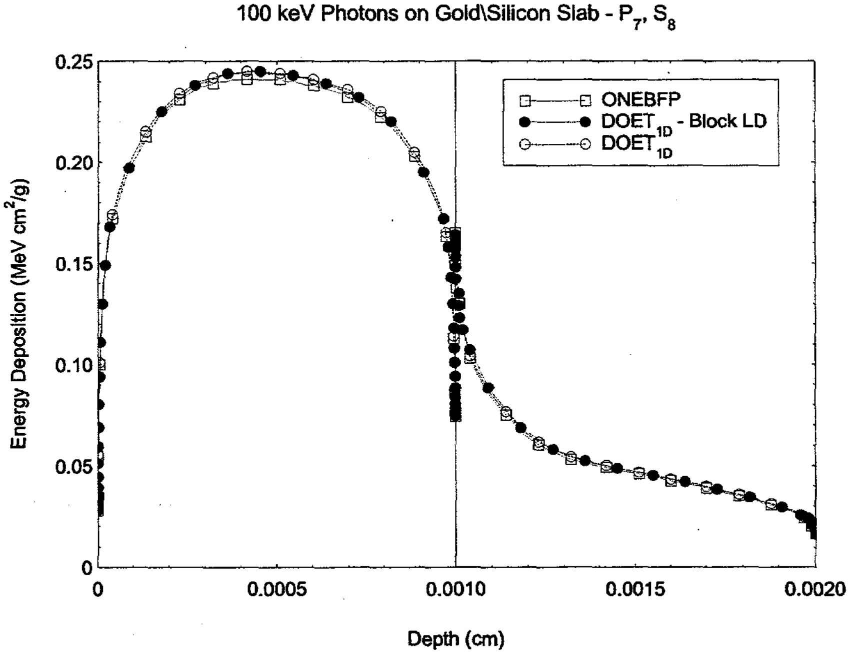

Figure A-4: 100 keV Photons on Au\Si Block LD Energy Deposition Profile

This page intentionally blank.

References

[1] L. J. Lorence, Jr. and D. E. Beutler. Radiation Transport Phenomena and Modeling Part A: Codes. Technical report, Sandia National Laboratories, Albuquerque, NM, 1997. Sandia Report SAND97-2135.

[2] B. C. Passenheim. *How To Do Radiation Tests.* Ingenuity Ink, San Diego, California, 1988.

[3] M. J. Berger. Monte Carlo Calculation of the Penetration and Diffusion of Fast Charged Particles. In B. Alder and S. Fernbach, editors, *Methods of Computational Physics Volume 1.* Academic Press, New York, 1963.

[4] J. A. Halbleib and T. A. Mehlhorn. The Integrated TIGER Series (ITS) of Coupled Electron/Photon Monte Carlo Transport Codes. *Nuclear Science and Engineering*, 92:338–339, 1986.

[5] E. E. Lewis and W. F. Miller, Jr. *Computational Methods of Neutron Transport.* American Nuclear Society, La Grange Park, Illinois, 1993.

[6] Oak Ridge National Laboratory. ONEDANT: A One-Dimensional, Multigroup, Diffusion-Accelerated Neutral Particle Transport Code. Technical report, Oak Ridge National Laboratory Code Distribution Center, Oak Ridge, Tennessee, 1980. CCC-428.

[7] T. A. Mehlhorn and J. J. Duderstadt. A Discrete Ordinates Solution of the Fokker-Planck Equation Characterizing Charged Particle Transport. *Journal of Computational Physics*, 38:86–106, 1982.

[8] K. Pryzbylski and J. Ligou. Numerical Analysis of the Boltzmann Equation Including Fokker-Planck Terms. *Nuclear Science and Engineering*, 81:92–109, 1982.

[9] L. J. Lorence, Jr., J. E. Morel, and G. D. Valdez. *Users Guide to CEPXS/ONEDANT: A One-Dimensional Coupled Electron-Photon Discrete Ordinates Code Package Version 1.0.* Sandia National Laboratories, Albuquerque, New Mexico, September 1989.

[10] D. E. Bartine, R. G. Alsmiller, Jr., F. R. Mynatt, W. W. Engle, Jr., and J. Bariah. Low-Energy Electron Transport by the Method of Discrete Ordinates. *Nuclear Science and Engineering*, 48:159–178, 1972.

[11] J. E. Morel. On the Validity of the Extended Transport Cross-Section Correction for Low-Energy Electron Transport. *Nuclear Science and Engineering*, 71:64–71, 1979.

[12] L. J. Lorence, Jr., W. E. Nelson, and J. E. Morel. Coupled Electron-Photon Transport Calculations Using the Method of Discrete Ordinates. *IEEE Transactions on Nuclear Science*, 32(6):4416–4420, 1985.

[13] L. J. Lorence, Jr. Electron Photoemission Predictions with CEPXS/ONETRAN. *IEEE Transactions on Nuclear Science*, 35(6):1288–1291, 1988.

[14] J. E. Morel. Personal Communications. LANL's ONEBFP code, 1997.

[15] J. F. Breismeister. *MCNP: Monte Carlo Coupled Neutron Photon Transport Code.* Los Alamos National Laboratory, Los Alamos, New Mexico, 1993.

[16] T. A. Wareing, J. M. McGhee, and J. E. Morel. Attila: A three-dimensional, unstructured tetrahedral mesh discrete ordinates transport code. *Transactions of the American Nuclear Society*, 75:146–147, 1996.

[17] W. F. Miller, Jr. An Analysis of the Finite Differences, Even-Parity, Discrete Ordinates Equations in Slab Geometry. *Nuclear Science and Engineering*, 108:247–266, 1991.

[18] J. A. Josef and J. E. Morel. Simplified Spherical Harmonic Method for Couple Electron-Photon Transport Calculations. *Physical Review E*, 57, Number 5:6161–6171, 1998.

[19] J. E. Morel and J. M. McGhee. A Self-Adjoint Angular Flux Equation. *Nuclear Science and Engineering*, 132:312–325, 1999.

[20] J. E. Morel and J. M. McGhee. A Diffusion-Synthetic Acceleration Technique for the Even-Parity S_n Equations with Anisotropic Scattering. *Nuclear Science and Engineering*, 120:147–164, 1995.

[21] T. Noh, W. F. Miller, Jr., and J. E. Morel. The Even-Parity and Simplified Even-Parity Transport Equations in Two-Dimensional x-y Geometry. *Nuclear Science and Engineering*, 123:38–56, 1996.

[22] Robley D. Evans. *The Atomic Nucleus.* Krieger Publishing Company, Malabar, Florida, 1955.

[23] James E. Turner. *Atoms, Radiation and Radiation Protection.* John Wiley and Sons, Inc., New York, second edition, 1995.

[24] L. J. Lorence, Jr., J. E. Morel, and G. D. Valdez. *Physics Guide to CEPXS: A Multigroup Coupled Electron-Photon Cross-Section Generating Code Version 1.0.* Sandia National Laboratories, Albuquerque, New Mexico, October 1989.

[25] G. I. Bell and S. Glasstone. *Nuclear Reactor Theory.* Krieger Publishing Company, Malabar, Florida, 1970.

[26] J. E. Morel. Fokker-Planck Calculations Using Standard Discrete Ordinates Transport Codes. *Nuclear Science and Engineering*, 79:340–356, 1981.

[27] J. E. Morel. Multigroup legendre coefficients for the diamond difference continuous slowing down operator. *Nuclear Science and Engineering*, 91:324–331, 1985.

[28] M. S. Lazo and J. E. Morel. A Linear Discontinuous Galerkin Approximation for the Continuous Slowing Down Operator. *Nuclear Science and Engineering*, 92:98–109, 1986.

[29] J. J. Honrubia and J. M. Aragones. Finite Element Method for Charged-Particle Calculations. *Nuclear Science and Engineering*, 93:386–402, 1986.

[30] M. L. Adams and W. R. Martin. Boundary Projection Acceleration: A New Approach to Synthetic Acceleration of Transport Calculations. *Nuclear Science and Engineering*, 100:177–189, 1988.

[31] K. M. Khattab and E. W. Larsen. Synthetic Acceleration Methods for Linear Transport Problems with Highly Anisotropic Scattering. *Nuclear Science and Engineering*, 107:217–227, 1991.

[32] R. E. Alcouffe. Diffusion Synthetic Acceleration Methods for the Diamond Differences-Discrete Ordinates Equations. *Nuclear Science and Engineering*, 64:344–355, 1977.

[33] W. F. Miller, Jr., E. E. Lewis, and E. C. Rossow. The Application of Phase-Space Finite Elements to the Two-Dimensional Neutron Transport Equation in X-Y Geometry. *Nuclear Science and Engineering*, 52:12–22, 1973.

[34] J. E. Morel. Personal Communications. Self-Adjoint Form of Transport Equation, 1997.

[35] L. J. Lorence, Jr., J. E. Morel, and E. W. Larsen. A S_2 Synthetic Acceleration Scheme for the One Dimensional S_n Equations with Linear Discontinuous Spatial Differencing. *Nuclear Science and Engineering*, 101:341–251, 1989.

[36] J. E. Morel and T. A. Manteuffel. An Angular Multigrid Acceleration Technique for S_n Equations with Highly Forward-Peaked Scattering. *Nuclear Science and Engineering*, 107:330–342, 1991.

[37] G. H. Golub and C. F. Van Loan. *Matrix Computations.* The John Hopkins University Press, Baltimore, Maryland, third edition, 1996.

[38] W. H. Press, S. A. Teukolsky, W. T. Vetterling, and B. P. Flannery. *Numerical Recipes in Fortran.* John Wiley and Sons, Inc., New York, second edition, 1992.

[39] L. J. Lorence, Jr. Personal Communications. SGEMP and IEMP problems for validation of code, January 2000.

DISTRIBUTION:

2 University of New Mexico
Department of Chemical and Nuclear Engineering
ATTN: A.K. Prinja
N.F. Roderick
Farris Engineering Center, Rm. 209
Albuquerque, NM 87131-1341

1 University of New Mexico
Department of Electrical and Computer Engineering
ATTN: S. Humphries
EECE Building, Rm. 125
Albuquerque, NM 87131-1356

1 Los Alamos National Laboratory
ATTN: J.E. Morel
MS D409
X-6 Transport Methods
Los Alamos, NM 87545

	MS		ORG
1	1166	C.R. Drumm	15332
1	1166	W.F. Fan	15332
1	1179	D.E. Beutler	15341
1	1179	B.P. Franke	15341
1	1179	R.P. Kensek	15341
10	1179	J. Liscum-Powell	15341
1	1179	J.R. Lee	15340
1	1179	L.J. Lorence	15341
1	1202	L.A. Miller	5902
1	9202	W.P. Ballard	8418
1	9018	Central Technical Files	8940-2
2	0899	Technical Library	9616
2	0612	Review and Approval Desk For DOE/OSTI	9612